Title

High Efficiency Terahertz Free Electron Laser

Author

Fisher, Andrew

Publication Date

2024

UNIVERSITY OF CALIFORNIA
Los Angeles

High Efficiency Terahertz Free Electron Laser

A dissertation submitted in partial satisfaction
of the requirements for the degree
Doctor of Philosophy in Physics

by

Andrew Charles Fisher

2024

ABSTRACT OF THE DISSERTATION

High Efficiency Terahertz Free Electron Laser

by

Andrew Charles Fisher
Doctor of Philosophy in Physics
University of California, Los Angeles, 2024
Professor Pietro Musumeci, Chair

Despite the rapid development of novel THz sources in the last few decades, free electron lasers remain attractive due to their unique advantages including frequency tunability and high peak power. While most THz-FEL facilities use optical cavities to build power over many passes, the ability to extract a significant fraction of the beam energy in a single pass paves the way towards high average power as the repetition rate of electron sources is increased.

In this dissertation, we study theoretically and experimentally a compact THz-FEL for improved single pass efficiency. At long wavelengths, FEL gain is limited by diffraction as well as slippage between the radiation and electron beam, requiring long bunch lengths for a sustained interaction. The introduction of a waveguide transversely confines the radiation and can be chosen to match the subluminal group velocity to the longitudinal electron beam velocity. This so-called zero-slippage operation extends the interaction length for short, high current beams allowing us to leverage developments in high brightness RF photoinjector sources. Strong seeding with a prebunched beam enables large decelerating gradients where resonance is maintained with strong undulator tapering, enhancing the extraction efficiency.

After beginning with the theory of waveguide FELs and zero-slippage resonance, we present our simulation code GPTFEL, a custom element built on top of the 3D particle tracking code General Particle Tracer. The code simulates free-space and waveguide FEL interactions by decomposing the electromagnetic fields into a basis of frequency and spatial modes, evolving the complex amplitudes according to energy conservation with the beam and enabling start-to-end beamline simulations within a single code. Waveguide dispersion is naturally included and for free-space interactions, a source dependent expansion is implemented to limit the required number of transverse modes.

Two Tessatron experiments were performed on the UCLA Pegasus beamline using a meter long, helical undulator designed for maximum FEL coupling. The undulator commissioning used both pulsed-wire and Hall probe measurements to minimize trajectory and phase errors. Due to the enclosed geometry and large beam trajectory amplitude, it was necessary to develop a 3D pulsed-wiring technique to align the wire and tune higher order field moments.

The first experiment demonstrated 10% energy efficiency from a 200 pC electron beam at 165 GHz by seeding with the beam compressed to sub-wavelength scale. To enhance the spectral range, a second experiment utilized beamline upgrades including laser shaping on novel photocathodes and a compact permanent magnet chicane to prepare a prebunched, multipeak charge distribution at the undulator. By operating with a beam energy above zero-slippage resonance, the frequency was tunable over the experimental energies from 500 to 700 GHz. Future paths of investigation, including resonance with higher waveguide modes or a rectangular geometry, can improve charge transmission and are promising avenues to further expand the spectral reach and application of the source.

The dissertation of Andrew Charles Fisher is approved.

Warren B. Mori

Seth J. Putterman

James Rosenzweig

Pietro Musumeci, Committee Chair

University of California, Los Angeles
2024

To my family..

Table of Contents

LIST OF FIGURES

List of Tables

Acknowledgments

Looking back on my years at UCLA, I consider myself fortunate to have worked in PBPL under an advisor like Pietro. Being a naïve first-year with minimal lab experience, he encouraged me towards experimental physics and taught me how to perform research. Despite having a busy schedule, he always made himself available for feedback about experiments, papers, or talks, and even managed to sneak in a few games of foosball. Now as an older graduate student, I appreciate more his ability to manage collaborations and projects as well as mentoring the graduate students. I honestly can't thank him enough for the impact he has had on my education and career. Thanks to the leadership of Pietro and Jaime, PBPL continues to be successful in research while maintaining a fun atmosphere and and sense of community.

There are many students and staff from my time at PBPL that I would like to mention. I'll always remember the good old days of foosball with Eric, Paul, River, Gerard L., Josh, Krish, Sophie, Max, Pratik, and David G. as well as the lunch and lab conversations with Walter, Monika, Yining, and Atharva. I want to thank the undergraduates, David D., Jason, and Veronica, for sharing in the monotony during the dark days of undulator tuning and pulsed-wiring. For the beamline experiments, a ton of credit goes to Youna who co-led the first THz FEL experiment and Alex for his troubleshooting and knowledge of the hardware. I'd like to thank my PBPL roommates: the Italians, Fabio and Gilles, for their cultural influence on me (however minimal it may be) and Max, for all our conversations and his willingness to take charge planning trips. Thanks to our postdoc and my officemate, Brian, for the daily chats, ping pong, and perfectly filling his role in the lab. I also want to thank Gerard A. and Oliver for their technical expertise and career advice.

I would like to mention a few collaborators that had a strong influence on my thesis work. I want to thank Bas van der Geer for his collaboration on GPT-FEL and for sharing some of his adventurous sailing stories. From Radiabeam, I'd like to thank Tara Hodgetts for her guidance and knowledge on the Theseus undulators (construction funded by SBIR/STTR DE-SC0017102 and DE-SC0018559) and Yung Chen for helping with fiducialization measurements.

I don't take for granted the funding that I have received as a graduate student and would like to thank the Schwinger Foundation for their generous financial support, as well as the U.S. DOE and NSF for supporting my research through grants DE-SC0009914, DE-SC0021190, and PHY-1734215.

Finally, I'd like to specifically mention Kyle Pepple and Tom Ekkens, two teachers that had an early impact on my academic journey. Most importantly, I'd like to acknowledge the support of my family. My brothers, Trent and Travis, set a high standard and kept me well-rounded beyond academics while our parents gave us the love, support, and opportunity necessary to succeed.

VITA

2014-2018	B.S. Math and Physics, Walla Walla University
2018-2019	Teaching Assistant, Physics and Astronomy Department, UCLA
2019-2024	Graduate Student Researcher under Pietro Musumeci, UCLA Particle Beam Physics Laboratory

PUBLICATIONS

Fisher, A., P. Musumeci, and S. B. Van der Geer. ”Self-consistent numerical approach to track particles in free electron laser interaction with electromagnetic field modes.” Physical Review Accelerators and Beams 23.11 (2020): 110702.

Fisher, A., et al. ”Single-pass high-efficiency terahertz free-electron laser.” Nature Photonics 16.6 (2022): 441-447.

Fisher, A., J. Jin, and P. Musumeci. ”Controlling Beam Trajectory and Transport in a Tapered Helical Undulator.” Journal of Synchrotron Radiation, under review, 2024.

Fisher, A., et al. ”Towards Higher Frequencies in a Compact Prebunched Waveguide THz-FEL.” Nature Communications, forthcoming, 2024.

CHAPTER 1

Introduction to Tapered FELs

1.1 Introduction

While interest in terahertz (THz) radiation (0.1-10 THz) dates back to the early 1900s [2], it remains an elusive region of the electromagnetic spectrum in terms of development of sources and detectors. Electronic sources including klystrons, traveling-wave tubes, and backward-wave oscillators are workhorses in the microwave regime, but have reduced power output above 100 GHz due to limitations associated with the wavelength-scale apertures and Ohmic losses in the waveguide structures [3]. On the other hand, advances in infrared laser technology do not directly translate to THz frequencies as photon energies are smaller than molecular band gaps and transitions are susceptible to thermal effects and phonon scattering [4]. Scientific and industrial interest has lead to a significant research effort in the last several decades with various THz sources under current development [5, 6] to fill this so-called "terahertz gap" with applications in time-domain spectroscopy, high-field resonant and non-resonant excitation of solid-state systems, fusion research and high-gradient acceleration, communications, medical or security imaging, and electron paramagnetic resonance [7, 8, 9, 10, 11, 12].

Free electron lasers (FELs), based on the ponderomotive interaction between a relativistic electron beam and electromagnetic field co-propagating in a magnetic undulator, are an attractive candidate for powerful THz sources. They enjoy unique advantages including frequency tunability, high peak power and repetition rates limited only by electron-beam availability. Many FEL facilities have played important roles in the development of THz science [13, 14, 15, 16, 17, 18], with more user facilities coming online [19, 20, 21] and even more planned for future years [22, 23, 24]. However, the impact of FELs extends across the electromagnetic spectrum from THz to hard X-Rays as up to multi-GeV electron beams are used to generate intense radiation down to angstrom wavelengths. There is even current interest in developing facilities with THz-Xray pump probe capabilities [25, 26].

At the same time, the FEL interaction presents some characteristic challenges in the long-wavelength regime as single-pass gain in the undulator is typically limited due to slippage and diffraction effects. The majority of these facilities use many-wavelengths-long electron bunches with relatively low peak current densities in a resonator configuration to build up power in an optical cavity. Advances in high-brightness (high current, low transverse emittance) electron-beam sources [27] enable the generation of ultrafast electron bunches with very high current densities and strong coupling with the radiation, but the difference in longitudinal velocity between the beam and radiation in the undulator leads to a slippage of the field over the current profile which is detrimental to efficient energy extraction for short beams.

Our research combines two different concepts in FEL physics to overcome these challenges and achieve high energy extraction efficiency in a single pass through the undulator. First, we introduce a waveguide that not only transversely contains the radiation, but more importantly matches the subluminal radiation group velocity to the average electron beam velocity. This eliminates slippage such that the radiation envelope remains temporally aligned with the electron beam during the entire interaction, allowing strong compression of the beam to increase FEL gain and generate several-cycle THz pulses with high peak power. This zero-slippage condition has been known for decades, and was recently demonstrated to create energy spread and streaking in a curved-parallel-plate waveguide [28, 29].

Secondly, building on the experience gained over the last decade of UCLA research into highly efficiency FEL and inverse-FEL interactions, we utilize strong seeding and use undulator tapering to enhance the superradiant emission from the electron beam. In a untapered FEL, the interaction length is limited by gain saturation when the decelerated electrons no longer resonate efficiently in the undulator. By tapering the undulator field or period to maintain resonance with the strongly decelerated electrons, it is possible to prolong the interaction beyond this limit. The Tapering Enhanced Stimulated Superradiant Amplification (TESSA) regime was successfully demonstrated at infrared frequencies [30], but with low gain relative to the strong seeding laser. Achieving high-gain at THz frequencies would be an important step towards the ultimate goal of increasing FEL efficiency at shorter (visible and ultraviolet) wavelengths. This dissertation presents the design and results of the two "Tessatron" THz-waveguide FEL experiments conducted on the Pegasus beamline at UCLA to demonstrate high-efficiency in a single pass.

1.1.1 Outline of dissertation

The outline of the dissertation is as follows. In this first chapter, we introduce FELs as one of several notable THz sources and provide a quantitative description of the dynamics in a tapered helical undulator. Important differences from the more common planar undulator geometry are mentioned. After considering the 1D low-gain regime and the pendulum equations describing Hamiltonian motion in the longitudinal phase space, we generalize to the 1D high-gain regime and describe exponential growth and saturation in FELs, motivating the need for tapering to further increase the efficiency. The history of tapered FELs and TESSA is described in more detail and we derive analytical 1D and 3D efficiency estimates for strong tapering in the post-saturation regime. Finally, we introduce waveguide mode theory and detail the zero-slippage operation in waveguide FELs.

The second chapter describes GPTFEL, a custom element developed for the particle tracking code GPT that self-consistently simulates the interaction between radiation and an electron beam in a waveguide or free-space. Though a variety of FEL codes exist, none were sufficient to model our novel waveguide scheme. The code is benchmarked against theory and a popular FEL code, GENESIS, in an FEL amplifier. Additionally, we discuss a connection between waveguide FELs and 1D theory where the beam area is simply replaced by an effective mode area.

Chapter 3 outlines the commissioning of the Theseus undulators used for the Tessatron experiments. The large wiggling trajectory of the nominal low energy beam requires an analysis of beam trajectory and transport, as well as the development of Hall probe and pulsed-wire tuning procedures to ensure correct tuning of the 3D fields, a challenge given the closed geometry of the undulator.

Finally, chapter 4 presents the Pegasus beamline at UCLA and the results of the Tessatron experiments. The first experiment successfully demonstrated high extraction efficiency through zero-slippage operation. The following (Tessatron2) experiment extended the spectral range of the THz-FEL source by seeding with a laser-shaped beam with improved compression in a compact, permanent magnet chicane. Limited frequency tunability was also achieved by detuning from the zero-slippage resonance.

1.2 THz Sources

The first coherent terahertz sources were far-infrared gas lasers developed in the 1960s that utilize transitions between molecular rotation or vibrational states of gas molecules, excited with optical pumping from a CO_2 laser. By using different gases, emission has been demonstrated at distinct lines throughout the terahertz region [31, 32]. They generate tens of milliwatts in continuous operation and up to megawatts in pulsed operation, but due to the limited photon conversion efficiency (0.1-10%) and relatively large footprint (10 cm by 1 m), they have been replaced in part by more compact systems.

For example, compact quantum cascade lasers (QCLs), first demonstrated in the 1990s, are able to generate higher (multi-watt) output powers in the range of 1-5 THz [33]. Instead of relying on electron transitions between the valence and conduction bands, QCLs utilize superlattices made from nanometer-thick layers of alternating semiconductor materials to create a periodic potential well structure that electrons can tunnel between. When a bias is applied, electrons move to higher energy states creating population inversion. The emission wavelength is determined by the superlattice design, and only limited tuning can be achieved with temperature control or discrete Vernier tuning [34]. To limit thermal effects, cryogenic cooling is required.

Laser-driven THz sources have grown in interest due to the recent availability and preva-

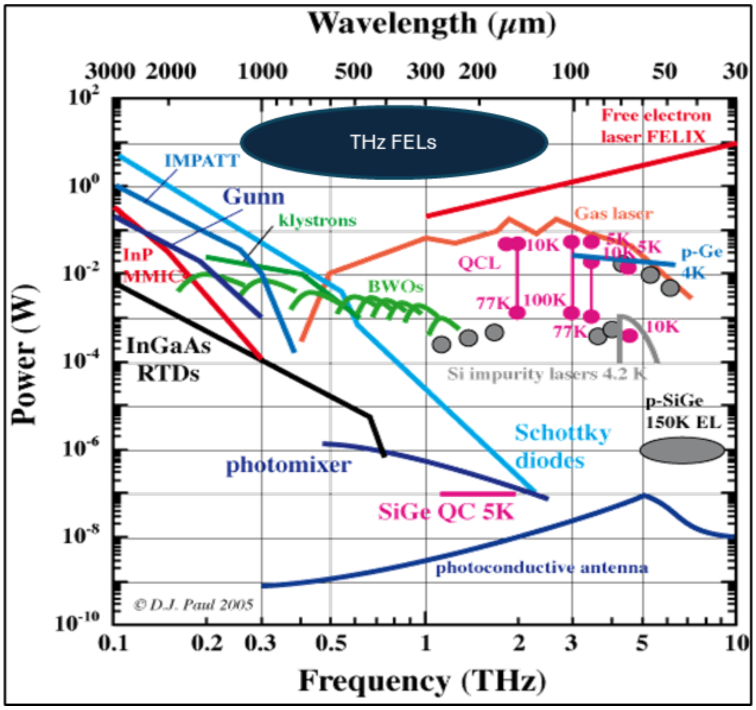

Figure 1.1: An overview of THz sources adapted from [1].

lence of high powered laser systems. Single cycle pulses around 1 THz can be generated through optical rectification of femtosecond pulses in nonlinear crystals such as zinc-telluride (ZnTe), lithium niobate ($LiNbO_3$), or organic crystals. The quadratic dependence of the crystal polarization with respect to the laser field generates a quasi-DC component that emits radiation at a much lower frequency. Phase matching along the crystal is necessary for maximizing the efficiency and can be achieved with pulsed-front tilting [35, 36]

Microwave sources have improved with fast-wave coupling schemes such as gyrotrons that can reach well into the sub-terahertz frequency range (few hundred gigahertz) with relatively higher power and efficiencies in the tens of percent [37, 38]. However, they are still based on the use of mildly or non-relativistic electron beams, reducing the frequency scalability and limiting the maximum peak power available.

Finally, accelerator-based sources are particularly attractive due to the scarcity of high power solid-state sources and because the required electron beam and undulator parameters are readily achievable with current technology [39, 40]. The resonant frequency in FELs can tuned over a large range by changing the beam energy or magnet gaps in the undulator.

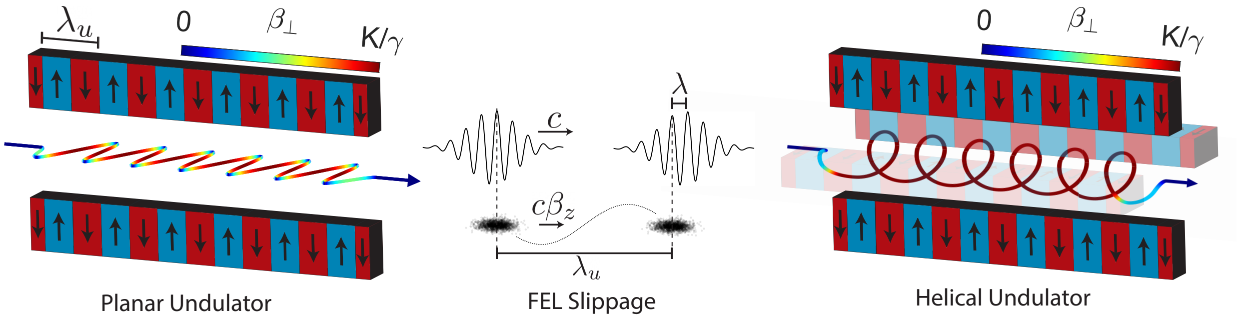

Figure 1.2: A depiction of electron beam trajectories in planar and helical undulator geometries as well as a geometrical interpretation for FEL slippage. The color-coded transverse velocity shows constant coupling in the helical geometry.

Additionally, improvements in electron beam sources and repetition rates will enable higher peak and average powers. We now present a quantitative analysis of 1D FEL dynamics in a helical undulator.

1.3 1D FEL Dynamics

1.3.1 Low Gain, Pendulum Equations

The FEL interaction describes energy exchange between a relativistic electron beam and a radiation field in the presence of a sinusoidal magnetic field, shown in Figure 1.2. A planar undulator consists of magnet arrays with alternating dipole fields that create a wiggling beam trajectory. The interaction can be improved by using a helical undulator where a second magnet array is added in the other perpendicular dimension, shifted by a quarter period, to generate a helical beam trajectory. Assuming a field amplitude B_0 and undulator period λ_u, the on-axis fields are given by

$$\mathbf{B}_u = -B_0 \Big(\pm \cos(k_u z)\hat{\mathbf{x}} + \sin(k_u z)\hat{\mathbf{y}} \Big) \tag{1.1}$$

where the ± denotes field helicity allowing resonance with right/left circularly polarized light. We define right/left circular polarization as clockwise/counter-clockwise rotation of the polarization vector in time at a given position as measured from the upstream source.

The transverse motion of the beam is dominated by the Lorentz forces of the undulator's magnetic fields. Neglecting the relatively small interaction with a radiation field, we have

$$\begin{aligned}\frac{d\mathbf{p}}{dt} &= \mathbf{F}\\ \frac{d}{dt}\left(\gamma mc\boldsymbol{\beta}_\perp\right) &= -ec(\boldsymbol{\beta}_\perp + \beta_z\hat{\mathbf{z}}) \times \mathbf{B}_u\end{aligned}$$

where γ is the relativistic factor related to beam energy by $\gamma = E/mc^2 \approx 1.96 \cdot E[\text{MeV}]$ and $c\boldsymbol{\beta} = \mathbf{v}$. For a relativistic electron beam, $|\boldsymbol{\beta}_\perp|/\beta_z \ll 1$ and $B_{u,z} \approx 0$ near the axis such that the forces are in the transverse plane due to the cross product with the longitudinal velocity, $\beta_z = \frac{1}{c}\frac{dz}{dt}$. We solve for $\boldsymbol{\beta}_\perp$ by inserting Eq. (1.1) and writing the right hand side as a total derivative.

$$\begin{aligned}\frac{d}{dt}\left(\gamma mc\boldsymbol{\beta}_\perp\right) &= eB_0\left(-\sin(k_u z)\frac{dz}{dt}\hat{\mathbf{x}} \pm \cos(k_u z)\frac{dz}{dt}\hat{\mathbf{y}}\right)\\ &= \frac{eB_0}{k_u}\frac{d}{dt}\Big(\cos(k_u z)\hat{\mathbf{x}} \pm \sin(k_u z)\hat{\mathbf{y}}\Big)\\ \boldsymbol{\beta}_\perp &= \frac{K}{\gamma}\Big(\cos(k_u z)\hat{\mathbf{x}} \pm \sin(k_u z)\hat{\mathbf{y}}\Big) \qquad (1.2)\end{aligned}$$

where $K = eB_0/mck_u \approx 0.934 \cdot B_0[\text{T}] \cdot \lambda_u[\text{cm}]$ is defined as the undulator strength parameter and describes the product of the total beam energy and peak transverse velocity. Practical field strengths are limited to less than 1 T while undulator periods are usually on the order of a few centimeters such that K is generally between 1 and 3. For a given beam energy γ, the longitudinal velocity can be written as

$$\beta_z = \sqrt{|\boldsymbol{\beta}|^2 - |\boldsymbol{\beta}_\perp|^2} \quad \implies \quad \beta_z \approx 1 - \frac{1+K^2}{2\gamma^2} \qquad (1.3)$$

where we assume the relativistic limit $\gamma \gg 1$. Ignoring initial conditions, we integrate for the beam position as

$$\mathbf{r}_\perp = \int c\boldsymbol{\beta}_\perp dt = \frac{1}{\beta_z}\int \boldsymbol{\beta}_\perp dz = \frac{K}{\gamma k_u \beta_z}\Big(\sin(k_u z)\hat{\mathbf{x}} \mp \cos(k_u z)\hat{\mathbf{y}}\Big) \qquad (1.4)$$

such that the wiggling trajectory radius is $|\mathbf{r}_\perp| = K/\gamma k_u \beta_z$. For low energy beams, the large trajectory causes sampling of non-zero B_z fields off axis that contribute to the Lorentz force and require corrections to the undulator parameter. This will be covered in detail with the undulator field expansions in Chapter 3.

We now introduce a right/left circularly polarized plane-wave field with an arbitrary phase shift ϕ, considering the low-gain limit where the amount of energy exchanged in the interaction is very small compared to the initial field energy. The electric field is given by

$$\mathbf{E}_l = E_0 \Big(\sin(kz - \omega t + \phi)\hat{\mathbf{x}} \pm \cos(kz - \omega t + \phi)\hat{\mathbf{y}} \Big) \tag{1.5}$$

As magnetic forces do no work, the relativistic energy of the particles changes only due to the work done on the beam by the electric field.

$$\frac{d}{dt}\left(\gamma mc^2\right) = \mathbf{F}\cdot\mathbf{v} = -ec\mathbf{E}_l\cdot\boldsymbol{\beta}_\perp$$

$$\frac{d\gamma}{dt} = \frac{-eE_0K}{mc\gamma}\Big(\sin(kz - \omega t + \phi)\cos(k_u z) + \cos(kz - \omega t + \phi)\sin(k_u z)\Big)$$

$$\boxed{\frac{d\gamma}{dt} = \frac{-ckK_lK}{\gamma}\sin(\theta)} \tag{1.6}$$

where $K_l = eE_0/mc^2k$ is the field strength parameter and $\theta = (k_u + k)z - \omega t + \phi$ is known as the ponderomotive phase which describes the effective interaction between the electrons and radiation. Assuming an infinitely long beam, the system is periodic and we can restrict our attention to a single period where $\theta \in [-\pi, \pi]$.

While this coupling is constant in a helical geometry, Figure 1.2 shows the sinusoidal trajectory in a planar undulator where the transverse velocity and coupling vanishes at the turning points. Additionally, the non-uniform β_z leads to a figure-8 motion in the beam reference frame. In this case, the deceleration is defined in terms of the average velocity and requires an additional factor of $JJ/2$ where $JJ = (J_0(G) - J_1(G))$, J_n is the nth Bessel function, and $G = K^2/4(1 + K^2/2)$. Depending on field strength, JJ ranges from 0.7 to 1 such that a helical undulator can achieve gradients a factor or 2 or larger than a planar undulator [41].

At different values of θ, electrons either give energy to or absorb energy from the radiation fields. For net energy change to occur, the ponderomotive phase must be nearly constant. The FEL phase resonance condition is derived by requiring the ponderomotive phase to be constant.

$$\frac{d\theta}{dt} = 0 \quad\Longrightarrow\quad \boxed{\omega = c\beta_z\Big(k_u + k\Big) \quad \text{for any } \omega(k)} \tag{1.7}$$

A physical explanation is that the radiation slips ahead of the electron beam one radiation wavelength every undulator period, as shown in Figure 1.2. Equation (1.7) describes FEL phase resonance for any dispersion relation $\omega(k)$, but to simplify the analysis (which so far extends generally to waveguide FELs) we now assume a free-space interaction and substitute the expression for β_z from Eq. (1.3),

$$\boxed{\lambda = \frac{\lambda_u}{2\gamma_r^2}(1 + K^2) \quad \text{assuming } \omega = ck} \tag{1.8}$$

giving the radiated wavelength in terms of the undulator period, undulator strength parameter and resonant beam energy, γ_r. This equation demonstrates the incredible tuning range of an FEL. For reasonable values of $K = 3$ and $\lambda_u = 2$ cm, varying the beam energy from 100 MeV to 10 GeV allows lasing from micron to attosecond wavelengths.

To understand the longitudinal phase space evolution for particles close to the resonant energy, we define the normalized energy variable $\eta = (\gamma - \gamma_r)/\gamma_r$ about the resonant particle at (θ_r, γ_r) and expand the rate of change equations to lowest order

$$\begin{aligned}
\dot\theta &= c\left(k_u\beta_z + k\beta_z - k\right) & \qquad \dot\eta &= \frac{1}{\gamma_r^2}\left(\dot\gamma\gamma_r - \dot\gamma_r\gamma\right) \\
&\approx ck_u\left(1 + \frac{k}{k_u}\left(\beta_z - 1\right)\right) & &\approx \frac{-ckK_lK}{\gamma_r^2}\left(\sin\theta - \sin\theta_r\right) \\
&\approx ck_u\left(1 - \frac{k}{\cancel{k_u}}\frac{1 + \cancel{K^2}}{2\gamma_r^2}(1 - 2\eta)\right) & & \\
&\boxed{\dot\theta = 2ck_u\eta} & &\boxed{\dot\eta = -ck_u\frac{2K_lK}{1 + K^2}\left(\sin\theta - \sin\theta_r\right)}
\end{aligned} \tag{1.9}$$

where $1/\gamma^2 \approx (1-2\eta)/\gamma_r^2$ and explicit reference to γ_r is removed with Eq. (1.8). This system can be expressed using Hamiltonian dynamics where

$$\boxed{H(\theta, \eta) = ck_u\left(\eta^2 - \frac{2K_lK}{1 + K^2}(\cos\theta + \theta\sin\theta_r)\right)} \tag{1.10}$$

with $\partial H/\partial\eta = \dot\theta$ and $\partial H/\partial\theta = -\dot\eta$. Equivalently, this can be derived as an approximation to the single particle Hamiltonian [42]. Hamiltonian theory states that particles follow paths of constant value, $H(\theta, \eta)$. Thus if a contour of the Hamiltonian encloses the resonant point (θ_r, η_r) and has value greater than $H(\theta_r, \eta_r)$, the interior is a stable region where particles rotate in phase space around the resonant position. The contour with maximal value is

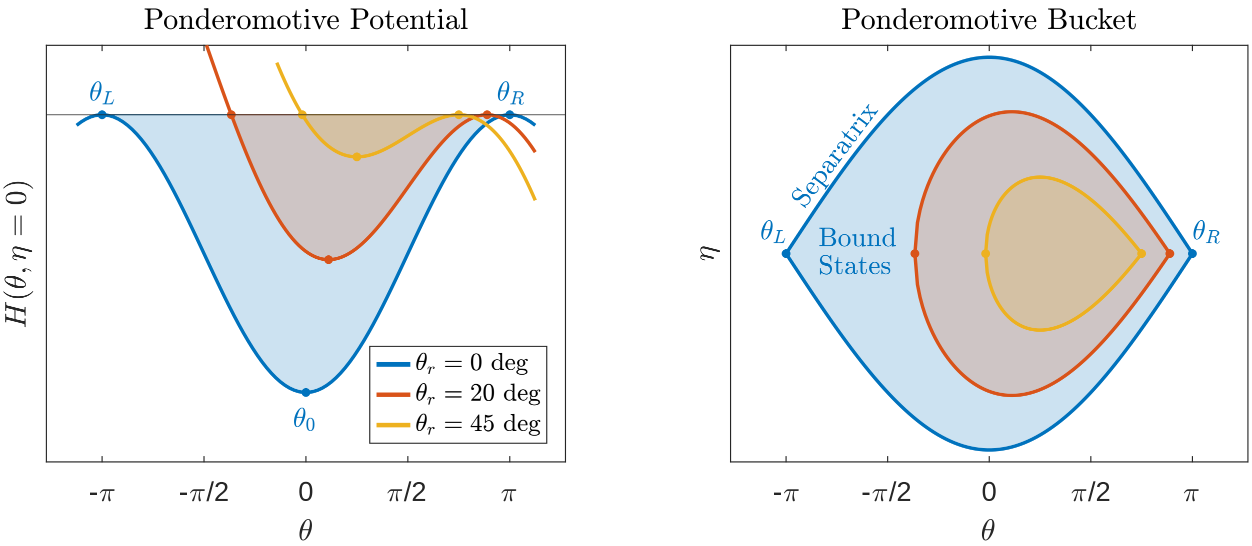

Figure 1.3: The ponderomotive potential and bucket for different resonant phases. For a bound state inside the separatrix, particles will rotate around the resonant point in the bucket and oscillate in the potential well.

known as the separatrix as it separates the stable, bound particles states from the scattered, unbounded particle states.

The function $H(\theta, 0)$ is referred to as the ponderomotive potential and is plotted in the left panel of Figure 1.3 for a few resonant phases. Recall from Eq. (1.6) that positive resonant phases corresponds to net deceleration. At negative resonant phases, particles experience net acceleration where that the ponderomotive potential is simply mirrored across the line $\theta = 0$. This is known as the inverse-FEL interaction where a powerful seed laser can be used to achieve large accelerating gradients. As we are only concerned with energy extraction, we assume $\theta_r \geq 0$ in our analysis.

The points of interest along the ponderomotive potential are the minimum (θ_0) and the bounds θ_L, θ_R which can be seen as stable and unstable turning points, respectively. Both θ_0 and θ_R are simply evaluated by setting the derivative of the potential equal to zero

$$\frac{\partial}{\partial\theta} H(\theta, 0) = 0 \implies \sin\theta = \sin\theta_r \tag{1.11}$$

where the two solutions in $[0, \pi]$ yield the expected trivial solution $\theta_0 = \theta_r$ and $\theta_R = \pi - \theta_r$. For $\theta_r \geq \pi/2$, the potential well vanishes and there are no bound trajectories. The left edge

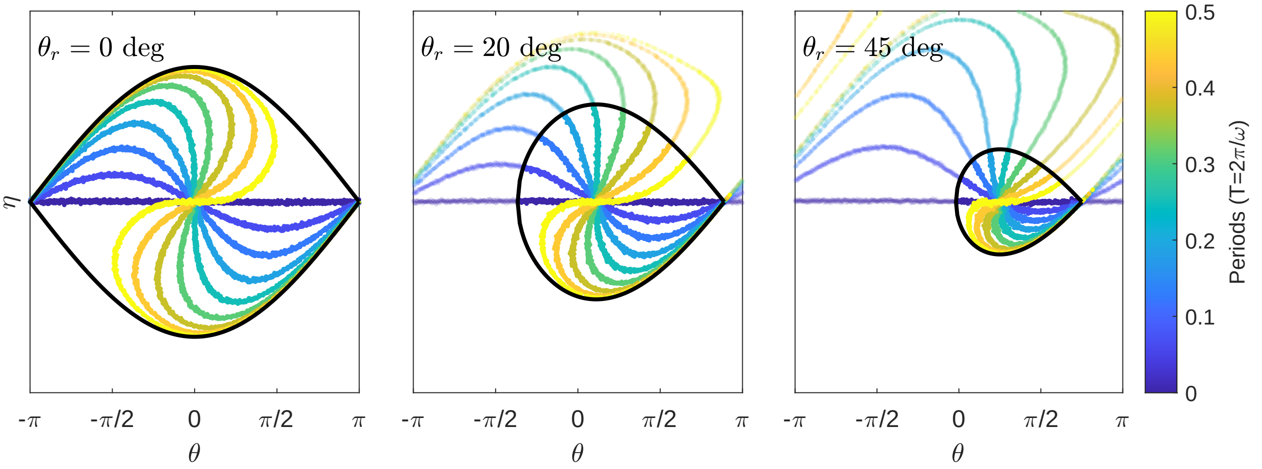

Figure 1.4: A comparison of 1D numerical simulations for $\gamma = 100$ against the Hamiltonian formalism. The simulation is run for half a synchrotron period and initially detrapped particles are given a reduced opacity. The minor discrepancies are due to the near-resonance approximation in the derivation of the Hamiltonian.

has to be solved numerically using $H(\theta_L, 0) = H(\theta_R, 0)$ as

$$\cos\theta_L + \theta_L \sin\theta_r = \cos(\pi - \theta_r) + (\pi - \theta_r)\sin\theta_r \tag{1.12}$$

The Hamiltonian is constant along the separatrix such that we can solve the boundary of the so-called ponderomotive bucket using $H(\theta, \eta) = H(\theta_R, 0)$ such that

$$\eta_{sep}^2 = \frac{2K_l K}{1+K^2}\Big(\cos\theta - \cos(\pi - \theta_r) + (\theta + \theta_r - \pi)\sin\theta_r\Big) \tag{1.13}$$

which is plotted in the right panel of Figure (1.3). It is clear that when targeting strong decelerating gradients at large resonant phases, the area of the ponderomotive bucket is decreased which limits the fraction of electrons that are trapped in the ponderomotive bucket from which energy can be extracted.

The system of Eq. (1.9) can also be expressed as a second order ordinary differential equation

$$\ddot{\theta} - \omega_0^2\Big(\sin\theta - \sin\theta_r\Big) = 0 \quad \text{where} \quad \omega_0 = 2ck_u\sqrt{\frac{K_l K}{1+K^2}} \tag{1.14}$$

which is identical to the motion of a simple pendulum when $\theta_r = 0$. If we consider small oscillations ($d\theta \ll 1$) around the resonant point in phase space such that $\theta = \theta_r + d\theta$,

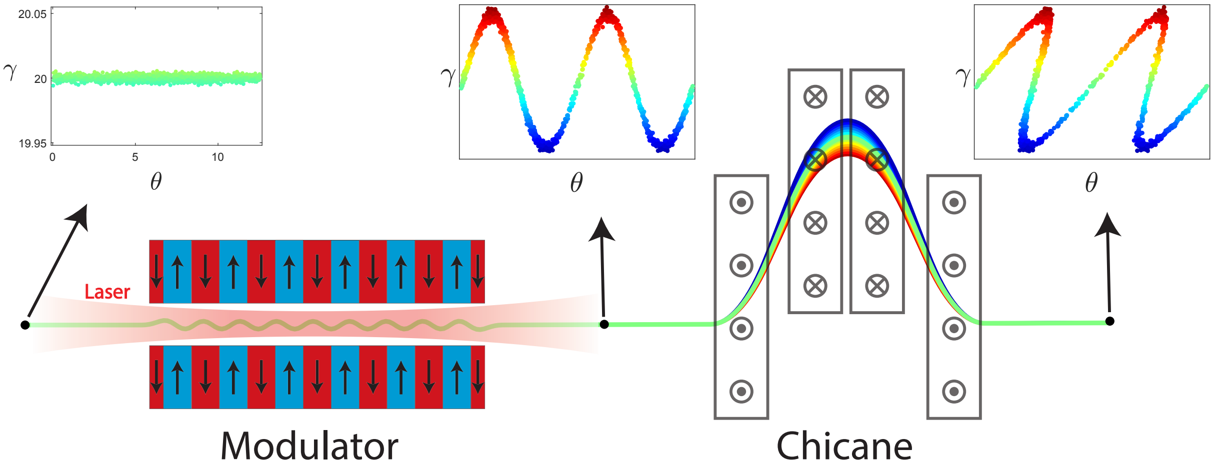

Figure 1.5: Schematic of a single buncher (not to scale) consisting of an untapered undulator section to modulate the beam energy and a dispersive chicane to create density bunching.

the differential equation simplifies to simple harmonic motion with an angular frequency of $\omega = \omega_0\sqrt{\cos\theta_r}$. Figure 1.4 shows a comparison between a 1D numerical simulation and the approximate Hamiltonian system. The simulation is run for half a synchrotron period $(0.5 * 2\pi/\omega)$ at an energy of $\gamma = 100$. Near resonance, particles complete half a rotation, but the angular velocity slows significantly for particles near the edge of the ponderomotive bucket. The intuition gained from this analysis of phase space evolution in the low-gain regime is relevant to high-gain interactions as well.

For example, we consider the trade off between electron trapping and deceleration gradient when optimizing overall efficiency. If we assume only electrons within the ponderomotive bucket are decelerated with a gradient proportional to $\sin\theta$, then the efficiency scales with $f_t \sin\theta_r$ where f_t is the fraction of trapped electrons. Clearly, larger efficiencies can be achieved if the electron beam is manipulated to increase the number electrons trapped within the bucket separatrix. Physically, this concentration in phase space corresponds to a periodic density modulation of the electron beam at the radiation wavelength known as microbunching or prebunching.

Figure 1.5 shows a beam can be prebunched using an untapered undulator (modulator) and dispersive chicane. In the modulator, the beam energy is modulated due to the FEL

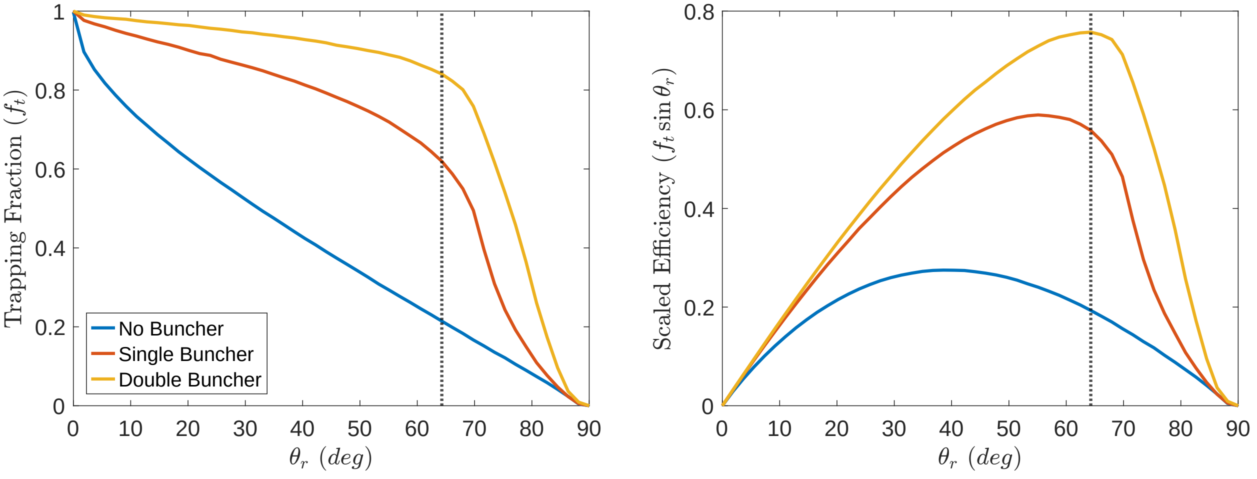

(a)

(b)

Figure 1.6: Optimization of low-gain efficiency with different prebunching schemes. (a) Trapping fraction generally decreases with resonant phase but bunchers retain stronger trapping at higher gradients. (b) Overall efficiency is increased and the optimal resonant phase shifts higher.

interaction with the seed laser. The chicane, composed of 4 dipole magnets, deflects the beam trajectory such that the path length is energy dependent and produces a shearing in the phase space as quantified by the R_{56} element of chicane transport matrix. Thus, the energy modulation is converted to density modulation that improves the capture in the final undulator (radiator). More complicated schemes with multiple modulator/chicane pairs can further improve the microbunching [43].

A general optimization of beam prebunching is complicated by specific design considerations for the undulators, electron beam, and laser transport. Instead, we present a simple example to demonstrate the importance of prebunching. For a single-buncher scheme, we fix the scaled modulator amplitude $A = \Delta\gamma/\sigma_\gamma = 30$ where $\Delta\gamma$ is the maximum energy modulation, and the scaled bucket height $A_{b0} = \sqrt{2K_l K/(1+K^2)}/\sigma_\gamma = 300$. For the double-buncher scheme, an additional upstream modulator/chicane pair is used to first concentrate most of the charge between $-\pi/2$ and $\pi/2$ using a small energy modulation and strong dispersion. Figure 1.6 shows the optimal trapping fractions and scaled efficiency as a

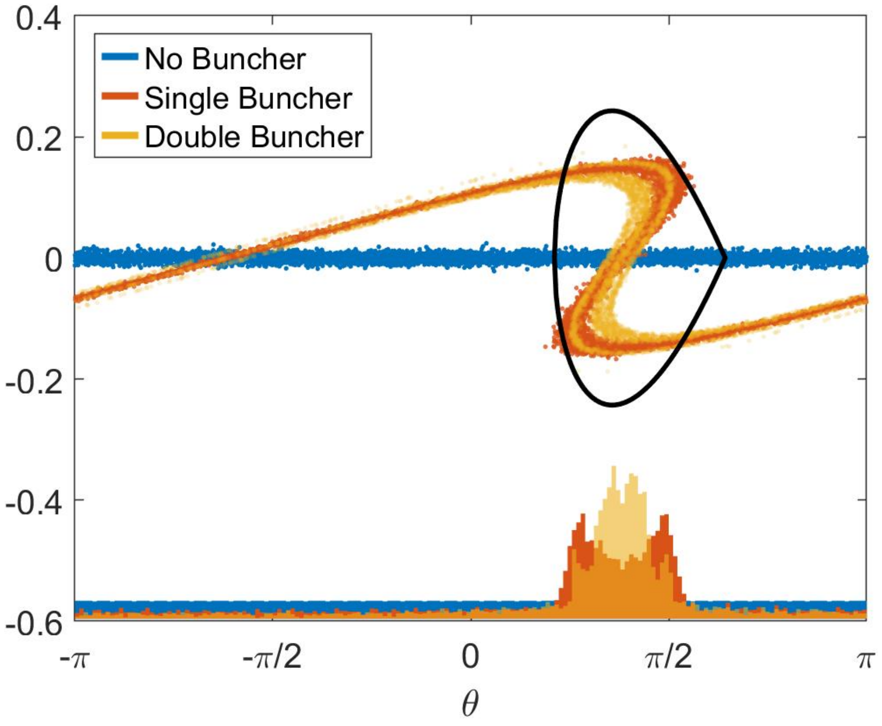

Figure 1.7: Phase spaces for $\theta_r = 65°$. Prebunching uses energy dimension to better fill ponderomotive bucket.

function of resonant phase or bucket size.

For most resonant phases, a single prebuncher provides a significant improvement in trapping fraction, leaving diminishing returns for the added complexity of additional prebunchers. The result of improved trapping is an increase in overall efficiency which occurs at larger deceleration gradients. Figure 1.7 shows the phase spaces at the optimal resonant phase $\theta_r = 65°$ for the double-buncher scheme indicated in the previous figures with black dotted lines. The bunchers utilize the energy dimension of the ponderomotive bucket to increase trapping. However, for a realistic beam with correlated energy chirp, the performance of the double-buncher scheme will degrade due to the strong dispersion applied.

So far our discussion of phase space dynamics has neglected the parameter tapering required to maintain resonance with the decelerated electrons. We see from the FEL resonance condition that for a fixed wavelength λ, the resonant energy can be adjusted by varying the undulator strength K or period λ_u. In general, tapering the period allows for a larger tuning range, but complicates the undulator design and is less versatile. Except for the most extreme cases, changing the undulator fields by adjusting the magnet gap is sufficient.

Conceptually, tapering should be applied such that the change in resonant energy matches the deceleration gradient of the interaction. Setting the derivative of Eq. (1.8) equal to Eq. (1.6) gives

$$\begin{aligned} \frac{1+K^2}{2\lambda}\frac{d\lambda_u}{dz} + \frac{\lambda_u K}{\lambda}\frac{dK}{dz} &= -2kK_l K \sin\theta_r \\ \implies \frac{dK}{dz} &= -2k_u K_l \sin\theta_r \quad \text{when} \quad \frac{d\lambda_u}{dz} = 0 \end{aligned} \tag{1.15}$$

where we assume a constant undulator period. Later, we will see a generalization of this tapering when discussing 1D efficiency in the high-gain regime. Note the tapering is implicitly designed for a fixed resonant phase and depends on field strength through the K_l parameter. As the separatrix depends on K, K_l and θ_r, optimal tapering may require varying the resonant phase as the field amplitude evolves. Among various tapering models developed [44, 45], one simple approach is to change the resonant phase such that the bucket area remains constant [46]. This limits the detrapping of electrons while also preventing growth in the longitudinal emittance. The tapering design should eventually be compared with simulations, but an analytic model is invaluable for fast estimates and experimental design.

1.3.2 High Gain

Until now, we have restricted our analysis to the low gain limit where changes in the field energy were considered negligible. We now allow the field amplitude to evolve due to interactions with the beam as described by Maxwell's wave equation,

$$\left(\nabla_\perp^2 + \frac{\partial^2}{\partial z^2} - \frac{1}{c^2}\frac{\partial^2}{\partial t^2}\right)\mathbf{E}(\mathbf{x}, z, t) = \mu_0 \frac{\partial \mathbf{J}}{\partial t} \tag{1.16}$$

though we continue to assume a free-space interaction with an infinitely long, periodic electron beam such that the field consists of a single frequency component. It is convenient to introduce complex notation and rewrite Eq. (1.5) as the real part of a complex field

$$\mathbf{E}(\mathbf{x}, z, t) = \mathrm{Re}\left\{\tilde{E}(z)e^{i(kz-\omega t)}\hat{\mathbf{n}}\right\} \quad \text{and} \quad \tilde{E}(z) = -ie^{i\phi}\sqrt{2}E(z) \tag{1.17}$$

where the unit vector $\hat{\mathbf{n}} = (\hat{\mathbf{x}} \pm i\hat{\mathbf{y}})/\sqrt{2}$ represents right/left circular polarization, $\tilde{E}(z)$ is the complex field amplitude, and $E(z)$ is a real-valued field amplitude analogous to E_0 in the low gain analysis.

After applying the dot product with $\hat{\mathbf{n}}^*$ to both sides, we apply the derivatives by inserting the frequency representation of the field,

$$\left(\cancel{\frac{\partial^2}{\partial z^2}} + 2ik\frac{\partial}{\partial z} - \cancel{k^2} + \cancel{\omega^2/c^2}\right)\tilde{E}(z)e^{i(kz-\omega t)} \tag{1.18}$$

where we utilize the slowly varying envelope approximation (SVEA) such that the field amplitude evolves slowly on wavelength scales ($\lambda\frac{\partial^2\tilde{E}}{\partial z^2} \ll \frac{\partial\tilde{E}}{\partial z}$).

For a collection of charged point particles, the 3D current density can be written as

$$\mathbf{J}_{3D}(\mathbf{x}, z, t) = \sum_{j=1}^{N_e} -e\mathbf{v}_j\delta(\mathbf{x} - \mathbf{x}_j(t))\delta(z - z_j(t)) \tag{1.19}$$

where j indexes each of the N_e electrons in a wavelength period and the dirac delta function $\delta(x)$ is defined as a distribution about 0 with unit area and infinitesimal width such that it satisfies the well-known sampling property $\int_{-\infty}^{\infty} f(x)\delta(x - x_0)dx = f(x_0)$.

The $\delta(\mathbf{x} - \mathbf{x}_j(t))$ sample the transverse distribution of the beam and assuming a gaussian with spotsize σ, we can simplify to a 1D current density by considering the density on axis or equivalently, dividing the 3D current density by the area of the transverse distribution.

$$\mathbf{J}_{1D}(z, t) = \frac{-e}{2\pi\sigma^2}\sum_{j=1}^{N_e} \mathbf{v}_j\delta(z - z_j(t)) \tag{1.20}$$

Because the field is a transverse wave, only the electron's transverse velocity is relevant to the interaction. We express the transverse velocity in an undulator from Eq. (1.2) as

$$\mathbf{v}_\perp(z) = \frac{\sqrt{2}cK}{\gamma}e^{-ik_u z}\hat{\mathbf{n}} \quad \text{and} \quad v_\perp(z) = \boldsymbol{v}_\perp(z) \cdot \hat{\mathbf{n}}^* \tag{1.21}$$

After substituting the current density and solving for the evolution of the real field, we find

$$\begin{aligned}\frac{d\tilde{E}}{dz} &= \frac{-i\mu_0}{2k}\left(\frac{\partial \mathbf{J}}{\partial t}\cdot\hat{\mathbf{n}}^*\right)e^{-i(kz-\omega t)} \qquad (1.22)\\ &= \frac{-i\mu_0}{2k}\frac{-e}{2\pi\sigma^2}\frac{\sqrt{2}cK}{\gamma}\sum_{j=1}^{N_e}e^{-i(kz+k_uz-\omega t)}c\beta_{z,j}\frac{\partial}{\partial z_j}\delta(z-z_j(t)) \qquad (1.23)\\ &= \frac{i\sqrt{2}e}{4\pi\epsilon_0\sigma^2}\frac{K}{\gamma}\frac{\beta_{z,j}}{k}\left(\sum_{j=1}^{N_e}e^{-i(kz+k_uz-\omega t)}\frac{\partial}{\partial z_j}\delta(z-z_j(t))\right) \qquad (1.24)\end{aligned}$$

where have applied the chain rule on $z_j(t)$. To evaluate the derivative, we derive an identify that utilizes symmetry of the delta function and integration by parts.

$$\begin{aligned}\int_{-\infty}^{\infty}f(z)\frac{\partial}{\partial z_j}\delta(z-z_j)dz &= -\int_{-\infty}^{\infty}f(z)\frac{\partial}{\partial z}\delta(z-z_j)dx\\ &= \int_{-\infty}^{\infty}\delta(z-z_j)\frac{\partial}{\partial z}f(z)dz - \cancelto{0}{[f(z)\delta(z-z_j)]\,|_{-\infty}^{\infty}}\\ &\boxed{f(z)\frac{\partial}{\partial z_j}\delta(z-z_j) = \delta(z-z_j)\frac{\partial}{\partial z}f(z)} \qquad (1.25)\end{aligned}$$

Beam energy loss $\gamma = \gamma(z)$ and tapering of the undulator field $K = K(z)$ are assumed negligible compared to the derivative of the exponential term ($\frac{dK}{dz}, \frac{d\gamma}{dz} \ll k_u + k$) such that $f(z) = e^{-i(kz+k_uz-\omega t)}$. After differentiating, further simplification is made by assuming only particles that satisfy the FEL resonance of Eq. (1.7) contribute to energy exchange such that $\gamma \to \gamma_r$. Inserting $\tilde{E}(z) = -ie^{i\phi}\sqrt{2}E(z)$ and taking real quantities gives

$$\frac{dE}{dz} \approx \frac{e}{4\pi\epsilon_0\sigma^2}\frac{K}{\gamma_r}\cancelto{1}{\frac{\beta_{z,j}(k_u+k)}{k}}\,\mathrm{Re}\left\{\sum_{j=1}^{N_e}ie^{-i\theta}\delta(z-z_j(t))\right\} \qquad (1.26)$$

where we identified the ponderomotive phase, θ. Due to the SVEA approximation, we can use period-averaging to replace the sum over individual electrons with a collective measure of coherence known as the bunching factor, $\langle e^{-i\theta_j}\rangle = \sum_{j=1}^{N_e}e^{-i\theta_j}/N_e$, which ranges from 0 (fully incoherent) to 1 (fully coherent). We take this opportunity to express the electron number in terms of the beam current

$$\sum_{j=1}^{N_e}\delta(z-z_j)e^{-i\theta} \approx \frac{\int_\lambda\sum_{j=1}^{N_e}\delta(z-z_j)e^{-i\theta}dz}{\int_\lambda dz} = \frac{\sum_{j=1}^{N_e}e^{-i\theta_j}}{\lambda} = \frac{N_e}{\lambda}\langle e^{-i\theta_j}\rangle = \frac{I}{ec}\langle e^{-i\theta_j}\rangle \qquad (1.27)$$

such that the final result can be expressed as

$$\boxed{\frac{dE}{dz} = \frac{IK}{4\pi\epsilon_0 c\sigma^2\gamma_r}\langle\sin\theta_j\rangle} \tag{1.28}$$

In agreement with conservation of energy, the equations describing evolution of the field and beam energy have a negative sine dependence on the ponderomotive phase. Furthermore, we see that beams with high current densities (high current and small spotsize) generate the strongest fields. One subtlety is that we have preemptively defined $E(z)$ to be a real quantity without allowing for the complex field phase ϕ to vary along the undulator. This is equivalent to assuming an appropriate tapering such that the electron beam remains centered at a given resonant phase. The addition of Eq. (1.28) to the system in (1.9) yields a description of FELs in the 1D, high gain regime.

$$\begin{aligned}
\frac{dE}{dz} &= \frac{IK}{4\pi\epsilon_0 c\sigma^2\gamma_r}\langle\sin\theta_j\rangle && \text{bunching} \to \text{field} \\
\frac{d\eta_j}{dz} &= \frac{-eK}{mc^2\gamma_r^2}E\Big(\sin\theta_j - \sin\theta_r\Big) && \text{field} \to \text{energy modulation} \\
\frac{d\theta_j}{dz} &= 2k_u\eta_j && \text{energy modulation} \to \text{bunching}
\end{aligned} \tag{1.29}$$

There is a clear feedback mechanism in these equations. First, a coherence in the beam density improves field emission. Second, increased fields lead to stronger energy modulation. Third, energy modulation leads to a bunching of the beam density, known as microbunching. The interaction can be seeded from any of the three components: a prebunched electron beam, an external laser, or a beam with energy modulation. In the absense of seeding, the interaction grows from random statistical noise in the beam, also called shot noise. Operating from self-amplified spontaneous emission (SASE) is how X-Ray FELs (XFELs) are able to generate sub-nanometer radiation.

1.3.3 Universal Scaling and Collective Variables

It is helpful to redefine the 1D system in terms of scaled, dimensionless variables that express important time and length scales that govern the FEL interaction across all parameter regimes. We assume an untapered undulator ($\theta_r = 0$) and begin by introducing the scaled length $\tilde{z} = 2k_u\rho z$ into the phase equation with the (as of now) undefined Pierce parameter ρ.

$$\frac{\partial\theta}{\partial\tilde{z}} = \tilde{\eta}_j \quad \text{where} \quad \tilde{\eta}_j \equiv \eta_j/\rho \tag{1.30}$$

After inserting into the energy equation and defining a scaled field variable $\tilde{a}$, we substitute all into the field equation and fix ρ such that the coefficient of the bunching factor is 1.

$$\frac{\partial\tilde{\eta}_j}{\partial\tilde{z}} - 2\tilde{a}\sin\theta_j \quad \text{where} \quad \tilde{a} \equiv \frac{eK}{4k_u\rho^2\gamma_r^2 mc^2}E \tag{1.31}$$

$$\frac{\partial\tilde{a}}{\partial\tilde{z}} = \frac{eIK^2}{\rho^3 32\pi\epsilon_0 mc^3\sigma^2\gamma^3k_u^2}\langle\sin\theta_j\rangle \equiv \langle\sin\theta_j\rangle \implies \rho = \left(\frac{eIK^2}{32\pi\epsilon_0 mc^3\sigma^2\gamma^3k_u^2}\right)^{1/3} \tag{1.32}$$

We rearrange and express in terms of undulator period or radiation wavelength as

$$\boxed{\rho = \left(\frac{1}{16\pi}\frac{I}{I_A}\frac{K^2}{\gamma^3}\frac{\lambda_u^2}{\mathcal{A}}\right)^{1/3} = \left(\frac{1}{4\pi}\frac{I}{I_A}\left(\frac{K}{1+K^2}\right)^2\frac{\gamma\lambda^2}{\mathcal{A}}\right)^{1/3}} \tag{1.33}$$

where $I_A = 4\pi\epsilon_0 mc^3/e = 17045$ A is the Alfvén current and $\mathcal{A} = 2\pi\sigma^2$ is the transverse beam area. In the next chapter, we show that the analogous ρ for a waveguide FEL simply replaces the beam area with a measure of the waveguide area (see Eq. 2.2).

The Pierce parameter describe the scaling for many properties of an FEL including the saturation power, saturation length, spectral bandwidth, and energy spread constraints for lasing.

$$P_{sat} = \rho P_{beam} = \rho\left(\frac{\gamma mc^2}{e}\right)I \qquad L_{sat} \approx \lambda_u/\rho \qquad \Delta\omega/\omega \approx \rho \qquad \Delta\gamma/\gamma < \rho \tag{1.34}$$

While a full characterization is outside the scope of this dissertation, we emphasize that the efficiency of an untapered undulator is limited to the value of ρ which is generally on the order of 10^{-3} to 10^{-2}. We make the connection between ρ and the 1D power gain length $P \propto e^{z/L_g}$ using a collective variable approach following [47]. In addition to the complex bunching factor $b = \langle e^{-i\theta_j}\rangle$, we define the collective momentum $P = \langle\eta_j e^{-i\theta_j}\rangle$ and treat $\tilde{a}$ as a complex quantity. Denoting $\partial/\partial\tilde{z}$ with primes, the system becomes

$$\begin{aligned}
\tilde{a}' &= ib \\
b' &= -i\langle\theta_j' e^{-i\theta_j}\rangle = -iP \\
P' &= \langle\tilde{\eta}_j' e^{-i\theta_j}\rangle - i\langle\tilde{\eta}_j\theta_j' e^{-i\theta_j}\rangle = -i\tilde{a} + \cancel{i\tilde{a}\langle e^{-i2\theta_j}\rangle} - \cancel{i\langle\tilde{\eta}_j^2 e^{-i\theta_j}\rangle}
\end{aligned} \tag{1.35}$$

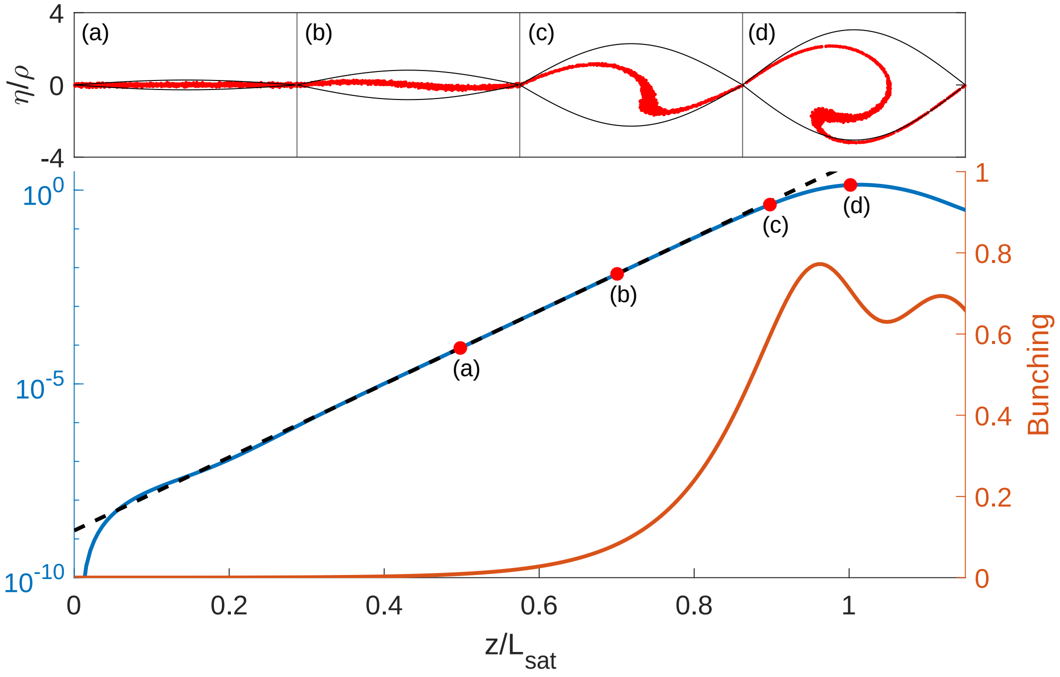

Figure 1.8: Simulation of the exponential growth in power and bunching in a 1D untapered FEL. Power and distance are scaled by P_{sat} and L_{sat} defined in Eq. (1.34) and plotted against the analytic gain length $L_g = \lambda_u/4\pi\sqrt{3}\rho$ (black dashed line). The longitudinal phase space and ponderomotive bucket are plotted at four points along the undulator.

where we neglect higher order terms in the momentum evolution. This can be expressed as a third order differential equation in the field $\tilde{a}''' = -i\tilde{a}$ where for the ansatz $\tilde{a} = e^{i\mu\tilde{z}}$, μ is given by the cubic roots of unity. The solution for exponential growth requires $\text{Im}\{\mu\} < 0$ such that the steady state growth for power is given by $|\tilde{a}|^2 \propto e^{i\sqrt{3}\tilde{z}} \equiv e^{z/L_g}$ where the gain length can be identified as

$$\boxed{L_g = \frac{\lambda_u}{4\pi\sqrt{3}\rho}} \tag{1.36}$$

The gain length is an important benchmarking tool for GPTFEL and other FEL simulations. Corrections for 3D effects including finite beam emittance, energy spread, and radiation diffraction commonly rely on fitting formulas developed by Ming Xie [48].

Figure 1.8 compares a simulation of exponential power growth $P(z) \propto e^{z/L_G}$ in an untapered FEL with the analytic estimates of Eqs. (1.34) and (1.36). The 1D simulation is seeded with a very small amount of density bunching and after an initial startup period grows exponentially in good agreement with the theory shown by the dashed black line. Additionally, the values for L_{sat} and P_{sat} correctly predict the position and power of saturation. The bunching is shown on a linear scale to make the exponential growth more apparent. Phase spaces are shown along the interaction along with the ponderomotive bucket approximations where we note the bucket height near saturation is on the order of ρ. The power saturates when the electrons reach a minimum energy at which point the power decreases as electrons begin to reabsorb energy from the fields.

1.4 TESSA Regime

The strong emission near saturation is due to the coherent emission of the bunched electron beam and can be described by a simple model where the total field is represented by the sum of sinusoids emitted from N_e electrons as

$$E \propto \sum_j E_0 e^{ik(z-z_j)} \tag{1.37}$$

The intensity relies on the point-wise distances and can be separated into diagonal and off-diagonal terms.

$$|E|^2 \propto \sum_{j,\ell} e^{ik(z_j-z_\ell)} = |E_0|^2 \left(N_e + \sum_{j\neq\ell} e^{ik(z_j-z_\ell)} \right) \tag{1.38}$$

For an unbunched beam, the off-diagonal terms average to zero and the intensity grows linearly with N_e. If the beam charge distribution instead has non-negligible bunching according to $f(z) = 1 + 2b\cos(kz)$, the remaining sum can be written as an expected value over the beam distribution

$$\sum_{j\neq\ell} e^{ik(z_j-z_\ell)} = N_e(N_e-1) \int_0^\lambda \int_0^\lambda f(z_1)f(z_2)e^{ik(z_1-z_2)} dz_1 dz_2 \approx N_e(N_e-1)b^2 \tag{1.39}$$

such that even a small amount of coherence leads to intensity scaling as N_e^2. The term superradiance was first coined by Dicke [49] in work relating to optic lasers, but has since been adopted for FELs to refer to the quadratic intensity scaling and the importance of beam microbunching for producing large intensities [50, 51].

In an untapered FEL, the high gain interaction length is limited by gain saturation which occurs when the electrons lose enough energy to drop out of resonance or when the efficiency is roughly equal to ρ. To maintain resonance with decelerated electrons, the undulator field strength or period length can be tapered. Interest in tapered FELs dates back to the first demonstration of FEL gain by Madey, et al in 1976 [52], with the seminal paper by Kroll, Morton, and Rosebluth [42] in 1981 which describes resonance for a tapered interaction. Experiments at Los Alamos and Lawrence Livermore National Laboratories demonstrated tapered interactions at 10.6 μm (3.7% efficiency) and 9 mm (34% efficiency) [53, 54], but a future effort to improve the efficiency at infrared wavelengths was not successful due to limitations in beam brightness [55].

In the last decade, interest in strong-tapering for improving FEL efficiency has renewed at UCLA [56, 57] partially motivated by the study of inverse-FELs where a strong laser seed can accelerate beams with gradients competitive with state of the art RF technology [58, 59]. To accelerate a significant fraction of the electrons, the beam must be microbunched at the radiation wavelength. In 2014, a collaboration between UCLA and Brookhaven National Lab lead to the Rubicon experiment which demonstrated over 50 MeV energy gain with a $\sim$ 100 MeV/m average accelerating gradient with a helical undulator geometry [60].

Due to the symmetric nature of the FEL interaction, the strong external seeding (laser and beam microbunching) that generated large accelerating gradients in inverse-FELs can similarly produce large decelerating gradients to maximize energy extraction from the electron beam. A follow-up experiment (appropriately named Nocibur) reversed the undulator tapering and decelerated 45% of the electrons from 65 MeV to 35 MeV resulting in 30% energy extraction efficiency [30]. This demonstrated Tapering Enhanced Stimulated Superradiant Amplification (TESSA) [61], in the low gain limit as the external 200 GW CO_2 laser dominated the output radiation. The name alludes to an analogy between FEL amplification due to strong seeding and the stimulated emission of photons in a solid-state laser.

The Tessatron experiments are intimately connected to this research, utilizing TESSA in conjunction with zero-slippage operation to produce a compact THz-FEL source. The future application of TESSA to visible frequencies is underway with the FAST-GREENS collaboration between UCLA, RadiaBeam Technologies, RadiaSoft, and Fermilab National Laboratory [62]. The program goal is to achieve record single-pass efficiency ($\sim 10\%$) and the first experimental measurements of the spectral and transverse profile characteristics of the amplified radiation, demonstrating a path to high power, short wavelength sources. Additionally, an oscillator configuration [63] could be used to significantly improve the average power with important applications for EUV lithography and molecular imaging [64, 65, 66].

1.5 Efficiency Estimates

1.5.1 1D Efficiency

An analytic estimate for the efficiency of the high-gain, 1D FEL system in the non-linear regime can be obtained using the resonate particle approximation which assumes that all trapped electrons behave similarly to a resonant particle ($\gamma_j \to \gamma_r$ and $\sin\theta_j \to \sin\theta_r$) and that untrapped electrons result in negligible energy transfer. The efficiency is then defined as the energy loss of the trapped electrons over the initial energy

$$\eta_{1D}(z) = f_t \left| \frac{\gamma_r(z) - \gamma_{r0}}{\gamma_{r0}} \right| \tag{1.40}$$

where we return to the original energy variable γ. With the resonant-particle approximation, we can integrate Eqs. (1.6) and (1.28) to find

$$\gamma_r(z) - \gamma_r(0) = -\frac{e}{mc^2} \int_0^z \frac{K(z)}{\gamma_r(z)} E(z) \sin\theta_r dz \tag{1.41}$$

$$E(z) = E_0 + \frac{I}{4\pi\epsilon_0 c\sigma^2} \int_0^z \frac{K(z)}{\gamma_r(z)} f_t \sin\theta_r dz \tag{1.42}$$

Note the resonant particle assumption leads to the bunching factor being approximated by $f_t \sin\theta_r$. Instead of preemptively defining a tapering, we assume that $K(z)/\gamma_r(z) \approx K_0/\gamma_{r0}$ (valid for small efficiencies) such that the integrands are simplified and $E(z)$ is seen to grow linearly in z. Inserting equation (1.42) into (1.41), we obtain the 1D efficiency estimate

$$\eta_{1D}(z) = \frac{e}{\gamma_{r0} mc^2}\left[E_0\left(\frac{K_0}{\gamma_{r0}} f_t \sin\theta_r\right) z + \frac{I}{8\pi\epsilon_0 c\sigma^2}\left(\frac{K_0}{\gamma_{r0}} f_t \sin\theta_r\right)^2 z^2\right] \tag{1.43}$$

$$\boxed{\eta_{1D}(z) = \frac{kK_l}{\gamma_{r0}}\left(\frac{K_0}{\gamma_{r0}} f_t \sin\theta_r\right) z + \frac{I}{I_A}\frac{1}{2\gamma_{r0}\sigma^2}\left(\frac{K_0}{\gamma_{r0}} f_t \sin\theta_r\right)^2 z^2} \tag{1.44}$$

which is a function of the product $f_t \sin\theta_r$ and we have simplified coefficients with the field strength parameter and Alfvén current. The linear and quadratic terms describe the effect of the seed laser and beam current density, respectively. We can also describe the evolution of the radiation power by $P_{rad} = P_0 + \eta_{1D} P_{beam}$ as

$$P_{rad} = P_0 + E_0\left(\frac{K_0}{\gamma_{r0}} I f_t \sin\theta_r\right) z + \frac{Z_0}{8\pi\sigma^2}\left(\frac{K_0}{\gamma_{r0}} I f_t \sin\theta_r\right)^2 z^2 \tag{1.45}$$

where $P_0 = 2\pi\sigma^2 E_0^2/Z_0$, $P_{beam} = I\gamma_{r0} mc^2/e$, and $Z_0 = 1/c\epsilon_0$ is the impedance of free space. Linear and quadratic coefficients for the tapering can be estimated from $K(z)/K_0 = \gamma_r(z)/\gamma_0$ by inserting $\gamma_r(z) = \gamma_{r0}(1 - t_1 z - t_2 z^2)$ into Eq. (1.40) to find $\eta_{1D}(z) = f_t\,(t_1 z + t_2 z^2)$ such that

$$\begin{gathered} K(z) = K_0(1 - t_1 z - t_2 z^2) \\ \text{where} \quad t_1 = \frac{kK_l K_0}{\gamma_{r0}^2}\sin\theta_r \quad \text{and} \quad t_2 = \frac{I}{I_A}\frac{K_0^2}{\gamma_{r0}^3}\frac{f_t \sin^2\theta_r}{2\sigma^2} \end{gathered} \tag{1.46}$$

Notice that in the low gain limit ($I = 0$), we can substitute the FEL resonance for γ_{r0}^2 and assume $(1 + K_0^2)/K_0^2 \approx 1$ to find

$$K(z) = K_0 - 2K_l k_u z \tag{1.47}$$

which agrees with low gain prediction of Eq. (1.15).

The 1D efficiency theory doesn't account for time-dependent effects as it assumes an infinitely long beam and most importantly doesn't include diffraction effects that will diminish efficiency. This is most clear for the limit $\sigma \to 0$ where the 1D efficiency diverges toward infinity. The 1D theory can be applied to waveguide FELs by replacing the beam area with the effective mode area defined in Eq. (2.2), but the effects of frequency dispersion must be considered for short beams.

1.5.2 3D Efficiency

We now seek to incorporate diffraction into the efficiency estimate while retaining the assumption of an infinitely long beam such that fields are represented by a single frequency. Inspired by the work of Saldin et al. [67], we augment the resonant particle approximation and assume the beam maintains a constant longitudinal bunching in order to compute the radiation field in the presence of diffraction. To this end, we build off the derivation for the 1D, high gain field evolution where the only differences are the inclusion of the transverse Laplacian $\nabla_\perp^2$ and a 3D current density given by

$$\mathbf{J}_\perp = -e\mathbf{v}_\perp n_\perp(r)\sum_{j=1}^{N_e}\delta(z - z_j(t)) \quad \text{and} \quad n_\perp(r) = \frac{1}{2\pi\sigma^2}e^{-r^2/2\sigma^2} \tag{1.48}$$

where $n_\perp$ is the transverse electron number density and $\mathbf{r}$ refers to the transverse position. The exact form of the longitudinal density is irrelevant as it will be period-averaged into the complex bunching factor $b \equiv \langle e^{-i\theta_j}\rangle$. Applying derivatives to the frequency representation of the field, we find

$$\left(\nabla_\perp^2 + \frac{2i\omega}{c}\frac{\partial}{\partial z}\right)E = S(r) \quad \text{where} \quad S(r) = -\frac{K\omega I b}{\epsilon_0 c^2\gamma}n_\perp(r) \tag{1.49}$$

Using a Green's function formulation, the field can be expressed as

$$E(z,\mathbf{r}) = -\int_0^z\int_0^\pi\int_0^\infty G(z-z',\mathbf{r}-\mathbf{r}')S(r')r'd\theta'dr'dz'$$

$$\text{where} \quad G(z-z',\mathbf{r}-\mathbf{r}') = \frac{1}{4\pi(z-z')}\exp\left(\frac{i\omega|\mathbf{r}-\mathbf{r}'|^2}{2c(z-z')}\right) \tag{1.50}$$

is the Green's function solution for the homogeneous paraxial wave equation and θ' is the angle between $\mathbf{r}$ and $\mathbf{r}'$ (note the integration limits). We expand $|\mathbf{r}-\mathbf{r}'|^2 = r^2 + r'^2 - 2rr'\cos\theta'$ and apply the Jacobi-Anger expansion, $e^{ia\cos\theta} = \sum_{n=-\infty}^{\infty} i^n J_n(a)e^{in\theta}$, where only the $n = 0$ term survives the azimuthal integral.

$$E(z,r) = \frac{K\omega I b}{\epsilon_0 c^2\gamma}\frac{1}{2\pi\sigma^2}$$

$$\times\int_0^z \frac{1}{4(z-z')}e^{i\omega r^2/2c(z-z')}\left[\int_0^\infty e^{i\omega r'^2/2c(z-z')}J_0\left(\frac{\omega r r'}{c(z-z')}\right)e^{-r'^2/2\sigma^2}r'dr'\right]dz' \tag{1.51}$$

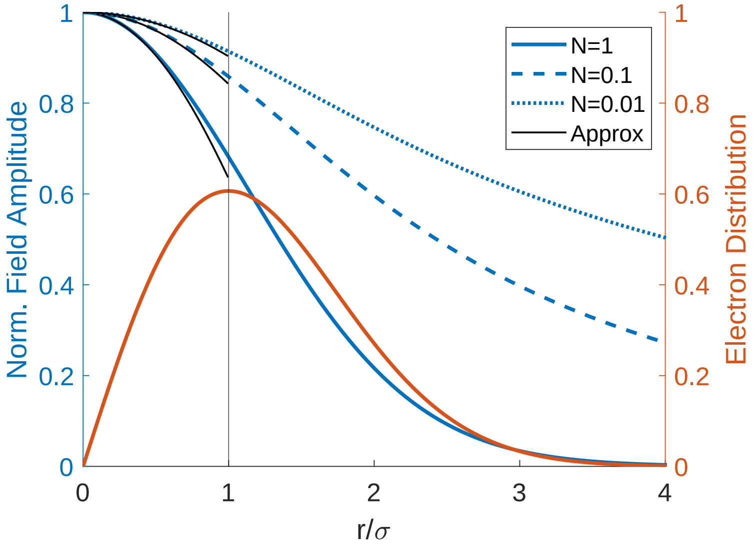

Figure 1.9: Radial dependence of the electron distribution and emitted field for various Fresnel numbers N. Near-axis approximations are shown in black.

Defining the scaled variables $\hat{z} = z/L_u$ and $\hat{r}^2 = kr^2/L_u$ where $k = \omega/c$ and L_u is the undulator length, as well as identifying the Fresnel number of the electron beam, $N = k\sigma^2/L_u$, the bracketed radial integral can be computed as

$$\int_0^\infty e^{i\hat{r}'^2/2(\hat{z}-\hat{z}')} J_0\left(\frac{\hat{r}\hat{r}'}{\hat{z}-\hat{z}'}\right) e^{-\hat{r}'^2/2N}\hat{r}'d\hat{r}' = \frac{2N(\hat{z}-\hat{z}')}{\hat{z}-\hat{z}'-iN}\exp\left(\frac{-\hat{r}^2}{2(\hat{z}-\hat{z}')}\frac{N}{(\hat{z}-\hat{z}'-iN)}\right) \tag{1.52}$$

using the identity $\int_0^\infty e^{-\alpha x}J_0(\beta\sqrt{x})dx = \frac{1}{\alpha}e^{-\beta^2/4\alpha}$. After some algebraic simplification, we have

$$E(z,r) = \frac{\omega KIb}{4\pi\epsilon_0 c^2\gamma}\int_0^{\hat{z}} \frac{d\hat{z}'}{\hat{z}-\hat{z}'-iN}\exp\left(\frac{i\hat{r}^2}{2(\hat{z}-\hat{z}'-iN)}\right) \tag{1.53}$$

Utilizing a near-axis expansion $e^{a\hat{r}^2} \approx 1 + a\hat{r}^2$, the final integration is simple and can be rewritten by expanding complex logarithms according to $\ln\left(ae^{i\theta}\right) = \ln(a) + i\theta$ to give

$$\boxed{E(z,r) \approx i\frac{\omega KIb}{4\pi\epsilon_0 c^2\gamma}\left[\arctan\left(\frac{\hat{z}}{N}\right) - \frac{i}{2}\ln\left(1+\frac{\hat{z}^2}{N^2}\right) - \frac{r^2}{2\sigma^2}\left(\frac{\hat{z}}{N+i\hat{z}}\right)\right]} \tag{1.54}$$

where the last term gives the off-axis correction. In the 1D, on-axis limit where the electron beam and seed spot sizes are large ($N \gg 1$), we recover equation (1.28) for the field evolution in the 1D high-gain regime where $\mathrm{Re}\{ib\} = \langle\sin\theta_j\rangle$. Figure 1.9 plots the exact numeric integration of Eq. (1.53) against the small $\hat{r}$ approximation of Eq. (1.54) at $\hat{z} = 1$

along with the electron radial distribution. For $N > 0.01$, it is clear that simply assuming the on-axis field would not be an accurate representation of the fields seen by the particles. In computing our analytic estimates, we evaluate Eq. (1.54) at the expected value of the beam distribution such that $r = \sigma$.

Under the assumption of constant bunching, Maxwell's equations are linear and we can include the presence of a seed field with waist size w_0 and position z_w by simply adding a TEM$_{00}$ gaussian mode

$$E_s(z) = E_0 \frac{w_0}{w(z)} e^{i(kz - \omega t + \psi(z))} \tag{1.55}$$

where $\psi(z) = -\arctan\left((z - z_w)/z_r\right)$ is the Guoy phase, $z_r = \pi w_0^2/\lambda$ is the Rayleigh length, and $w(z) = w_0\sqrt{1 + (z - z_w)^2/z_r^2}$ is the transverse spotsize where λ is the seed wavelength. We define the ponderomotive phase relative to the seed field such that $\theta = (k + k_u)z - \omega t$. The electron bunch should be injected at the resonant phase of the seed field where the ponderomotive potential is deepest and the energy acceptance is large such that $\phi_b(0) = \theta_r - \psi(0)$ where $b = |b|e^{i\phi_b}$. When the beam size is on the order of the seed waist, a correction term is needed to account for particles sampling off-axis fields. This is achieved by scaling the seed field with the convolution of the electron beam density with the seed's radial dependence.

$$\int_0^{2\pi} \int_0^{\infty} \left(\frac{1}{2\pi\sigma^2} e^{-r^2/2\sigma^2} \right) e^{-r^2/w(z)^2} r dr d\theta = \frac{w(z)^2}{w(z)^2 + 2\sigma^2} \equiv \xi_s \tag{1.56}$$

Particles are expected to follow the phase of the total field such that the 3D efficiency estimate can be expressed as a semi-analytic formula in terms of the total amplitude of the combined seed and emitted fields.

$$\boxed{\eta_{3D}(z) = \frac{e}{\gamma_0 mc^2} \frac{K}{\gamma} f_t \sin\theta_r \int_0^z |\xi_s E_s(z) + E(z)| dz} \tag{1.57}$$

For an example, we consider the experimental parameters for the high efficiency FAST-GREENS experiment at 515 nm in Table 1.1. Simulations of the first two undulator sections disregard the break section between the undulators to be consistent with the analytic model.

The microbunched beam is prepared using a single-buncher scheme with $\Delta\gamma \approx 1.4$ energy modulation and $R_{56} \approx 100\mu m$ dispersion to achieve a bunching factor of 0.7.

Table 1.1: Parameters for the 515 nm FASTGREENS Experiment

Electron Beam		Radiation and Undulator	
Energy	220 MeV	λ	515 nm
Energy Spread	0.1 %	Input Power	1 GW
$\|b\|$	0.7	Rayleigh Length	1.41 m
$\epsilon_{n,x}, \epsilon_{n,y}$	3 mm·mrad	Waist location	0.4 m
I_{peak}	500 A	K_{rms}	2.23
σ_x, σ_y	100 μm	λ_u	3.2 cm
		L_u	1.92 m

To first make a direct comparison to 1D theory, we consider the zero current limit for various seed waist sizes (or rayleigh lengths) shown in Figure 1.10, where the seed power is adjusted to maintain an identical peak-field. In the large waist limit, the 1D and 3D estimates converge nicely in agreement with the simulated efficiencies. For moderately small waists, simulations track with the 3D estimate while a strong discrepancy develops at short rayleigh lengths. While it is true that the correction in Eq. 1.56 doesn't account for transverse phase dependence, we expect this to have a small effect on phase space dynamics. More importantly, the inlay shows that the assumption of a constant bunching is violated as the bunching phase drifts with the field phase. The electrons are trapped in the ponderomotive potential of the total radiation field and in the presence of very strong diffraction ($z_r < 0.5$) the phase drift is fast enough to cause many particles to become detrapped, leading to smaller efficiencies. In practice, a small seed waist is unfavorable as it limits the interaction length with the electrons, such that this discrepancy for large seed diffraction will have little practical effect. Additionally, the electrons can be injected at a different phase or energy to try to limit the detrapping.

Figure 1.11 shows the estimated and simulated frequencies as a function of Fresnel number where the parameter is tuned by varying the electron beam spotsize. GPT simulations use

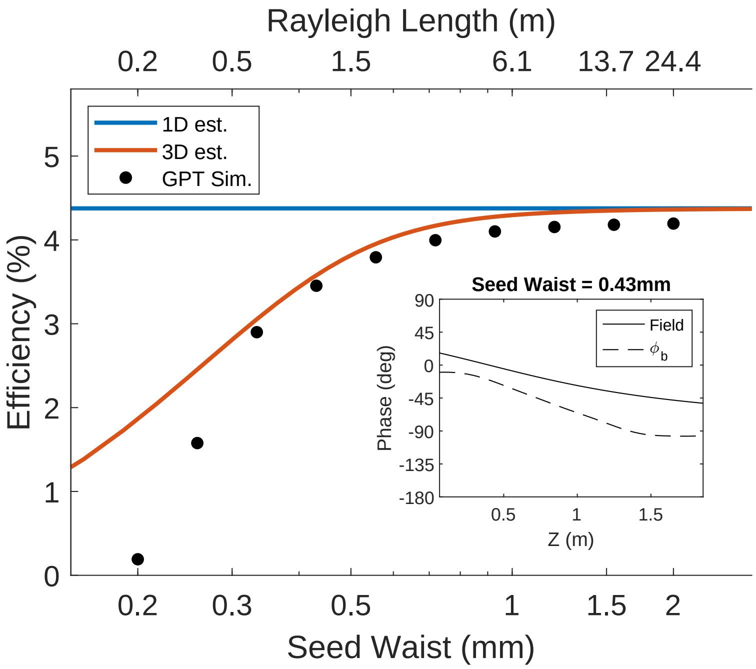

Figure 1.10: Comparison of simulated and analytic efficiencies in the zero-current limit as a function of seed waist. Contrary to the fixed bunching approximation, the inlay shows that the bunching phase drifts along with the diffracting radiation seed.

a fixed gaussian mode for the seed and a GPTFEL element with 61 free-space modes to model the emitted field. The solid and dashed lines show the 3D estimate with and without the correction factor from Eq. (1.56). Without the correction, the 1D and 3D efficiency estimates converge, while the corrected estimate and simulated efficiency continue to decrease due to the violation of $\sigma \ll w(z)$. At small spotsizes the 1D efficiency incorrectly diverges, emphasizing the need for an efficiency estimate that can include diffraction effects. When the electron spotsize becomes comparable to the trajectory radius, $r_\perp = K/\gamma k_u$, it is necessary to model with an effective spotsize given by $\sigma_{eff} = \sqrt{\sigma^2 + r_\perp^2}$.

Figure 1.12 shows the phase evolution of the fields and complex bunching along the undulators with initial phases labeled in red. The seed field diffracts independent of the interaction. The emitted field starts with phase $\pi/2$ larger than the bunching, but lowers quickly due to strong diffraction as its waist is on the order of the beam spotsize. The complex bunching is phase-locked to the ponderomotive potential of the total field, as predicted.

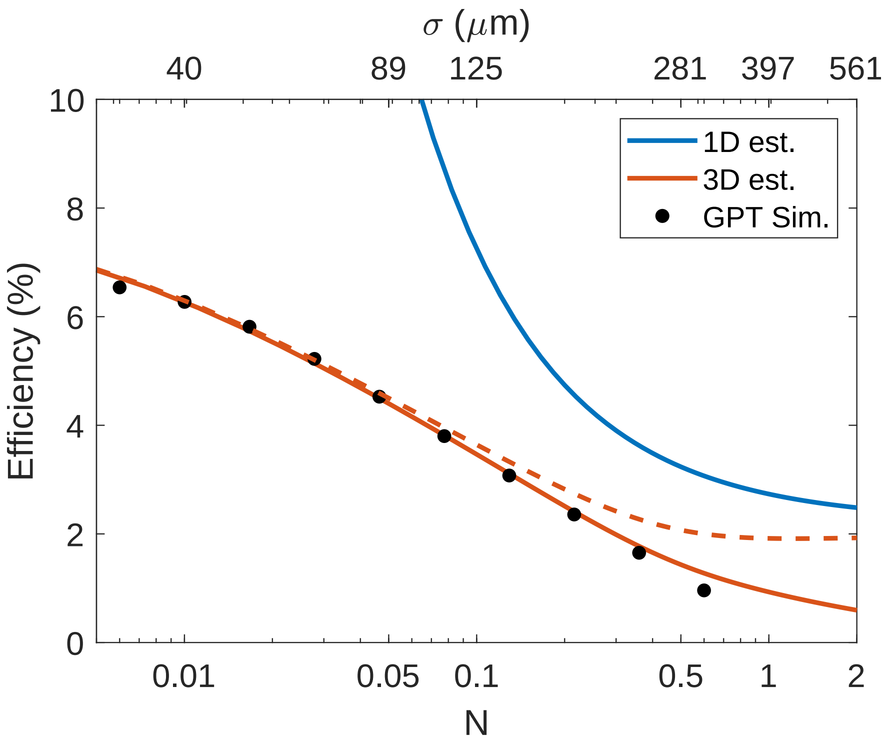

Figure 1.11: Comparison of simulated and analytic efficiencies as a function of Fresnel number N. Dotted line shows 3D estimate without convolution correction term from Eq. (1.56) for small seed waist.

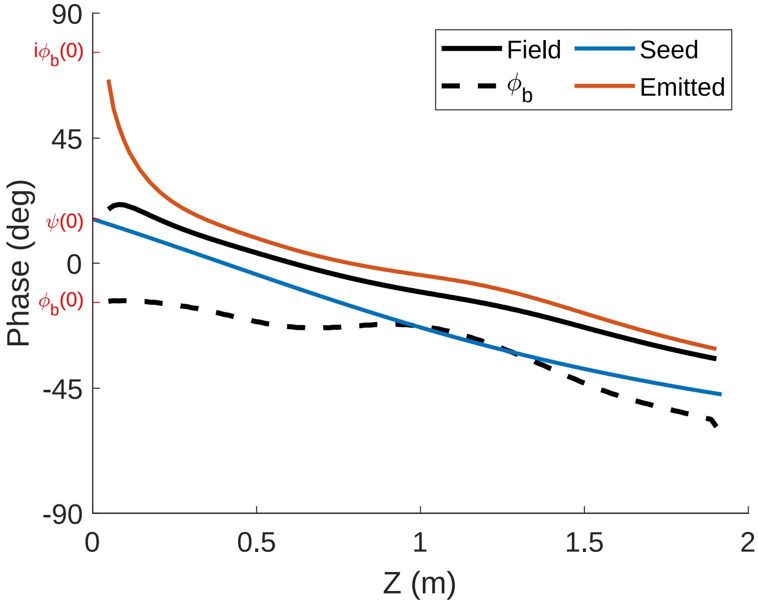

Figure 1.12: Evolution of phases along the undulators with theoretical initial phases shown in red. The electron bunching is phase-locked to the total field due to the ponderomotive potential.

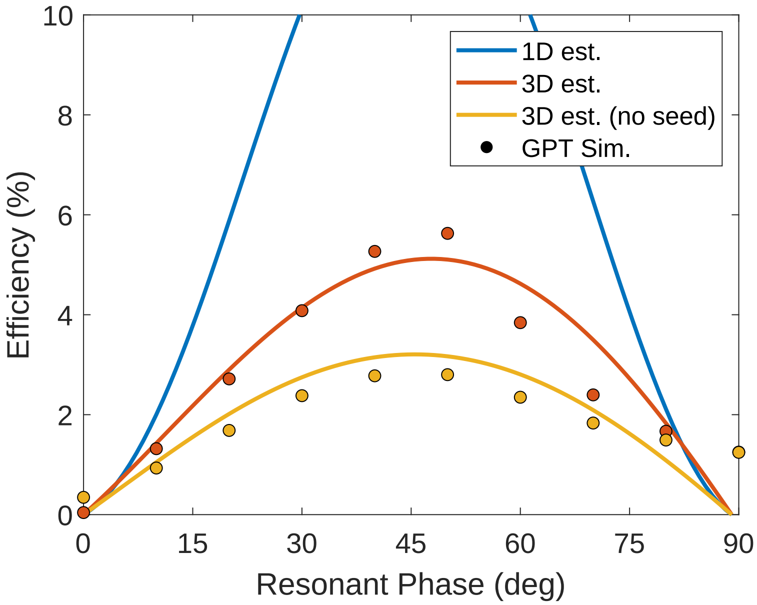

Figure 1.13: Comparison of simulated and theoretical efficiencies as a function of tapering defined by the resonant phase, θ_r. While the importance of external seeding is seen explicitly in the increased efficiency, it is also necessary for prebunching.

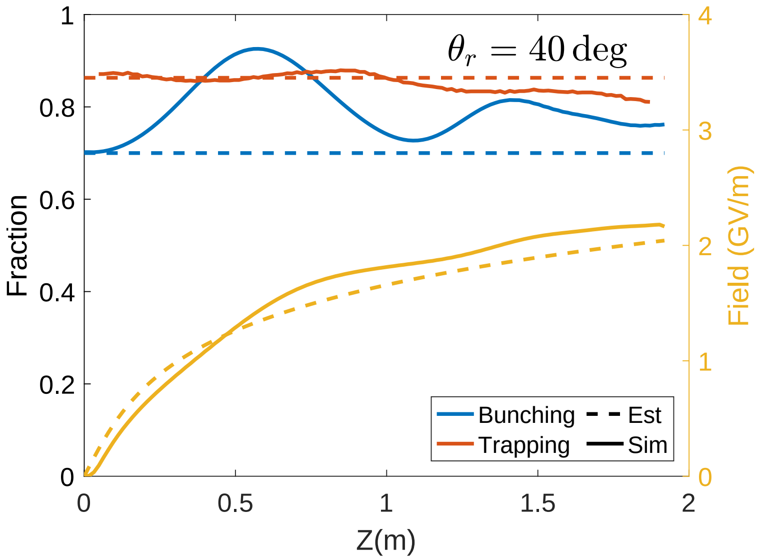

Figure 1.14: A comparison of simulated and theoretical beam and field characteristics with seeding at $\theta_r = 40°$. Bunching undulates due to synchrotron oscillations in the longitudinal phase space.

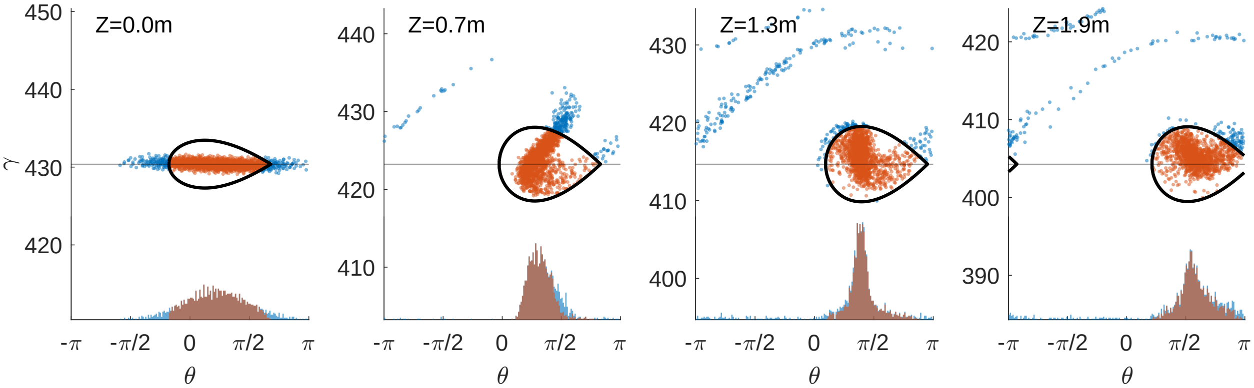

Figure 1.15: Simulated phase space evolution of seeded FEL for $\theta_r = 40°$. The tapering-defined resonant energy (horizontal line) and ponderomotive bucket are plotted along with the beam. Trapping is show by the coloring.

Finally, we consider variations in the tapering by changing the resonant phase. Figure 1.13 plots the analytic estimates against simulation with and without a seed field. The simulation tracks well with estimates though there is a noticeable drop around 50 deg in the seeded case due to detrapping. The importance for external laser seeding can be seen explicitly in the increase efficiency (linear term of Eq. (1.43) from 1D theory) as well as implicitly in the need to produce a bunched beam with large bunching factor.

Figure 1.14 shows bunching and trapping fractions along with emitted field for the seeded simulation at $\theta_r = 40$. The dashed and solid lines show estimated and simulated values, respectively. The amplitude of the emitted field aligns nicely with theory even though the assumption of constant bunching phase is technically violated. The bunching factor undulates due to synchrotron oscillations in the ponderomotive bucket, but remains close to its estimate value. The theoretical trapping fraction f_t is computed using a sinusoidal longitudinal density $1 + 2b\cos(kz)$, where b is the bunching factor. The distribution is unphysical for $b > 0.5$, but provides a good estimate for the simulation. It is clear that detrapping is starting to occur in the second undulator, which worsens at higher resonant phases causes the drop in efficiency above $\theta_r \sim 50^\circ$. This suggesting the estimated tapering is too aggressive at higher resonant phases. In the limit as $\theta_r \to 90^\circ$, the simulated efficiencies do not drop to zero even though particles immediately become detrapped as there is still a small amount of deceleration. The phase space evolution is shown in Figure 1.15 along with the tapering-defined resonant energy and ponderomotive bucket where coloring indicates trapping of the electrons.

1.6 Waveguide FELs

Until now, we have described the FEL interaction in free space, without any materials or boundaries near the interaction. However, at long wavelengths the FEL interaction is degraded by excessive radiation diffraction and slippage. A waveguide can be added to contain the radiation transversely at the cost of introducing an aperture and power attenuation not seen in the free-space FEL. Another important advantage is the ability to choose waveguide dimensions such that the subluminal group velocity of the radiation matches the average longitudinal velocity of the waveguide. This zero-slippage operation extends the interaction length for high current, compressed electron beams that emit strong electric fields. In this section we develop the theory for waveguide modes necessary to setup a discussion of the GPTFEL code as well as introduce the details of the zero-slippage condition essential to the operation of the UCLA THz Waveguide FEL.

We begin by considering the electromagnetic fields in a conducting waveguide with the general form

$$\mathbf{E}(\mathbf{x}, z, t) = \left(\mathbf{E}_\perp(\mathbf{x}) + \hat{\mathbf{z}}E_z(\mathbf{x})\right) e^{ik_z z - i\omega t} \tag{1.58}$$

Waveguides support traveling wave solutions in two distinct set of bases referred to as transverse electric and transverse magnetic modes defined by $E_z = 0$ and $H_z = 0$ with Neumann or Dirichlet boundary conditions, respectively. TEM modes ($E_z = H_z = 0$) do not exist as the application of Gauss's Law $\nabla \cdot \mathbf{E} = 0$ and Ampere's Law $\nabla \times \mathbf{B} = 0$ prohibit a non-zero solution. We assume vacuum in the waveguides which is necessary for electron propagation. The general field descriptions are derived in [68] as

$$\begin{array}{ll} \text{Transverse Electric (TE)} & \text{Transverse Magnetic (TM)} \\ E_z = 0, \quad \left.\dfrac{\partial H_z}{\partial \hat{\mathbf{n}}}\right|_S = 0 & H_z = 0, \quad E_z|_S = 0 \\ \left(\nabla_\perp^2 + k_\perp^2\right) H_z = 0 & \left(\nabla_\perp^2 + k_\perp^2\right) E_z = 0 \\ \mathbf{H}_\perp = \dfrac{ik_z}{k_\perp^2}\nabla_\perp H_z & \mathbf{E}_\perp = \dfrac{ik_z}{k_\perp^2}\nabla_\perp E_z \\ \mathbf{E}_\perp = \dfrac{-\omega\mu_0}{k_z}\left(\hat{\mathbf{z}} \times \mathbf{H}_\perp\right) & \mathbf{H}_\perp = \dfrac{\omega\epsilon_0}{k_z}\left(\hat{\mathbf{z}} \times \mathbf{E}_\perp\right) \end{array} \tag{1.59}$$

where S denotes the waveguide boundary surface, $\hat{\mathbf{n}}$ denotes the boundary normal, and $\nabla_\perp^2$ and $\nabla_\perp$ represent the transverse Laplacian and gradient for the given geometry.

Waveguide modes exhibit dispersion where frequencies propagate at different speeds according to

$$\omega^2/c^2 = k_z^2 + k_\perp^2 \tag{1.60}$$

where the phase and group velocities are defined by $v_p = \omega/k_z$ and $v_g = d\omega/dk_z$. The group velocity (evaluated at the central frequency) describes the speed of the waveform envelope and is constrained by causality to be less than to the speed of light with equality in the free-space/large aperture limit. The phase velocity describes the speed of the wavefront and is greater than or equal to the speed of light as it can be shown from Eq. 1.60 that $v_p v_g = c^2$. A derivation of diffraction effects including the group velocity dispersion, $\beta_2 = \partial^2 k/\partial\omega^2$, is given in Appendix B.

Each waveguide mode has a cutoff frequency $\omega_c = ck_\perp$, which denotes the lowest frequency capable of propagation. At lower frequencies, k_z is imaginary and the complex exponential in Eq. (1.58) leads to an exponential decay of the fields in the so-called evanescent modes. Single-mode operation in a waveguide occurs at frequencies where only the fundamental mode can propagate. If operated at higher frequencies, the waveguide becomes over-moded and multiple modes can propagate.

In a waveguide, power is absorbed due to ohmic losses in the walls with an attenuation constant β_{wg} defined as

$$P(z) = P(0)e^{-2\beta_{wg}z} \quad \text{or} \quad \beta_{wg} = -\frac{1}{2P}\frac{dP}{dz} \tag{1.61}$$

where the time averaged power P flowing down the waveguide can be computed from a surface integral over the pointing vector $\mathbf{S} = \mathrm{Re}\left(\mathbf{E} \times \mathbf{H}^*\right)/2$. The ohmic losses due to the non-ideal conduction in the waveguide and skin depth penetration of the fields is commonly expressed as power loss per area of wall. We can express the power lost per unit length by performing a contour integral around the waveguide boundary.

$$\frac{dP}{dz} = \oint \frac{dP}{dA} d\ell$$

It can be shown [68] that for a generic TE mode

$$\beta_{wg} = \frac{\oint |H_z|^2 + |\hat{\mathbf{n}} \times \mathbf{H}_\perp|^2 d\ell}{4\sigma\delta P} \quad \text{where} \quad P = \frac{\omega k_z \mu_0}{2k_\perp^2} \iint |H_z|^2 dA \tag{1.62}$$

where σ is the material conductivity, $\delta = 2/\mu\sigma\omega$ is the skin depth, and μ is the magnetic permeability of the material. For most materials, it can be assumed that $\mu \approx \mu_0$.

1.6.1 Circular Waveguide

We first consider a circular waveguide geometry used for the Tessatron Waveguide FEL experiments. The Laplacian and gradient are given by $\nabla_\perp^2 = \frac{\partial^2}{\partial r^2} + \frac{1}{r}\frac{\partial}{\partial r} + \frac{1}{r^2}\frac{\partial^2}{\partial \phi^2}$ and $\nabla_\perp = \hat{\mathbf{r}}\frac{\partial}{\partial r} + \hat{\boldsymbol{\phi}}\frac{1}{r}\frac{\partial}{\partial \phi}$ and the Helmholtz equation can be solved with a separable solution, $\mathcal{R}(r)\Phi(\phi)$. The azimuthal function $\Phi(\phi)$ must be 2π-periodic in ϕ such that $\partial^2\Phi/\partial\phi^2 = -m^2\Phi$ where m is an integer. The double degeneracy that exists for $|m| > 0$ represents right/left circular polarizations.

Table 1.2: Tabulated zeros for J_m and J'_m

n	$J_0(x)$	$J_1(x)$	$J_2(x)$	$J'_0(x)$	$J'_1(x)$	$J'_2(x)$
1	2.4048	3.8317	5.1356	3.8317	1.8412	3.0542
2	5.5201	7.0156	8.4172	7.0156	5.3314	6.7061
3	8.6537	10.1735	11.6198	10.1735	8.5363	9.9695

The radial differential equation

$$r^2\frac{\partial^2\mathcal{R}}{\partial r^2} + r\frac{\partial\mathcal{R}}{\partial r} + (r^2 k_{mn} - m^2)\mathcal{R} = 0 \tag{1.63}$$

is satisfied by Bessel functions $J_m(k_{mn}r)$ where the boundary conditions for TE and TM modes allow discrete solutions in terms of the nth zero of J_m or J'_m. Table 1.2 shows the zeros for the first few Bessel functions. The longitudinal fields are given by

$$\begin{aligned} &(\text{TE}) \quad H_z^{mn}(r,\phi) = H_0 J_m(k_{mn}r)e^{\pm im\phi} \quad \text{where} \quad k_{mn} = w_{mn}/R, \quad J'_m(w_{mn}) = 0 \\ &(\text{TM}) \quad E_z^{mn}(r,\phi) = E_0 J_m(k_{mn}r)e^{\pm im\phi} \quad \text{where} \quad k_{mn} = u_{mn}/R, \quad J_m(u_{mn}) = 0 \end{aligned} \tag{1.64}$$

where H_0 and E_0 are normalization constants. The cutoff frequency occurs in the fundamental TE11 mode at $\omega_c = 1.8412c/R$.

Only modes with non-zero transverse electric fields on axis can resonant with an electron beam in a waveguide FEL. To identify right-circularly polarized resonant modes ($m > 0$), we convert the cylindrical transverse electric fields to cartesian using the small-argument expansion of the Bessel function, $J_m(r) \approx r^m/2^m m! + \mathcal{O}(r^{m+2})$. For TM modes, we compute the transverse fields from the gradient of E_z^{mn} directly as

$$\begin{aligned}
\mathbf{E}_\perp(r,\phi) &= \frac{ik_z}{k_\perp^2}\nabla_\perp E_z = E_0\frac{ik_z}{k_\perp^2}\left(\hat{\mathbf{r}}\frac{\partial}{\partial r} + \hat{\boldsymbol{\phi}}\frac{1}{r}\frac{\partial}{\partial \phi}\right) J_m(k_\perp r)e^{\pm im\phi} \\
&\approx E_0\frac{ik_z}{k_\perp^2}\frac{k_\perp^m r^{m-1}}{2^m(m-1)!}e^{\pm im\phi}\left(\hat{\mathbf{r}} \pm i\hat{\boldsymbol{\phi}}\right) \\
&= E_0\frac{ik_z}{2k_\perp}\left(\hat{\mathbf{x}} \pm i\hat{\mathbf{y}}\right) \quad \text{where} \quad m = 1 \qquad (1.65)
\end{aligned}$$

where $|\mathbf{E}_\perp(r=0)| \neq 0$ only for $m = 1$. Thus, out of all the TM modes, only the TM_{1n} modes can resonate with an electron beam. The TE modes have a similar mathematical structure such that we can borrow from Eq. (1.65) and similarly find resonance occurs only in TE_{1n} modes.

$$\begin{aligned}
\mathbf{E}_\perp &= -\frac{i\omega\mu_0}{k_\perp^2}\left(\hat{\mathbf{z}} \times \nabla_\perp H_z\right) \\
&= -H_0\frac{i\omega\mu_0}{k_\perp^2}\frac{k_\perp^m r^{m-1}}{2^m(m-1)!}\left(\hat{\mathbf{z}} \times (\hat{\mathbf{x}} \pm i\hat{\mathbf{y}})\right) \\
&= \mp H_0\frac{\omega\mu_0}{2k_\perp}(\hat{\mathbf{x}} \pm i\hat{\mathbf{y}}) \quad \text{where} \quad m = 1 \qquad (1.66)
\end{aligned}$$

Figure 1.16 plots the first few resonant circular waveguide modes. As n increases, the area of the uniform field region diminishes. We choose to normalize modes according to $|\mathbf{E}_\perp(r=0)| = 1$ such that $E_0 = \sqrt{2}k_\perp/k_z$ and $H_0 = \sqrt{2}k_\perp/\omega\mu_0$.

We now compute the power attenuation for the fundamental TE_{11} waveguide mode used in the experiments. It can easily be shown that $|\hat{\mathbf{r}} \times \mathbf{H}_\perp|^2 = \frac{k_z^2}{r^2k_\perp^4}|H_z|^2$. The integrand of the contour integral is constant along the boundary ($r = R$) such that the integral simply contributes a factor of $2\pi R$. The area integral is solved by

$$\int_0^R J_1(k_{11}r)^2 r dr = \frac{R^2}{2}\left(J_0(w_{11})^2 + J_1(w_{11})^2 - \frac{2}{w_{11}}J_0(w_{11})J_1(w_{11})\right) \qquad (1.67)$$

such that after rearranging constants we find

$$\beta_{wg} = \frac{w_{11}^2\delta}{2R^3k_z}\left(1 + \frac{k_z^2R^2}{w_{11}^4}\right)\left(\frac{J_1(w_{11})^2}{J_0(w_{11})^2 + J_1(w_{11})^2 - 2J_0(w_{11})J_1(w_{11})/w_{11}}\right) \qquad (1.68)$$

where the units of β_{wg} are np/m and 1 dB/1 np = 8.69. The attenuation is a function of frequency through the longitudinal wavevector $k_z(\omega)$ and the skin depth $\delta(\omega) = \sqrt{2/\omega\mu\sigma}$

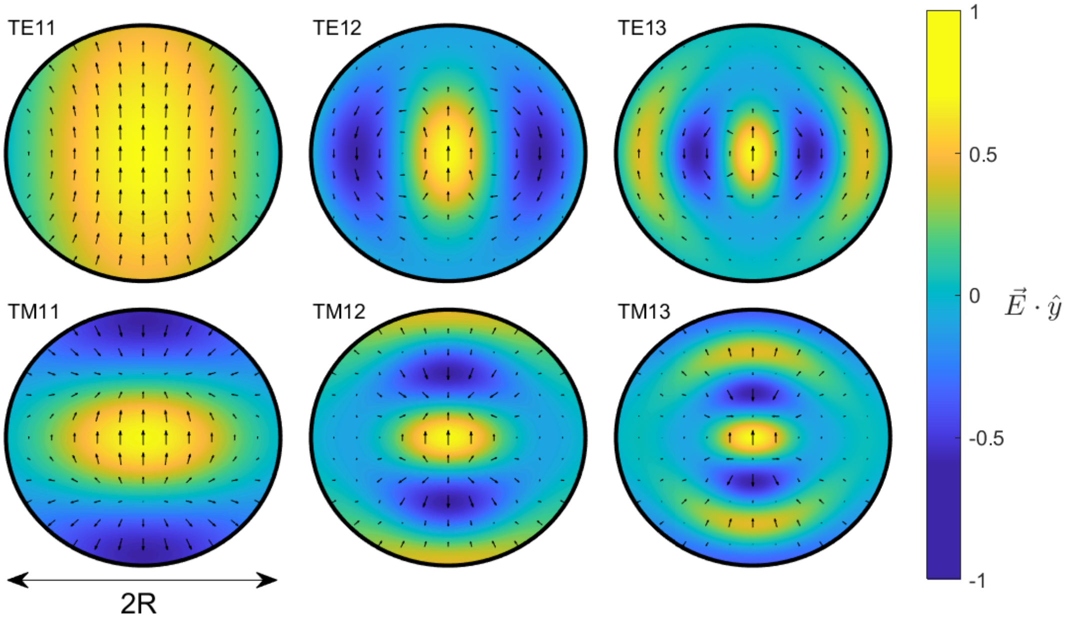

Figure 1.16: The first few FEL-resonant (m=1) modes for a circular waveguide. Arrows show local field polarization with phase chosen such that polarization is $\hat{\mathbf{y}}$ on axis. Coloring shows coupling with resonant electrons ($\mathbf{v} = v\hat{\mathbf{y}}$).

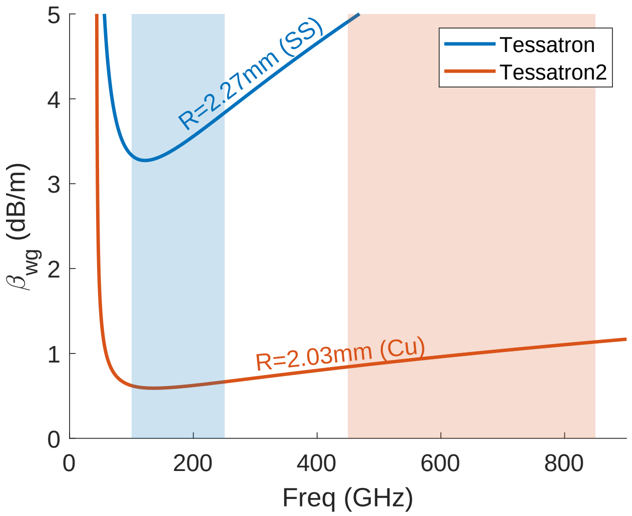

Figure 1.17: Waveguide power attenuation for the Tessatron experiments. Tessatron used a 5.54 mm ID stainless steel vacuum pipe which doubled as a waveguide while Tessatron2 used a 4.06 mm ID copper waveguide. The experimental frequency ranges are shaded.

where σ is the material conductivity. At THz frequencies, skin depths are limited to a few micron such that the thickness of the waveguide walls has negligible effect on the attenuation. Figure 1.17 shows the attenuation constants for the waveguide materials used in the two Tessatron experiments along with the experimental frequency range. The sub-optimal stainless steel material in the first experiment was due the fact the vacuum pipe itself served as the waveguide, leading to 30% loss in THz energy in the 1 meter waveguide. Using a copper waveguide in the following experiment reduced the attenuation loss to 5%.

1.6.2 Rectangular Waveguide

Next we consider a rectangular waveguide geometry with walls at $x = 0$, $x = a$ and $y = 0$, $y = b$ with a cartesian Laplacian given by $\nabla_\perp^2 = \frac{\partial^2}{\partial x^2} + \frac{\partial^2}{\partial y^2}$. Using the separable solution $X(x)Y(y)$ and applying boundary conditions we find

$$\begin{aligned} &\text{(TE)} \quad H_z^{mn} = H_0 \cos(k_x x)\cos(k_y y) \\ &\text{(TM)} \quad E_z^{mn} = E_0 \sin(k_x x)\sin(k_y y) \end{aligned}$$

where $k_x = m\pi/a$, $k_y = n\pi/b$, and $k_{mn} = \sqrt{k_x^2 + k_y^2}$. The mode indices m and n run over non-negative integers except for TM_{m0}, TM_{0n}, and TE_{00} where the fields are trivially zero. The cutoff frequency occurs in the fundamental TE_{10} mode assuming $a > b$ such that $\omega_c = c\pi/a$.

The transverse electric fields computed from Eq. (1.59) share a similar transverse dependence on x and y and are given by

$$\begin{aligned} &\text{(TE)} \quad \mathbf{E}_\perp^{mn} = H_0 \frac{i\omega\mu_0}{k_\perp^2}\Big(- k_y \cos(k_x x)\sin(k_y y)\hat{\mathbf{x}} + k_x \sin(k_x x)\cos(k_y y)\hat{\mathbf{y}}\Big) \\ &\text{(TM)} \quad \mathbf{E}_\perp^{mn} = E_0 \frac{ik_z}{k_\perp^2}\Big(k_x \cos(k_x x)\sin(k_y y)\hat{\mathbf{x}} + k_y \sin(k_x x)\cos(k_y y)\hat{\mathbf{y}}\Big) \end{aligned}$$

We assume without loss of generality that the waveguide is used in a planar undulator with B_y field and sinusoidal beam trajectory in $\hat{\mathbf{x}}$. Only fields where $E_x(a/2, b/2) \neq 0$ support resonance with an electron beam, requiring even m and odd n indices. The first few TE resonant modes are shown in Figure 1.18. Normalizing such that $|\mathbf{E}_\perp(a/2, b/2)| = 1$ fixes

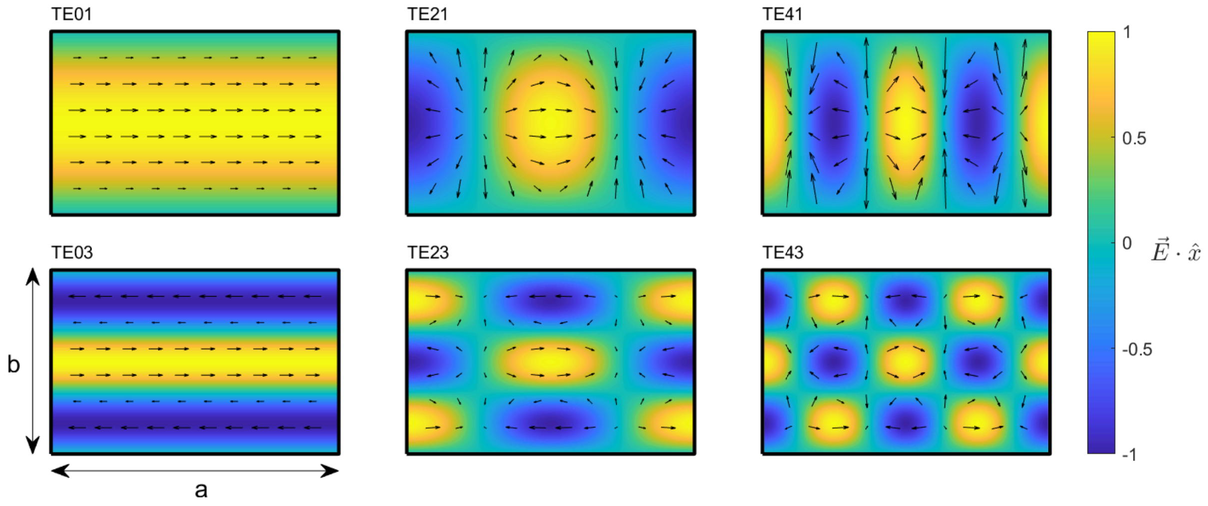

Figure 1.18: The first few FEL-resonant TE rectangular waveguide modes where m is even and n is odd. The transverse field dependence is nearly identical for TM modes except TM_{0n} modes do not exist. Arrows show local field polarization with phase chosen such that polarization is $\hat{\mathbf{x}}$ on axis. Coloring shows coupling with resonant electrons ($\mathbf{v} = v\hat{\mathbf{x}}$)

$H_0 = k_\perp^2/\omega\mu_0 k_y$ and $E_0 = k_\perp^2/k_z k_x$. The equivalent TM modes are nearly identical except that the TM_{0n} modes do not exist.

1.6.3 Zero Slippage

In a waveguide FEL, the waveguide dimensions can be tuned to match the radiation group velocity to the average longitudinal velocity of the electron beam, effectively eliminating FEL slippage [69, 70, 71]. This enables strong compression of the beam which greatly increases the current density for effective FEL seeding. In addition to the waveguide dispersion relation (1.60) and FEL phase resonance condition (1.7), the zero-slippage condition introduces an additional "group-resonance" constraint on the FEL parameters.

$$\boxed{c\beta_z = v_g = \frac{c^2 k_z}{\omega}} \tag{1.69}$$

Thus for fixed undulator and waveguide parameters, zero-slippage can only be achieved at a singular frequency, restricting the precious frequency tunability of the FEL interaction.

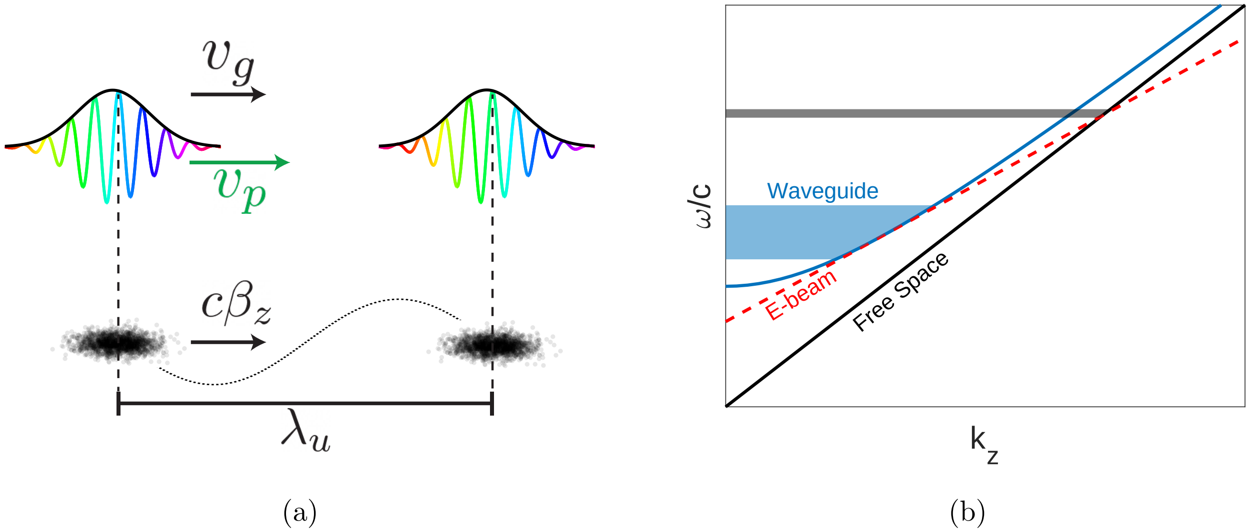

Figure 1.19: Zero-slippage in time and frequency domain. a) The colored phase fronts slip past the beam according to the FEL phase-resonance condition while the waveform envelope remains temporally aligned. b) Satisfying both the phase and group resonance conditions corresponds to matching the point and slope of the waveguide dispersion curve, enabling a large-bandwidth interaction that supports the generation of several-cycle radiation pulses.

In the Tessatron2 experiment, we will seek a compromise between minimal slippage and maximal tunability by operating detuned from the zero-slippage condition.

We present the derivation for zero-slippage in a circular waveguide mode, but geometry only affects $k_\perp$ such that the analysis can be quickly adapted to other geometries. To apply to TE and TM modes generally, we let $k_\perp = \eta/R$ where η can represent either of the tabulated Bessel zeros u_{mn} or w_{mn}.

Figure 1.19a shows a schematic of zero slippage where the colored phasefronts move at the phase velocity and continue to slip past the electron beam one wavelength every period in accordance with the phase-resonance condition. However, the envelope of the waveform (shown in black) moves at the group velocity which remains temporally aligned with the electrons which allows for an extended interaction. To determine parameter relations at zero-slippage, we assume the undulator and waveguide properties K and $k_\perp(R)$ are fixed, and solve for ω, k_z, and $\beta_z(\gamma)$ using our three conditions. Values at zero-slippage resonance are denoted with a zero subscript and we utilize the shorthand $\gamma_z^2 = \gamma^2/(1+K^2) = 1/(1-\beta_z^2)$.

$$k_z + k_u = \frac{\omega}{c\beta_z} = \frac{\omega^2}{c^2 k_z} = \frac{k_z^2 + k_\perp^2}{k_z} \quad \text{by} \quad (1.69) \quad \text{and} \quad (1.60) \tag{1.70}$$

$$\boxed{\implies k_{z0} = k_\perp^2/k_u \implies \omega_0 = \frac{ck_\perp}{k_u}\sqrt{k_\perp^2 + k_u^2} \implies \beta_{z0} = \frac{k_\perp}{\sqrt{k_\perp^2 + k_u^2}}, \quad \gamma_{z0} = \sqrt{1 + \frac{k_\perp^2}{k_u^2}}}$$

where the solution of k_{z0} is easily back-substituted to solve for ω_0 and β_{z0}. It can be more insightful to instead generate a quadratic equation in ω describing the phase resonance curves by solving Eq. (1.7) for k_z and substituting into Eq. (1.60).

$$\begin{aligned} 0 &= \omega^2(1 - 1/\beta_z^2) + \omega(2ck_u/\beta_z) - c^2(k_u^2 + k_\perp^2) \\ &= \omega^2 - 2ck_u\beta_z\gamma_z^2\omega + c^2\beta_z^2\gamma_z^2(k_u^2 + k_\perp^2) \quad \text{where} \quad -\beta_z^2\gamma_z^2 = \frac{1}{1 - 1/\beta_z^2} \end{aligned}$$

$$\boxed{\omega = ck_u\beta_z\gamma_z^2\left(1 \pm \sqrt{1 - \frac{k_u^2 + k_\perp^2}{k_u^2\gamma_z^2}}\right)} \tag{1.71}$$

Figure 1.19b shows a comparison of the dispersion in a waveguide and free-space FEL. In a free-space FEL, the phase resonance is represented by the point of intersection with the electron beam dispersion leading to a narrow bandwidth as required by slippage in the temporal domain. On the other hand, the additional zero slippage condition in a waveguide FEL is geometrically represented as matching the slope of the waveguide and electron beam dispersions. The tangential intersection leads to a large bandwidth of frequencies that can be excited, enabling the generation of short, few cycle waveforms. It can been seen in Eq. (1.71) that the requirement for a singular solution (zero discriminant) gives the same zero-slippage value of γ_z as in Eq. (1.70) matching our physical intuition. If the energy is detuned above the zero slippage condition, there are now two frequencies that can simultaneously lase in the FEL. Conversely, at energies below the zero-slippage condition there is no lasing that can occur. For realistic beams with 3D effects including energy spread and finite emittance, the electron beam dispersion curve thickens and the optimal overlap with the waveguide dispersion will occur at a small positive energy detuning.

From Eq. (1.71) we also gain solutions for the frequency and waveguide radius as a

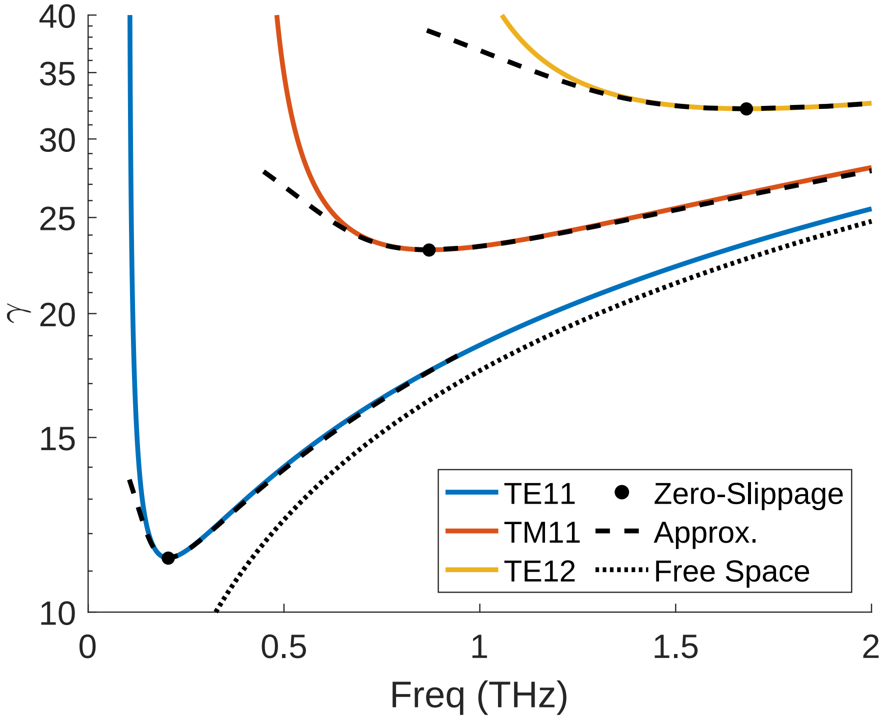

Figure 1.20: Phase resonance curves for the first few circular waveguide modes along with the free-space limit (black line) and analytic approximations (black dashed lines).

function of beam energy.

$$\omega_0 = ck_u\beta_{z0}\gamma_{z0}^2 \qquad \text{and} \qquad R_0 = \frac{\eta}{k_u\sqrt{\gamma_{z0}^2 - 1}} \tag{1.72}$$

It is interesting to note that in the relativistic limit $\beta_{z0} \approx 1$, the resonant frequency is exactly one half that of an FEL in free-space as computed from Eq. (1.8). We can expand the quadratic in ω about the zero-slippage solution, defining $\gamma_z = (1 + \delta_\gamma)\gamma_{z0}$ such that

$$\omega = \omega_c\left(1 + 2\delta_\gamma\right)\left(1 \pm \sqrt{2\delta_\gamma}\right) \tag{1.73}$$

which describes the two resonant frequency branches at higher energies. Figure 1.20 shows the actual numeric solutions and approximations for the first few resonant modes of the 4.06 mm diameter waveguide used in the Tessatron2 experiment, bound below and above by the waveguide cutoff frequency and free-space resonance asymptote. The energy dependence of the lasing is clear as well as the increasing frequencies of the zero-slippage condition for higher order which helps compensate for the lack of tunability due to the extra condition. The approximation is very accurate for the high frequency branch where the resonant frequency varies significantly with the beam energy while the low frequency branch deviates due to the lower bound of the mode's cutoff frequency.

From Eq. (1.72), we see that increasing the resonant frequency requires higher energy beams and smaller waveguide dimensions, introducing challenges for full charge transmission through the undulator. The ratio of the beam trajectory amplitude to waveguide radius is bounded and nearly constant for fixed K.

$$\frac{r_{max}}{R} = \frac{K}{R k_u \gamma_0 \beta_{z0}} = \frac{1}{\eta}\frac{K}{\sqrt{1+K^2}}\frac{1}{\beta_{z0}\sqrt{1+k_u^2/k_\perp^2}} \approx \frac{1}{\eta}\frac{K}{\sqrt{1+K^2}} \leq \frac{1}{\eta} \tag{1.74}$$

where we assume the relativistic limit $\gamma \gg 1$ such that $k_\perp/k_u \gg 1$ For example, in the fundamental TE11 mode, $1/\eta = 0.543$ such that the beam trajectory is roughly 1/2 the waveguide radius. While the ratio is bounded, the challenge of full transmission does increase for smaller waveguide dimensions due to the finite matched spotsize $\sigma_x = \sqrt{\epsilon_n \lambda_u / 2K}$ and undulator tuning/alignment tolerances. The undulator tuning poses novel challenges as the large beam trajectory samples fields off axis, requiring strategies for ensuring correct tuning of the 3D undulator fields. Lasing with a higher order mode reduces tolerances on charge transmission at the cost of reduced coupling with the electron beam. A more promising direction is to utilize a rectangular waveguide with a planar undulator geometry where the aspect ratio of the waveguide aperture can be chosen to optimize charge transmission without affecting the coupling.

CHAPTER 2

GPTFEL and start-to-end simulations

2.1 Motivation

Numerical simulations have played a significant role in the development of FELs. As FEL theory [72, 73] only admits analytical solutions under strong approximations, accelerator physicists have developed an assortment of numerical approaches over the years to better understand the details of the evolution of charged particles and electromagnetic fields in their interaction through magnetic undulators.

There are a large variety of FEL simulation codes and many good reviews on the subject have been given [74, 75, 76]. These range from fast one dimensional models (Perseo [77], Perave [78]) which help in quick design studies and can be used to explore time-dependent and nonlinear effects, to more complete 3D simulations (Ginger [79], Genesis 1.3 [80], Fast [81], Puffin [82], Minerva [83]) which include transverse effects and can simulate wakefields and complex beam distributions with correlations between the phase spaces. Each code has been (at least initially) developed to solve a particular FEL problem, but it has often been the case that, by comparing and understanding the various assumptions in each model, insights on the various physical processes taking place in an FEL system have been gained.

Here we introduce yet another instance of a three dimensional FEL simulation based on the decomposition of the electromagnetic field in a discrete set of transverse and frequency modes. In this respect it is more similar to the family of frequency-based codes like Puffin or Minerva. The GPTFEL code is built as an expansion of the widely available General Particle Tracer code (GPT) for charged particle simulations [84]. In this sense, it can use a complete set of already built-in functions for beam transport and interface seamlessly with photoinjector [85] and CSR calculations [86]. This choice also brings several important advantages. Similarly to Puffin and Minerva, the calculation does not resort to period averaging and a full (simulated or even measured) undulator field map can be used to track the particles. The effects of the interaction at the undulator entrance and exit can therefore be correctly evaluated. Furthermore, GPT functions allow space charge effects to be naturally incorporated, including the transverse space charge effects that play a significant role in the beam transport and evolution at low energies.

The code can be used to simulate both free-space and waveguide propagating electromagnetic fields and naturally takes into account dispersive properties the medium. In free-space there is some freedom in choosing the basis for the field expansion, making it possible to take advantage of the Source Dependent Expansion [87, 88] algorithm to reduce the number of modes needed to accurately describe the field and significantly speed up the calculation, a capability that also exists in Minerva.

In this chapter, we first derive the modal expansion and detail the numerical implementation of the equations in the simulation [89]. We then present three different application examples. The first is a simple seeded FEL amplifier in vacuum (analyzed both in a helical and planar geometry). The second applies to the strongly nonlinear regime beyond saturation and refers to initial simulations of the TESSA266 experiment [90] which was adapted into the FASTGREENS experiment after complications due to the COVID pandemic. The third example is a waveguide-THz FEL operating in the zero-slippage regime [69]. Finally, we conclude the chapter by making a connection between waveguide FELs and 1D FEL theory to benchmark the code for circular and rectangular waveguide geometries.

2.2 Theory

2.2.1 3D Frequency Domain Analysis

To begin our derivation of the GPTFEL equations, we return to the full 3D wave equation (see Eq. (1.16)) and relax the time-independent assumption of periodicity. To this end, we require a full Fourier representation of the complex field.

$$\mathbf{E}(\mathbf{x}, z, t) = \frac{1}{2\pi}\int_{-\infty}^{\infty} \tilde{\mathbf{E}}(\mathbf{x}, k, t)e^{ikz-i\omega t}dk \tag{2.1}$$

Each frequency component can be further decomposed into an orthogonal mode basis labeled by index q such that $\tilde{\mathbf{E}}(\mathbf{x}, k, t) = \sum_q a_q(t)\boldsymbol{\Theta}_q(\mathbf{x}, k)$ where $\boldsymbol{\Theta}_q$ is a solution to the homogeneous wave equation. We normalize the modes to unity amplitude on axis, $|\boldsymbol{\Theta}_{q,\perp}(\mathbf{x} = \mathbf{0})| = 1$, and define the mode area $\mathcal{A}_q$ as

$$\iint \boldsymbol{\Theta}_q^* \boldsymbol{\Theta}_q' d\mathbf{x} = \delta_{qq'}\mathcal{A}_q \tag{2.2}$$

After inserting the expansion for the field, the left hand side (LHS) of the wave equation can be written as

$$LHS = \frac{1}{2\pi}\int_{-\infty}^{\infty}\left(\cancel{\ddot{a}_q(k,t)} + \frac{2i\omega}{c^2}\dot{a}_q(k,t)\right)\boldsymbol{\Theta}_q(\mathbf{x}, k)e^{ikz-i\omega t}dk \tag{2.3}$$

where we assume the slowly varying envelope approximation (SVEA) for the field such that the second order derivative can be neglected. To evaluate the right hand side, we express the beam current density as a sum over delta functions

$$\mathbf{J}(\mathbf{x}, z, t) = \sum_j q_j \mathbf{v}\delta(\mathbf{x} - \mathbf{x}_j(t))\delta(z - z_j(t)) \quad \text{and} \quad \mathbf{v}(z) = \frac{\sqrt{2}cK_{rms}}{\gamma}e^{-ik_u z}\hat{\mathbf{n}} + c\beta_z\hat{\mathbf{z}} \tag{2.4}$$

where the longitudinal beam velocity can couple to the E_z field in TM waveguide modes. We note that K_{rms} is equal to $K/\sqrt{2}$ or K for planar or helical geometries, and use $\hat{\mathbf{n}} = (\hat{\mathbf{x}} + ip\hat{\mathbf{y}})/\sqrt{1+p^2}$ where the parameter p can specify planar (0) or right/left circular (± 1) polarization. We make use of the shorthand notations $n_x = 1/\sqrt{1+p^2}$ and $n_y = p/\sqrt{1+p^2}$ to generalize equations for any polarization.

It is not computationally feasible to track all the electrons in a real beam, so we instead model the the beam with a smaller number of macroparticles with charge q_j. In order to compare with the LHS, we rewrite the source term using nested Fourier transforms giving

$$RHS = \frac{\mu_0}{2\pi}\frac{\partial}{\partial t}\left(\int_{-\infty}^{\infty}\int_{-\infty}^{\infty}\mathbf{J}(\mathbf{x}, z', t)e^{-ikz'}dz'e^{ikz}dk\right) \tag{2.5}$$

such that the $\int_{-\infty}^{\infty} dk$ integrands are equivalent. We integrate over z' using the delta function sampling property and apply the time derivative using chain rule on $\mathbf{x}_j(t)$ and $z_j(t)$ to find

$$\frac{2i\omega}{c^2}\dot{a}_q(k,t)\boldsymbol{\Theta}_q(\mathbf{x})e^{-i\omega t} = \mu_0\sum_j q_j\left(\mathbf{v}_j \cdot \nabla_j\right)\left(e^{-ikz_j}\mathbf{v}_j\delta(\mathbf{x} - \mathbf{x}_j(t))\right) \tag{2.6}$$

where $\nabla_j = \hat{\mathbf{x}}\frac{\partial}{\partial x_j} + \hat{\mathbf{y}}\frac{\partial}{\partial y_j} + \hat{\mathbf{z}}\frac{\partial}{\partial z_j}$. We solve for the evolution of the mode amplitudes by multiplying by $\mathbf{\Theta}^*_{q'}$ and integrating over the transverse coordinates

$$\dot{a}_q(k,t) = \frac{-i\mu_0 c^2}{2\omega \mathcal{A}_q} \sum_j q_j \left(\mathbf{v}_j \cdot \nabla_j\right) \left(e^{-ikz_j + i\omega t}(\mathbf{v}_j \cdot \mathbf{\Theta}^*_{q,j})\right) \tag{2.7}$$

where $\mathbf{\Theta}_{q,j}$ refers to evaluating the qth mode at the jth particle position.

The terms with transverse derivatives are negligible as the transverse velocity is much smaller than the longitudinal velocity and the spatial dimensions of the mode (waveguide aperture or free-space mode waist) are larger than the radiation wavelength. It can also be reasonably assumed that K and γ have slow dependence on z_j ($\frac{\partial K}{\partial z}, \frac{\partial \gamma}{\partial z} \ll k + k_u$), such that applying $\partial/\partial z_j$ gives

$$\dot{a}_q(k,t) = -\sum_j \frac{q_j}{2\epsilon_0 \mathcal{A}_q} \left[\frac{c\beta_z}{\omega}(k + k_u)\right] \left((\mathbf{v}_{\perp,j} \cdot \mathbf{\Theta}^*_{q,j}) + \frac{k}{k + k_u}(\mathbf{v}_{z,j} \cdot \mathbf{\Theta}^*_{q,j})\right) e^{-ikz_j + i\omega t} \tag{2.8}$$

Only electrons that are nearly resonant with the given mode will significantly contribute to a net energy exchange, such that the bracketed term can be approximated as 1. Additionally, the undulator period can be assumed much larger than the radiation wavelength to combine terms.

$$\dot{a}_q(k,t) = -\sum_j \frac{q_j}{2\epsilon_0 \mathcal{A}_q} \left(\mathbf{v}_j \cdot \mathbf{\Theta}^*_{q,j}\right) e^{-ikz_j + i\omega t} \tag{2.9}$$

If the undulator period is passed as a parameter there is no necessity for these two approximations in the code, but in practice the simulation results are nearly identical.

Equation (2.9) can also be derived from energy conservation. The total radiation energy energy is given the volume integral over the energy density

$$W = \int_V \frac{\epsilon_0}{2} \operatorname{Re}\{\mathbf{E}\}^2 + \frac{1}{2\mu_0} \operatorname{Re}\{\mathbf{B}\}^2 dV = \int_V \frac{1}{2}\epsilon_0 |\mathbf{E}|^2 dV \tag{2.10}$$

where the energy stored in magnetic fields is equal to energy in the electric fields. Utilizing the frequency domain representation of the field allows the transverse integral to be evaluated over the modes.

$$W = \frac{\epsilon_0}{2}\frac{1}{2\pi} \int \sum_q |a_q|^2 \mathcal{A}_q dk \tag{2.11}$$

The rate of change in the electromagnetic energy is equal to the negative of the work done on the particles,

$$
\begin{aligned}
\frac{dW}{dt} &= -\sum_j q_j \operatorname{Re}\{\mathbf{E}(\mathbf{x}_j, z_j, t)\} \cdot \operatorname{Re}\{\mathbf{v}_j\} \\
\int \sum_q \frac{a_q^*}{2\pi} \left[\dot{a}_q \frac{\epsilon_0 \mathcal{A}_q}{2} \right] dk + \text{c.c.} &= -\sum_j \frac{q_j}{4} \left(\mathbf{E}^*(\mathbf{x}_j, z_j, t) \cdot \mathbf{v}_j \right) + \text{c.c.} \\
&= \int \sum_q \frac{a_q^*}{2\pi} \left[-\sum_j \frac{q_j}{4} e^{-ikz_j + i\omega t} (\mathbf{\Theta}_{q,j}^* \cdot \mathbf{v}_j) \right] dk + \text{c.c.} \qquad (2.12)
\end{aligned}
$$

where terms that do not satisfy the resonant condition average to zero in the sum over particles. Finally, equating the coefficients of a_q^* gives the same result as Eq. (2.9). In other words, the evolution of the amplitude of each electromagnetic mode in the system is simply calculated by tracking the energy changes induced by that mode on the particles. Finally, we include a term for the waveguide attenuation, $c\beta_{wg} a_q$, with β_{wg} defined by Eq. (1.62) such that

$$
\boxed{\dot{a}_q = -\sum_j \frac{q_j}{2\epsilon_0 \mathcal{A}_q} (\mathbf{v}_j \cdot \mathbf{\Theta}_{q,j}^*) e^{-ikz_j + i\omega t} - c\beta_{wg} a_q} \qquad (2.13)
$$

2.2.2 Numerical Implementation

In order to extend the capabilities of GPT to self-consistently calculate the interaction with the radiation modes in the undulator, we based our development on the built-in GPT function gauss00mf which computes the interaction for the gaussian modes of an optical resonator. In the numerical model, the continuous integral over spatial frequencies is approximated using a discrete basis of spatial frequency modes

$$
\mathbf{E}(\mathbf{x}, z, t) = \sum_q \sum_i (u_{qi} + i v_{qi}) \mathbf{\Theta}_{qi}(\mathbf{x}, k_i, t) e^{ik_i z - i\omega_i t} \qquad (2.14)
$$

where q and i index transverse modes and spatial frequencies. With respect to the previous section, u_{qi} and v_{qi} now represent the real and imaginary parts of the actual electric field amplitudes which have absorbed the user-defined mode separation interval Δk and the $1/2\pi$ from the Fourier transform. Consequently, the source term in Eq. (2.13) also gains an additional factor of $\Delta k/2\pi$.

In the input file, the user can specify the number of frequency modes (N_m) and the interval (f_{min}, f_{max}) for the simulation. That choice of interval and associated spectral resolution should be taken judiciously to include the resonant frequency of the system and to correctly simulate the radiation bandwidth. Since the latter depends on various factors including the gain parameter, the length of the undulator, and the electron bunch length, it is always advisable to check the results for consistency and convergence as the number of modes and their separation is varied. For a simulation of N_m modes, each simulated mode represents $dN_m = 2L(f_{max} - f_{min})/cN_m$ physical modes such that the effective round trip periodicity is reduced to $L_{rt} = 2L/dN_m$ where $\Delta k = 2\pi/L_{rt}$. Thus, the effect of discretization involves

$$\frac{1}{2\pi}\int dk \rightarrow \sum_i \frac{\Delta k}{2\pi} \quad \text{and} \quad a_q \rightarrow a_{qi}\frac{2\pi}{\Delta k} \quad \text{where} \quad \frac{\Delta k}{2\pi} = \frac{dN_m}{2L} \tag{2.15}$$

To define general equations for electric fields and mode evolution for both waveguide and free-space modes, it is convenient to describe modes in terms of their real and imaginary components (dropping the spatial and frequency indices for clarity).

$$\boxed{\mathbf{\Theta} \equiv (\Theta_{xR} + i\Theta_{xI})\hat{\mathbf{x}} + (\Theta_{yR} + i\Theta_{yI})\hat{\mathbf{y}} + (\Theta_{zR} + i\Theta_{zI})\hat{\mathbf{z}}} \tag{2.16}$$

For free-space interactions, we choose the Laguerre-Gaussian modes in polar coordinates. Assuming azimuthal symmetry, the modes can be expressed in terms of the single index q as

$$\mathbf{\Theta}_{qi}(r,z) = \frac{1}{\sqrt{1+\alpha_i^2}} L_q\left(\frac{2r^2}{w_i^2}\right) e^{-r^2/w_i^2}\ e^{i\alpha_i r^2/w_i^2 - i(2q+1)\psi_i}\ \hat{\mathbf{n}} \tag{2.17}$$

where L_q refers to Laguerre polynomials, $\alpha_i = (z - z_w)/z_{r,i}$ and $w_i = w_{0,i}\sqrt{1+\alpha_i^2}$ describe the location and size of the mode waist in terms of the rayleigh length $z_{r,i} = k_i w_{0,i}^2/2$, and $\psi_i = \tan^{-1}(\alpha_i)$ is the Guoy phase. It is straightforward to identify the real and imaginary components for Eq. (2.16).

For waveguide modes, the analytic expressions for transverse fields in TE and TM modes are given by Eq. (1.59) in terms of derivatives of the non-zero longitudinal field. Cartesian derivatives can be sampled numerically with finite differences for any waveguide geometry such that the components of the complex mode are easily given by

$$\begin{aligned}
&\text{(TE)} \quad \boldsymbol{\Theta} = \frac{\omega\mu_0}{k_\perp^2}\left(-\frac{\partial H_{zI}}{\partial y} + i\frac{\partial H_{zR}}{\partial y}\right)\hat{\mathbf{x}} - \frac{\omega\mu_0}{k_\perp^2}\left(-\frac{\partial H_{zI}}{\partial x} + i\frac{\partial H_{zR}}{\partial x}\right)\hat{\mathbf{y}} + 0\hat{\mathbf{z}} \qquad (2.18)\\
&\text{(TM)} \quad \boldsymbol{\Theta} = \frac{k_z}{k_\perp^2}\left(-\frac{\partial E_{zI}}{\partial x} + i\frac{\partial E_{zR}}{\partial x}\right)\hat{\mathbf{x}} + \frac{k_z}{k_\perp^2}\left(-\frac{\partial E_{zI}}{\partial y} + i\frac{\partial E_{zR}}{\partial y}\right)\hat{\mathbf{y}} + \left(E_{zR} + iE_{zI}\right)\hat{\mathbf{z}}
\end{aligned}$$

The fields are then given by summations over the spatial and frequency modes

$$\boxed{\begin{aligned}
E_x(\mathbf{x}_j, z_j, t) &= \sum_q \sum_i u_{qi}\left(\Theta_{xR}^{qi}\cos\theta_i - \Theta_{xI}^{qi}\sin\theta_i\right) - v_{qi}\left(\Theta_{xR}^{qi}\sin\theta_i + \Theta_{xI}^{qi}\cos\theta_i\right)\\
E_y(\mathbf{x}_j, z_j, t) &= \sum_q \sum_i u_{qi}\left(\Theta_{yR}^{qi}\cos\theta_i - \Theta_{yI}^{qi}\sin\theta_i\right) - v_{qi}\left(\Theta_{yR}^{qi}\sin\theta_i + \Theta_{yI}^{qi}\cos\theta_i\right)\\
E_z(\mathbf{x}_j, z_j, t) &= \sum_q \sum_i u_{qi}\left(\Theta_{zR}^{qi}\cos\theta_i - \Theta_{zI}^{qi}\sin\theta_i\right) - v_{qi}\left(\Theta_{zR}^{qi}\sin\theta_i + \Theta_{zI}^{qi}\cos\theta_i\right)\\
\mathbf{B}_\perp &= \frac{1}{\omega_i}\hat{\mathbf{k}}_i \times \mathbf{E}\\
B_z(\mathbf{x}_j, z_j, t) &= \sum_q \sum_i u_{qi}\left(H_{zR}^{qi}\cos\theta_i - H_{zI}^{qi}\sin\theta_i\right) - v_{qi}\left(H_{zR}^{qi}\sin\theta_i + H_{zI}^{qi}\cos\theta_i\right)
\end{aligned}} \qquad (2.19)$$

where $\theta = k_z z_j - \omega t$ and $H_z = 0$ for free space and TM waveguide modes. The source code is simplified by further defining $\mathbf{T} = \boldsymbol{\Theta}e^{i\theta}$ such that

$$T_{\xi R} = \Theta_{\xi R}\cos\theta - \Theta_{\xi I}\sin\theta \quad \text{and} \quad T_{\xi I} = \Theta_{\xi R}\sin\theta + \Theta_{\xi I}\cos\theta \qquad (2.20)$$

for $\xi \in \{x, y, z\}$.

From these fields, the electromagnetic forces acting on the particles are computed at each time step. Particle velocities and positions are then used to self-consistently calculate the evolution of the mode amplitudes according to the discretized mode evolution equation

$$\dot{a}_{qi} = -\frac{dN_m}{2L}\sum_j \frac{q_j}{2\epsilon_0\mathcal{A}_q}(\mathbf{v}_j \cdot \boldsymbol{\Theta}_{qi,j}^*)e^{-ik_i z_j + i\omega_i t} - c\beta_{wg}a_{qi} \qquad (2.21)$$

A subtle point is that the GPT code provides real macroparticle velocity components $\text{Re}\{\mathbf{v}_\perp\} = v_x\hat{\mathbf{x}} + v_y\hat{\mathbf{y}}$ while the GPTFEL equations are defined with a complex transverse velocity, $\mathbf{v}_\perp(z) = \frac{\sqrt{2}cK_{rms}}{\gamma}e^{-ik_u z}\hat{\mathbf{n}}$. This leads to an additional factor of 2 in the transverse terms such that the explicit code implementation is given by

$$\boxed{\begin{aligned} \dot{u}_{qi} &= -\sum_j F_j\left(2v_xT_{xR}+2v_yT_{yR}+v_zT_{zR}\right)-c\beta_{wg}u_{qi} \\ \dot{v}_{qi} &= +\sum_j F_j\left(2v_xT_{xI}+2v_yT_{yI}+v_zT_{zI}\right)-c\beta_{wg}v_{qi} \end{aligned}} \tag{2.22}$$

where $F_j = dN_m \cdot q_j/4\epsilon_0\mathcal{A}_qL$. The discretized energy is given by

$$W = \frac{2L}{dN_m}\frac{\epsilon_0}{2}\sum_q\sum_i |a_{qi}|^2\mathcal{A}_{qi} \tag{2.23}$$

It is also possible to run the code in single frequency mode where the field is assumed to be perfectly periodic, with only one spatial frequency term in Eq. (2.14). In this case, the effective round trip length is simply λ such that $L = \lambda/2$ and $dN_m = 1$. The electron beam charge must be scaled to represent the charge within one period and the time-averaged power is found by multiplying Eq. (2.23) by c/λ.

2.2.2.1 Mode Initialization and Output

Simulations can be seeded with a gaussian field in the fundamental mode, parameterized by a bandwidth σ_f about the central frequency $f_0 = f_{min}/2 + f_{max}/2$. The mode amplitudes, $A_{qi} = \sqrt{u_{qi}^2 + v_{qi}^2}$, are initialized by specifying the peak field E_0 in $\hat{\mathbf{x}}$ according to

$$\textbf{if}\quad q=0\quad\textbf{then}\quad A_{qi}n_x = \frac{E_0e^{-(f_i-f_0)^2/2\sigma_f^2}}{\sum_i e^{-(f_i-f_0)^2/2\sigma_f^2}}\quad\textbf{else}\quad A_{qi}=0 \tag{2.24}$$

where $f_i = f_{min} + i\frac{f_{max}-f_{min}}{N_m-1}$. For helical geometries, this definition is consistent with Eq. (1.5). The initial mode phases, $\phi_{qi} = \arctan(u_{qi}/v_{qi})$, are determined by specifying the initial location of the gaussian pulse, dz, relative to the cavity center. We can identify $\phi_{qi} = -k_idz$ from an explicit waveform shift in z.

$$\sum_i A_{qi}e^{ik_i(z-dz)} = \sum_i A_{qi}e^{i\phi_{qi}}e^{ik_iz} \implies \phi_{qi} = -k_idz \tag{2.25}$$

In waveguide simulations, the pulse shape is maintained under shifting and no dispersion is introduced. In free-space simulations, the shift does not change the location of the mode

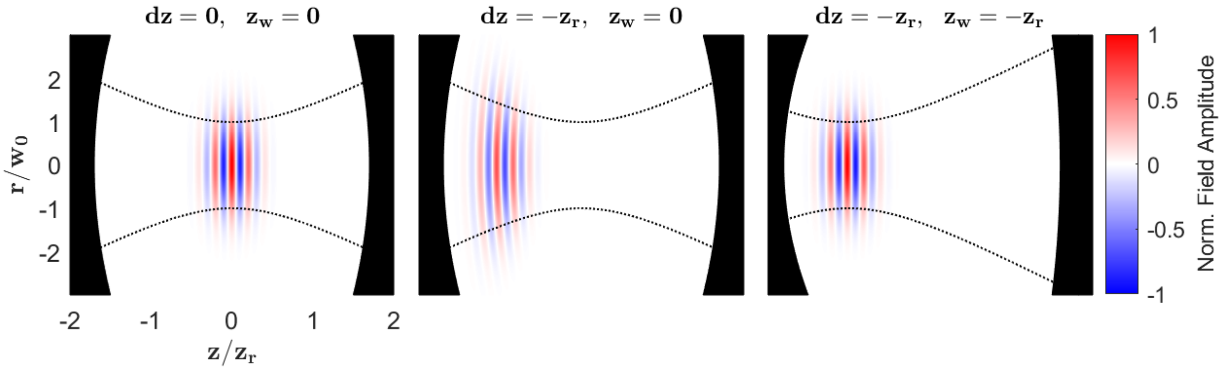

Figure 2.1: Initialization of a gaussian seed in the optical cavity. The parameter dz changes the pulse position while z_w controls the location of the mode waist.

waist which is specified relative to the cavity center with z_w to initialize α_i in $\mathbf{\Theta}_{qi}$ as depicted in Figure 2.1.

The temporal waveform has a periodicity of $2L/dN_m$ determined by the user-specified frequency resolution and is represented by the position vector $\mathbf{z}_t$ which spans from $-L/dN_m$ to L/dN_m with sufficiently small spacing to resolve f_{max}. The field outputs, E_{xt} and E_{yt}, travel in the radiation frame as the position of the electron beam is modeled by $z = dz + v_g t$.

$$\boxed{\begin{aligned} \mathbf{E}_{xt} &= \sum_i A_i n_x \cos\Big(k(\mathbf{z}_t + dz + v_g t) - \omega t + \phi_i\Big) \\ \mathbf{E}_{yt} &= \sum_i A_i n_y \sin\Big(k(\mathbf{z}_t + dz + v_g t) - \omega t + \phi_i\Big) \end{aligned}} \tag{2.26}$$

The instantaneous power can be computed from the flow of energy density through a cross-sectional area.

$$\mathbf{P}_t \ = \ v_g \iint \frac{1}{2}\epsilon_0 |\mathbf{E}|^2 d\mathbf{x} \ = \ \frac{v_g \epsilon_0}{2} \iint |\mathbf{\Theta}|^2 \left(\mathbf{E}_{xt}^2 + \mathbf{E}_{yt}^2\right) d\mathbf{x} \ = \ \frac{v_g \epsilon_0 \mathcal{A}}{2} \left(\mathbf{E}_{xt}^2 + \mathbf{E}_{yt}^2\right) \tag{2.27}$$

2.2.3 Quiet Start

In multifrequency simulations where many longitudinal wavenumbers and corresponding frequencies are used to simulate the field along a finite length bunch, it is critical to pay attention to the details associated with loading the particle coordinates in the simulation. Because it is common to have a much smaller number of macroparticles than real number of

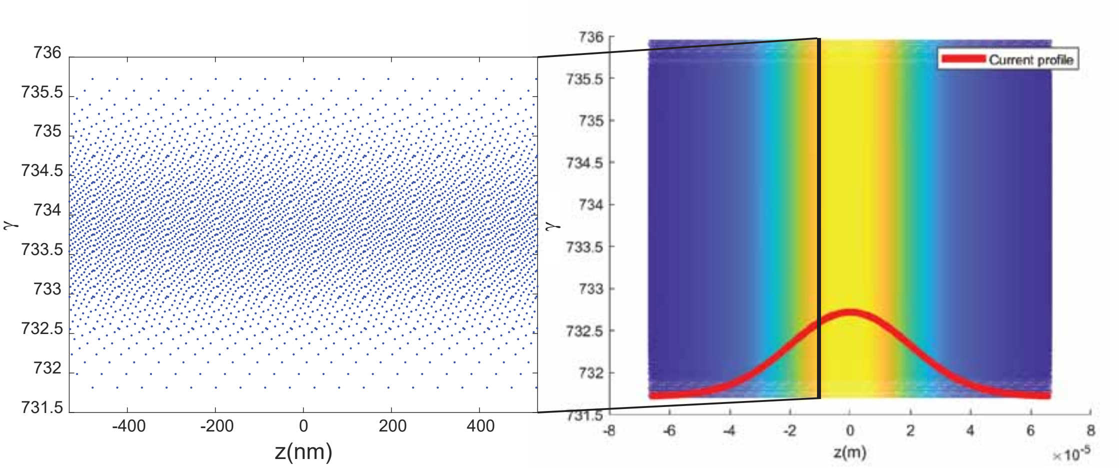

Figure 2.2: left) Longitudinal phase space distribution with quiet loading for time-independent (i.e. single frequency) simulation. right) Longitudinal phase space distribution for multifrequency simulation. Particles are color coded by their charge weight. The projection onto the z-axis shows the Gaussian current profile.

electrons, the noise in the bunching source term can be unacceptably high, causing unphysical growth of the field along the undulator.

This problem is common and well discussed in the vast literature of simulations for FELs [91, 92]. While there are a number of possible solutions, our situation is slightly complicated as we need to ensure that the intrinsic bunching is and remains very small for all of the discrete frequencies in the simulation. This first requires equally distributing particles in the z-coordinate over a length $L_{rt} = 2\pi/\Delta k$. For example in Fig. 2.2 we show the input phase space when the simulation spans a bandwidth of 3 % around the central wavelength of 266nm. In this case, the beam longitudinal profile (a gaussian with rms bunch length 30 μm) is initialized by assigning a different charge weight to each macroparticle. When shot-noise effects are desired, each macroparticle's position is shifted by a small Δz according to well described algorithms [93, 94] to achieve the correct statistics.

In addition, it is important to make sure that the noise from other coordinates would not contribute to a growth of the bunching as the beam propagates in the absence of an interaction. This is taken care of by mirroring the energy, transverse coordinates, and

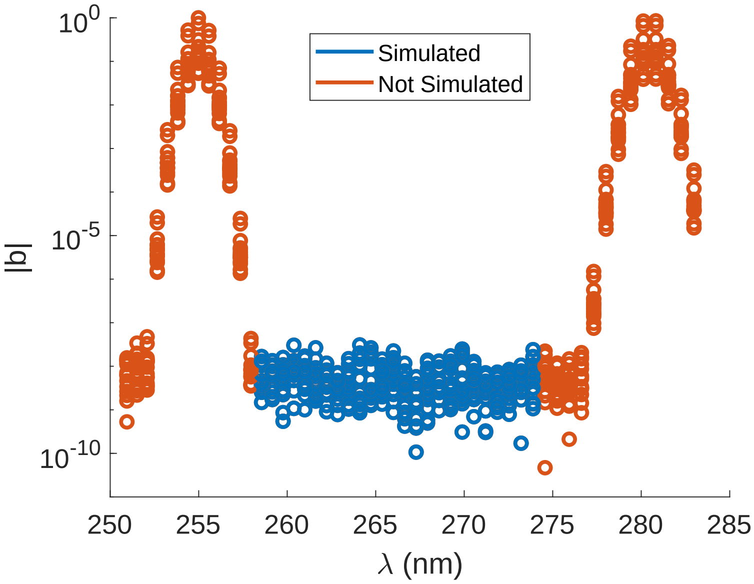

Figure 2.3: Bunching as a function of wavelength at various points along beam propagation. The original 5D phase space is mirrored over 80 bins to sustain minimal bunching over the simulated bandwidth.

momenta over a large number of 5D phase space bins. The number of bins (typically larger than 32) should be chosen such that bunching in the absense of an interation remains small for all the discrete frequencies included in the simulations, as demonstrated in Figure 2.3.

2.3 Free-Space Simulations

2.3.1 Source Dependent Expansion

In free-space FEL simulations, the effectiveness of the Laguerre-Gaussian mode expansion depends critically on the initialization of the waist size and location to accurately model the field transversely and in the absence of prior knowledge the simulation should include a large number of spatial modes. In many cases, for example when the FEL is seeded with an external laser and the radiation's transverse profile is mainly dominated by one or a few modes, it is a good approximation to truncate the sum to only include a small number of terms. However, in the case of an FEL amplifer a large number of modes will be needed to simulate the gain guiding over an extended length as shown in Figure 2.4.

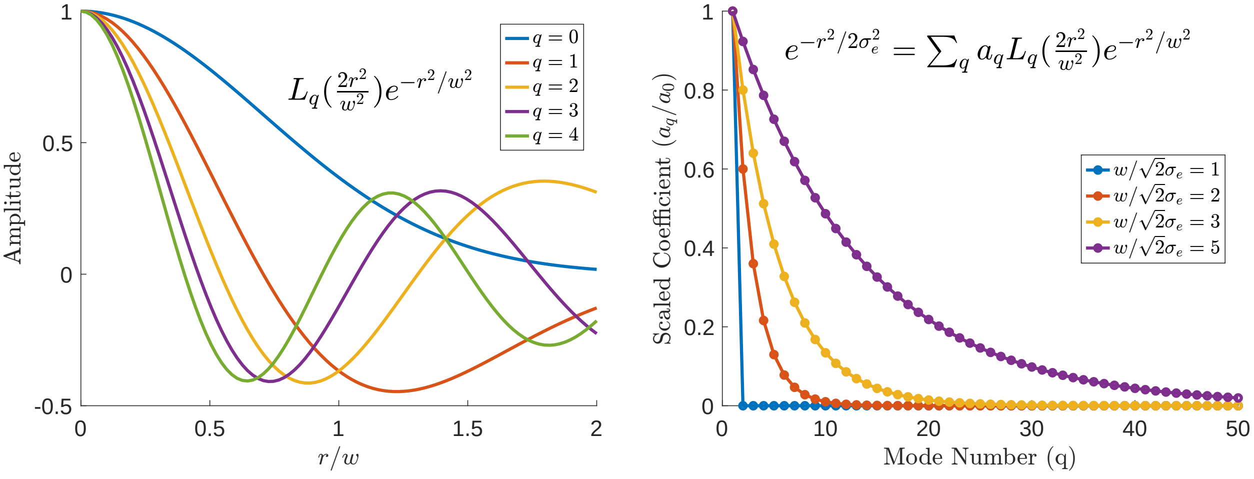

(a) (b)

Figure 2.4: Spatial Modes. a) The first 5 spatial modes of the free-space Laguerre basis. b) The number of necessary modes increases as the radiation waist diffracts, demonstrating the utility of a Source Dependent Expansion.

To minimize the number of necessary modes and proportionally speed up the computational time of the simulation, it is possible to take advantage of a source dependent expansion (SDE) algorithm [87, 88] where the waist size and location are able to evolve dependent on the source. The idea is to insert the field decomposition of equation (2.14) directly into the wave equation (2.30), allowing the position and waist of the mode to vary in time, $\alpha_i(t)$ and $w_i(t)$. The result will be recursive mode excitation equations where evolution of a given mode depends on the amplitude of adjacent modes in the expansion. The time dependent Laguerre-Gaussian modes are given by

$$\begin{aligned}\mathbf{\Theta}_{qi}(r,t) = \frac{1}{\sqrt{1+\alpha_i(t)^2}} L_q\left(\frac{2r^2}{w_i(t)^2}\right) \exp\left[-r^2/w_i(t)^2\right] \\ \times \exp\left[i\alpha_i(t)r^2/w_i(t)^2 - i(2q+1)\arctan(\alpha_i(t))\right]\hat{\mathbf{n}} \quad (2.28)\end{aligned}$$

with mode areas defined by Eq. (2.2).

$$\mathcal{A}_{qi} = \frac{\pi w_i(t)^2}{2(1+\alpha_i^2(t))} \quad (2.29)$$

To avoid repetition, we refer to [95] which performs the GPTFEL derivation from the wave equation specifically under the assumption of a transversely polarized field $\mathbf{\Theta}_{qi} = \Theta_{qi}\hat{\mathbf{n}}$

such that

$$\left(\frac{\partial^2}{\partial r^2}+\frac{1}{r}\frac{\partial}{\partial r}+\frac{2i\omega_i}{c^2}\frac{\partial}{\partial t}\right)\left(\sum_q a_{qi}(t)\Theta_{qi}(\mathbf{x},k_i,t)\right)=S_i(\mathbf{x},k_i,t)$$

$$\text{where}\quad S_i(\mathbf{x},k_i,t)=\frac{dN_m}{2L}\sum_j -i\mu_0 q_j c\beta_{z,j}(k_u+k_i)\left(\mathbf{v}_j\cdot\hat{\mathbf{n}}^*\right)\delta(\mathbf{x}-\mathbf{x}_j(t))e^{-ikz_j+i\omega_i t} \quad (2.30)$$

To simplify the algebra, we change the transverse variable to $\xi_i=\frac{2r^2}{w_i^2}$ and temporarily redefine the complex amplitudes and spatial modes by absorbing the Guoy phase and mode normalization into the complex amplitude.

$$\left(\frac{\partial}{\partial t}-\frac{4ic^2}{\omega w^2}\left(\xi\frac{\partial^2}{\partial\xi^2}+\frac{\partial}{\partial\xi}\right)\right)\left(\sum_q \hat{a}_q(t)\hat{\Theta}_q(\xi,t)\right)=-\frac{ic^2}{2\omega}S\quad\text{where}\quad\hat{a}_q=\frac{a_q e^{-i(2q+1)\psi}}{\sqrt{1+\alpha^2}}$$

$$\text{and}\quad\hat{\Theta}_q(\xi,t)=\Theta_q(\xi,t)\sqrt{1+\alpha^2}e^{i(2q+1)\psi}=L_q\left(\xi\right)e^{(i\alpha-1)\xi/2} \quad (2.31)$$

Because frequencies evolve independently, we drop the frequency index i for clarity. Differentiation with respect to time and argument is denoted by dots and primes, respectively.

After carefully applying derivatives, we utilize the following Laguerre identities

$$\begin{aligned}0&=\xi L_q''(\xi)+(1-\xi)L_q'(\xi)+qL_q(\xi)\\ \xi L_q'(\xi)&=qL_q(\xi)-qL_{q-1}(\xi)\\ \xi L_q(\xi)&=(2q+1)L_q(\xi)-(q+1)L_{q+1}(\xi)-qL_{q-1}(\xi)\end{aligned} \quad (2.32)$$

to remove any explicit ξ dependence and collect coefficients to get

$$-\frac{ic^2}{2\omega}S=\sum_q \dot{\hat{a}}_q\Theta_q+A_q\hat{a}_q\hat{\Theta}_q-i(q+1)B\hat{a}_q\hat{\Theta}_{q+1}-i(q)B^*\hat{a}_q\hat{\Theta}_{q-1}$$

$$\text{where}\quad A_q=\frac{\dot{w}}{w}+i(2q+1)\left(\frac{c^2(1+\alpha^2)}{\omega w^2}-\frac{\alpha\dot{w}}{w}+\frac{\dot{\alpha}}{2}\right)$$

$$\text{and}\quad B=\left(\frac{c^2}{\omega w^2}(\alpha^2-1)-\frac{\alpha\dot{w}}{w}+\frac{\dot{\alpha}}{2}\right)+i\left(\frac{c^2}{\omega w^2}2\alpha-\frac{\dot{w}}{w}\right) \quad (2.33)$$

Using the orthonormality property $\int_0^\infty\hat{\Theta}_q\hat{\Theta}_q^*d\xi=\delta_{q,q'}$ by multiplying $\hat{\Theta}_{q'}^*$ and integrating $\int_0^\infty d\xi$ leads to the mode excitation equation for the source-dependent system

$$\dot{\hat{a}}_q+A_q\hat{a}_q-iqB\hat{a}_{q-1}-i(q+1)B^*\hat{a}_{q+1}=\hat{F}_q$$

$$\text{where}\quad\hat{F}_q=\frac{-ic^2}{\pi\omega w^2}\int S(r)\hat{\Theta}_q^*(r)d^2\mathbf{x} \quad (2.34)$$

where we have subsequently let $q' \to q$ and note that $a_q = 0$ when $q < 0$. The evolution of the mode parameters is determined by B,

$$\boxed{\dot{w} = \frac{2c^2\alpha}{\omega w} - wB_I \qquad \text{and} \qquad \dot{\alpha} = \frac{2(1+\alpha^2)c^2}{\omega w^2} + 2B_R - 2\alpha B_I} \tag{2.35}$$

where in the limit $B \to 0$, we recover the free-diffraction limit of $\alpha_i(t) = ct/z_{r,i}$ and $w_i(t) = w_{0,i}\sqrt{1 + c^2t^2/z_{r,i}^2}$.

We now revert back to our original definitions of the complex amplitude and spatial modes, multiplying both sides by $\sqrt{1+\alpha^2}e^{i(2q+1)\psi}$. The source term is simplified by inserting $S(r)$ from Eq. (2.30) and again particles satisfy FEL resonance.

$$F_q = \sqrt{1+\alpha^2}\cancel{e^{i(2q+1)\psi}} \times \frac{-ic^2}{\pi\omega w^2}\int S(r)\Theta_q^*(r)\sqrt{1+\alpha^2}\cancel{e^{-i(2q+1)\psi}}d^2\mathbf{x} \tag{2.36}$$

$$= \frac{dN_m}{2L}\frac{2(1+\alpha^2)}{\pi w^2}\sum_j \frac{-q_j}{2\epsilon_0}(\mathbf{v}_j \cdot \hat{\mathbf{n}}^*)\Theta_{q,j}^* e^{-ikz_j + i\omega t} \tag{2.37}$$

$$\boxed{F_{qi} = -\frac{dN_m}{2L}\sum_j \frac{q_j}{2\epsilon_0\mathcal{A}_{qi}}(\mathbf{v}_j \cdot \boldsymbol{\Theta}_{qi,j}^*)e^{-ik_iz_j + i\omega_i t}} \quad \text{by} \quad (2.29) \tag{2.38}$$

Adding the frequency indices and expressing A_q in terms of B with $G_i = \frac{2}{1+\alpha_i^2}(B_{R,i} - \alpha_i B_{I,i})$, we find

$$\boxed{\begin{aligned} \dot{a}_{qi} = F_{qi} + (B_{I,i} + \alpha_i G_i + i(2q+1)(G_i - B_{R,i}))\, a_{qi} & \\ + iqBe^{2i\psi_i}a_{q-1,i} + i(q+1)B^*e^{-2i\psi_i}a_{q+1,i} & \end{aligned}} \tag{2.39}$$

where we recover Eq. (2.21) in the $B \to 0$ limit.

Giving freedom for the modes to evolve means the system is no longer fully determined and needs an additional constraint. One idea is to assume N modes are sufficient to model the transverse profile and require $a_q = 0$ for $q \geq N$. Using Eq. (2.34) for $q = N$, we can solve for B as

$$B_i = \frac{iF_{N,i}}{Na_{N-1,i}}e^{-2i\psi_i} \tag{2.40}$$

While the system is now fully defined, the solution is divergent when $a_{N-1,i} \approx 0$. If the highest order spatial mode is not sufficiently seeded, the simulation will produce erroneous results. For this reason, the SDE method works best with a limited (≤ 10) number of spatial modes.

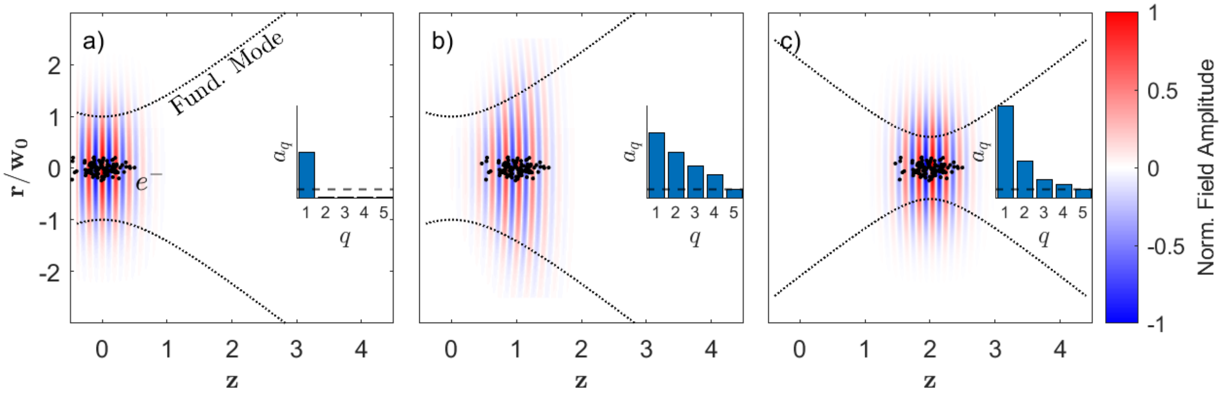

Figure 2.5: SDE Thresholding. a) At $z = 0$, the electrons see a Gaussian seed focused at its waist. Only the first spatial mode has a non-zero coefficient, such that SDE evolution is unstable and the simulation continues with non-SDE dynamics. b) The amplitude of the highest simulated spatial mode now exceeds the user-specific threshold (black dotted line) and the simulation allows SDE dynamics. c) The waist size and location of the mode basis is now changed according to SDE, reducing the number of required spatial modes.

One possible correction is to include a threshold such that when a_{N-1} is small, the modes evolve according to non-SDE dynamics until the amplitude is safely nonzero. This is depicted schematically in Figure 2.5. A closer inspection of Eq. (2.35) suggests the distance $c/|B|$ sets the scale for the variation of the mode parameters and can be used as a threshold. For example, modes evolve according to SDE dynamics only if $c/|B| > L_{thresh}$ where the input parameter L_{thresh} is interpreted as the minimum length scale for mode evolution.

While this is our current implementation for SDE modes, there are other interesting strategies to consider. For example, if a_{N-1} is small we could additionally check if the a_0 mode amplitude was sufficient to compute B for $N = 1$, allowing a middle step between full SDE and no SDE. It is also possible to utilize a sigmoid function such as $B = (1+10^{(a_{N-1}-a_c)/w_a})^{-1}$ to continuously turn on SDE as a function of the a_{N-1} amplitude where a_c and w_a specify the position and width of the transition region. For problems with strong gain guiding, we could assume a constant moving waist where $\alpha = 0$ and $w = w_0$. This greatly simplifies the mode evolution

$$\dot{a}_{qi} = \left((2q+1)B_i\right)a_{qi} + iqBa_{q-1} + i(q+1)Ba_{q+1,i} + F_{qi} \tag{2.41}$$

and removes the divergent behavior in the small field limit.

In practice, the application of flexible SDE modes requires more care and intuition that using a fixed mode basis. However, they provide the ability to achieve reasonable results with fast simulations that compute only a handful of spatial modes. When accuracy is paramount, it can be preferable to run a non-SDE simulation with many modes.

2.3.2 Genesis Comparison

We benchmark GPTFEL against Genesis in two examples targeting different regimes of FEL operation. The first case is a classical single-pass FEL seeded, untapered amplifier which will enable a quantitative comparison with the semi-analytical Ming Xie gain length formulas for both planar and helical geometries. The second example was relevant to the TESSA266 experiment as it was originally planned for the LEA beamline at the APS linac in Argonne National Laboratory aiming at very high conversion efficiency at 266nm.

This case serves to illustrate the capability of using a 3D magnetic field map for a fairly complicated segmented tapered undulator. The code compares well with a traditional FEL code like Genesis, even deep in the non-linear regime. The details of the beam transport (injection, entrance and exit sections and especially undulator break sections) can only be included in Genesis by using a linear beam transport approximation. GPT follows the evolution of the beam distribution along the beamline using fieldmaps for all the magnetic elements (undulators, quadrupoles, and phase shifter dipoles) and calculates energy exchange using the self-consistent interaction with the free-space modes. The results allow us to quantitatively include the effects of the entrance and exit sections (which add an effective 0.5 periods of interaction on each side of the undulator) and the trajectories after the prebuncher and in between the undulators.

The parameters for the amplifier example are reported in Table 2.1 and somewhat arbitrarily chosen to be similar to an un-tapered version of the TESSA266 experiment. The main differences are that a 200 period long undulator (with no break-section) is used for this example and the input seed power is lowered to 10 kW. An analytical model for the undulator magnetic field is used. The beam is transversely matched to the undulator natural focusing (equally distributed in the horizontal and vertical plane) so that the rms spot size remains nearly constant along the undulator. The main goal of this example is to benchmark GPTFEL against the fitting formulas for the 3D gain length of an untapered FEL amplifier and compare with a conventional FEL code like Genesis. We also used this example to evaluate the performance of the single mode SDE approximation versus a simulation with $n = 11$ azimuthally symmetric Laguerre Gaussian SDE modes to decompose the electromagnetic field. GPTFEL took 1.5 minutes to simulate 76800 particles on an 8 processor for the single SDE mode and 5 minutes for 11 SDE modes.

Table 2.1: Parameters for the 266 nm FEL amplifier simulation.

Electron Beam		Radiation and Undulator	
Energy	375.5 MeV	λ_1	266 nm
Energy Spread	0.1 %	Input Power	10 kW
RMS Bunch length	20 μm	Rayleigh Length	1.41 m
$\epsilon_{n,x}, \epsilon_{n,y}$	2 mm·mrad	Waist location	0 m
I_{peak}	1 kA	K_{rms}	2.82
σ_x, σ_y	72.5 μm	λ_u	0.032 m

The time-independent, single frequency results for the planar and helical geometries are shown in Figure 2.6 and compared with Genesis 1.3. When using multiple spatial modes, the gain lengths in the planar and helical case are in good agreement (within 10 %) of the semi-analytical and numerical model predictions. The radiation spot sizes defined by $\sigma_r^2 = \frac{1}{2}\frac{\int r^2|E|^2 d^2\mathbf{x}}{\int |E|^2 d^2\mathbf{x}}$ also closely follow the prediction. Note that while a single SDE mode is able to achieve qualitative results up to and near saturation, a larger number of spatial modes is required to correctly simulate the evolution of the radiation profile after saturation.

The multi-frequency simulation used an SDE gaussian mode for 31 spatial frequencies with a 6% bandwidth to simulate 128,000 particles in 23 minutes. The user-defined parameter

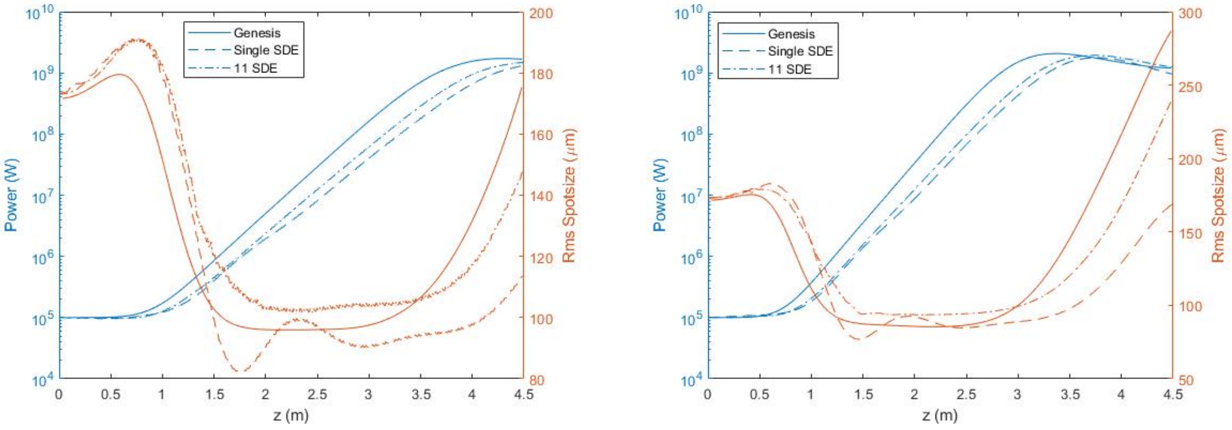

Figure 2.6: A comparison of GPTFEL running with SDE versus Genesis 1.3. left) The predicted gain length for the planar amplifier is 0.287 m. Simulating with SDE and a single spatial mode overshoots by 16%. Running with 11 SDE spatial modes reduces the error to 5.9%. right) The predicted gain length for the helical amplifier is 0.224 m. Simulating 1 and 11 SDE modes leads to errors of 15% and 8.2%, respectively

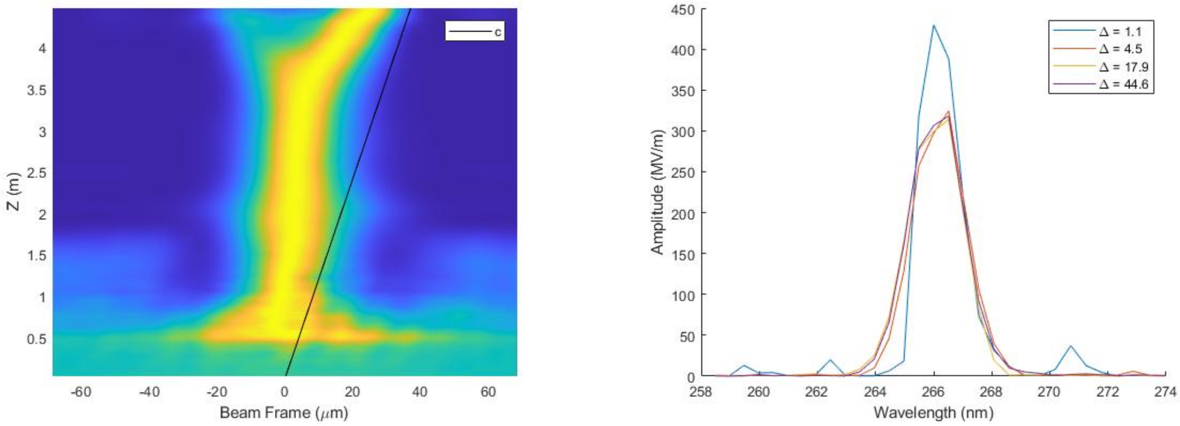

Figure 2.7: GPTFEL results for 31 spatial frequencies, each with a single gaussian transverse mode. a) Waterfall plot of normalized power. b) Spectrum at P=0.1 GW for different thresholds on SDE interaction. Δ is the ratio of L_{thresh} to the theoretical gain length. Numerical errors occur when $\Delta \leq 1$ because noise in the small amplitude, higher order modes quickly excite significant changes in the mode parameters. This suggests L_{thresh} should be set to roughly 5 times the theoretical gain length for convergent results.

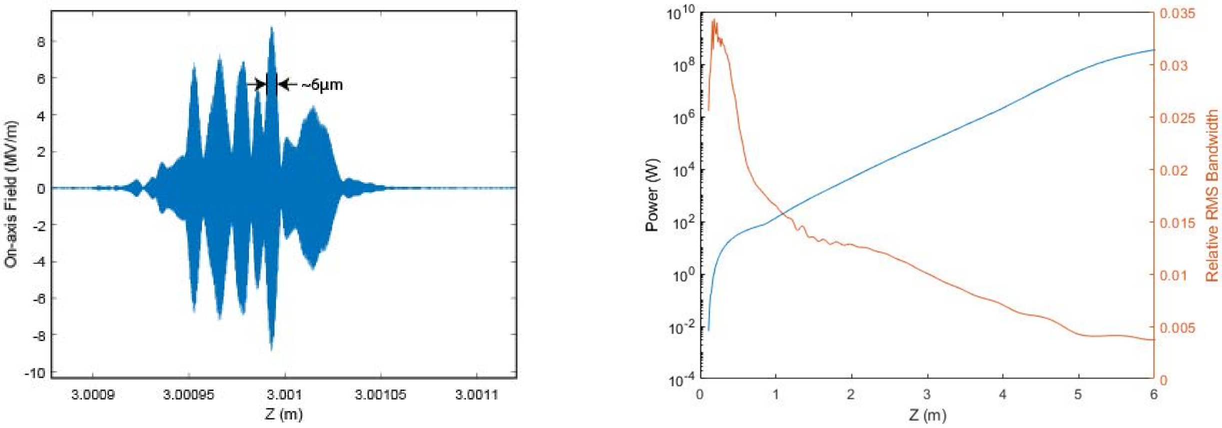

Figure 2.8: Results from shot noise amplifier simulation with undulator entrance at Z=0.1 m. a) On axis field profile at Z=3 m showing the characteristic spike structure. b) Peak power and relative RMS spectral bandwidth.

L_{thresh} limits the spot size variation along the undulator. Figure 2.7a shows a waterfall plot in the electron beam frame normalized at each z position to display the relative velocity of the radiation wavepacket, which is close to the beam velocity in the exponential regime and becomes superluminal in the non linear regime [96]. In Figure 2.7b, the spectrum just before saturation is shown as a function of L_{thresh} normalized to the gain length. If an increased spectral resolution is required, computation time scales linearly with number of tracked modes.

SDE modes can reduce the number of spatial modes needed when a strong seed or strong bunching is present. On the other hand, if the amplification starts from shot noise seeding, simulations should be performed using a larger number of non-SDE modes as the transverse mode is not predefined. Figure 2.8 shows results for a helical FEL amplifier with no external seed power using 91 frequencies and 31 spatial modes. As expected, the pulse temporal profile after amplification exhibits a sequence of temporal spikes of characteristic length equal to the FEL cooperation length which in our case is $L_{cop} = L_g \cdot \lambda/\lambda_u = 2.5$ μm. The evolution of the energy (power integrated along the pulse) and the spectrum bandwidth are also consistent with SASE FEL theory [97].

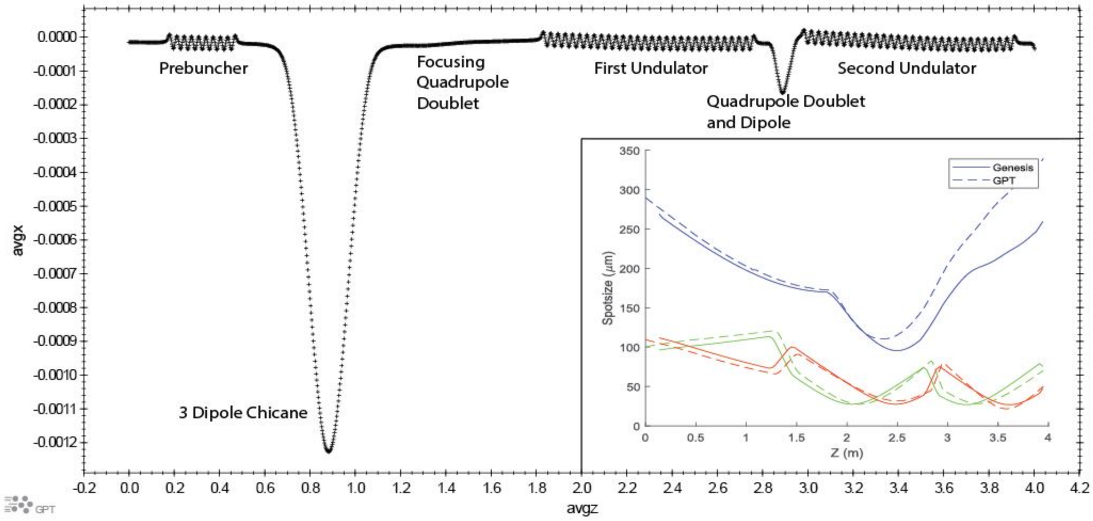

Figure 2.9: Trajectory and electron beam and radiation spot size (inset) along the TESSA Beamline

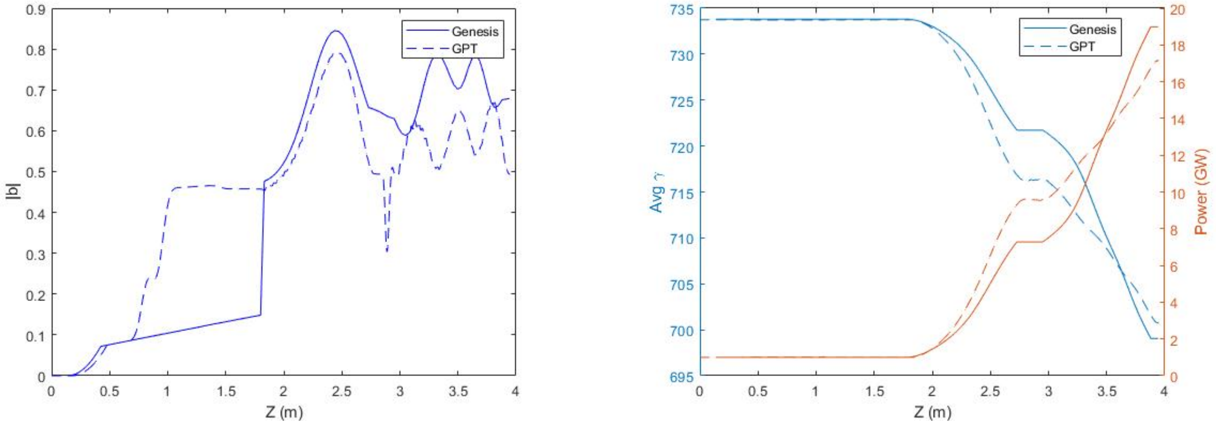

Figure 2.10: Particle bunching and energy exchange in the first two tapered undulators of the TESSA beamline.

2.3.3 TESSA 266 Experiment

In this next example we take advantage of the GPT functions to track the electron beam in the fairly complex transport line of the TESSA 266 experiment. The beamline includes a short, 8 period undulator followed by a 3 dipole chicane to convert the imprinted energy modulation into microbunching. Quadrupole doublets match the beam transversely into the focusing channel of each 0.96 meter, strongly tapered undulator section. A small dipole is placed between the second quadrupole doublet so that the three magnets can be used as a phase shifter between the undulator sections.

The GPT transport functions are used to set up the trajectory and the beam optics prior of turning on the seed and the FEL interaction module. Our time-independent simulation of the TESSA266 beamline includes 21 higher order spatial modes to ensure an accurate modeling of the radiation profile. A 1 GW peak power input radiation pulse is focused at the entrance of the tapered undulator to a waist of 0.3 mm. The simulation is compared with Genesis results, but it should be noted that GPTFEL uses full 3D magnetic field maps for the undulators as well as for the dipoles and quadrupoles in the system. The magnetic field in the chicane dipoles is fine tuned to maximize the bunching and simultaneously optimize the injection phase of the beamlets relative to the radiation phase at the entrance of the tapered undulator. In Genesis, both the R56 and phase shifts are applied post-facto to the beam distribution at the entrance of the tapered undulator, explaining the large difference in the bunching factor evolution in Fig. 2.10a. In practice, the phase shifter between the tapered undulator sections had to be re-optimized to account for the additional slippage incurred by the beam when passing in the entrance and exit section of the wigglers. This is accomplished by horizontally shifting the quadrupoles in opposite directions to steer the beam and tuning the magnetic field amplitude of the dipole to recover a straight trajectory while maximizing the energy exchange in the second undulator. Figures 2.10b and 2.9 show the energy exchange and beam trajectory in the undulators.

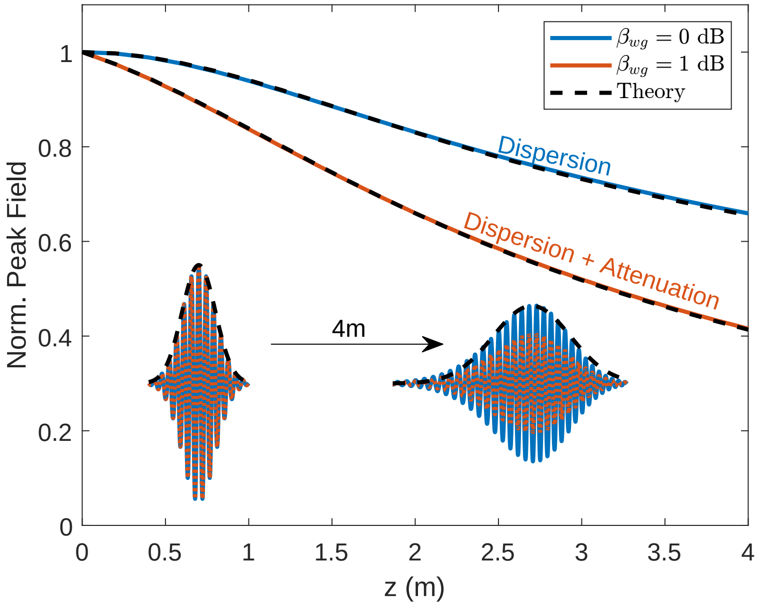

Figure 2.11: Benchmarking dispersion and attenuation in GPTFEL against analytic theory. A large-bandwidth gaussian pulse is propagated through a waveguide without an electron beam. Consistent with theory, the peak field decays due to ohmic losses and the frequency dispersion which broadens the temporal profile. The theory does not include higher order terms beyond the group velocity dispersion which are responsible for the asymmetry of the dispersed pulse.

2.4 Waveguide Simulations

2.4.1 Zero-slippage THz Amplifier

The modal decomposition of GPTFEL is perfect for handling waveguide simulations, naturally incorporating dispersion and power attenuation as demonstrated in Figure 2.11. As a final example, we simulate zero-slippage operation in a circular waveguide FEL using parameters (listed in Table 2.2) that resemble the Tessatron experiments.

The beam is given a cosine density distribution, $n(z) \propto 1 + \frac{b}{2}\cos(kz)$, over four radiation wavelengths with a bunching factor of $b = 0.4$ to model the generation of four beamlets off the cathode from laser shaping. The zero-slippage resonance occurs at a frequency of 0.22 THz, allowing an extended interaction between the radiation and short electron beam.

The undulator fields are tapered quadratically to maintain resonance with the decelerated electrons.

Table 2.2: Simulation Parameters for zero-slippage waveguide FEL

Electron Beam		Undulator/Waveguide	
Energy	6 MeV	f_{res}	0.22 THz
σ_γ/γ	1%	L_u	96 cm
$\|b\|$	0.4	K_{rms}	2.27
$\epsilon_{n,x}, \epsilon_{n,y}$	3 mm·mrad	λ_u	3.2 cm
Q_{tot}	300 pC	R	2 mm
σ_x, σ_y	100 μm		

Figure 2.12 shows the final longitudinal phase space where 8% of the electron beam energy is converted into coherent radiation. Energy conservation is satisfied in the simulation as shown in the inlay. The output radiation field is aligned to the fields experienced by the particles, with are slightly reduced due to the off-axis trajectory. The the waveguide eliminates diffraction, but it is clearly shown that dispersion has an effect on the fields and ponderomotive trapping across the four beamlets.

The radiation spectrum and power are shown in Figure 2.13. The zero-slippage condition produces a large-bandwidth interaction at the resonant frequency (dashed line). The slight redshift can be attributed to 3D effects including energy spread and finite emittance. We confirm the integrated power matches the energy computed by summing over individual frequency modes.

2.4.2 Connection to 1D Theory

The dynamics of single-frequency operation in a waveguide is analogous to 1D FEL theory. In order to maintain consistent definitions of field (similar to Eq. (1.17)), the complex mode amplitude should be written as $a_q = -i\sqrt{2}E(t)e^{i\phi}$. For large wiggling trajectories, we include a mode sampling factor $\langle\Theta_q\rangle$ that corrects for reduced fields off-axis. However, we do not

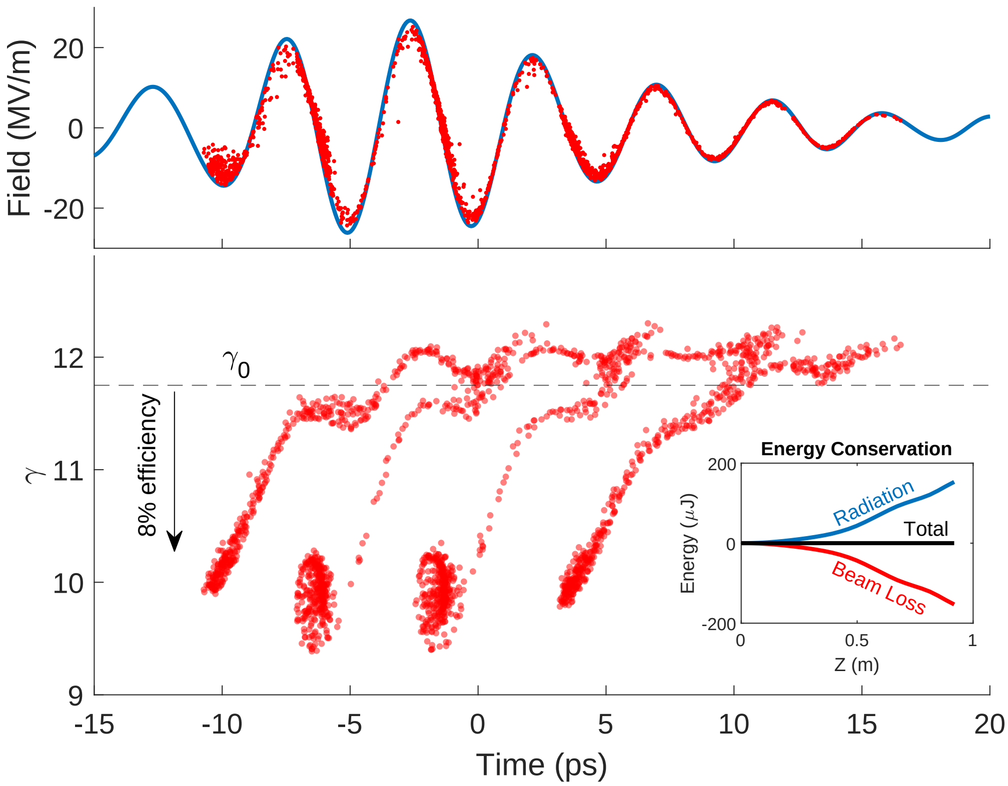

Figure 2.12: Radiation waveform and beam longitudinal phase space at the end of the undulator. With energy conservation satisfied in the simulation, 8% of the beam energy is converted to radiation. Dispersion is clearly visible in the temporal fields.

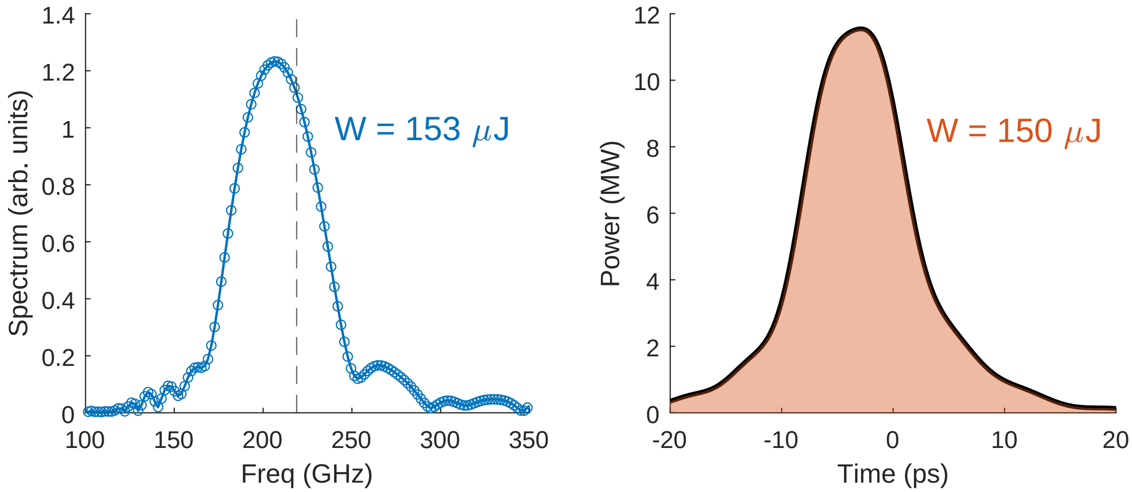

Figure 2.13: Radiation spectrum and power. Zero-slippage operation produces a large bandwidth pulse. Total energy is consistent between frequency domain and time domain.

account for the non-zero E_z fields seen off-axis in TM modes which have significant effect on the gain length.

Substituting Eq. (2.4) for $\mathbf{v}$, simplifying the complex phases into the ponderomotive phase $e^{-i\theta_j}$, and rewriting in terms of the beam current $I = ce/\lambda = ce/L$, we can express the field evolution as

$$\frac{dE}{dz} = \frac{IK\langle\Theta_q\rangle}{2\epsilon_0 c\mathcal{A}_q\gamma_r}\langle\sin\theta_j\rangle \tag{2.42}$$

where a comparison with Eq. (1.28) reveals the beam area has been replaced by the effective waveguide mode area. The mode sampling factor also corrects the field source term in the equation for energy modulation. Thus, a dimensionless scaling of the waveguide system leads to the modified Pierce parameter

$$\boxed{\rho = \left(\frac{\langle\Theta_q\rangle^2}{16\pi}\frac{I}{I_A}\frac{K^2}{\gamma^3}\frac{\lambda_u^2}{\mathcal{A}_q}\right)^{1/3} \quad \text{where} \quad L_g = \frac{\lambda_u}{4\pi\sqrt{3}\rho}} \tag{2.43}$$

In the previous chapter, we showed that only TE$_{1n}$ and TM$_{1n}$ modes can resonant with an electron beam in a circular waveguide. The TE mode areas are computed as

$$\begin{aligned}
\mathcal{A}_{1n} &= \int_0^{2\pi}\int_0^R |\mathbf{E}_\perp|^2 r\,dr\,d\phi \\
&= \frac{4\pi}{k_\perp^2}\int_0^R r\left(\frac{\partial}{\partial r}J_1(k_\perp r)\right)^2 + \frac{1}{r}J_1(k_\perp r)^2\,dr \\
&\boxed{\mathcal{A}_{1n} = 2\pi R^2\left(J_0^2(w_{1n}) + (1-2/w_{1n}^2)J_1^2(w_{1n})\right)}
\end{aligned} \tag{2.44}$$

where the TM$_{1n}$ mode areas are equivalent with the replacement $w_{1n} \to u_{1n}$.

To compute the mode sampling factor, we consider an electron with position $\mathbf{r}_e$ and velocity $\mathbf{v}_e$ in a helical trajectory such that $\mathbf{r}_e \cdot \mathbf{v}_e = 0$. In a TE mode, the dependence of the coupling with respect to the trajectory radius can be written (up to a complex phase) as

$$\begin{aligned}
\left|\mathbf{v}_e \cdot \mathbf{E}_\perp\right|_{\mathbf{r}=\mathbf{r}_e} &\propto E_\phi\Big|_{r=r_e,\ \phi=0} \propto J_0\left(\frac{w_{1n}r_e}{R}\right) - J_2\left(\frac{w_{1n}r_e}{R}\right) \\
&\Longrightarrow \boxed{\langle\Theta_{1n}\rangle = J_0\left(\frac{w_{1n}r_e}{R}\right) - J_2\left(\frac{w_{1n}r_e}{R}\right) \quad \text{(TE)}}
\end{aligned} \tag{2.45}$$

Similarly, using E_ϕ for TM modes gives

$$\boxed{\langle\Theta_{1n}\rangle \equiv \frac{2R}{u_{1n}r_e}J_1\left(\frac{u_{1n}r_e}{R}\right) \quad \text{(TM)}} \tag{2.46}$$

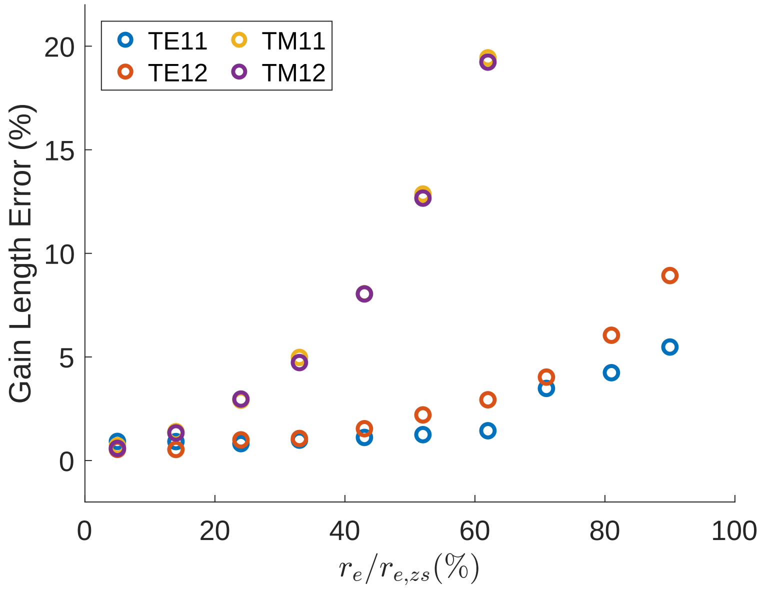

Figure 2.14: Gain length errors as a function of wiggling trajectory radius expressed relative to the zero-slippage trajectory radius.

Both expressions are normalized to make $\langle\Theta_{1n}\rangle = 1$ on-axis. At zero-slippage resonance where $w_{1n}r_e/R \approx u_{1n}r_e/R \approx K/\sqrt{1+K^2}$ by Eq. (1.74), the TE and TM corrections evaluate to 0.65 and 0.88, respectively, in the $K \gg 1$ limit.

Figure 2.14 compares the gain length from single-frequency GPTFEL simulations in a circular waveguide against the theory in Eq. (2.43). The beam is given a slight density modulation (0.005 bunching factor) to seed the interaction. Figure 2.14 shows the relative gain length errors for the first four waveguide modes as a function of trajectory radius relative to the zero-slippage trajectory radius. In the high energy limit where particles are close to the axis, the simulations converge to the analytic theory ($< 1\%$ error). As the beam energy is reduced, the non-zero E_z fields in the TM modes act to resist the natural FEL microbunching, increasing the gain length. On the other hand, the TE modes maintain fairly good agreement ($< 10\%$) out to the zero-slippage limit.

In a rectangular waveguide, only modes with even m and odd n indices can resonate and

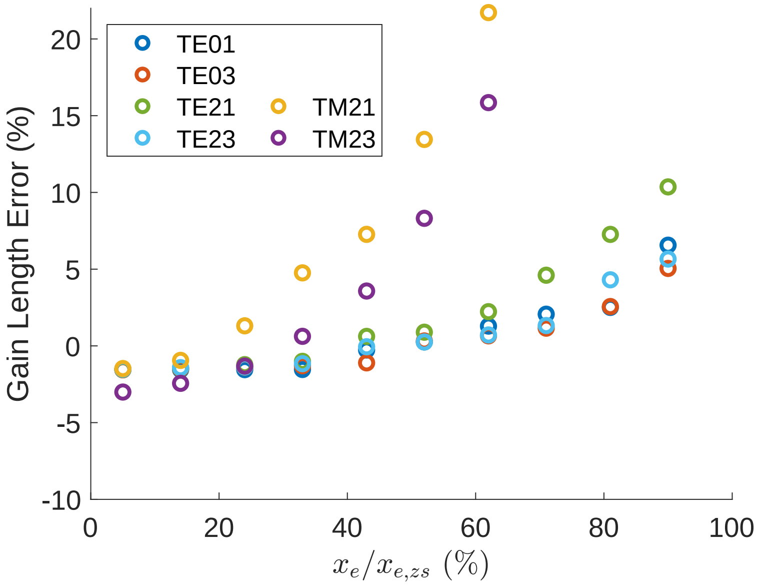

Figure 2.15: Simulated gain length errors for modes in rectangular waveguide as a function of wiggling trajectory amplitude expressed relative to the zero-slippage trajectory amplitude.

TM_{0n} modes do not exist. The mode area calculations are straightforward and give

$$\begin{aligned} &(\text{TE}) \quad \mathcal{A}_{0n} = \frac{ab}{2} \quad \text{else} \quad \mathcal{A}_{mn} = \frac{ab}{4}\left(1 + \frac{k_x^2}{k_y^2}\right) \\ &(\text{TM}) \quad \mathcal{A}_{mn} = \frac{ab}{4}\left(1 + \frac{k_y^2}{k_x^2}\right) \end{aligned} \tag{2.47}$$

As a beam propagates in a planar undulator, recall there is no coupling at the trajectory turning points and maximal coupling when the transverse velocity is largest as the beam crosses through the axis. For this reason, the wiggling amplitude of the trajectory has minimal effect on resonance and the mode sampling factor is simply $\langle \Theta_{mn} \rangle = 1$.

Similar to Figure 2.14, we benchmark the rectangular waveguide simulations for various modes in Figure 2.15. Again, we see that all simulations converge to the analytic gain length in the high energy limit. The TE modes maintain agreement at lower energies while the coupling in TM modes suffer from non-zero E_z fields.

CHAPTER 3

Undulator Commissioning

3.1 Introduction

Undulator technology is pivotal to the operation of FELs and different schemes have been researched to improve on the original permanent magnet undulator, each with their relative advantages and disadvantages. Superconducting undulators currently provide the largest peak fields and shortest undulator periods, making them attractive for generating high-energy X-rays [98, 99] at the cost of additional complexity while simpler hybrid undulators similarly improve the magnetic fields by using iron poles to focus the magnetic flux of permanent magnets [100]. To optimize energy extraction from the beam, it is necessary to employ a helical geometry with strongly-tapered fields, which is best achieved by a permanent magnet design with linear magnetic response.

In the last decade, tapered helical undulator technology has been developed for high gradient inverse-FEL and FEL experiments through a collaboration between UCLA and Radiabeam Technologies. This work has culminated in the design of the Theseus undulators for the FASTGREENS experiment, planning to target 10% efficiency at 255 nm in four 1-meter long undulator sections. The design is based on permanent magnet Halbach arrays held together by four strongbacks with machined slots so magnets can be moved perpendicular to the beam axis with tuning screws, enabling tapering and tuning of the field amplitude and the particle trajectories. The helical geometry enjoys an increase in the FEL coupling by at least a factor of two compared to planar undulators, but the enclosed geometry creates engineering challenges for magnetic field measurements, beam diagnostics, and vacuum pumping.

One of the Theseus undulators was borrowed for the Tessatron waveguide FEL experiments. The low beam energy required for zero-slippage operation causes the electrons to wiggle with a beam trajectory amplitude which is roughly half of the waveguide radius, experiencing large focusing forces and strong coupling between the transverse coordinates. This poses a significant challenge in controlling the beam trajectory and transport including full transmission of the injected beam charge through the small waveguide aperture.

Therefore, it is important to understand the optical characteristics of helical undulators for low energy beams and develop a strategy for measuring and tuning the good field region of these devices. Traditional on-axis Hall probe or pulsed-wire measurements are not sufficient to ensure correct tuning of the off-axis fields in the closed geometry. In order to optimize the beam trajectory and ensure maximal charge transmission through the waveguide, we utilize a pulsed-wiring setup and leverage the ability to translate the wire transversely with respect to the magnetic axis to sample and correct the off-axis fields.

This chapter discusses the commissioning of the Theseus undulators (Figure 3.1) for the Tessatron experiments and is organized as follows. We first present the most general expression for the field in a helical undulator and discuss the resulting beam dynamics, showing the importance of the off-axis fields in the optical properties of the device. Next, we present the tuning and magnetic design of the Theseus undulators and introduce Hall probe tuning procedures including corrections for probe position and angle errors. Finally, we derive the theory for pulsed-wire measurements and discuss limitations due to wire sag and dispersion. Transverse wire scans are used to identify the magnetic axis from the local field concavity as well as measure integrated effects of higher order field moments on the beam trajectory. In order to guide the tuning of quadrupole and sextupole moments in the undulator field, we present an analytic model that accurately predicts the effects of varying magnet positions to correct the 3D fields and minimize deviations in the off-axis trajectories.

3.2 Theory

3.2.1 Beam Dynamics

The most general expression for the field of a helical undulator can be constructed from the separated variable solution to the Laplace equation ($\nabla^2\psi = 0$) for the magnetic scalar potential of a single undulator array with $\lambda_u = 2\pi/k_u$ periodicity in the z-direction. Superposing the potentials for two planar arrays, phase shifted by 90 degrees and rotated with respect to each other, we can write

$$\psi = \frac{B_0}{\alpha k_u}\sinh(\alpha k_u x)\cos(\beta k_u y)\cos(k_u z) + \frac{B_0}{\alpha k_u}\sinh(\alpha k_u y)\cos(\beta k_u x)\sin(k_u z) \tag{3.1}$$

using normalized transverse wavenumbers $\alpha = k_x/k_u$ and $\beta = k_u/k_u$ which satisfy $\alpha^2 - \beta^2 = 1$ due to the Laplace condition $k_x^2 - k_y^2 = k_u^2$. Here, we have chosen the sign of the phase shift to construct right-handed fields.

In general, α is real due to the longitudinal fringe fields of each magnet while β can be real or imaginary depending on the magnetic profile due to the transverse pole geometry as shown in Figure 3.2. For a concave pole shaping, the imaginary β results in an exchange between harmonic functions and hyperbolic functions. As an example, for the bifilar coil case of Madey's original FEL we have $\alpha^2 = 1/4$ and $\beta^2 = -3/4$ such that both traverse functions are hyperbolic. On the other hand, the Theseus undulators (Figure 3.1) are designed with convex pole shaping to maximize the undulator field.

The magnetic field $\mathbf{B} = -\nabla\psi$ is the gradient of the scalar potential and an expression for the fields of the helical undulator near its axis can be obtained through a small-argument expansion for the hyperbolic and harmonic functions,

$$\begin{aligned}
B_x/B_0 &= -\left(1 + \frac{{k_u}^2}{2}(\alpha^2 x^2 - \beta^2 y^2)\right)\cos(k_u z) + \left({k_u}^2\beta^2 xy\right)\sin(k_u z)\\
B_y/B_0 &= -\left(1 + \frac{{k_u}^2}{2}(\alpha^2 y^2 - \beta^2 x^2)\right)\sin(k_u z) + \left({k_u}^2\beta^2 xy\right)\cos(k_u z)\\
B_z/B_0 &= k_u x\sin(k_u z) - k_u y\cos(k_u z)
\end{aligned} \tag{3.2}$$

such that the on-axis fields match Eq. (1.1).

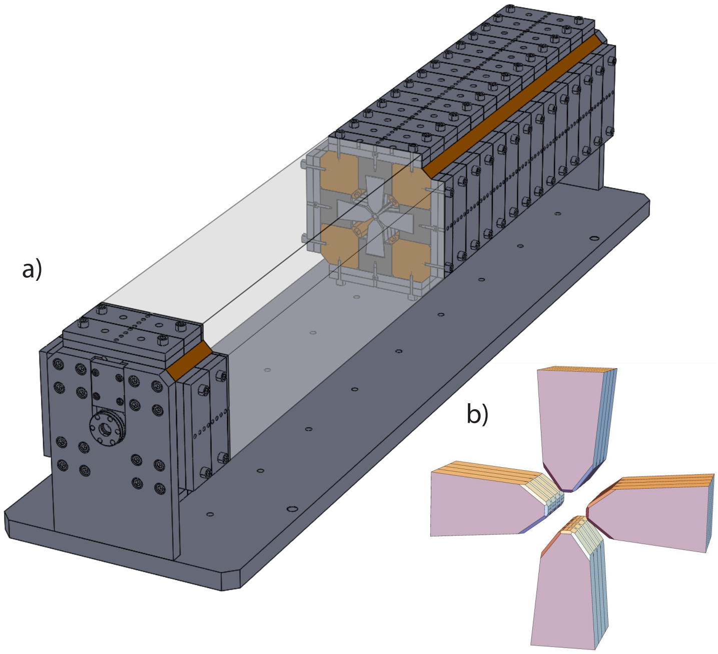

Figure 3.1: Theseus Undulator. a) Helical geometry consisting of two permanent magnet, Halbach arrays. b) A single period modeled in RADIA with magnetic chamfering.

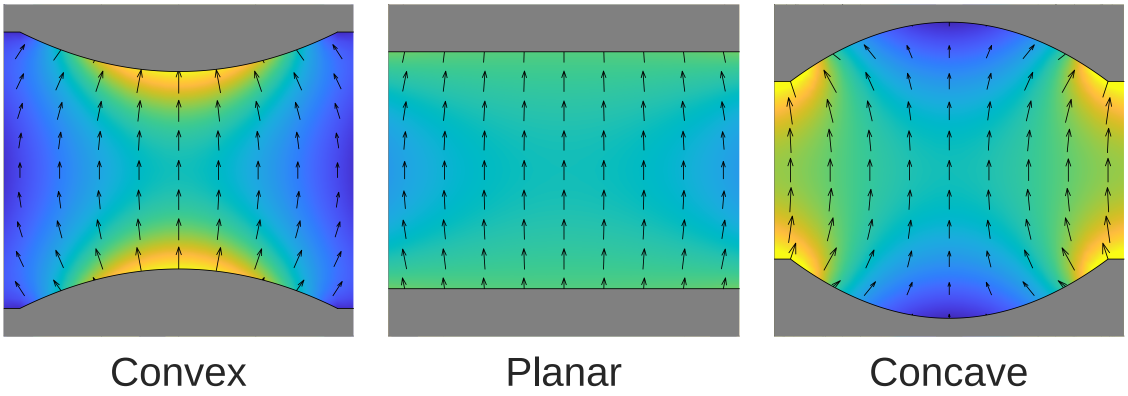

Figure 3.2: Simulations of magnetic fields in the transverse plane for different pole shaping.

Now we review the dynamics of relativistic electrons in the helical undulator to highlight the role of α and β in the beam transport and the coupling between the transverse planes at low energy. Closely following the work of [101, 102], it is helpful to start with the single particle Hamiltonian in terms of the undulator magnetic vector potential ($\mathbf{B} = \nabla \times \mathbf{A}$),

$$H = \sqrt{(\mathbf{p} - e\mathbf{A})^2c^2 + m^2c^4} = \gamma mc^2 \tag{3.3}$$

$$\begin{aligned}
A_x\frac{k_u}{B_0} &= -\left(1 + \frac{{k_u}^2}{2}(\alpha^2y^2 - \beta^2x^2)\right)\cos(k_uz) - \left({k_u}^2\beta^2xy\right)\sin(k_uz) \\
A_y\frac{k_u}{B_0} &= -\left(1 + \frac{{k_u}^2}{2}(\alpha^2x^2 - \beta^2y^2)\right)\sin(k_uz) - \left({k_u}^2\beta^2xy\right)\cos(k_uz) \\
A_z\frac{k_u}{B_0} &= 0
\end{aligned} \tag{3.4}$$

where the constant particle energy is defined in terms of the relativistic beam factor. Note we assume negligible interaction with the field $\mathbf{E} = -\nabla\Phi - \partial\mathbf{A}/\partial t$ such that $\Phi \approx 0$ and the vector potential is prescribed entirely by the undulator fields. Hamilton's equations of motion give the following system of equations.

$$\begin{aligned}
\dot{p}_x &= -\frac{\partial H}{\partial x} = \frac{e}{\gamma m}\frac{\partial \mathbf{A}}{\partial x}\cdot(\mathbf{p} - e\mathbf{A}) & \qquad \dot{x} &= \frac{\partial H}{\partial p_x} = \frac{p_x - eA_x}{\gamma m} \\
\dot{p}_y &= -\frac{\partial H}{\partial y} = \frac{e}{\gamma m}\frac{\partial \mathbf{A}}{\partial y}\cdot(\mathbf{p} - e\mathbf{A}) & \qquad \dot{y} &= \frac{\partial H}{\partial p_y} = \frac{p_y - eA_y}{\gamma m}
\end{aligned} \tag{3.5}$$

It is customary to evaluate the beam dynamics specified by the Hamiltonian by separating the solution of the beam trajectory $\mathbf{r}$ into a fast oscillation ($\mathbf{r}_f = x_f\hat{\mathbf{x}} + y_f\hat{\mathbf{x}}$) and slow drift ($\mathbf{r}_s = x_s\hat{\mathbf{x}} + y_s\hat{\mathbf{x}}$) such that $\mathbf{r} = \mathbf{r}_f + \mathbf{r}_s$. The fast oscillations are obtained by neglecting the off-axis contribution to the vector potential. In this case, we find the helical trajectory given by

$$\dot{x}_f = \frac{cK}{\gamma}\cos(k_uz) \quad \text{and} \quad \dot{y}_f = \frac{cK}{\gamma}\sin(k_uz) \tag{3.6}$$

which is another derivation of the transverse velocity already seen in Eq. (1.2) where $K = eB_0/mck_u$ is the undulator strength parameter. Integrating with the change of coordinates $z = c\beta_zt$, the full trajectory is given by

$$x = x_s + \frac{K}{\gamma k_u\beta_z}\sin(k_uz) \quad \text{and} \quad y = y_s - \frac{K}{\gamma k_u\beta_z}\cos(k_uz) \tag{3.7}$$

The slow drift is evaluated by substituting (3.7) into (3.5), applying period-averaging, and expanding to lowest order in $\mathbf{p}$ and $\mathbf{r}_s$. After collecting terms, normalizing the momentum $\hat{\mathbf{p}} = \mathbf{p}/\gamma m c \beta_z$, and converting to spatial derivatives, we find

$$\frac{d\hat{p}_x}{dz} = -k_u^2\delta^2 x_s - k_u\delta^2\hat{p}_y \qquad \frac{dx_s}{dz} = \hat{p}_x - k_u\delta^2 y_s \tag{3.8}$$

$$\frac{d\hat{p}_y}{dz} = -k_u^2\delta^2 y_s + k_u\delta^2\hat{p}_x \qquad \frac{dy_s}{dz} = \hat{p}_y + k_u\delta^2 x_s \tag{3.9}$$

where $\delta = K/\sqrt{2}\gamma\beta_z$ details the orders for the relativistic approximation $\gamma \gg 1$. This system is notably independent of the magnet poleshapes and transverse wavenumbers since each nonvanishing term only contains the combination $\alpha^2 - \beta^2$ which is constrained to be 1. In other words, though the off-axis field expansion can vary locally, the average effect on the particle trajectory depends only on the Laplace condition and is the same regardless of the details of the undulator magnet technology. The system of coupled equations can be reduced to

$$\frac{d^2\xi}{dz^2} = 2k_u\delta^2 i\frac{d\xi}{dz} - k_u^2\delta^2\xi \tag{3.10}$$

keeping the lowest order terms in δ where $\xi = x_s + iy_s$.

A guess of the form $\xi = e^{ik_\pm z}$ yields $k_\pm = \pm k_u\delta\left(\sqrt{1+\delta^2} \pm \delta\right) \approx \pm k_0 + \delta k_0$ where $k_0 = k_u K/\sqrt{2}\gamma\beta_z$ and the full solution is a linear combination $\xi = c_1 e^{ik_+ z} + c_2 e^{ik_- z}$ with complex constants. Expressions for x_s and y_s are found by taking the real and imaginary parts yielding

$$x_s = (c_{1R} + c_{2R})C_0C_\delta - (c_{1I} + c_{2I})C_0S_\delta + (-c_{1I} + c_{2I})S_0C_\delta - (c_{1R} - c_{2R})S_0S_\delta \tag{3.11}$$

$$y_s = (c_{1I} + c_{2I})C_0C_\delta + (c_{1R} + c_{2R})C_0S_\delta + (c_{1R} - c_{2R})S_0C_\delta + (-c_{1I} + c_{2I})S_0S_\delta \tag{3.12}$$

where $c_1 = c_{1R} + ic_{1I}$, $c_2 = c_{2R} + ic_{2I}$, and we use the short-hand notation $S_0 = \sin(k_0 z)$, $C_0 = \cos(k_0 z)$, $S_\delta = \sin(\delta k_0 z)$ and $C_\delta = \cos(\delta k_0 z)$. The real constants are expressed in terms of the input beam coordinates as

$$c_{1R} = \frac{1}{2k_0}y'_{s0} + \frac{1-\delta}{2}x_{s0} \qquad c_{1I} = \frac{-1}{2k_0}x'_{s0} + \frac{1-\delta}{2}y_{s0} \tag{3.13}$$

$$c_{2R} = \frac{-1}{2k_0}y'_{s0} + \frac{1+\delta}{2}x_{s0} \qquad c_{2I} = \frac{1}{2k_0}x'_{s0} + \frac{1+\delta}{2}y_{s0} \tag{3.14}$$

where $x'_{s0} = dx_{s0}/dz$ and $y'_{s0} = dy_{s0}/dz$ refer to the initial trajectory angles.

Recasting x_s, x'_s, y_s, y'_s in terms of $x_{s0}, x'_{s0}, y_{s0}, y'_{s0}$ we can identify the 4x4 linear transfer matrix for the undulator:

$$R = \begin{pmatrix} R_1 & R_2 \\ -R_2 & R_1 \end{pmatrix} \tag{3.15}$$

where

$$R_1 = \begin{pmatrix} C_0 C_\delta + \delta S_0 S_\delta & \frac{1}{k_0} S_0 C_\delta \\ -k_0(1-\delta^2) S_0 C_\delta & C_0 C_\delta - \delta S_0 S_\delta \end{pmatrix}$$

$$\text{and} \quad R_2 = \begin{pmatrix} -C_0 S_\delta + \delta S_0 C_\delta & -\frac{1}{k_0} S_0 S_\delta \\ k_0(1-\delta^2) S_0 S_\delta & -C_0 S_\delta - \delta S_0 C_\delta \end{pmatrix} \tag{3.16}$$

In the ultrarelativistic limit, $\delta \to 0$ and the R_1 matrix provides the natural undulator focusing effect with the well-known $\beta = \frac{1}{k_0} = \frac{\sqrt{2}\gamma}{K k_u}$. At lower beam energies the dynamics are more complex and one has to take into account the coupling terms. The R_2 block matrix clearly indicates that low energy transport inside the undulator can not be decoupling even in the linear transport approximation.

We compare the linear matrix transport against numerical integration of the Lorentz force equation in Figure 3.3 using the particle tracking code GPT [103] at two different energies (relativistic factor $\gamma = 200$ and $\gamma = 20$) where the beams are given an initial x-offset of 500 μm in an undulator with $K = 2.18$. The period-averaged slow drift $\mathbf{r}_s$ is plotted on top of the semi-transparent trajectory $\mathbf{r}$. At lower beam energies, significant coupling is introduced in addition to the shortening of the betatron oscillation period, but the matrix transport still accurately tracks the average position of the beam.

Figure 3.4 compares the results of matrix transport through the Tessatron undulator against beam centroid measurements performed at the UCLA Pegasus laboratory for an input beam energy of $\gamma = 14.5$. The beam centroid is measured on a screen 14 cm downstream of the undulator while the horizontal and vertical beam angles are adjusted with a calibrated steering magnet 8 cm upstream of the entrance. The orientation of the centroid measurements with respect to steering is consistent with the matrix transport where the

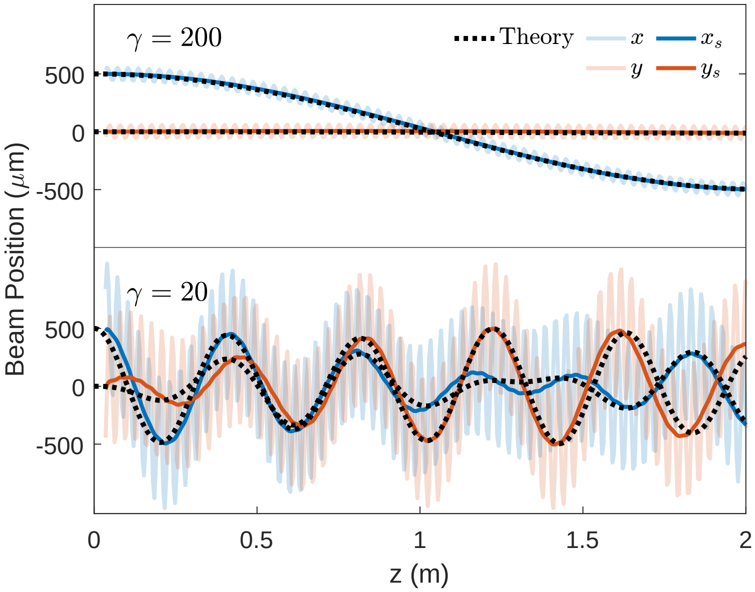

Figure 3.3: Comparing undulator focusing matrix transport against particle-tracking simulation at high and low beam energies. The period-averaged and full simulated trajectory ($\mathbf{r}_s$ and $\mathbf{r}$) are plotted against the matrix transport theory.

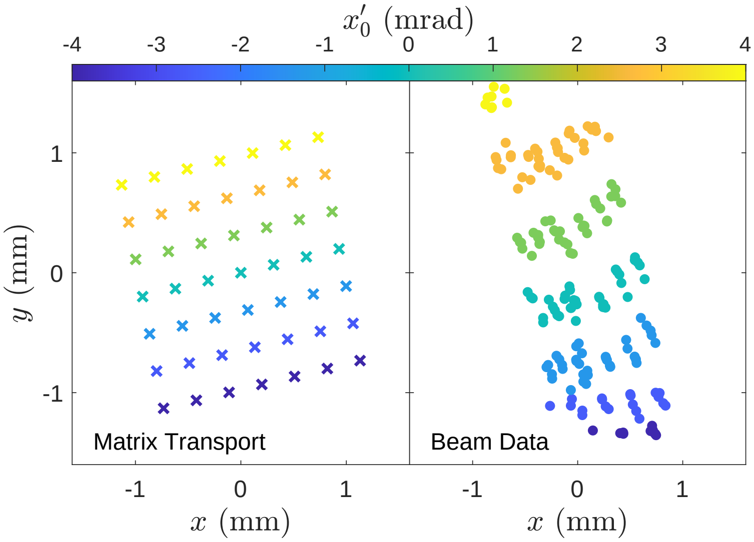

Figure 3.4: Comparison between matrix transport and beam measurement. A 2D raster scan of an upstream steering magnet (8 cm before undulator) varies the beam injection angle and the centroid is measured on a screen 14 cm downstream of the undulator exit.

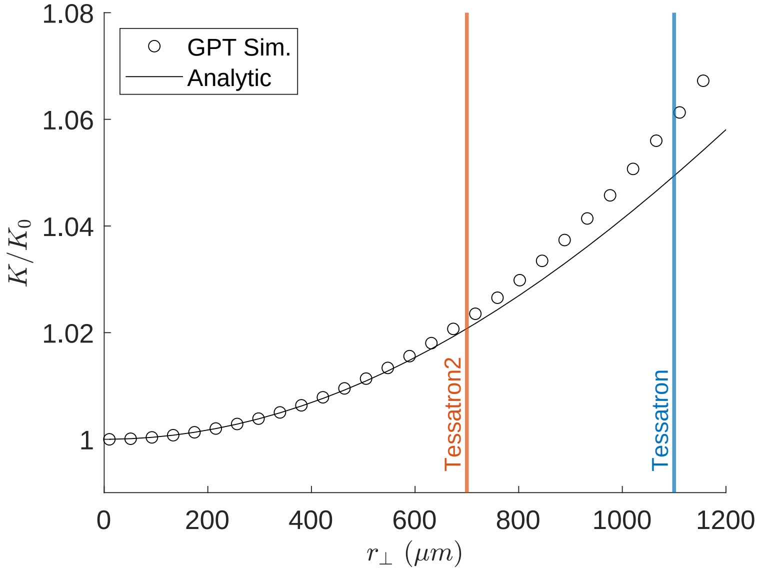

Figure 3.5: Corrections to the undulator strength parameter due to stronger transverse fields and non-zero B_z fields off-axis.

coloring highlights transverse coupling as changes in horizontal steering lead to vertical deflections out of the undulator. The asymmetry seen in the beam data can be produced in GPT simulations by varying the initial alignment into the undulator.

In addition to coupled focusing, low energy beams have an increased wiggling amplitude such that the electrons samples stronger transverse fields and non-zero B_z fields that contribute to the Lorentz force and alter the undulator strength parameter defined by $\beta_z = \sqrt{1 + \frac{1+K^2}{\gamma^2}}$ which can alternatively be expressed as $K = \gamma\beta_\perp$. The transverse velocity can be computed by considering the cyclotron motion in the transverse plane given by $\gamma mc^2|\boldsymbol{\beta}_\perp|^2/|\mathbf{r}_f| = F_r$ where F_r is the radial Lorentz force given by

$$\mathbf{F}_r = ec\Big(\beta_z B_y(\mathbf{r}_f) - \beta_y B_z(\mathbf{r}_f)\Big)\hat{\mathbf{x}} + ec\Big(\beta_x B_z(\mathbf{r}_f) - \beta_z B_x(\mathbf{r}_f)\Big)\hat{\mathbf{y}} \tag{3.17}$$

where the full radial Lorentz force is computed along the fast trajectory of Eq. (3.7) using the nominal parameter $K_0 = eB_0/mck_u$. Expanding to lowest order in K_0 and γ, we find

$$K = K_0\left(1 + \frac{9K_0^2}{8\gamma^2} + \mathcal{O}(1/\gamma^4) + \mathcal{O}(K_0^4/\gamma^4)\right) \tag{3.18}$$

The strong focusing affects the transverse coupling and was included in the matrix transport of Figures 3.3 and 3.4. Figure 3.5 benchmarks Eq. (3.18) against GPT simulations as a function of wiggling amplitude using nominal parameters from the Tessatron experiments. In this extreme example, operation at the zero-slippage waveguide resonance for the Tessatron experiments requires beam trajectories with an amplitude of roughly half the waveguide radius of 2 mm. There is little effect on resonance, though, as the beam energy can be changed to compensate for errors in K.

3.2.2 Theseus Undulators

The Theseus undulators were designed to maximize the coupling between a relativistic beam and radiation field for high efficiency experiments. They are comprised of two planar Halbach magnet arrays rotated 90° and shifted a quarter period relative to each other. A Halbach array (Figure 3.6d) includes additional magnets with longitudinal magnetization to close the magnetic circuit, enhancing fields near the axis and reducing stray fields outside the undulator . The NdFeB permanent magnets (Figure 3.6e) have a residual magnetization of 1.18 T and are glued into holders with an angled notch to help resist the strong attractive forces between opposing magnets. The undulators contain 30 periods of length $\lambda_u = 3.2$ cm including entrance and exit periods which are designed using 2 mm, 4 mm, and 6 mm length magnets to keep the electron beam trajectory close to the beam axis [104]. Thus, a full undulator is comprised of 484 magnets with an overall length of 96 cm. Three dimensional magnetostatic simulations were completed using RADIA [105], a software developed at the European Synchrotron Radiation Facility.

Figure 3.6a and b show a schematic and image of the tuning design. Strongbacks made from 360 brass span the full undulator length and provide the rigidity necessary to withstand the magnets forces. Magnet gaps are adjusted via 8-32 tuning screws with 800 μm travel per rotation. Hardstops limit the minimum gap to 5.58 mm to avoid damage to the vacuum pipe (5.56 mm OD). The maximum gap is 7.5 mm, but shims can be inserted under the tuning plates to increase the gap further. It was decided to chamfer the magnets for safer handling, though it was later realized during characterization and confirmed with magnetostatic simulations that this led to a non-negligible 10% reduction in magnetization strength.

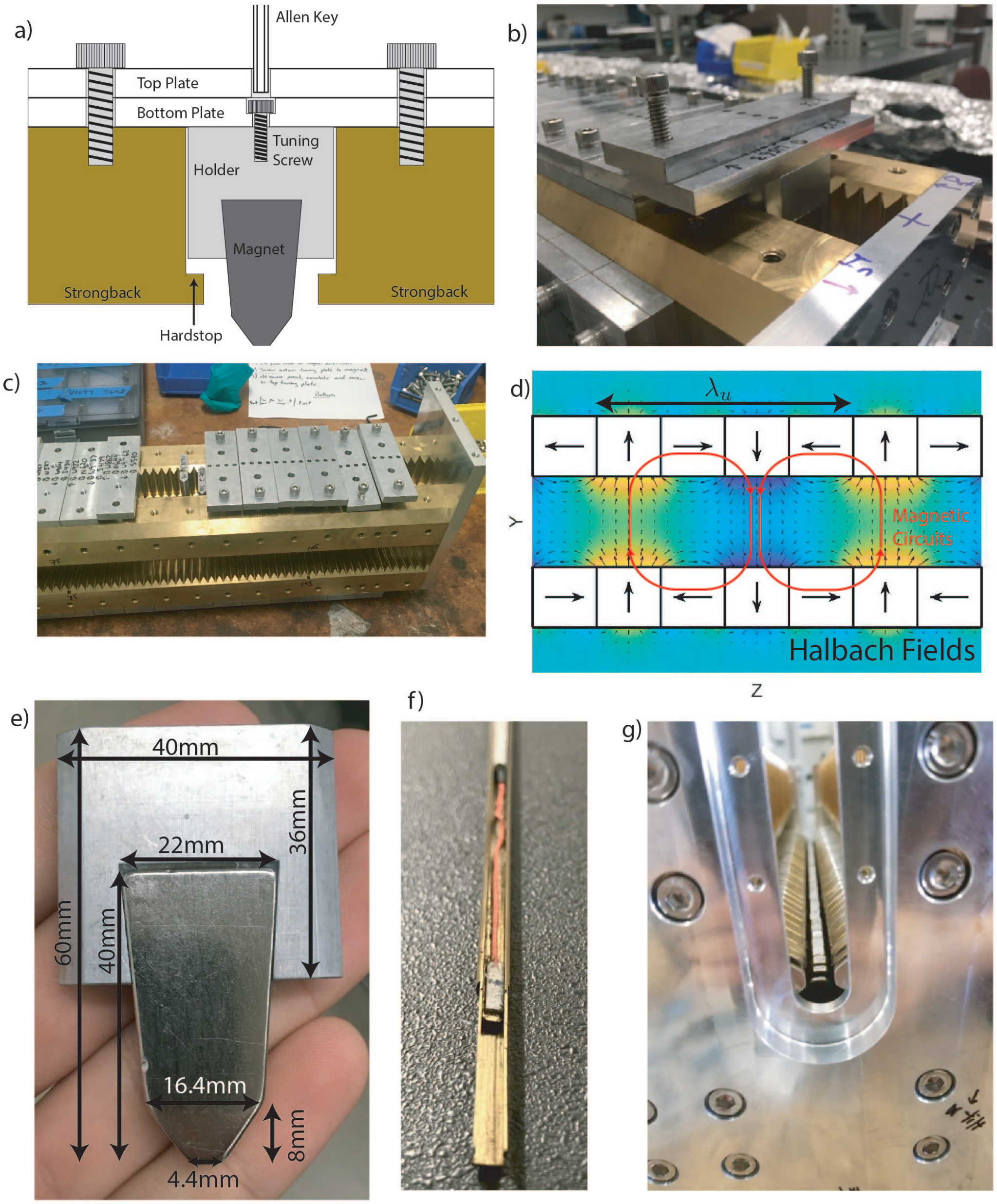

Figure 3.6: Undulator construction. The magnet gap is tuned by adjusting a tuning screw held between the tuning plates (a) and (b). The undulator is assembled (c) by inserting magnets (e) into grooves in the undulator strongback. Each tuning plate covers 4 magnets (1 period) of the undulator. The Halbach array (d) utilizes magnets with longitudinal magnetization to help close the magnetic circuits, reducing stray fields and making the inner fields more robust to external influences. The Hall probe (f) is glued to a flat rode that slides along a fix u-shaped channel. An end view (g) shows the magnet gaps before installation of the vacuum pipe.

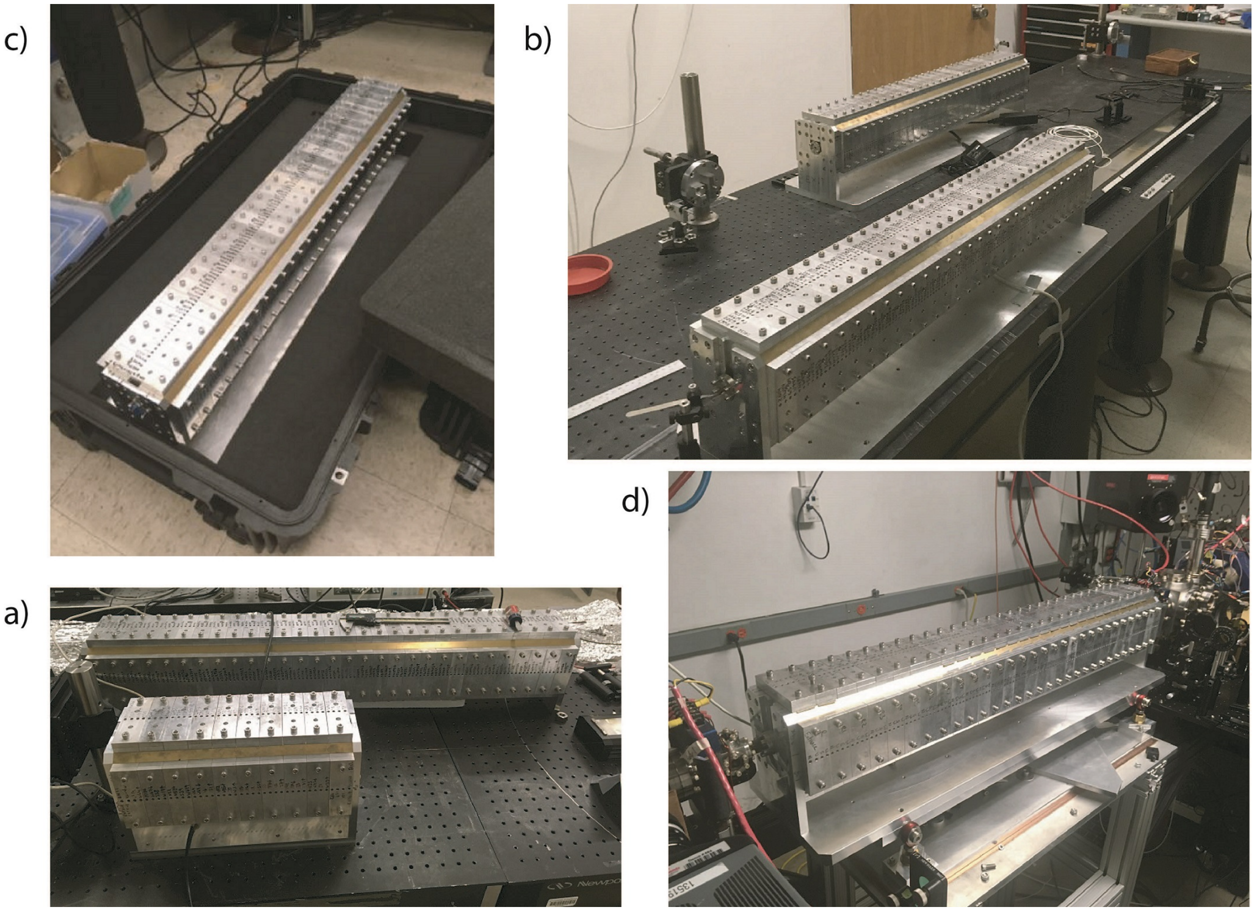

Figure 3.7: Completion of undulator tuning. The prebuncher and Theseus 1 (a) were the first undulators tuned and shipped to Fermilab for the FASTGREENS experiment. Six months later Theseus 2 and 3 (b) were constructed and tuned at UCLA. Theseus 2 was shipped to Fermilab (c) while Theseus 3 was installed on the Pegasus beamline (d) for the Tessatron experiments.

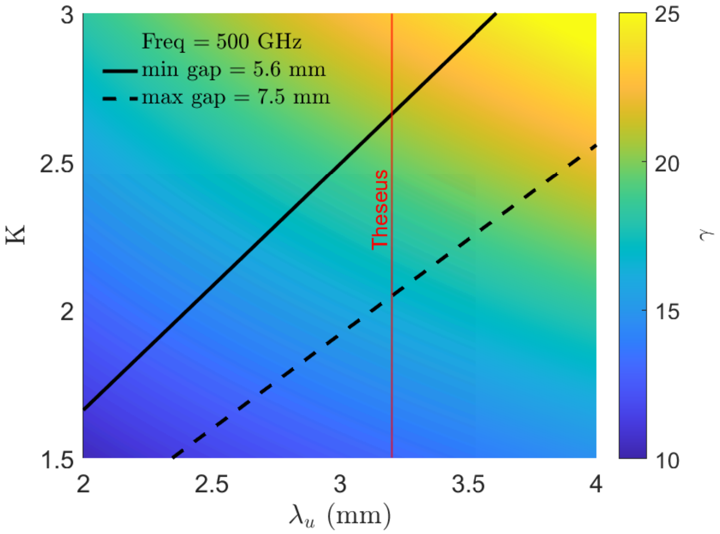

Figure 3.8: Undulator performance as a function of period. The design period of 3.2 cm is shown by the red line and the colored background indicates the beam energy required for zero-slippage resonance at $f = 500$ GHz.

The undulator performance as a function of period is shown in Figure 3.8, along with the beam energy required for zero-slippage resonance at $f = 500$ GHz. The maximum field at mimimum gap is 890 mT corresponding to $K = 2.66$.

The full undulator periods are tuned with Hall probe scans to first minimize errors in the fields, then to minimize slippage or phase error between the electrons and radiation. A pulsed-wire bench allows instantaneous measurements of the first or second field integrals for tuning the beam trajectory in the entrance and exit periods. By scanning the wire transversely, higher order field moments can be tuned to ensure accuracy in the off-axis fields.

3.3 Hall Probe Measurements

The enclosed geometry of the helical undulator significantly increases the difficulty of Hall probe measurements necessary for tuning the undulator fields. Figure 3.6f shows the probe transport design where the probe head is glued to a flat brass piece which slides along a

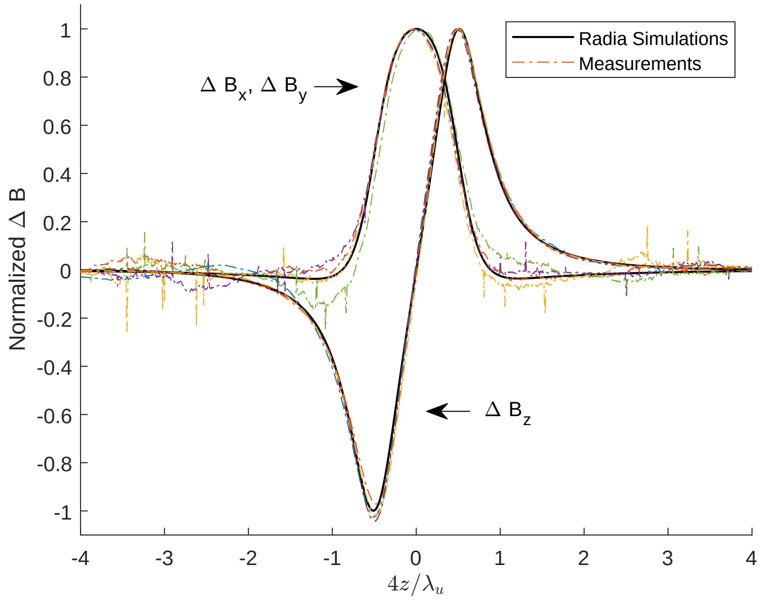

Figure 3.9: Tuning Eigenfunctions. A comparison between simulated and measured eigenfunctions for the transverse and longitudinal magnetic fields.

hollowed out brass rod. The rod diameter is chosen to fit snugly inside the vacuum pipe which can be tensioned with vacuum screws. The rod is held fixed relative to the undulator with set screws and a clamp such that the probe (Senis HS probe with F3A transducer calibrated to 0.1%) can be moved along the undulator with a 1 m translation stage (Zaber A-LST1000A-C) with 2 μm resolution. Due to the fragility of the flat brass piece, measurements were only performed while pulling the probe which was manually reset between scans. Before measurements, the probe warms up for 15 min so the sensors to reach steady state and field offsets are measured in a zero-gauss chamber. Errors in the probe's traverse position and roll angle, expected due to warping of the brass rod during machining and the inability to observe the probe's motion in the undulator, were corrected in post-processing.

The hall probe scans yield measurements of $B_x(z)$, $B_y(z)$, and $B_z(z)$ with 50 steps per period. The absence of soft magnetic materials in the undulator allowed the tuning to rely on the superposition where the change in total field is equivalent to the sum of the adjustments from individual magnets. The normalized change in transverse and longitudinal fields for each magnet (called the tuning eigenfunctions) were simulated in RADIA and are compared with measurements in Figure 3.9. After a Hall probe scan, a Matlab script minimizes

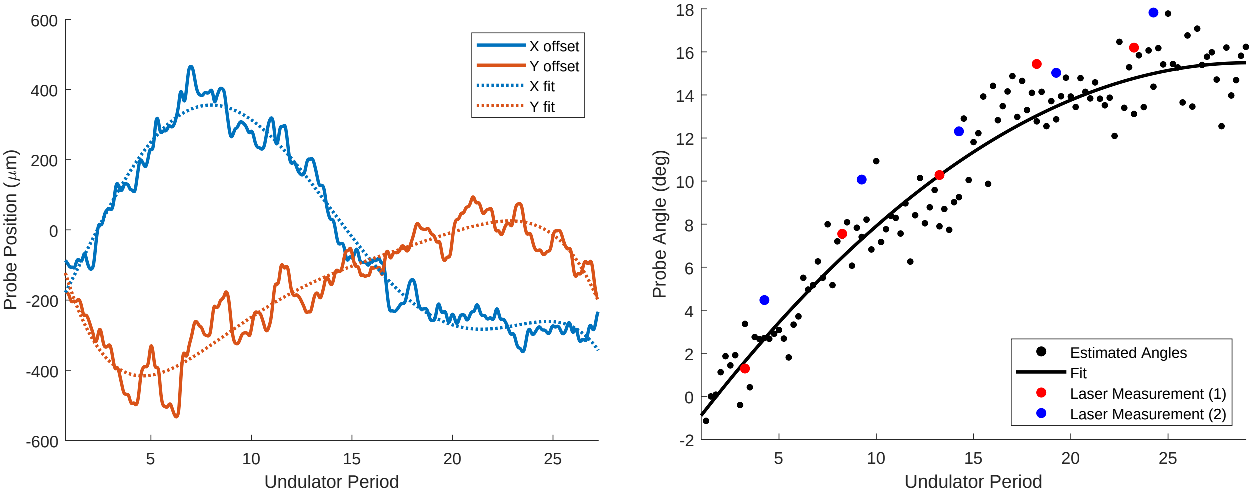

(a) (b)

Figure 3.10: Measurement of errors in Hall probe position and angle. a) The amplitude and phase of B_z indicate the probe offset. Polynomial fits are used to compute the effective on-axis fields. b) Probe angle is inferred from changes in the field periodicity and confirmed against laser measurements off a mirror glued next to the probe head.

the difference between the measured fields and the simulated target field by adjusting the eigenfunction coefficients at each magnet. To speed up the optimization and ensure convergence, the transverse and longitudinal fields are tuned individually, allowing the movement of opposite magnets which produce similar eigenfunctions to be grouped together, halving the number of variables. After a successful optimization, the script prints out the eigenfunction coefficients (mT units) at all magnet positions. For each adjustment, the probe is first positioned at the eigenfunction maximum (differs depending on magnetization or field component) and the magnet pair is moved equal amounts to change the field by the quoted coefficient.

The optimization fundamentally relies on the probe accurately measuring the fields along a fixed axis in the undulator. Systematic twisting or bending of the tuning carriage caused by machining errors or gravitational sag is accounted for by utilizing the field expansion from Eq. (3.2). From the expression of B_z, it can be seen that a transverse error in probe position results in a sinusoidal B_z field where the amplitude and phase indicate the amount

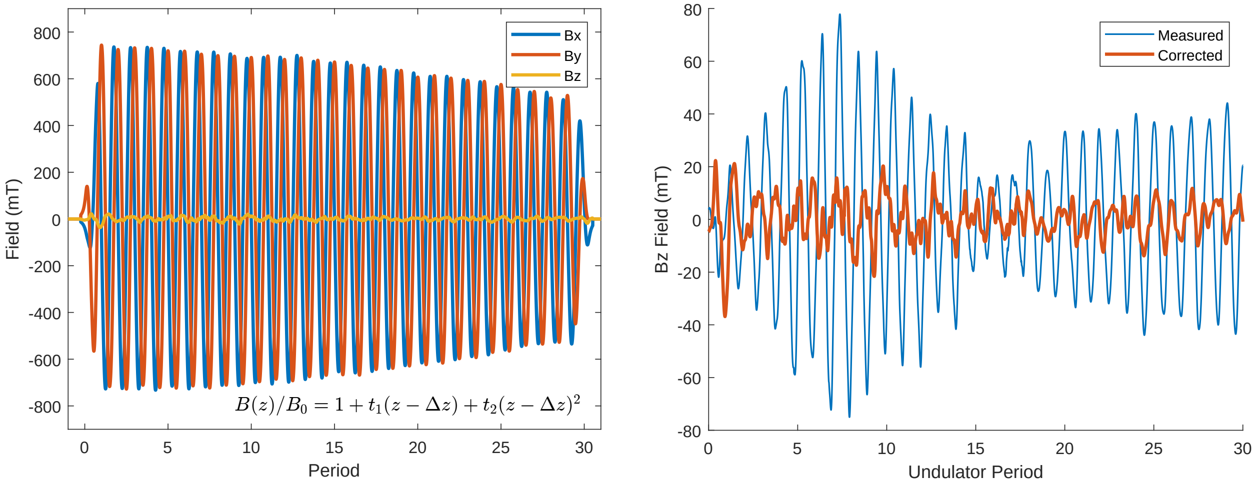

(a) (b)

Figure 3.11: Hall probe measurements (corrected for probe position and offset) of the undulator fields for the Tessatron Experiment. a) Strong undulator tapering is necessary to target high efficiency. b) The B_z component emphasizes the need for corrections to the field measurements.

and direction of the probe offset such that

$$\mathbf{r}_{hp,\perp}(z) = \frac{-1}{B_0\pi}\int_{z-\lambda_u/2}^{z+\lambda_u/2} B_z(z)\Big[\cos(k_u z)\hat{\mathbf{x}} + \sin(k_u z)\hat{\mathbf{y}}\Big]dz \tag{3.19}$$

Additionally, an error in the probe angle manifests as a shift of the perceived peak field positions z_c and a change in the measured period lengths. Since the probe position is well-known from the micron accuracy of the translation stage, the probe angle can be inferred from

$$\theta_{hp}(z_c) - \theta_{hp}(0) = \frac{\pi}{2}\left(z_c - \frac{\lambda_u}{4}\text{round}\left(z_c\frac{4}{\lambda_u}\right)\right) \tag{3.20}$$

Figure 3.10 shows errors in probe angle and position from a Hall probe measurement. Using smooth polynomial fits, the fields are transformed to the effective on-axis field. The ability to infer probe offset was corroborated by directly influencing bends in the vacuum pipe through torque on the flanges. The probe twist was confirmed by removing the top array of magnets and measuring the angular deflection of laser light off a small mirror on the flat rod. Figure 3.11a shows the corrected on-axis fields for the first Tessatron experiment, with

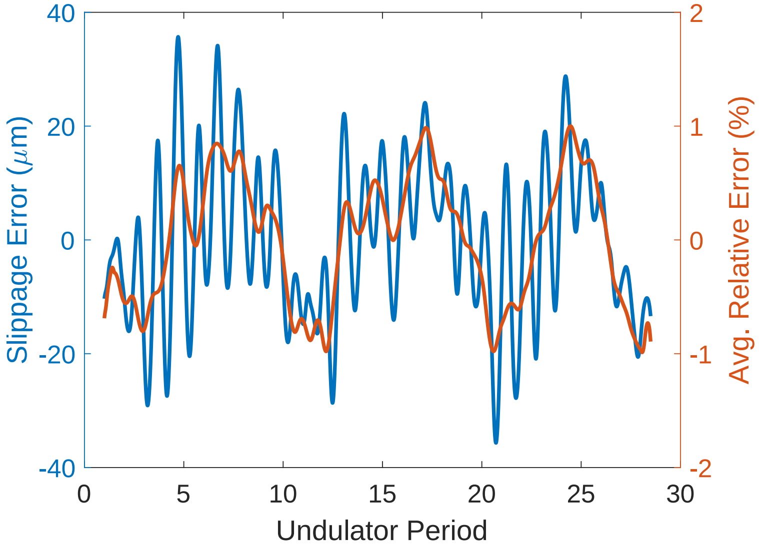

Figure 3.12: Slippage errors for the Tessatron2 Experiment. Phase errors are found scaling by $2\pi/\lambda_r$ where the resonant wavelength is $\lambda_r = 1.5$ mm.

strong field tapering to target high extraction efficiency. The importance of the correction is seen in the significant reduction of the B_z component (Figure 3.11b) which should be zero for ideal fields.

While minimizing the residuals between the measured undulator fields and simulated design fields is sufficient for coarse tuning, a more appropriate figure of merit is the slippage or phase error [106]. Field errors cause deviations in the longitudinal beam velocity and ponderomotive phase of the electrons which can lead to detrapping. In an FEL, the slippage between the radiation wavefronts and the electron beam is given by

$$S = \int \left(\frac{\omega}{k_z} - c\beta_z \right) dt \approx \int \left(\frac{\omega}{ck_z} - 1 + \frac{1}{2\gamma^2} + \frac{\beta_x^2 + \beta_y^2}{2} \right) dz \tag{3.21}$$

where we use the change of variables $z \approx ct$. The first three terms are constant and the undulator parameter is defined by $\beta_x^2 + \beta_y^2 = K^2/\gamma^2$ such that the slippage grows linearly as $\frac{K^2}{2\gamma^2}$. For this reason, after computing the transverse velocities from the measured magnetic fields, a linear fit of the slippage with known γ reveals the tuned K parameter. The residuals from the linear fit give the slippage errors, which can equivalently be expressed as phase errors by scaling by $2\pi/\lambda_r$ where λ_r is the resonant wavelength. Figure 3.12 shows the tuned slippage error for the Tessatron 2 experiment. The THz waveguide FEL is particularly robust to phase errors (up to 10%) as the rapid field growth produces a deep ponderomotive potential well where the particles are stably trapped.

3.4 Pulsed-Wire Measurements

3.4.1 Setup

A pulsed-wire bench allows for instantaneous measurement of the first and second field integrals and are especially useful in small-aperture magnetic structures [107, 108]. In addition to tuning the beam trajectory in the entrance and exit periods, we describe how the scheme can be used to fidicialize the magnetic axis and tune off-axis fields necessary for transmission of low energy beams.

Figure 3.13 shows a schematic and pictures of the UCLA pulsed-wire bench where a 50 μm diameter CuBe wire is strung through the undulator and tensioned over a pulley with a hanging weight. The wire end holders each have four machined ficualization cups for referencing the wire position. A function generator passes square current pulses through the wire such that the magnetic forces excite a pair of left/right traveling waves. For an undulator with N_u periods of length λ_u, we will show the time-dependent wire deflection is proportional to either the first or second field integral in the limit of very short or infinitely long pulse durations.

The wire deflection is measured in both transverse dimensions with laser-photodiode pairs. The inlay shows that after passing through a 50 μm slit, the laser light is partially blocked by the wire such that the photodiode voltage varies in relation to the wire displacement. Nonlinearity is introduced due to diffraction between the slit and wire. To allow a full undulator measurement before interference from reflections, the wire must extend at least half the undulator length beyond the laser-diode pairs. Measurements are captured on an oscilloscope triggered by the function generator. Oil dampers enable higher repetition rates (Figure 3.14) such that errors can be reduced by averaging over many ($\sim$ 30) shots, while also damping noise due to air currents and table vibrations.

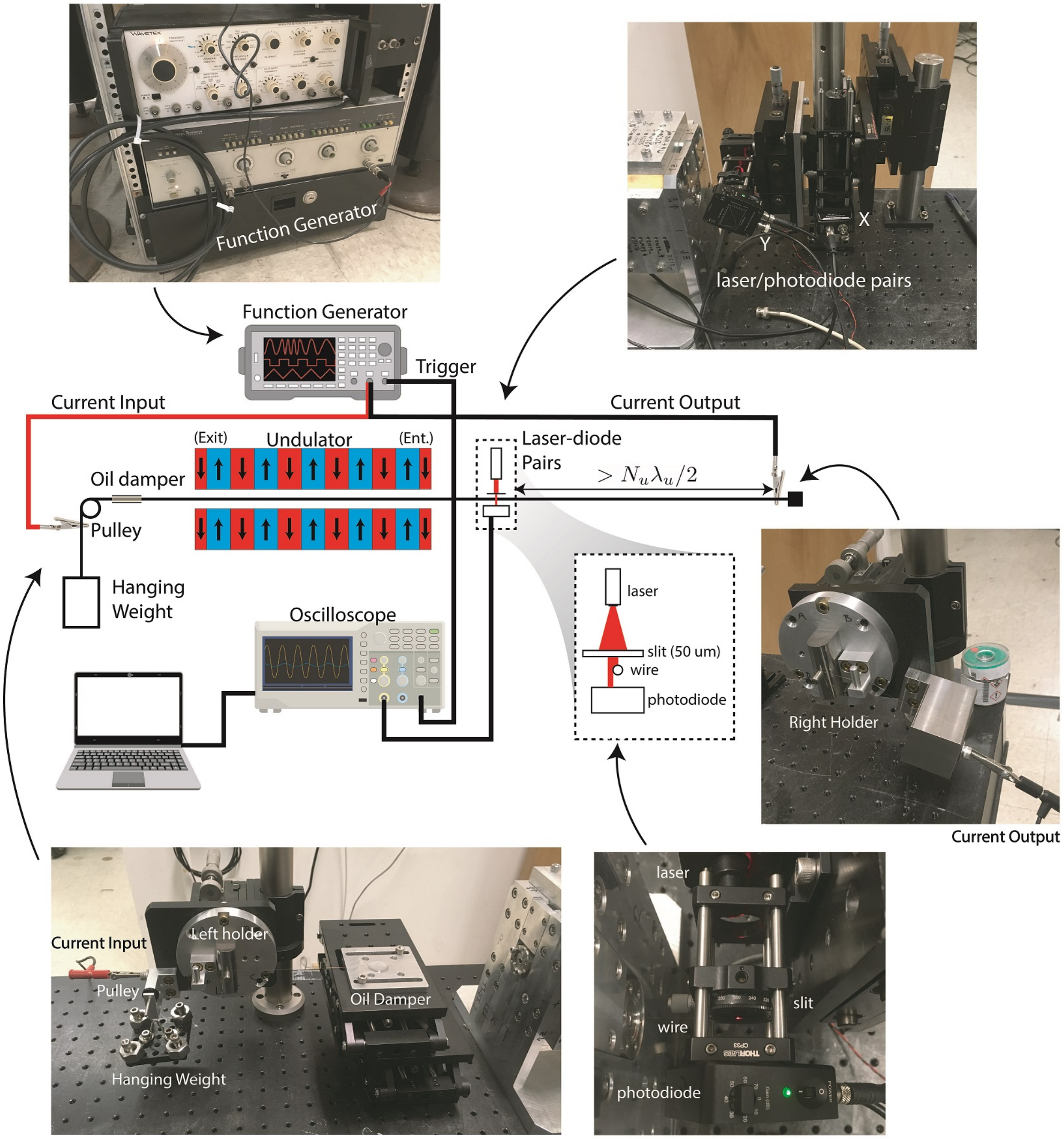

Figure 3.13: Schematic and pictures of the pulsed-wire measurement bench at UCLA.

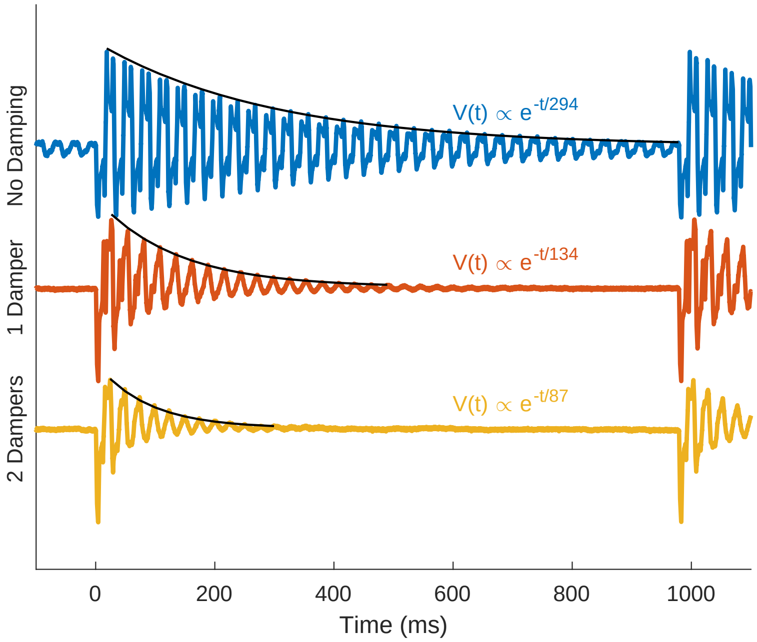

Figure 3.14: The use of one or two oil dampers significantly decreases the attenuation time constant allowing a higher repetition rate and averaging over more shots.

3.4.2 Theory

We now derive the time-dependence of the vibration waves on a string with tension T and linear density λ in the presence of undulator fields $B(z)$. The 1D solution to the vibrating string PDE with initial conditions $u(z,0) = f(z)$ and $\partial u(z,0)/\partial t = g(z)$ is given by d'Alemberts formula

$$\frac{\partial^2 u}{\partial t^2} = c_w^2 \frac{\partial^2 u}{\partial z^2} \quad \Longrightarrow \quad u(z,t) = \frac{1}{2}\left(f(z+c_w t) - f(z-c_w t)\right) + \frac{1}{2c_w}\int_{z-c_w t}^{z+c_w t} g(z')dz' \quad (3.22)$$

where the wave velocity on the wire c_w is initially assumed constant and equal to $c_0 = \sqrt{T/\lambda}$.

We first consider the limit of a short current pulse ($c_0\delta t \ll \lambda_u$) with amplitude I and duration δt such that the vibrational waves travel negligibly short distances in δt relative to the undulator period. The wire is initially at rest, $f(z) = 0$, with a velocity given by the magnetic force on the wire, $g(z) = I\delta t B(z)/\lambda$. Using Eq. (3.22), the displacement at $z = 0$ is given by

$$\boxed{u_\delta(t) = \frac{I\delta t}{2c_0\lambda}\int_0^{c_0 t} B(z')dz' \qquad (c_0\delta t \ll \lambda_u)} \quad (3.23)$$

where we assume undulator fields are nonzero only for positive z. The measured deflection for a short pulse is thus proportional to the first derivative of the field and the electron transverse velocity.

We can now generate the response for a pulse of arbitrary duration Δt using Eq. (3.23) by modeling the current pulse as a sum of short pulses with δt spacing from 0 to Δt. The contribution of the jth pulse at $t_j = j \cdot \delta t$ is given by $u_\delta(t - t_j)$. In the limit $\delta t \to dt'$, the sum becomes an integral where $t_j \to t'$ and we find

$$u_\Delta(t) = \sum_j u_\delta(t - t_j) = \frac{I}{2c_0\lambda} \int_0^{\min(t,\Delta t)} \int_0^{c_0(t-t')} B(z'')dz''dt' \tag{3.24}$$

where $\min(t, \Delta t)$ is used to handle the two cases where $t < \Delta t$ and $t > \Delta t$. If we now assume an infinite pulse duration such that the pulse is on for the entire measurement ($\Delta t > N_u\lambda_u$), we can redefine redefine $t' = t - t'$ and let $z' = c_0t'$ and $z = c_0t$ to give

$$\boxed{u_\infty(t) = \frac{I}{2c_0^2\lambda} \int_0^{z} \int_0^{z'} B(z'')dz''dz' \qquad (c_0\Delta t > N_u\lambda_u)} \tag{3.25}$$

where the measured deflection is proportional to the second integral of the field and the electron beam trajectory.

The are a few practical limitations to this ideal analysis [109]. First, the wire will sag according to the equation of a catenary $y(z) = \frac{g\lambda}{T}\cosh\left(\frac{Tz}{g\lambda}\right)$ where $g = 9.81$ m/s^2. For a wire of total length L, the maximum sag is $S = y(L/2) - y(0)$ and evaluates to

$$S = \frac{T}{g\lambda}\left(\cosh\left(\frac{Lg\lambda}{2T}\right) - 1\right) \approx \frac{g\lambda L^2}{8T} \tag{3.26}$$

In long undulators, the use of ultralight dielectric threads have been used to support the wire outside the undulator, but it is simpler and sufficient to account for sag using the off-axis expansion of the undulator fields [110, 111]. In our setup, the CuBe wire with a mass density of 8.25 g/cm^3 and maximum tensile strength of 800 MPa such that the sag in a 2-meter wire is roughly 50 μm and had negligible effect on the measurements.

Another important consideration is dispersion in the wire such that the wave speed is a function of frequency $c_w(k)$ where $\omega = c_wk$. Euler-Bernoulli analysis for beam deflection

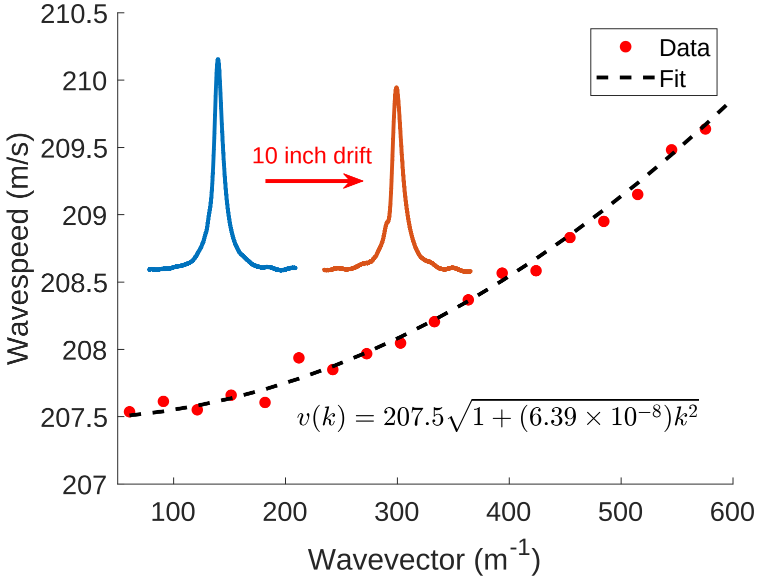

Figure 3.15: Pulsed-wire dispersion fit to Euler-Bernoulli theory from two laser measurements with 10 inch separation. Using the dispersion fit, distorted measurements can be corrected with numerical algorithms.

predicts a dispersion according to

$$c(k) = c_0\sqrt{1+\frac{EI}{T}k^2} \tag{3.27}$$

where EI is the flexural rigidty. The wire dispersion can be fit from only two measurements of the same waveform at two positions separated by a distance Δz. A delay of $\Delta z/c_w(\omega)$ in the time domain corresponds to a phase shift of $-\omega\Delta z/c_w(\omega)$ in the frequency domain such that by comparing the phases of the Fourier transforms, we can estimate the wave velocity as a function of frequency. Figure 3.15 depicts the two temporal measurements before and after a 10 inch drift where the phase velocity is fit with Eq. (3.27) over frequencies with non-negligible amplitudes returning the fit values $c_0 = 207.5$ m/s and $EI/T = 6.39\times10^{-8}$ Nm^2. Once the dispersion is known, the effect on measured signals can be removed using appropriate correction algorithms [112, 113], which we now discuss in detail.

To incorporate dispersion into our theoretical formulation, we need to express the undulator fields as a sum over spatial frequencies using a Fourier transform, $B(z) = \int_{-\infty}^{\infty}\tilde{B}(k)e^{ikz}dz$, where d'Alemberts formula is applied separately to each frequency. After integrating over z', we find

$$u_{\delta,disp}(t) = \frac{I\delta t}{2\lambda}\int_{-\infty}^{\infty}\frac{-i}{\omega}\tilde{B}(k)\left(e^{ic_wkt} - \cancel{e^{-ic_wkt}}\right)dk \tag{3.28}$$

using the fact that fields only exist for $z > 0$ to neglect summing over waves propagating to the right. Similar to before, we model an arbitrary pulse duration of $\Delta t \leq t$ as an integral over $u_{\delta,disp}$.

$$\begin{aligned} u_{\Delta,disp}(t) &= \frac{I}{2\lambda}\int_{-\infty}^{\infty}\int_{0}^{\Delta t}\frac{i}{\omega}\tilde{B}(k)e^{-ic_wk(t-t')}dt'dk \qquad (3.29)\\ &= \int_{-\infty}^{\infty}\left(\frac{I}{2\lambda}\,\frac{e^{ic_wk\Delta t}-1}{c_w^2k^2\left(k\frac{\partial c_w}{\partial k}+c_w\right)}\tilde{B}(k)\right)e^{-i\omega t}d\omega \qquad (3.30)\\ &\equiv \int_{-\infty}^{\infty}H(k)e^{-i\omega t}d\omega \qquad (3.31)\end{aligned}$$

where we change the variable of integration from k to ω and define the transfer function $H(k)$. Similarly, we can define $H_0(k)$ in the zero-dispersion limit.

$$\begin{aligned} u_{\Delta}(t) &= \int_{-\infty}^{\infty}\left(\frac{I}{2\lambda}\,\frac{e^{ic_0k\Delta t}-1}{c_0^3k^2}\tilde{B}(k)\right)e^{-i\omega t}d\omega\\ &\equiv c_0\int_{-\infty}^{\infty}H_0(k)e^{-ic_0kt}dk \qquad (3.32)\end{aligned}$$

As a final step, we note the two practical limits of $F(k) = H_0(k)/H(k)$ for a short ($\Delta t = \delta t$) and infinitely long pulse ($\Delta t = t$).

$$\boxed{F_\delta(k) = \left(\frac{c_w(k)}{c_0}\right)\left(\frac{c_w(k)}{c_0}+\frac{k}{c_0}\frac{\partial c_w}{\partial k}\right) \quad \text{where} \quad \frac{e^{ic_0k\delta t}-1}{e^{ic_wk\delta t}-1}\approx\frac{c_0}{c_w}} \tag{3.33}$$

$$\boxed{F_\infty(k) = \left(\frac{c_w(k)}{c_0}\right)^2\left(\frac{c_w(k)}{c_0}+\frac{k}{c_0}\frac{\partial c_w}{\partial k}\right) \quad \text{where} \quad \frac{e^{ic_0kt}-1}{e^{ic_wkt}-1}\approx 1} \tag{3.34}$$

We are now able to describe the procedure for removing known dispersion from a measured signal taken with a short or long current pulse. Note that this algorithm also corrects for the finite width of a short current pulse. First, compute the Fourier transform of the measured signal.

$$H(\omega) = \frac{1}{2\pi}\int_{-\infty}^{\infty}u_{\Delta,disp}(t)e^{i\omega t}dt \tag{3.35}$$

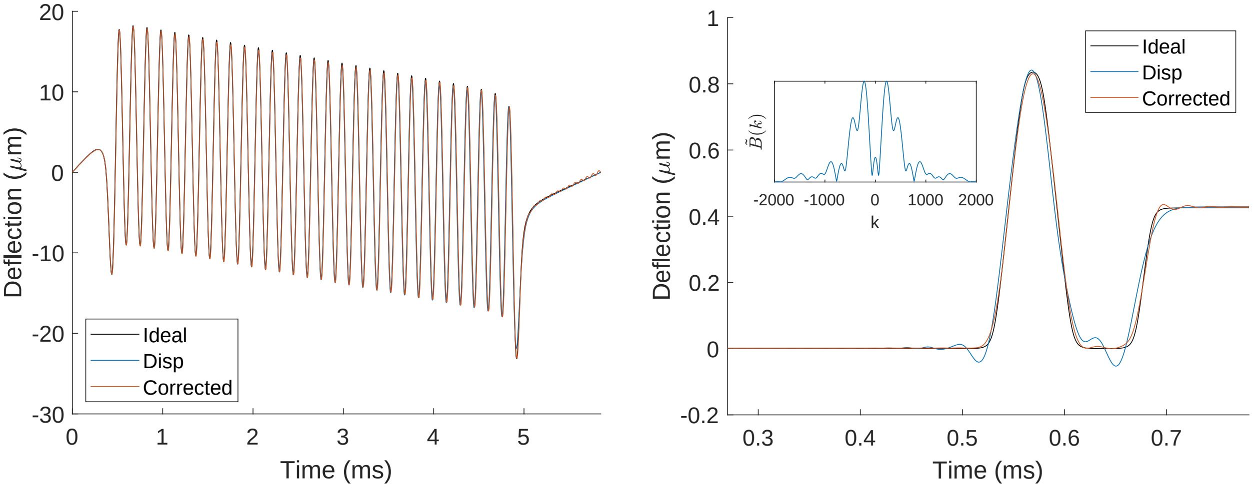

(a) (b)

Figure 3.16: Dispersion in undulator using long current pulse. Dispersion in PMQ using short pulsed.

Assuming small relative changes in wave speed, the dispersion relation of Eq. (3.27) can be inverted through an expansion as

$$k \approx \frac{\omega}{v_0}\sqrt{1 - \frac{EI}{T}\frac{\omega^2}{v_0^2}} \tag{3.36}$$

to compute $H(k)$. A small subset of the $k(\omega)$ with non-negligible amplitudes can be chosen to speed up the computation. Next, compute $H_0(k)$ by scaling with the appropriate transfer function from Eq. (3.33). Finally, the dispersion-corrected signal, $u_\Delta(t)$ can be numerically integrated for different times using Eq. (3.32). An inverse Fourier transform cannot be used because the k values are not uniformly distributed.

Figure 3.16a applies the correction algorithm to a simulated measurement of the trajectory in a Theseus undulator. The effect of dispersion is hardly noticeable except for the last field peak, suggesting that dispersion correction was not necessary for the undulator tuning. In general, distortion is largely dependent on the measurement bandwidth with the strongest effects seen at the beginning and end of the signal. By maximizing the wire tension ($>$ 80% of the nominal tensile strength), we achieved a relatively small dispersion parameter, $EI/T \approx 6.4 \times 10^{-8}$ m^2 and minimized the wire sag. On the other hand, Figure 3.16b shows a simulated measurement of a permanent magnet quadrupole triplet with large bandwidth

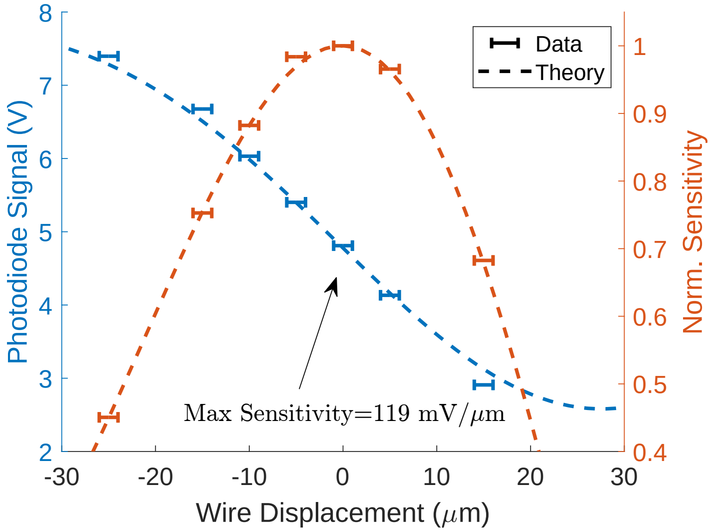

Figure 3.17: Pulsed-wire calibration. Sensitivity is defined as change in voltage over wire displacement. Normalized sensitivity is proportional to the sinusoidal amplitudes of undulator beam trajectory measurements.

such that distortion is clearly visible. The correction algorithm recovers the ideal signal with minimal error.

3.4.3 Calibration and Wire Alignment

Another deviation from ideal theory involves nonlinearity in the calibration curve of Figure 3.17 due to laser diffraction between the slit aperture and the wire. The dotted lines show numerical simulations of the diffraction in good agreement with the measurements. The nonlinear dependence is easier to observe in the measurement sensitivity, defined as the derivative of the photodiode voltage with respect to the wire displacement. Notably, for undulator measurements the normalized sensitivity is proportional to the change in trajectory amplitude as the laser photodiode pair is moved across the wire. Our setup achieves a maximum sensitivity of 119 mV/μm and though resolution was limited by the 8bit oscilloscope, a higher sensitivity improves the signal to noise ratio.

Before tuning, the wire must be aligned to the undulator magnetic axis. The tensioned wire behaves like a high energy (> 1 GeV) beam that is little affected by undulator focusing

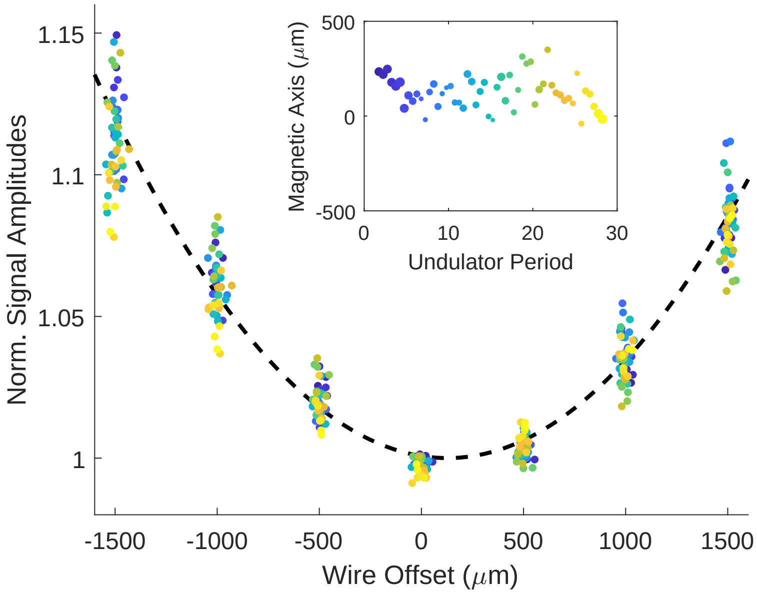

Figure 3.18: Wire alignment. The position of the magnetic axis along the undulator is inferred from the variation in field strength measured by the change in signal amplitudes. The inlay shows the symmetry axes of quadratic fits at each magnet position along the undulator.

such that the relative field strengths can be inferred from the trajectory amplitudes at different transverse wire positions. Quadratic fits of the field concavity at each magnet provide an estimate of the magnetic axis along the undulator. Figure 3.18 shows data for normalized amplitudes in $\hat{\mathbf{y}}$ as a function of wire offset in $\hat{\mathbf{x}}$, matching the theoretical concavity $1 + \alpha^2 k_u^2 x^2/2$ denoted by the black curve. The inlay plots the symmetry axes of the quadratic fits with marker size determined by the fit residuals, allowing repeatable identification of the magnetic axes to an accuracy of 100 μm.

The concavity fits are better constrained with large wire offsets, the field errors can produce strong deflections in the wire such that the sensitivity changes appreciably along the measurement (see Figure 3.17). This is corrected with a nonlinear calibration of the normalized sensitivity as a function of voltage $S(v)$ through repeated measurements where the laser is scanned across the wire as shown in Figure 3.19.

It is important to have a robust algorithm for computing signal amplitudes. To estimate peak locations in the presence of noise or strong deflections, it is better to smooth with a

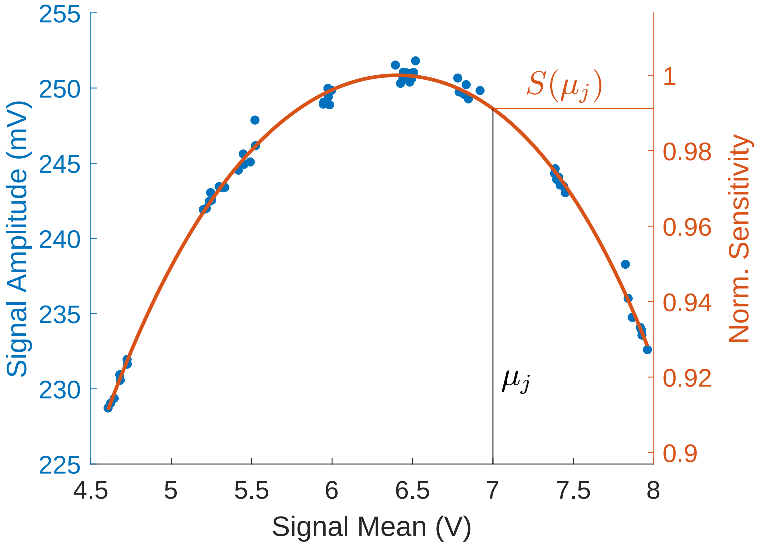

Figure 3.19: Nonlinear correction for signal amplitudes. By calibrating the normalized sensitivity as a function of voltage, individual signal amplitudes can be corrected based on their mean voltage.

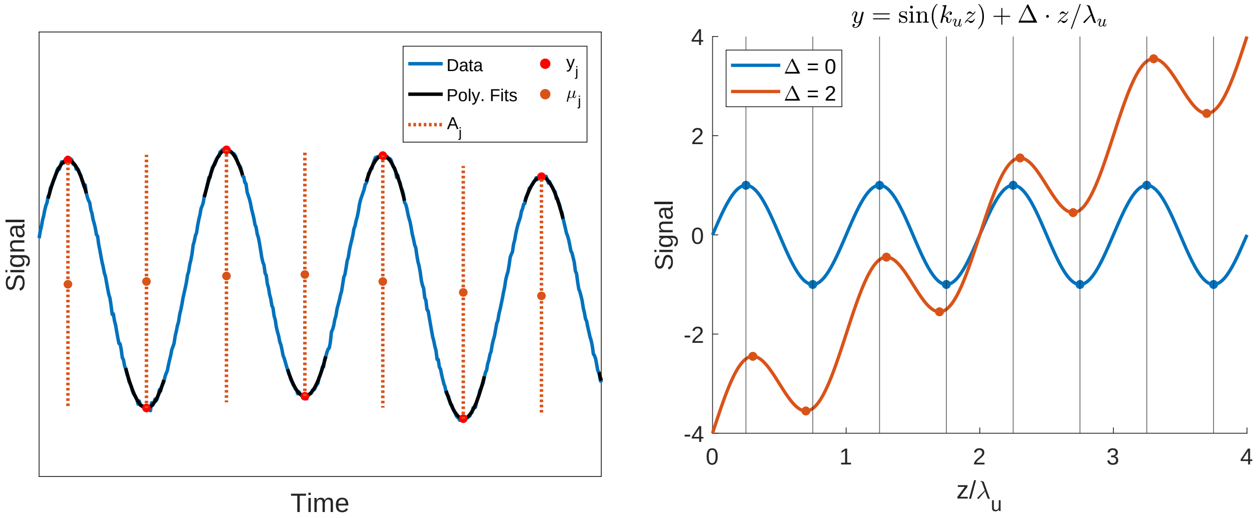

(a)

(b)

Figure 3.20: Calculation of signal amplitudes. a) Given estimate locations, peaks are evaluated with polynomial fits. Amplitudes and means are computed from neighboring peak values. b) Strong linear deflections shift peak locations and reduce measured amplitudes.

Savitzy-Golay filter and then numerically differentiate. The signal peaks are then shifted a quarter period relative to the clearly identifiable derivative peaks which can are found with built-in peak finding algorithms such as MATLAB's *findpeaks* function. Given an estimate location, the signal peaks y_j are calculated with polynomial fits over nearby data points as shown in Figure 3.20a. The signal mean voltages, $\mu_j = y_{j-1}/4 + y_j/2 + y_{j+1}/4$, and amplitudes, $A_j = y_{j-1}/2 - y_j/4 + y_{j+1}/2$, are evaluated using the values of neighboring peaks. As previously mentioned, the mean voltages are used with $S(\mu_j)$ to correct for the nonlinear calibration.

Additionally, strong linear deflections of the sinusoidal waveform shifts peak positions such that measured peak-to-peak amplitudes are reduced (Figure 3.20b). From the simple model $\sin(k_u z) + \Delta z/\lambda_u$, it can be shown the amplitudes are decreased by the factor $1 - \frac{1}{2}\left(\frac{\Delta}{2\pi}\right)^2$ where Δ is the change in voltage over a period divided by the amplitude.

Once identified, the magnetic axis is fiducialized (Figure 3.21) for accurate installation on a beamline. A laser tracker accurately measures (to within 25 μm) the distance to the retroreflector when placed in each of the fiducial cups (marked in red). This method is superior to robotic-arms for measuring large dimensions as errors do not compound with distance. Four fiducial cups are machine into each wire holder and four are glued onto the undulator. The left and right wire holders have been characterized such that the wire end positions can be determined from the fiducial measurements.

3.4.4 Higher-moment corrections

By measuring local field concavity, we can identify the magnetic axis along the undulator. However, it is also necessary to minimize errors in the integrated fields (beam trajectory) off-axis. For example, Figure 3.22 shows pulsed-wire measurements of the beam trajectory after hall-probe tuning for the Tessatron THz-FEL experiment, before and after 3D pulsed-wire tuning. Ideally, the measured trajectories would be straight and independent of the wire's transverse position, but the initial off-axis measurements clearly exhibit strong deflections at localized magnet positions. This demonstrates the need for a 3D pulsed-wire procedure

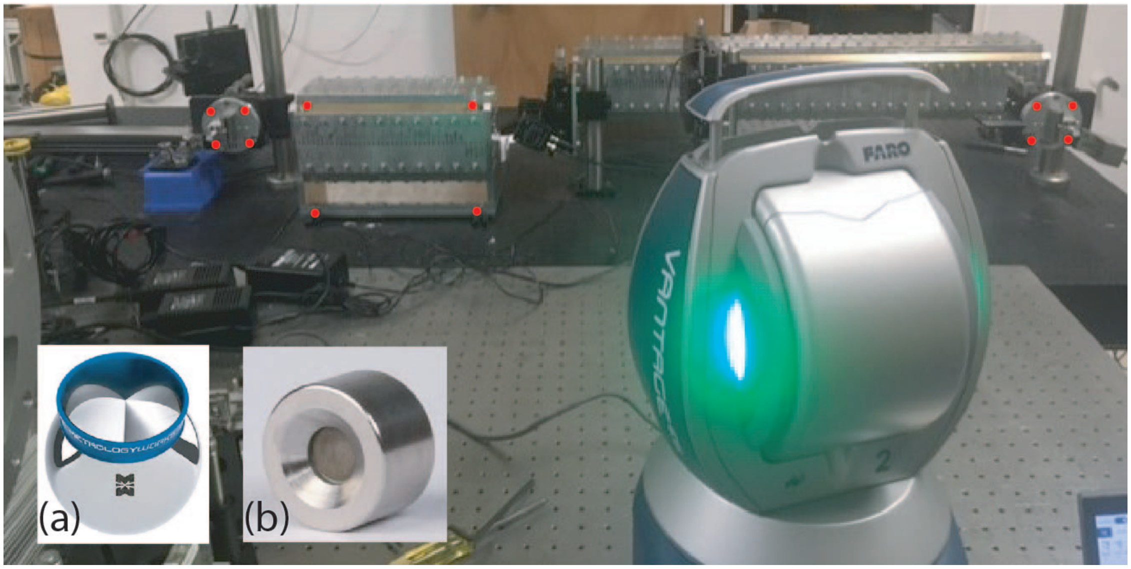

Figure 3.21: Fiducialization of the FASTGREENS prebuncher. The laser-tracker accurately measures the distance to the retroreflector (a) when placed in each of the fiducial cups (b). Locations of fiducial cups are marked in red.

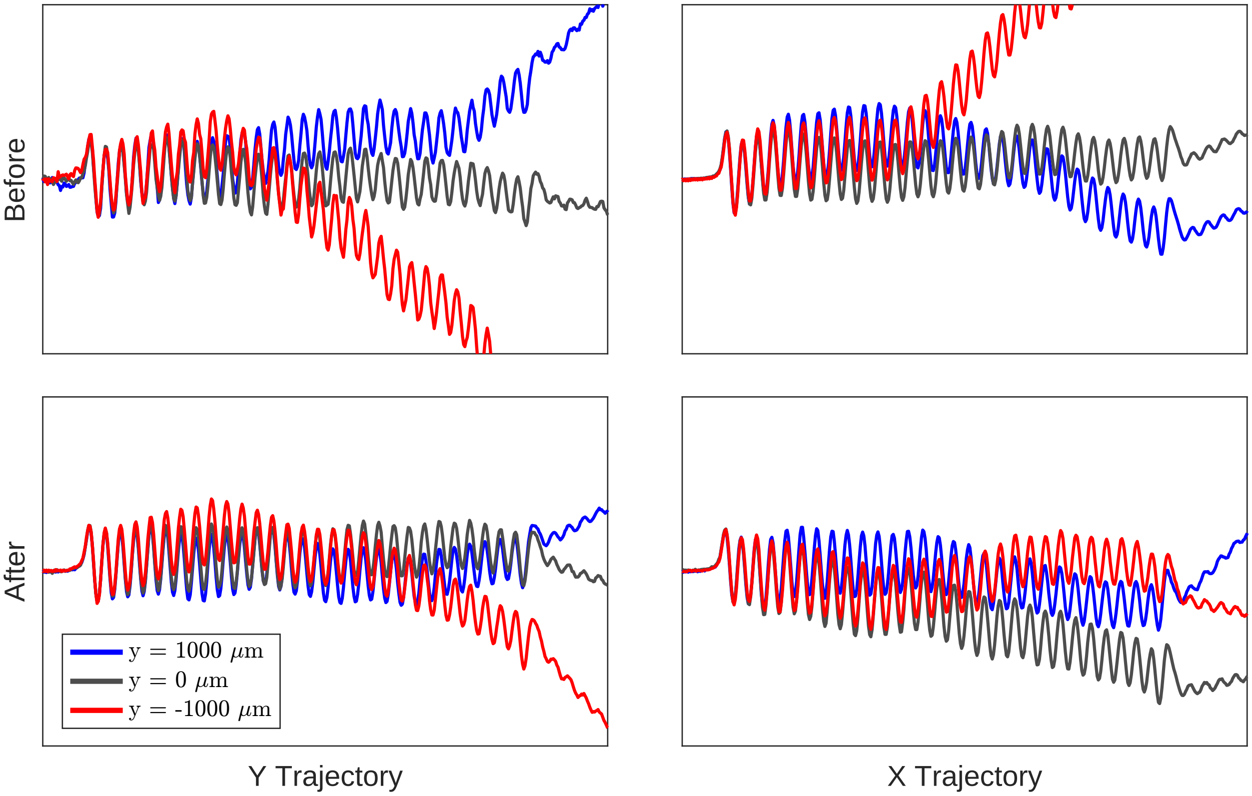

Figure 3.22: Off-axis pulsed-wire measurements before and after 3D pulsed-wire tuning.

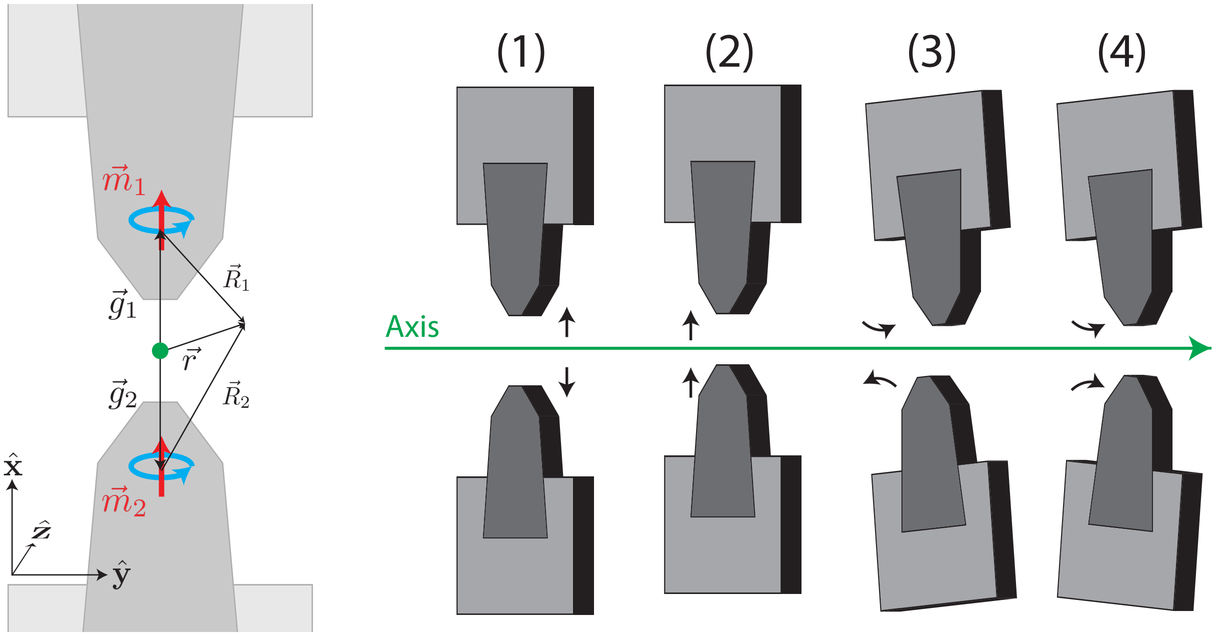

Figure 3.23: Schematic of toy dipole model. The four tuning cases represent changes in magnet gap and magnetization angle in the transverse plane.

to tune the integrated higher order field moments when low energy beams travel far off-axis. In fact, it is good to remember that in a helical trajectory the beam never sees the on-axis fields.

To describe the effect of magnet adjustments on undulator fields and integrated beam trajectories, we examine a simple empirical toy-model where a pair of undulator magnets is represented by two pure magnetic dipoles. The strength and separation of the dipoles are fit to RADIA simulations of Theseus magnets with $B_0 = 730$ mT peak field and 7.1 mm full-gap such that each magnet is best modeled by a dipole with $m = 1.59 \times 10^6$ A·mm^2 located 7.33 mm inside the magnet tip. While this model is fit to fields, we later verify that it performs sufficiently well in describing the effect of tuning on beam trajectories.

In our model, dipoles are nominally placed at $\mathbf{g} = \pm g\hat{\mathbf{x}}$ with moments $\mathbf{m} = m\hat{\mathbf{x}}$ as shown in Figure 3.23. We allow small adjustments to the position (δg in $\pm\hat{\mathbf{x}}$) and magnetization angle ($\mathbf{m} = m\cos\theta\hat{\mathbf{x}} + m\sin\theta\hat{\mathbf{y}}$) to simulate tuning of the magnet gaps and slight changes in the magnet angle, where the tuning space is spanned by four different cases.

The fields of each dipole are expressed by

$$\mathbf{B}(\mathbf{r}, \delta g, \theta) = \frac{B_0}{4}\left(\frac{3\left(\hat{\mathbf{m}}\cdot\hat{\mathbf{R}}\right)\hat{\mathbf{R}} - \hat{\mathbf{m}}}{\tilde{R}^3}\right) \tag{3.37}$$

where $B_0 = m\mu_0/\pi g^3$ and $\tilde{R} = R/g$ where tildes generally indicate normalization by the nominal half-gap g. Summing both dipole fields and Taylor expanding about the axis yields the dipole field with a higher-order skew sextupole field as expected from the general undulator expansion in Eq. (3.2).

$$\mathbf{B}(z = 0) = B_0\left(1 + \frac{6}{2}(2\tilde{x}^2 - \tilde{y}^2)\right)\hat{\mathbf{x}} - B_0 6\tilde{x}\tilde{y}\ \hat{\mathbf{y}} \tag{3.38}$$

Note that the asymmetry of the dipole model ($\alpha/\beta = 1.414$) is in fairly good agreement with the Theseus fields ($\alpha/\beta = 1.319$). The transverse velocity is given by an integral over the Lorentz force as

$$\boldsymbol{\beta}_\perp(\mathbf{r}_\perp, \delta g, \theta) = -\frac{e}{\gamma mc}\left(\hat{z}\times\int_{-\infty}^{\infty}\mathbf{B}_\perp dz\right) \tag{3.39}$$

Remembering $\mathbf{m}\cdot\hat{\mathbf{z}} = 0$, the integral over the transverse field can be evaluated in terms of $\mathbf{R}_\perp$ for each dipole as

$$\boldsymbol{\beta}_\perp(\mathbf{r}_\perp, \delta g, \theta) = -\frac{\beta_{\perp,0}}{4}\left[\hat{\mathbf{z}}\times\left(\frac{4(\hat{\mathbf{m}}\cdot\tilde{\mathbf{R}}_\perp)\tilde{\mathbf{R}}_\perp}{\tilde{R}_\perp^4} - \frac{2\hat{\mathbf{m}}}{\tilde{R}_\perp^2}\right)\right] \tag{3.40}$$

where $\beta_{\perp,0} = egB_0/\gamma mc$. To describe the net change in beam trajectory, we consider the relative change in the transverse velocity given by $\delta\boldsymbol{\beta} = \left(\boldsymbol{\beta}_\perp(\mathbf{r}_\perp, \delta g, \theta) - \boldsymbol{\beta}_\perp(\mathbf{r}_\perp, 0, 0)\right)/\beta_{\perp,0}$. Summing the contributions of each dipole for the four cases and expanding to lowest order yields

$$\begin{aligned}
\delta\boldsymbol{\beta}_1 &= 2\delta\tilde{g}\left(\hat{\mathbf{y}} + 12\left(\tilde{x}\tilde{y}\hat{\mathbf{x}} + \frac{1}{2}(\tilde{x}^2 - \tilde{y}^2)\hat{\mathbf{y}}\right)\right) && \text{dipole + sextupole}\\
\delta\boldsymbol{\beta}_2 &= 6\delta\tilde{g}\left(\tilde{y}\hat{\mathbf{x}} + \tilde{x}\hat{\mathbf{y}}\right) && \text{quadrupole}\\
\delta\boldsymbol{\beta}_3 &= \theta\left(-\hat{\mathbf{x}} + 6\left(-\frac{1}{2}(\tilde{x}^2 - \tilde{y}^2)\hat{\mathbf{x}} + \tilde{x}\tilde{y}\hat{\mathbf{y}}\right)\right) && \text{dipole + skew sextupole}\\
\delta\boldsymbol{\beta}_4 &= 2\theta\left(-\tilde{x}\hat{\mathbf{x}} + \tilde{y}\hat{\mathbf{y}}\right) && \text{skew quadrupole}
\end{aligned} \tag{3.41}$$

where $\delta\tilde{g} = \delta g/g$ and terms are grouped into different magnetic moments. The first and third cases show that altering the magnet position or angle in opposite directions can be used to

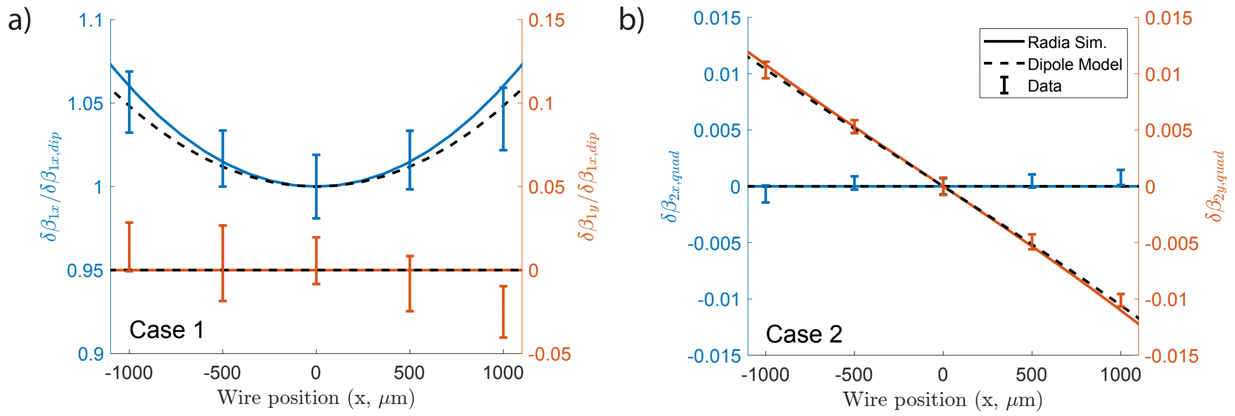

Figure 3.24: A comparison of measured and theoretical deflections due to magnet tuning as a function of transverse wire position. For case 1, opening the magnet gaps leads to a clear sextupole dependence on top of the dipole kick. In case 2, shifting the magnet gap creates a quadrupole dependence. Measurements are in agreement with RADIA simulations and the dipole model.

tune the dipole fields in $\hat{\mathbf{y}}$ and $\hat{\mathbf{x}}$. To simultaneously tune the regular and skew sextupole moments, one must utilize adjustments in the other magnet array with magnetization in $\hat{\mathbf{y}}$ found by the coordinate transformation $x \rightarrow y$ and $y \rightarrow -x$. Quadrupole fields can be tuned using the second and fourth cases where the magnet position or angle are altered similarly and only skew or regular quadrupole moments are generated to first order.

Figure 3.24 benchmarks the analytic dipole model against pulsed-wire data and an ideal RADIA simulation using numerical integration of Theseus magnet fields. The first two cases are considered as it is easier to accurately adjust the magnet gaps with fine adjustments. Both components of $\delta\boldsymbol{\beta}_1(\tilde{y}=0)$ and $\delta\boldsymbol{\beta}_1(\tilde{y}=0)$ are plotted as a function of wire position along the x-axis. The magnet gaps are tuned by $\delta g = 200$ μm which corresponds to a quarter-turn of the 8-32 tuning screws with 784 μm/rev pitch.

Pulsed-wire measurements of the beam trajectory were taken in both transverse dimensions at each wire position before and after the tuning a magnet pair. For each offset, reference measurements are subtracted and the residual signals are period-averaged to eliminate any remaining periodicity. Linear fits are applied to the waveform before and after the tuned magnet pair such that the change in slope is proportional to the change in velocity. The proportionality constant includes the calibrated conversions from time and voltage to position, i.e., the voltage amplitude of an individual measurement can be related to the nominal beam trajectory amplitude in the undulator. The data is plotted with error bars showing the standard deviation of 30 measurements.

Figure 3.24a shows the net change in normalized velocity of the first case normalized by the dipole field. The measurement variation is relatively large as the concavity of the sextupole moment occurs on top of a large dipole field. This produces a strong deflection in the wire requiring corrections to the non-uniform sensitivity along the measurement and reducing the voltage resolution of the 8bit scope measurement. The data shows a clear sextupole dependence in $\hat{\mathbf{x}}$ with minimal effect in $\hat{\mathbf{y}}$. In the figure we also show the results of RADIA simulations where the same magnet adjustment are performed on the Halbach array. The agreement between the dipole model, the simulations and the data is remarkable and can be used to guide the undulator tuning with quick convergence. In Figure 3.24b we show the quadrupole moments resulting from shifting the magnet offsets in the same direction (i.e. second case from Figure 3.23). In this case, the measurements, which match closely the prediction from our simple two-dipole model and the RADIA simulations, are more accurate since there is no undulator dipole component and the variance is smaller.

Guided by Eq. (3.41), appropriate magnet pairs can be adjusted to tune the deflections seen in Figure 3.22. In practice, the corrections are limited by the tuning range and precision when adjusting magnet angles. The phase error between the beam and radiation was only 1% after Hall probe tuning such that the main limitation for high efficiency is charge transmission through the undulator. The red and blue trajectories in Figure 3.22 measure the field integrals along the wire axis and do not exactly represent the fields seen by the helical trajectory of a low energy beam. Instead, we approximate the true beam trajectory as the average of pulsed-wire measurements at wire offsets of ± 1000 μm in $\hat{\mathbf{x}}$ and $\hat{\mathbf{y}}$. The final averaged trajectories are tuned flat to a centroid deviation of less than 300 μm from the axis, sufficiently smaller than the mm-scale wiggling amplitude and the 2 mm waveguide inner radius employed in the experiments.

CHAPTER 4

Tessatron Experiments

4.1 Introduction

The Tessatron experiments are demonstrations of a compact, single-pass THz waveguide FEL on the Pegasus beamline at UCLA. Zero-slippage operation enables compression of the electron beam to increase the current density and provide seeding at the long wavelengths. The helical Theseus undulator, designed to optimize FEL coupling, allows strong field tapering to extract a significant fraction of the electron beam energy.

We begin the chapter by introducing the layout and operation of the Pegasus beamline for the first Tessatron experiment, including an overview of the software controls. Next, we present the experimental results demonstrating zero-slippage operation and large (10%) extraction efficiency. The second experiment seeks to improve the spectral range and frequency tunability of the FEL by detuning from the zero-slippage resonance. We discuss the major beamline upgrades including novel photocathodes that enabled lossy laser shaping, a compact permanent-magnet chicane for compression, and a solenoid for beam matching into the undulator. After sharing the experimental results, we finish by considering future implementations including resonance with higher order waveguide modes and the use of an optical cavity.

4.2 Pegasus Beamline

The Pegasus beamline is a university-sized ($\sim$ 10 m) accelerator beamline at UCLA capable of producing electron beam energies up to 8 MeV with bunch charges ranging from hundreds of femtocoulombs to hundreds of picocoulombs. It supports a variety of research including ultrafast electron diffraction, microscopy, cathode characterization, and the study of dielectric and THz acceleration schemes to name a few [114, 115, 116, 117, 118].

4.2.1 Layout

The electron beamline sits in a concrete-shielded bunker with interlocked door where the creation of an electron beam requires simultaneous laser and radio-frequency (RF) power for the photo-emission and acceleration of electrons in the gun. These two systems are synchronized to a master low-level signal (2.856 GHz) produced from an analog or digital RF board.

The drive laser (Titanium-Sapphire system from Amplitude) can produce 23 mJ at 800 nm and consists of a laser oscillator and regenerative amplifier. The oscillator is mode-locked to a 79.33 MHz down-conversion of the master signal and the power buildup/release from the regenerative amplifier is controlled with pockel cells, which provide a trigger for each shot. The laser pulse is split by a polarized beamsplitter into two paths known as the infrared (IR) and ultraviolet (UV) lines. The relative laser strength in each path is adjusted with a half-wave plate before the beamsplitter. The IR path is propagated to the bunker and will be used for the electro-optic sampling measurement described in the second Tessatron experiment. On the UV path, a frequency-doubling crystal first creates 400 nm light, then the two wavelengths are combined in a frequency-summing crystals to generate 266 nm UV light. The temporal overlap is fine tuned with a delay stage and the conversion efficiency can be attenuated with a remote-controlled polarizer, allowing the operator to control the UV pulse energy which determines the emitted electron beam charge. Additionally, the laser pulse can be shaped into distinct beamlets using a set of birefringent α-BBO crystals capable of generating 0.5, 1, 2, 4, 8, and 16 picosecond time delays. The light is transported to the bunker with UV-mirrors that pass the residual 400 nm and 800 nm wavelengths into beam blocks. Finally, the remaining UV is clipped with an iris aperture and imaged onto the cathode in the gun, allowing control of the transverse beam size. A virtual cathode diagnostic for

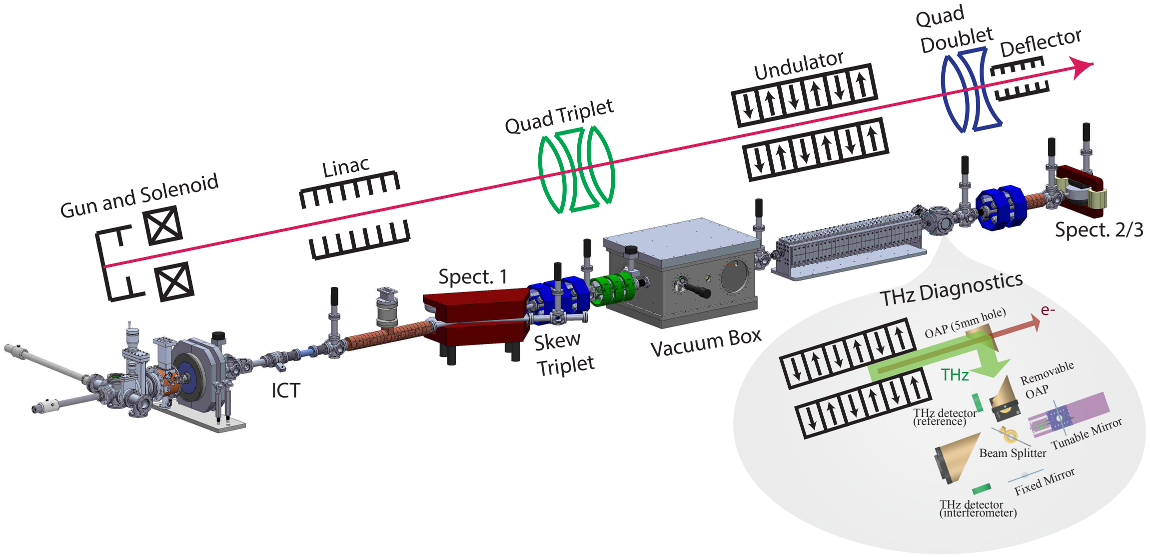

Figure 4.1: Schematic of Pegasus beamline and THz diagnostics for Tessatron.

the cathode laser spotsize is achieved by placing a beamsplitter before the vacuum window such that a small percentage ($\sim 1\%$) of the laser energy is reflected onto a screen with the same path length as to the cathode, and viewed with a CCD camera.

The master low-level signal is also send to the klystron room after passing through a control room phase shifter that the operator uses to adjust RF timing relative to the laser. The signal is amplified to a kilowatt before seeding the modulator and klystron capable of producing 10 MW of pulsed RF power. The RF is propagated to the bunker in a waveguide filled with high dielectric sulphur-hexafluoride gas to increase the electric field break-down limit. A waveguide splitter sends power to the gun as well as the booster linac cavity where a relative phase difference is adjusted with a stepper-motor controlled phase-shifter. Alternately, the linac power can be redirected into an absorbing load to effectively turn off the linac cavity.

The main beamline and THz diagnostics for the first Tessatron experiment are depicted in Figure 4.1. Bunch charges up to 200 pC are generated from copper photocathodes and accelerated to a total energy of 3.6 MeV in the 1.6-cell S-band RF gun. The bunch charge is measured non-destructively by a turbo integrating current transformer (ICT) and a solenoid focuses the beam into an 11-cell S-band high-shunt-impedance linac with peak gradient of 20 MV/m, capable of accelerating the beam to 8 MeV. The energy distribution can be measured on spectrometer 1 (radius of curvature of 0.67 m and bending angle of 45 deg). The beam is focused transversely using a quadrupole triplet located just before a 29-inch long vacuum box. The beam position and angle into the undulator is adjusted with two steering magnets to optimize transmission and THz generation. The spent beam passes through a 5 mm diameter hole in an off-axis parabolic mirror (OAP) which reflects the generated radiation out of the beamline to the THz diagnostics. A quadrupole doublet focuses the beam into an transverse deflector (9.6 GHz with 500 kV maximum deflecting voltage), allowing longitudinal phase space measurements on spectrometer 2 (radius of curvature of 0.93 m, bending angle of 45deg). The energy acceptance is limited to ±9% due to a 12 mm aperture in the vacuum pipe. The expected deceleration ($> 25\%$) requires stitching of several spectrometer measurements such that a third low-resolution spectrometer using a short rectangular dipole was installed to independently confirm the average beam loss and validate the stitching approach.

A short 4.7 mm diameter extension pipe transports the THz from the end of the undulator to the focal point of a gold-coated OAP, which reflects and collimates the radiation at 90° out of the beamline through a z-cut quartz window to a diagnostics table. The total energy in the radiation pulse can measured by placing a removable 50 mm diameter OAP mirror immediately outside the vacuum window to focus the radiation onto a 9 mm diameter pyroelectric Gentec terahertz detector.

When the last OAP is removed, the collimated terahertz radiation propagates to a Michelson interferometer where a lossy (30%) beamsplitter separates the radiation along two paths. After reflecting off mirrors, the beams recombine and are focused onto a pyroelectric detector that can record the field autocorrelation of the radiation pulse by varying the path length difference in the interferometer.

It was expected that roughly 13% and 10% energy losses would be incurred from the waveguide out-coupling and THz window, respectively. Additionally, the strong diffraction caused significant clipping on in-vacuum apertures. To better characterize these losses, a

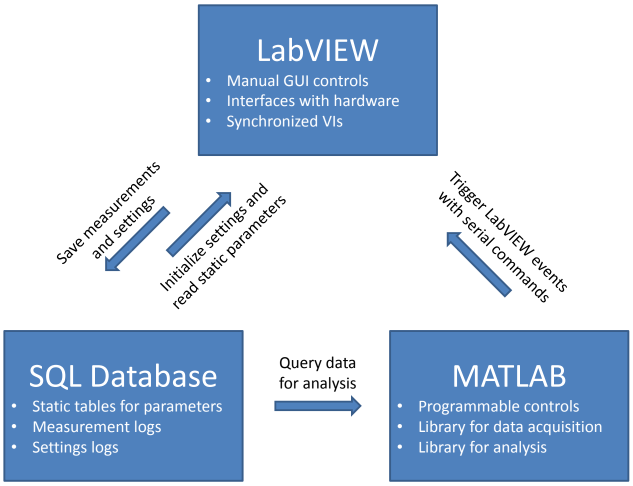

Figure 4.2: Structure and organization of Pegasus beamline controls software.

10 mW continuous-wave 140-GHz radiation source was placed at the entrance of the undulator and it was found that only 27% of the radiation at the undulator exit was successfully collected at the detector. In fact, the signal on the interferometer is less than 10% of the reference signal due to the large absorption of the beamsplitter and additional diffraction losses caused by the relatively small-aperture, 40 mm diameter terahertz window.

4.2.2 Software and Controls

The organization and structure of the beamline software and controls are outlined in Figure 4.2. LabVIEW VIs provide the main graphical user interfaces for controlling the beamline settings (magnet currents, motor positions, shutters, screens) which are logged in an SQL database along with hardware measurements (charge, vacuum levels, camera images, RF amplitude/phase). The dynamic tables are synchronized (Appendix A) on the same primary key that uniquely identifies each electron beam shot on the beamline. Additionally, static tables are used to store various parameters (calibrations, camera and motor settings, hardware IP and COM addresses) which can be read into LabVIEW, along with previous magnet settings.

While the VIs interface well with hardware, coding even simple algorithms or logic into the visual-programming language is tedious. For this reason, a Matlab interface was developed that provides programmatic control of the LabVIEW VIs. The communication utilizes a network TCP/IP connection where serial commands of the form $key = value$ trigger events identical to a manual input. Dedicated scripts take care of the network connection and error handling, such that new users can quickly develop their own scripts for data acquisition. In additional to speed and flexibility, this approach fosters collaboration between users as the centrally located scripts can be viewed and copied by others. More complicated features include outlier detection, automatic image gain adjustment, and real-time plotting can be used to ensure a sufficient amount of quality data is acquired. A separate library of Matlab functions also provides common database queries and analysis routines to simplify the initial data analysis.

4.3 Tessatron

The goal of the first Tessatron experiment was to demonstrate record extraction efficiency at THz wavelengths by utilizing two different concepts in FEL physics, namely zero-slippage and strong tapering of the undulator to enhance stimulated superradiant emission from the injected electron bunch. To achieve strong decelerating gradients in the absence of an external laser, seeding must be provided by a microbunched, high current beam where the 1D efficiency is proportional to the product of the current and bunching factor (see Eq. (1.54)). At long wavelengths, this can be achieved by compressing the beam to a bunch length smaller than a radiation wavelength. The linac cavity can be operated off-crest to imprint a negative energy chirp on the beam, leading to compression in the drift between the linac and undulator.

Figure 4.3a shows GPT simulations of the beam compression at the undulator entrance as a function of linac phase. Longitudinal Coulomb repulsion decreases at relativistic energies due to length contraction, implying the strongest space charge effects occur in the gun before the electrons have been accelerated to relativistic speeds. The inlay shows that higher bunch

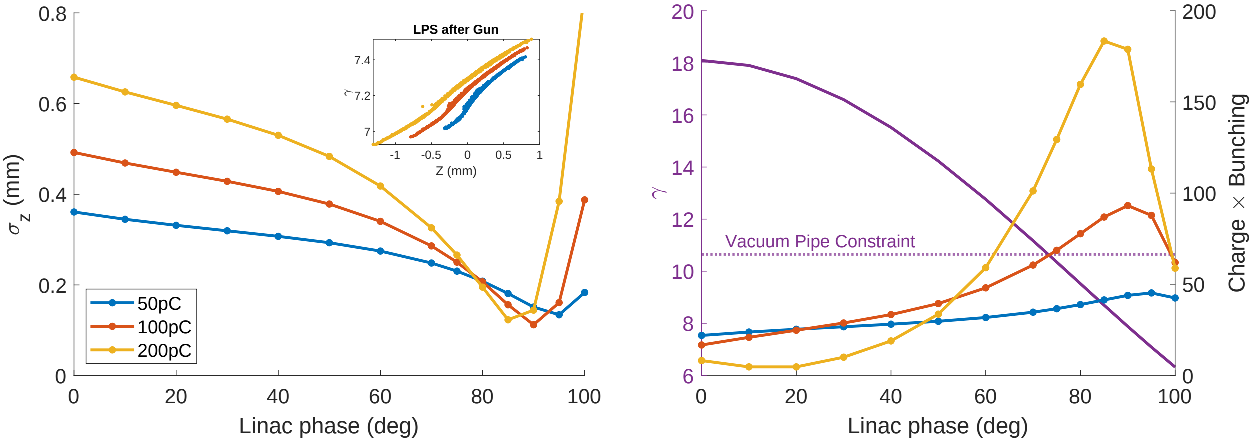

(a)

(b)

Figure 4.3: Beam compression and FEL seeding as a function of linac phase and beam charge. a) Full compression requires a large, negative energy chirp provided by linac operation far off-crest. b) Large seeding occurs for high beam charge near full compression, but the radius of the undulator vacuum pipe restricts zero-slippage operation to $\gamma > 10.65$.

charges indeed lead to longer, positively-chirped beams at the exit of the gun. For linac phases below 70°, limited compression is applied in the drift space and the bunch charge plays a significant role on the bunch length at the undulator. At phases above 70°, however, it is the higher charge beams that first reach full compression. This is because the position of maximal compression is determined by energy chirp alone, and though the high charge beams are initially longer, they have smaller energy chirp after then gun such that the linac can imprint a larger negative chirp for compression.

Figure 4.3b plots the beam energy versus linac phase as well as the scaled 1D efficiency (charge times bunching) where the bunching factor is computed at the γ-dependent frequency of the zero-slippage condition. For low compression, increased charge reduces bunching such that the 1D efficiency suffers. On the other hand, at full compression the bunching factor is nearly independent of charge and the 1D efficiency increases proportional to beam charge. Zero-slippage resonance at a lower beam energy requires a larger waveguide aperture such that the custom-made vacuum pipe from MDC (outer diameter of 5.56 mm and inner diameter of 4.55 mm) places a lower limit on the beam energy.

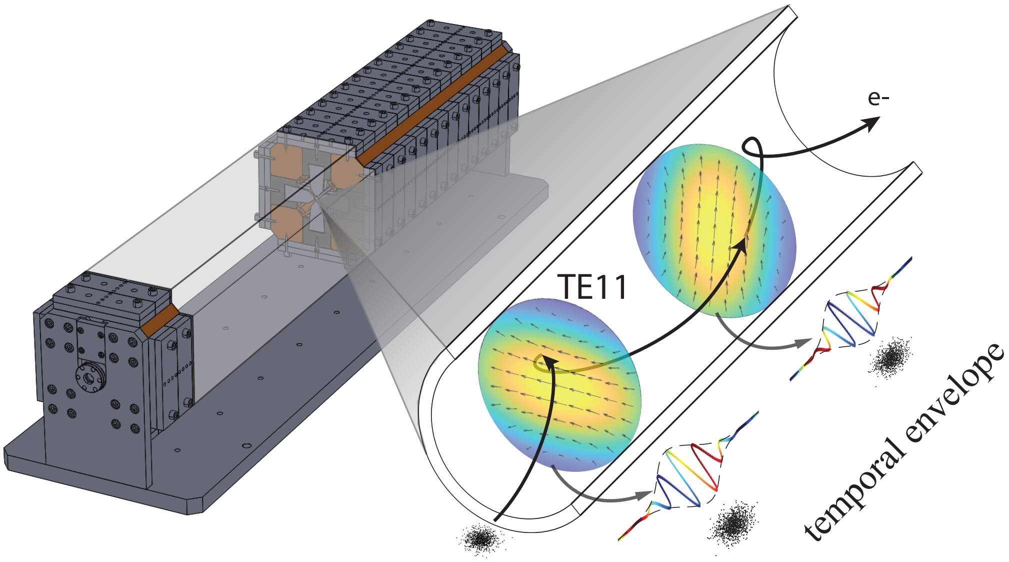

Figure 4.4: A cartoon of the zero-slippage resonance between the electron beam and the TE11 waveguide mode in the undulator. The temporal envelope of the radiation remains aligned to the electrons as the superluminal phase fronts move past.

In fact, it was decided to use the vacuum pipe itself as the waveguide to allow operation at the highest efficiency. Ohmic losses are incurred from the non-optimal conduction in the stainless steel vacuum pipe, but the choice also greatly simplifies the beam-waveguide alignment along the undulator. A schematic of the FEL interaction is shown in Figure 4.4. For a peak undulator field of $B_0 = 730$ mT, resonance with the fundamental TE_{11} circular waveguide mode where $k_\perp = 1.8412/R$ occurs at a frequency of 165 GHz for a beam energy of $\gamma = 10.65$, where a 5% off-axis correction to K is included due to the large wiggling amplitude of the electron beam trajectory (Figure 3.5).

The beam transport is shown in Figure 4.5a. After exiting the gun, the diverging beam is focused with a solenoid to a waist in the linac cavity and then focused at the undulator entrance with a quadrupole triplet. A larger beam size at the quadrupoles increases their focusing strength but can introduce non-linear off-axis field errors. The real limitation is the 1.15 m drift between the quadrupoles and undulator entrance due to beamline space

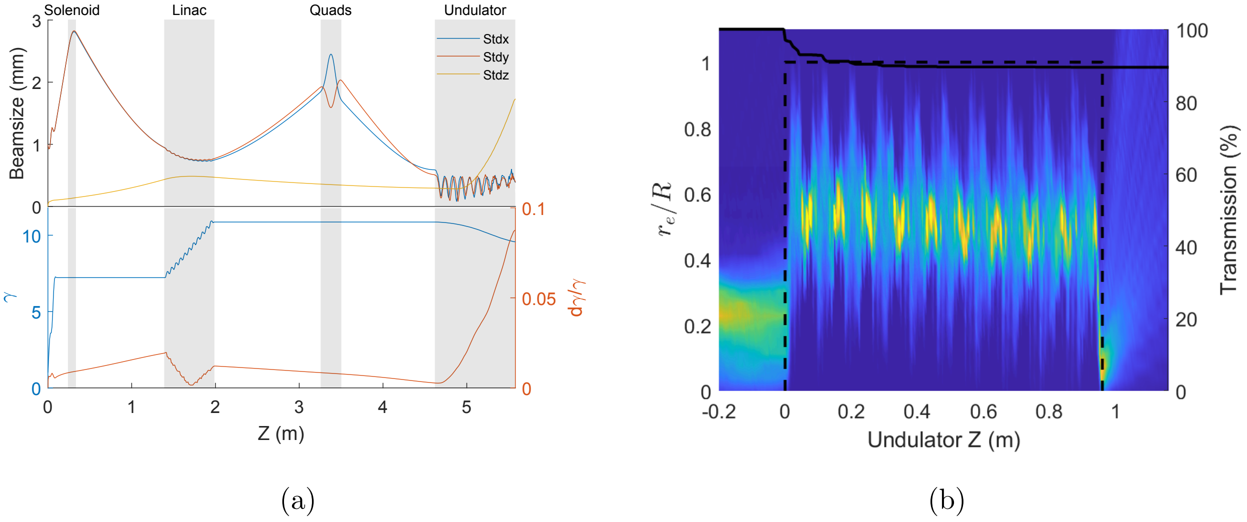

Figure 4.5: Simulated Beam Transport. a) Beam sizes, energy, and energy spread along the Pegasus beamline. b) Charge transmission and radial electron position along the undulator.

constraints which limits the minimum focused spotsize to 600 μm, much larger than the ideal matched spotsize of 150 μm. The resulting betatron oscillations (with $\sqrt{2}\gamma\lambda_u/K = 21$ cm period) are clearly seen in the undulator.

Operating the linac far off-crest leads to increased energy spread that is generally detrimental to FEL interactions. However, during the drift compression, space charge forces act to compensate the strong energy chirp, resulting in a relatively low energy spread at the undulator. Additionally, the broad gain curve at zero-slippage can allow successful trapping of electrons even in the presence of relatively large energy spread.

A significant challenge in this experiment was achieving high charge transmission through the undulator. Figure 4.5b shows the simulated transmission and radial beam distribution relative to the vacuum pipe which is shown with dotted lines. In this ideal simulation, already 10% of the charge is lost due to the unmatched spotsize at the undulator entrance and further losses are expected due to trajectory tuning errors or misalignment of the vacuum pipe.

The effect of tapering is evident in maintaining a constant average trajectory radius ($\propto K/\gamma$) as the beam decelerates. To obtain an initial estimate for the undulator tapering

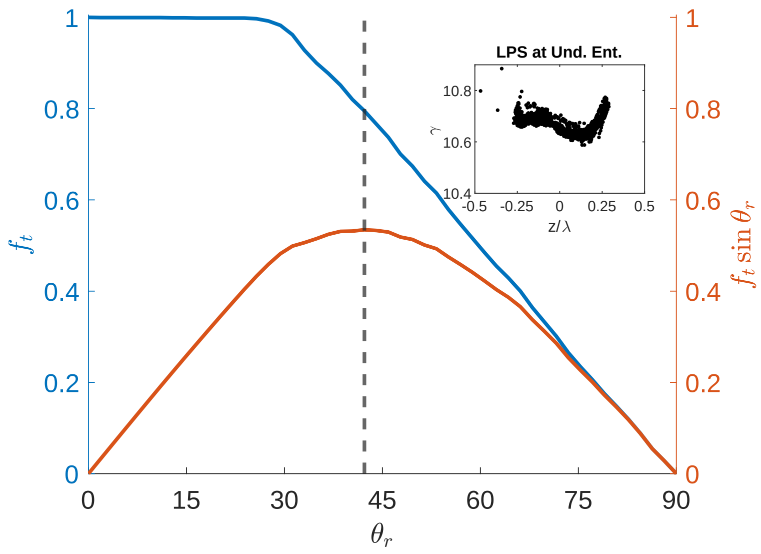

Figure 4.6: Optimization of $f_t \sin\theta_r$ for the simulated longitudinal phase space at the undulator entrance.

we return to 1D FEL theory where it was shown by Eq. (2.42) that for a waveguide FEL, the beam area is replaced with the effective mode area along with a mode sampling factor. To compute the efficiency at zero-slippage, we also need to include the effects of power attenuation and dispersion on the evolution of the field amplitude, dE/dz. Attenuation can be included with the scale factor $e^{-\beta_{wg} z}$ where β_{wg} is defined by Eq. (1.68). Additionally, Appendix B shows that the amplitude of a gaussian waveform is reduced by $(1 + \beta_2^2 c^4 z^2/\sigma_z^4)^{-1/4}$ due to the group velocity dispersion, $\beta_2 = \frac{\partial^2 k}{\partial \omega^2}$. In the absence of a seed field, the efficiency estimate is given by a numeric integral including these scale factors as

$$\eta(z) = \frac{I}{I_A}\frac{K_0^2}{\gamma_{r0}^3}\left(f_t \sin\theta_r\right)^2 \frac{2\pi}{\mathcal{A}_{11}}\langle\Theta_{11}\rangle^2 \int_0^z \int_0^{z'} \left(1 + \frac{\beta_2^2 c^4 z''^2}{\lambda^4}\right)^{-1/4} e^{-\beta_{wg} z''} dz'' dz' \tag{4.1}$$

where $\langle\Theta_{11}\rangle = 0.71$ for the fundamental TE$_{11}$ mode at zero-slippage, $\beta_{wg} = 0.39$ for the stainless steel vacuum pipe, and we assume $\sigma_z \approx \lambda$ for a compressed beam. The product $f_t \sin\theta_r$ can be optimized for the simulated phase space at the undulator entrance as shown in Figure 4.6 where the optimal resonant phase is $\theta_r = 42°$ where $f_t = 0.8$. Using these values, the estimate efficiency in the 1-meter undulator is 27%! This demonstrates the power of zero-slippage operation as the compressed 200 pC beam is able to continuously interact with

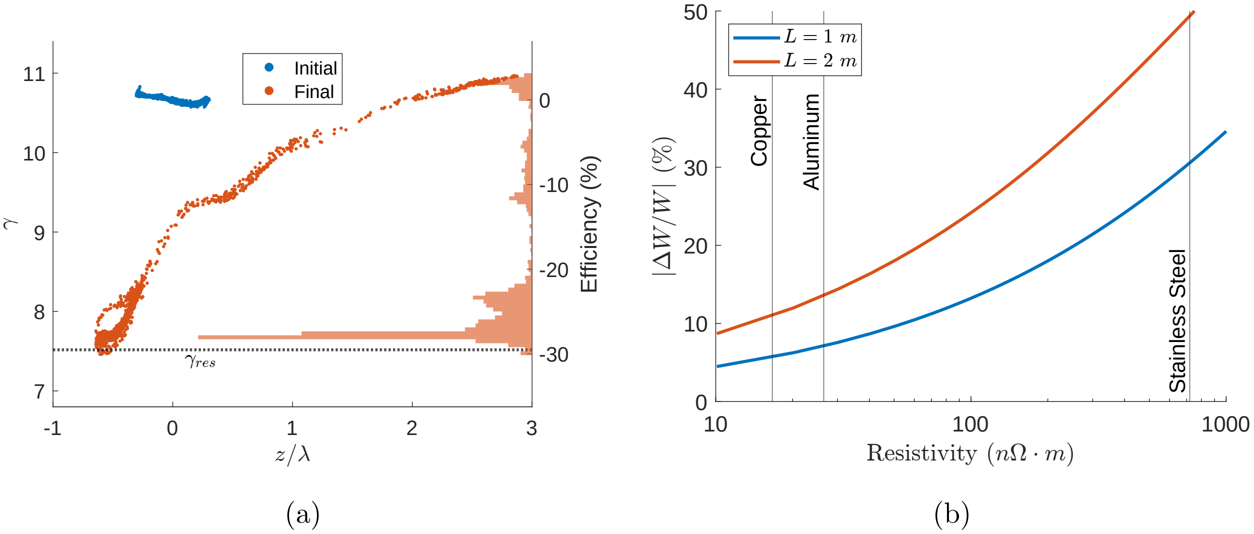

Figure 4.7: a) Initial and final phase spaces of a GPTFEL simulation of the undulator. While some particles detrap, the majority are decelerated $> 20\%$. b) Change in THz energy and beam deceleration due to waveguide resistivity in the 1-meter vacuum pipe.

the radiation along the entire undulator.

The undulator tapering can be obtained from a quadratic fit calculated from the efficiency $\eta(z)$ as

$$K(z) = \sqrt{\left(1 + K_0^2\right)\left(1 - \eta(z)/f_t\right)^2 - 1} \approx K_0(1 - t_1 z - t_2 z^2) \tag{4.2}$$

where $t_1 = 0.08$ and $t_2 = 0.44$. Figure 4.7a shows the initial and final longitudinal phase space for a GPTFEL simulation using the estimate tapering with waveguide attenuation. The resonant energy at the end of the undulator is shown by the black dotted line. While some of the electron beam has become detrapped, a majority experienced significant deceleration resulting in an overall efficiency of 22%.

The finite resistivity leads to a fraction of the THz energy being absorbed in the vacuum pipe. If we assume uniform emission along the undulator, the reduction in THz energy due to attenuation can be estimated by

$$\left|\frac{\Delta W}{W}\right| = \frac{P_0 L - \int_0^L P_0 e^{-2\beta_{wg} z} dz}{P_0 L} = 1 - \frac{1}{2\beta_{wg} L}\left(1 - e^{-2\beta_{wg} L}\right) \tag{4.3}$$

as shown in Figure 4.7b for two undulator lengths. In our 1-meter stainless steel vacuum pipe, the loss is approximately $|\Delta W/W| \approx 30\%$. Clearly, this can be reduced by changing

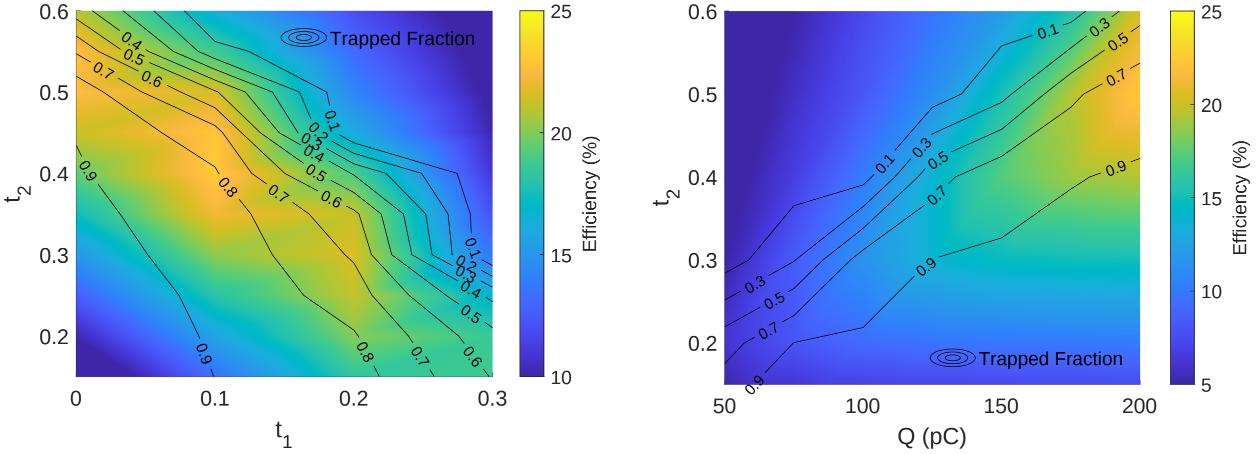

(a)

(b)

Figure 4.8: Simulations showing the efficiency and trapped fraction at the end of the undulator. a) Linear and quadratic tapering varied for a 200 pC beam. b) Quadratic tapering ($t_1 = 0$) with different beam charge.

the waveguide material, but an additional option would be to use grooved waveguides to reduce the attenuation losses further [119].

In Figure 4.8a, simulated efficiencies and trapping fractions at the end of the undulator are shown for various field taperings. The highest efficiencies occur for trapping fractions around 0.8, which agrees with Figure 4.6. Additionally, the tapering region with high efficiency is quite large and suggests the interaction is robust to small changes in the tapering profile. This is to be expected from the deep ponderomotive potential and broadened gain curve at zero-slippage that maintains trapping of electrons slightly detuned from resonance.

The amount of charge transmission through the the undulator is a pivotal parameter for choosing a design tapering. For example, with only 50% transmission, the theoretical tapering reduces to $t_1 = 0.04$ and $t_2 = 0.24$ with a 15% efficiency. Figure 4.8b plots efficiency and trapping fraction against a purely quadratic tapering and bunch charge. This is simulated by transporting a full 200 pC to the undulator, then reducing the charge at the entrance to approximate realistic charge loss. It was decided to conservatively tune the undulator with $t_1 = 0$ and $t_2 = 0.35$ after a delay of 50 mm to compromise between the possibilities of high or low charge transmission. For low transmission, the initial slow tapering would be able

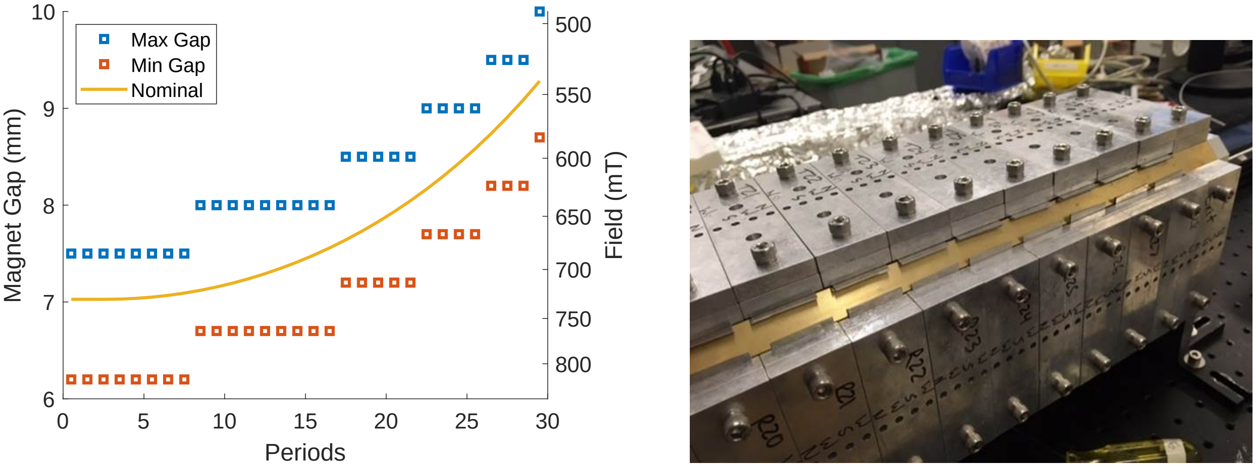

(a) (b)

Figure 4.9: Undulator Field Tapering. a) Shims with 250 μm thickness are added under the tuning places of each period to keep the nominal field centered in the magnet tuning range. b) A picture of the shimmed undulator on the tuning bench.

to maintain a large trapping fraction in the first half of the undulator. On the other hand, with high transmission the strong tapering in the second half of the undulator could still decelerate the beam a significant amount.

The nominal tapering is shown by Figure 4.9a in terms of field strength and full magnet gap along the undulator where 250 μm shims were added under the tuning plates of each period to center the nominal field in the magnet tuning range. The relationship between gap and field was simulated in Radia and confirmed against Hall probe measurements. Figure 4.9b shows a picture of the shimmed undulator.

4.3.1 Experimental Results

The FEL interaction was established by recording the energy profiles of the beam from the high-resolution magnetic spectrometer as well as the terahertz radiation energy measured by the reference pyrodetector as a function of the input beam charge. In the contour plot in Figure 4.10a, the energy spectra are normalized to better highlight the evolution of the energy distribution as the terahertz FEL interaction grows in strength. For charges above 50pC, in

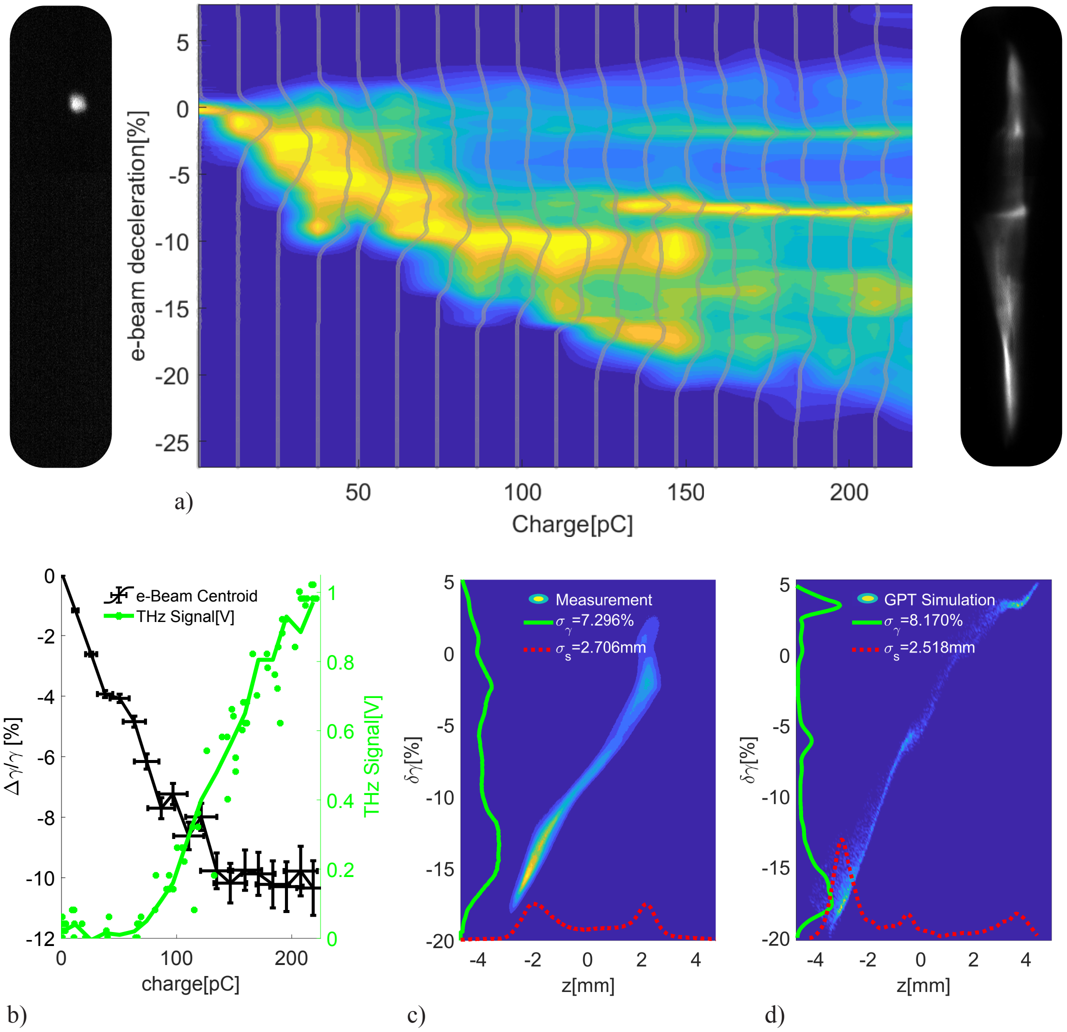

Figure 4.10: Electron beam and THz energy measurements. a) High-resolution electron-beam spectra as a function of the charge injected into the undulator. Two reference raw spectrometer images for the lowest (left) and highest (right) charge are also shown. b) Relative beam energy centroid variation and terahertz pulse energy from the reference pyrodetector corresponding to a. The horizontal error bars correspond to the width of the charge bins, which is chosen to be equal to the r.m.s. charge fluctuations. The vertical errors on the centroid data represent the r.m.s. of the beam centroid distribution calculated over ≥ 10 images. Measured (c) and simulated (d) longitudinal phase spaces for a 150-pC injected beam charge. For this comparison, the longitudinal phase space at the exit of the undulator is propagated up to the deflector plane located 6.5 m from the cathode.

conjunction with the appearance of a clear signal on the pyrodetector (Figure 4.10b), the electron-beam spectrum broadens and redshifts to a lower mean beam energy. The spectra also develop large and deep modulations that are characteristic signatures of the FEL longitudinal phase space dynamics occurring in the tapered undulator [30]. At the highest injected beam charge (220pC), the average beam energy decreases by 10%, with some particles losing more than 20% of their initial kinetic energy. Taking into account the terahertz pyroelectric detector calibration and the losses in the terahertz transport line, the maximum signal recorded on the detector yields an estimated terahertz energy at the undulator exit of 50 μJ, which is in good agreement with the average energy loss by the electron beam, considering the stainless-steel waveguide losses and that only 40% of the injected charge is transmitted through the undulator. We note that the charge values reported in the figures refer to ICT measurements before the undulator. The transmission through the undulator and 5 mm hole in the OAP was strongly energy-dependent, monotinically decreasing from full transmission at high injection energies to below 40% for lower energies. As mentioned, this is due to the inability to focus the beam to the matched spotsize and the significant trajectory radius (1.1 mm at $\gamma = 10.6$) inside the undulator which reduces the clearance and makes it difficult to precisely tune the undulator field quality using conventional hall probe or pulsed wire methods which assume small deviations from the beam axis.

The terahertz signal and the associated electron spectra are well correlated with the injected charge through the undulator (Figure 4.10b), with output fluctuations of less than 10% for a given input charge, mostly attributable to energy and pointing fluctuations. The overall stability is remarkable for a single-pass FEL in the absence of an external radiation seed signal, and is explained by the initial bunching from the compressed electron beam, which effectively works as a FEL seeding signal.

The X-band deflector located after the undulator can be used to streak the beam vertically and visualize the longitudinal phase space on the spectrometer screen. A sample phase space corresponding to 150 pC injected charge is shown in Figure 4.10d. Although the resolution of the longitudinal phase space measurement is blurred from the large transverse size of the beam in the deflector and relatively large emittance of the beam after the undulator,

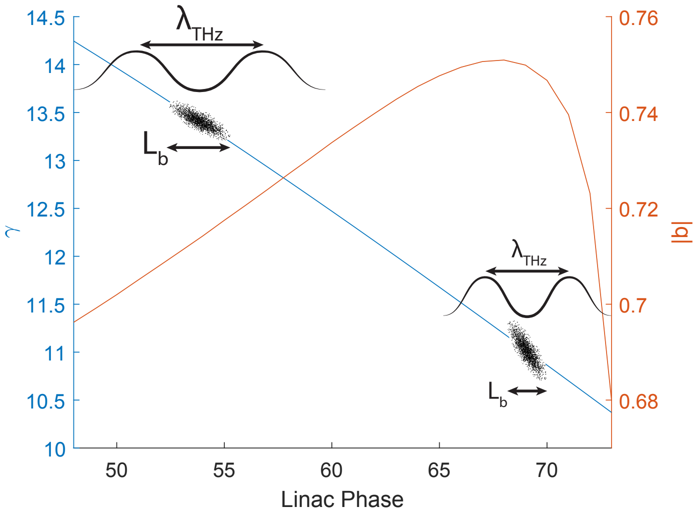

Figure 4.11: Bunching remains nearly constant as the linac phase is used to change the beam energy. This is due to the fact that the less-compressed high energy beams resonate at lower frequencies.

the most salient features in the beam distribution, such as chirp, energy spread and bunch length, are well reproduced in the measured image. A single decelerating bucket can be identified, in good agreement with the simulation results.

The resonant nature of the interaction was then studied by adjusting the linac phase to vary the initial beam energy. We note the bunching factor remains constant (Figure 4.11) as the higher energy beams experience less compression but resonate at lower frequencies such that the ratio of bunch length to radiation wavelength is unchanged. The spectral content was measured using the Michelson interferometer as shown in Figure 4.12. Two sample autocorrelation traces and the associated Fourier transforms are displayed for beam energies near (blue) and above (orange) the expected zero-slippage resonant value. Clear differences in period and radiation pulse length can be observed in the corresponding spectra. A more complete scan of the peak frequency and spectral bandwidth is reported in Figure 4.12c,d where beamline measurements are compared with GPT simulations. Notably, the peak frequency is observed to decrease when increasing the beam energy, a behaviour peculiar for FEL physics, but well reproduced by the simulations and explained by the quadratic

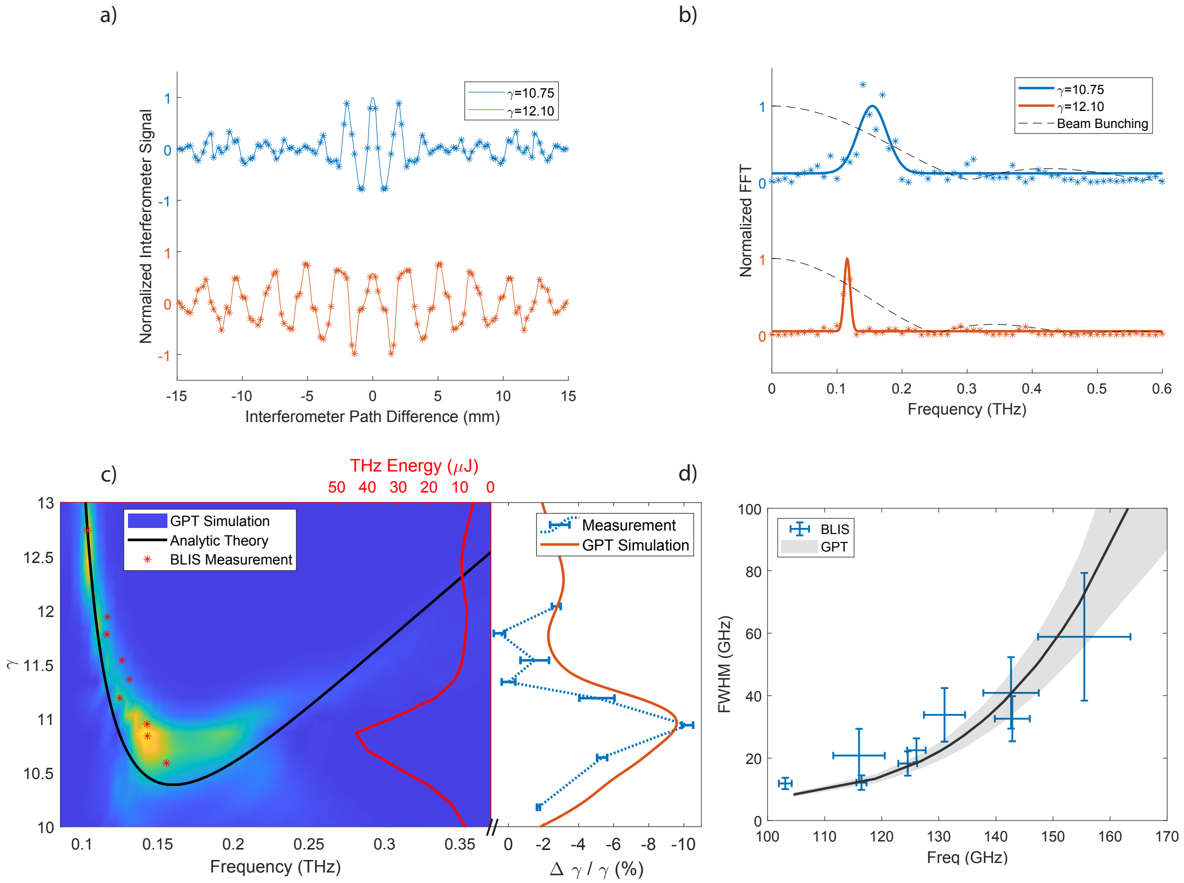

Figure 4.12: Interferometry measurements. a) Interferometer traces for input beam energies near (blue) and above (orange) the zero-slippage condition. b) Power spectrum of the emitted radiation, computed from a fast Fourier transform (FFT) of the interferometer traces and plotted together with the beam bunching factors obtained from beam dynamics simulations. c) The interferometer peak frequency measurements are compared to general particle tracer (GPT) simulations and to the theoretical phase-resonance curves. The simulated pulse energies show a maximum interaction at a slight positive energy detuning. Measurements of FEL efficiency versus input electron-beam energy are plotted against GPT results. The error bars in the energy loss data represent the r.m.s. of the distribution calculated over $\geq$10 images. The charge in these simulations is scaled by the observed transmission through the undulator. d) Terahertz spectrum bandwidth (FWHM) shown as a function of the peak radiation wavelength for measurements and simulation. Errors bars represent 95% confidence intervals of Gaussian fits to the spectral peaks, like those shown in b.

dispersion of the waveguide FEL. The low frequency branch dominates the interaction as the compressed beam has a smaller bunching factor at higher frequencies. In Figure 4.12d the spectrum full-width at half-maximum (FWHM) is plotted versus the peak frequency. When approaching the zero-slippage condition at 165 GHz, the radiation pulse is only a few cycles long and its relative bandwidth approaches 50%. This occurs for an injection normalized energy $\gamma = 11$, where the largest amount of terahertz energy is predicted and the largest relative deceleration in the electron-beam spectrum is measured.

The measurements and simulations both predict that the largest terahertz pulse energy is produced from beams slightly detuned from the analytic zero-slippage condition. This is due to the beam energy spread and transverse emittance, which contribute to a finite bandwidth for the electron-beam dispersion line as shown in Figure 4.13a. Electrons with energies below the zero-slippage resonant condition cannot be phase-matched with the electomagnetic field, so a higher injection mean energy maximizes the number of particles participating in the interaction.

Figure 4.13b shows the simulated evolution of the electron-beam and terahertz energy. The behavior is initially quadratic, matching the expected tapering curve. Further into the undulator, charge losses and dispersive effects limit the energy exchange as the field amplitude reaches nearly 15 MV/m in the waveguide. The insets show two different snapshots of the longitudinal profile of the electric field along the undulator exhibiting the strong chirp characteristic of a large-bandwidth pulse propagating in a waveguide.

4.4 Tessatron2

The Tessatron experiment successfully demonstrated the use of zero-slippage and strong undulator tapering to achieve 10% efficiency in a single pass of a 1 meter undulator, opening the door to high average power applications with increased electron beam repetition rate. However, the additional zero-slippage constraint restricts resonance to a single frequency for a given undulator and waveguide aperture, undermining FEL tunability. It also puts tight tolerances on transverse alignment and matching of the beam through the undulator

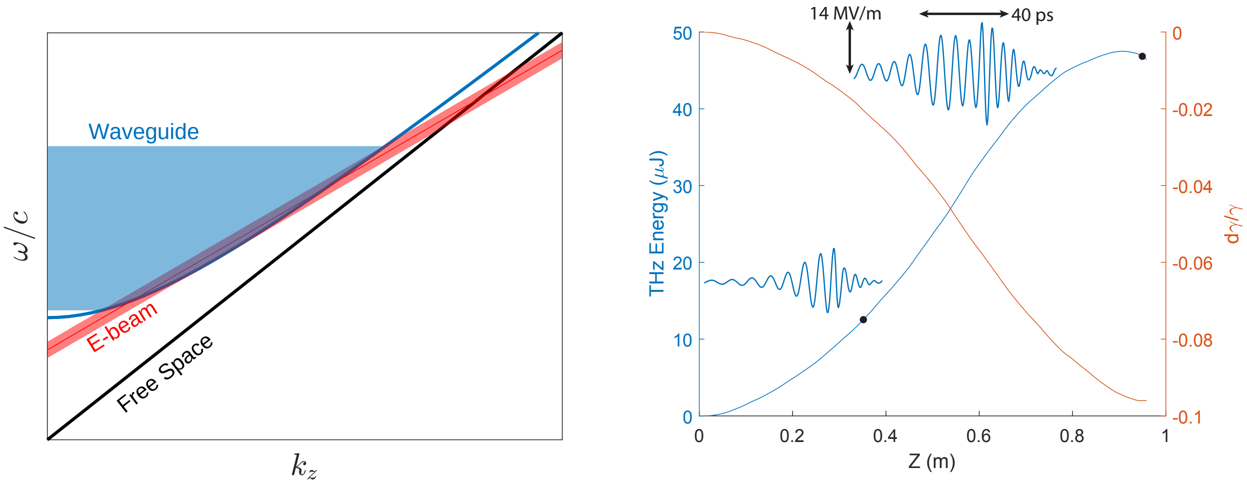

(a) (b)

Figure 4.13: 3D dispersion and simulation. a) Beam emittance and energy-spread broaden the electron-beam dispersion such that more frequencies resonate at a slight energy detuning. b) Simulated beam deceleration and terahertz growth along the undulator. The insets of the THz field show frequency chirp due to waveguide dispersion.

as the wiggling trajectory amplitude becomes comparable with the waveguide size, making it challenging to transmit the full charge through the system. In order to recover frequency tunability, it is possible to purposefully detune the beam energy from the zero-slippage condition, striking a compromise between maximal tunability and minimal slippage in the FEL. Increasing the beam energy has the additional advantages of easing the charge transmission in the system as well as increasing the frequency of the generated radiation.

In this regime off the zero-slippage condition, though, the strategy of fully compressing a beam to sub-wavelength scale is limited by strong space charge forces as well as the slippage introduced by the group velocity mismatch. In order to preserve the compactness of the system, effective seeding for the FEL interaction can be obtained by injecting a multicycle-long beam with strong spectral form factor at the system's resonant wavelength [50]. Over the years, various schemes have been developed to control the longitudinal beam profile and generate microbunching at the ps-scale, including photocathode laser shaping [120, 121], energy modulation of the beam on the ps-time scale [122, 123] and dispersive

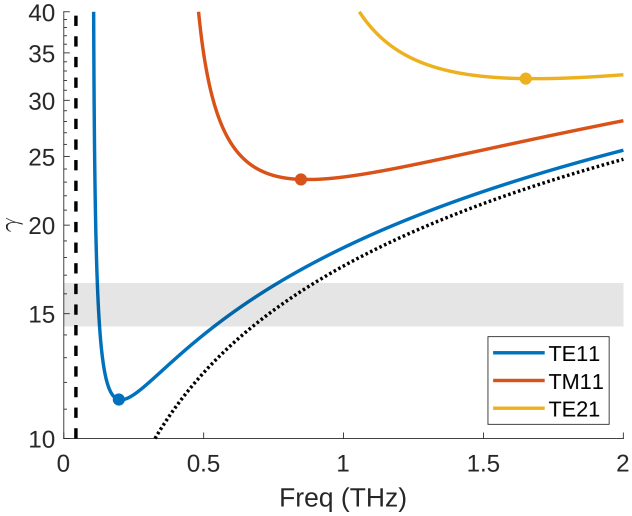

Figure 4.14: Phase resonance curves of the 3 lowest modes for the 4.05 mm diameter waveguide used. Markers indicate group resonance and dashed/dotted lines show the bounding fundamental cutoff frequency and free-space limit, respectively. The beam energy range of the experiment is shaded.

section masking [124, 125]. For high current applications ranging from coherent radiation generation to wakefield acceleration, it has been shown that space charge effects can be used to effectively enhance the bunching content by controlling the evolution of the space-charge induced beam plasma oscillations [126, 127].

For these reasons, a follow-up experiment was purposed and completed on the Pegasus beamline along with several beamline upgrades. First, the copper cathodes were replaced with novel multi-alkali photocathodes with high quantum efficiency (QE) enabling lossy laser-shaping with birefringent α-BBO crystals without compromising bunch charge. Next, a compact permanent-magnet chicane was designed for installation in the vacuum box, providing sufficient compression for high charge beams and reducing the necessary energy chirp from the linac allowing operation at higher beam energies. A second solenoid was installed after the chicane to provide strong focusing for matching the beam into the undulator. Finally, instead of using an interferometer to measure the terahertz autocorrelation signal, the temporal waveform is measured directly using a single-shot electro-optic sampling diagnostic.

In order to target higher frequencies, a larger vacuum pipe from Nor-Cal ($ID = 4.93$ mm,

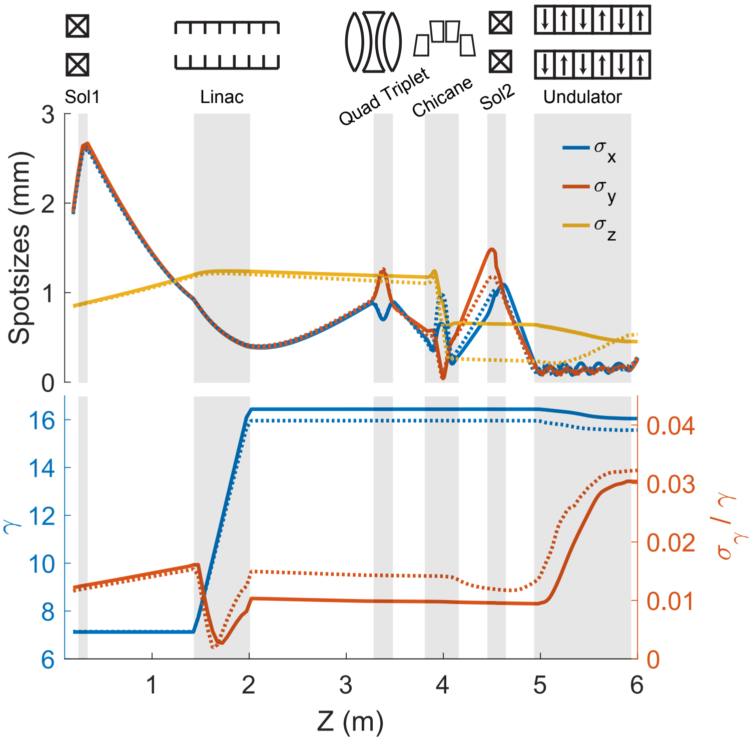

Figure 4.15: Start-to-end particle tracking simulations along the UCLA Pegasus beamline. Top) Evolution of the x,y,z rms moments of the particle distribution. Bottom) Energy and energy spread of the beam along the beamline. Solid and dotted lines show transport of beamlets and smooth longitudinal profile, respectively.

$OD = 6.35$ mm) was used with a copper waveguide ($ID = 4.06$ mm, $OD = 4.76$ mm) that fit tight inside the vacuum pipe, eliminating the need for separate alignment. The waveguide was cut such that it extended to the focus of the OAP, eliminating the need for the 1.33" bellows that mostly responsible for clipping THz in the vacuum system.

Figure 4.14 shows the energy range of the experiment (shaded) determined by the chicane energy acceptance to be between $7.5 - 8.5$ MeV. For the same peak field of $B_0 = 730$ mT, zero-slippage resonance is reduced to $\gamma = 11.35$, where the low frequencies (~ 120 GHz) are bound below by the nominal waveguide cutoff frequency while the high frequency branch can be tuned in the range 500-700 GHz.

Start-to-end GPT simulations of the beam transports are shown in Figure 4.15 for the two different schemes of laser temporal shapes employed in the experiment, i.e. a sequence of

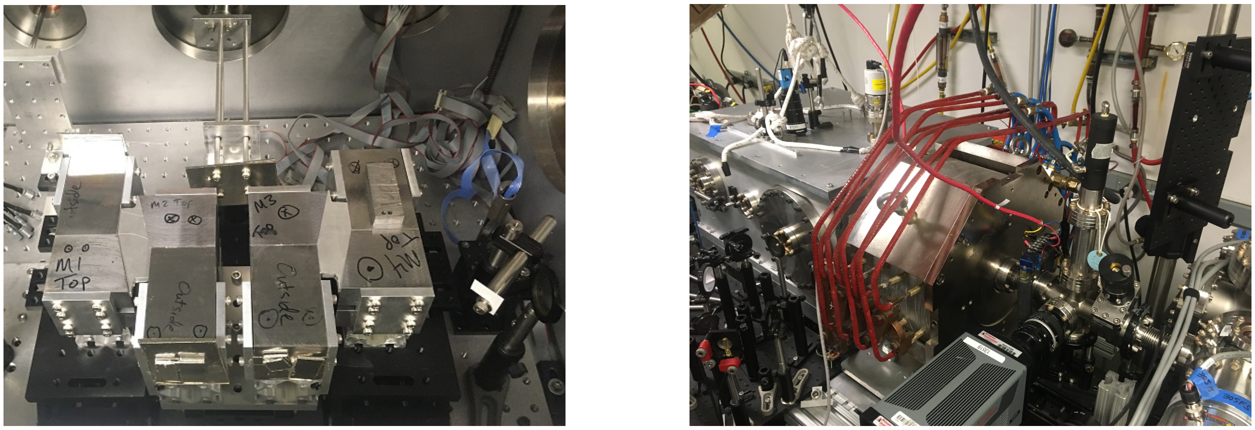

(a)

(b)

Figure 4.16: The permanent magnet chicane (a) and second solenoid (b) installed on the Pegasus beamline.

well-separated beamlets and a smooth flat-top longitudinal profile represented by solid and dotted lines, respectively. The initial transport is similar to the previous experiment, except that bunch charges can now exceed 250 pC with laser shaping. The booster linac cavity is adjusted in phase and amplitude to both accelerate the beam and imprint a tunable energy chirp for compressing the beam in the permanent magnet chicane. A quadrupole triplet focuses the beam into the permanent magnet chicane (Figure 4.16a) where the dipole entrance and exit angles are shaped to symmetrize the focusing in the horizontal and vertical planes. After the chicane, the diverging beam is matched into the undulator with the second solenoid (Figure 4.16b) as shown by the minimal betatron oscillations in the undulator. Note that while the linac phase was tuned to achieve maximal compression for the smooth distribution, the beam distribution was undercompressed to generate a multi-cycle charge density explaining the differences in bunch length evolution.

4.4.1 Beam Generation

The Na-K-Sb cathodes for this experiment were grown at Cornell and transported to UCLA in a vacuum suitcase. They provide an order of magnitude improvement in QE compared to photocathodes, and while a full characterization of the photoemitted beam characteristics is

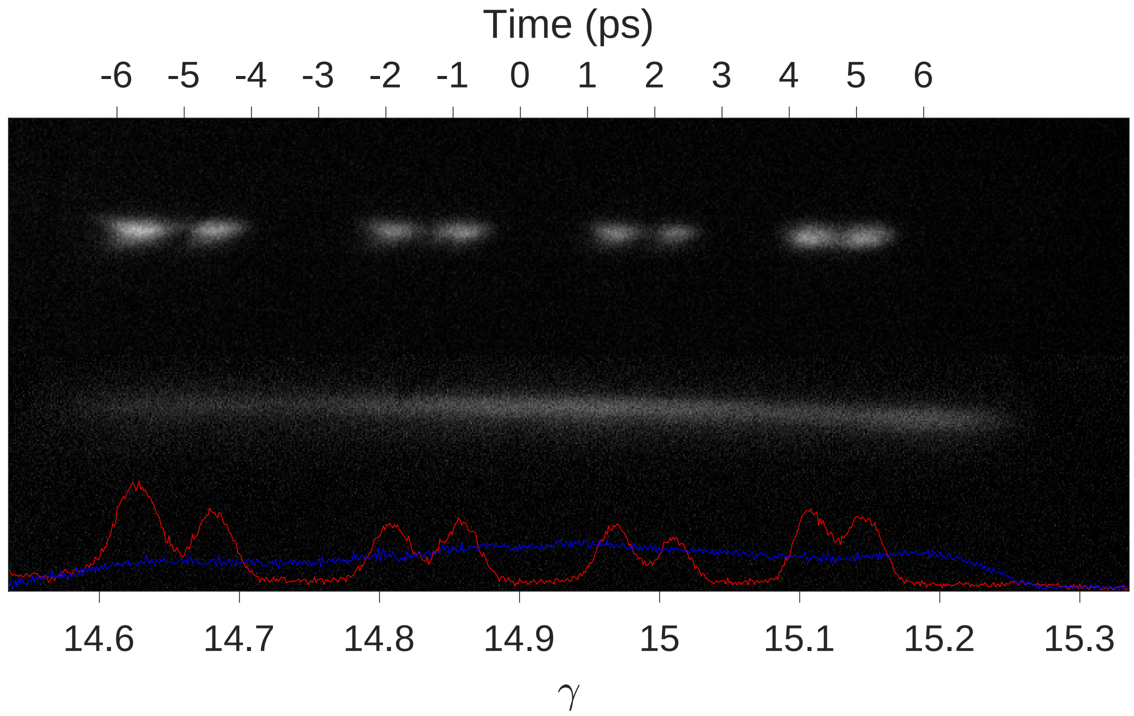

Figure 4.17: Spectrometer measurements of beamlets and smooth charge distributions created with α-BBO crystals and fused silica rod. Energy is mapped to time using simulations calibrated to linac measurements.

beyond the scope of this paper, a maximum QE approaching 1 % in the UV and charges up to 500 pC were recorded at Pegasus.

In practice, the 100 fs FWHM initial laser pulse is shaped using different thickness birefringent α-BBO crystals [128]. A 150 mm long dispersive fused silica rod can also be added when a smooth profile is desired. Stretching of the photocathode laser pulse reduces the beam current density in the gun significantly reducing space charge induced energy modulations. Most importantly, as described below, it is possible to generate a well separated train of beamlets to enhance the seeding at higher frequencies in the FEL. This is critical when the FEL is detuned from group resonance since a fully compressed single bunch no longer efficiently couples to radiation. In this case, the slippage-dominated interaction instead favors a more advanced pulse shaping scheme with strong bunching in multicycle beams.

Figure 4.17 demonstrates pulse shaping as measured on the energy spectrometer at low charge when the linac phase is set 40 deg off crest. The beamlet distribution is generated

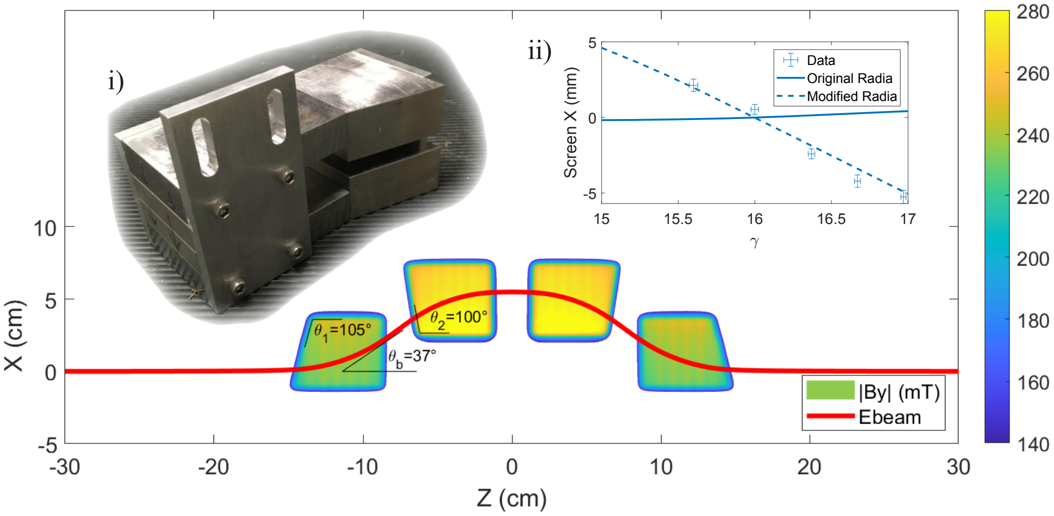

Figure 4.18: Simulated chicane fields with beam trajectory. i) A photo of an as built single dipole magnet. ii) Energy dispersion measurements from screen 83 cm downstream of chicane exit plotted against the original and modified RADIA chicane models.

with a series of 8, 4, and 1 mm crystals (inducing 8, 4 and 1 ps delays at the cathode) where the 1 mm crystal is used to maximize the charge per beamlet without sacrificing beamlet separation. The smooth distribution utilized an additional 2 mm crystal with the 150 mm-long UV fused silica smoothing rod. For higher charges, the beam undergoes longitudinal space charge oscillations [126] and the energy distribution is not a good representation of the temporal profile.

4.4.2 Chicane

A compact, permanent magnet chicane was used to compress the beam within a short distance which fitting within the space constraints on the beamline. The R56 design value of 6.4 cm allows for reaching full compression with a limited energy chirp, minimizing the reduction in FEL gain associated to the beam energy spread. The chicane is comprised of four C-shaped NeFeB permanent magnet based dipoles (shown in Figure 4.18i inlay) with 8 mm gap and peak fields up to 250 mT [129, 130]. Each dipole magnet consists of two $50 \times 50 \times 12.5$ mm^3 NeFeB magnets inside a yoke of 1006 High Carbon Steel. The outer

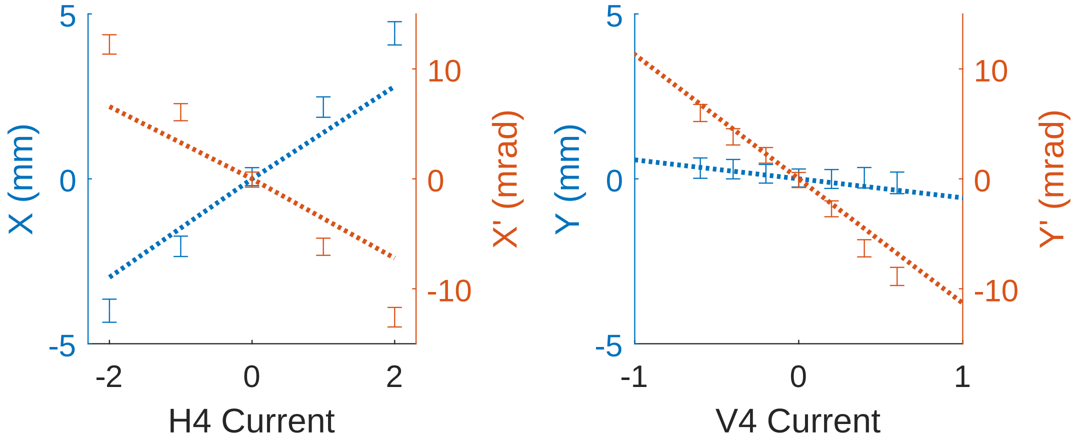

Figure 4.19: Exit position and angle measurements as a function of upstream steering against modified RADIA model. Data inferred from two screens 15 cm and 83 cm downstream.

and inner chicane magnets are offset -13 mm and -50 mm in $\hat{\mathbf{x}}$ relative to the beam axis to target an energy acceptance of $\gamma \in [15, 17]$, limited by the large bending angle ($\theta_b = 37°$).

The pole angles (θ_1, θ_2) were chosen to equally distribute focusing between the transverse dimensions while maintaining zero dispersion in simulations. Note that the choice $\theta_2 > 90$ deg was necessary to compensate for the simulated x-dependence in peak fields, seen in Figure 4.18. The magnet fields are tuned offline with iron shims and online with a motorized shunt across the inner-chicane magnets. Figure 4.19 shows chicane focusing measured with raster scans of a steering magnet 26 cm upstream of the chicane entrance, imparting a 5 mrad/A kick with beam position measured on two screens, 15 cm and 83 cm downstream of the chicane exit.

During the experiment, it was observed the chicane did in fact exhibit a small negative energy dispersion, although at a level where beam matching into the undulator was not compromised. Figure 4.18ii shows data and simulations for the chicane dispersion as measured on a screen 83 cm downstream of the chicane. Hall probe measurements performed after the chicane was removed from the beamline showed little x-dependence in the magnetic fields with the simulation discrepancy due to an incorrect value for the magnetic susceptibility of the carbon steel yoke. Corrected simulations show agreement with the measured dispersion data while suggesting minimal dispersion for $\theta_2 = 90°$. Measurements of chicane focusing

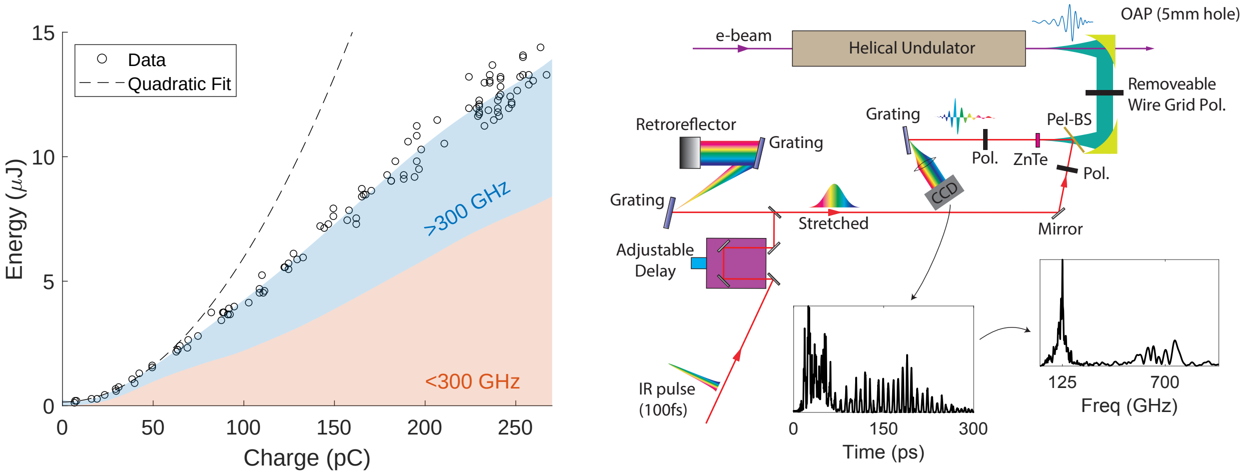

(a) (b)

Figure 4.20: THz measurements. a) Energy recorded with the pyro detector as function of the injected bunch charge as measured with an integrated current transformer located between the gun and the linac. Shading shows simulated energy content of high and low frequency. The black dotted line is a fit to the data for charge below 50 pC where transmission losses are negligible showing the expected quadratic growth. b) Schematic of the EOS measurement with measured temporal intensity and computed spectrum for beamlet distribution at $\gamma = 16.3$.

(Figure 4.19) inferred from two downstream screens as a function of upstream steering align with the corrected simulations, demonstrating good agreement in the transverse dynamics.

4.4.3 THz Diagnostics

Figure 4.20a shows a measurement of THz pulse energy as a function of the nominal bunch charge for a smooth beam distribution. Since the charge measurement is before the undulator, it does not account for transmission losses in the waveguide. Below 50 pC, the energy grows quadratically as expected for superradiant emission. As the charge is increased, space charge effects cause a decrease in bunching and an increase in transmission losses through the undulator, resulting in sub-quadratic energy growth. Note that these pulse energies have not been corrected for the estimated 35% loss in THz transport. At the maximum injected charge of 350 pC, we measured 18.5 uJ at the detector (estimated 28 uJ before losses) and 160 pC transmitted through the 1-meter undulator in rough agreement with the expected quadratic dependence. The efficiency in this experiment is notably lower than the previous experiment [131] due to the reduced initial bunching factors at higher frequencies, and, even more importantly, to the slippage effects which stretch the radiation pulse and lower the decelerating field amplitude in the undulator.

In Fig, 4.20a we also show simulated results for the energy content at frequencies above and below 300 GHz, which the pyro-detector can not distinguish and simply adds up. Integrating photons over the entire spectral range completely hides the complexity of the radiation pulse structure. To better understand the behavior of the system, the pyro-detector is replaced with a ZnTe crystal and a single-shot, cross-polarized electro-optic sampling (EOS) measurement of the temporal profile of the field [132] is implemented as shown in Figure 4.20b. In this measurement, the time-trace of the THz FEL electric field is encoded in the spectrum of a synchronized chirped IR pulse and can be retrieved in a single shot which is critical to eliminate issues related to timing jitter which severely limit the resolution above 500 GHz. In the time-traces of the pulse, corresponding to an input energy of 8.1 MeV, it is immediate to observe a leading high frequency pulse followed by a low frequency tail. The high frequencies are at the limit of measurement resolution while the low frequencies experience greater slippage and fill a majority of the waveform. Due to the large dispersion (and hence delay) between high and low frequency components in the waveguide, the entire radiation pulse covers a window of nearly 200 ps, so that a complete measurement with sufficient resolution requires stitching together multiple EOS images, each covering a 65 ps time window. The timing is adjusted with a calibrated delay stage and $\sim$ 30 single-shot EOS images are averaged at each position after subtracting temporal jitter. A Fourier transform of the EOS trace shows peaks in the spectral response at 125 GHz and 700 GHz, matching the analytical predictions for the resonant frequencies at the injected beam energy from Fig. 4.14.

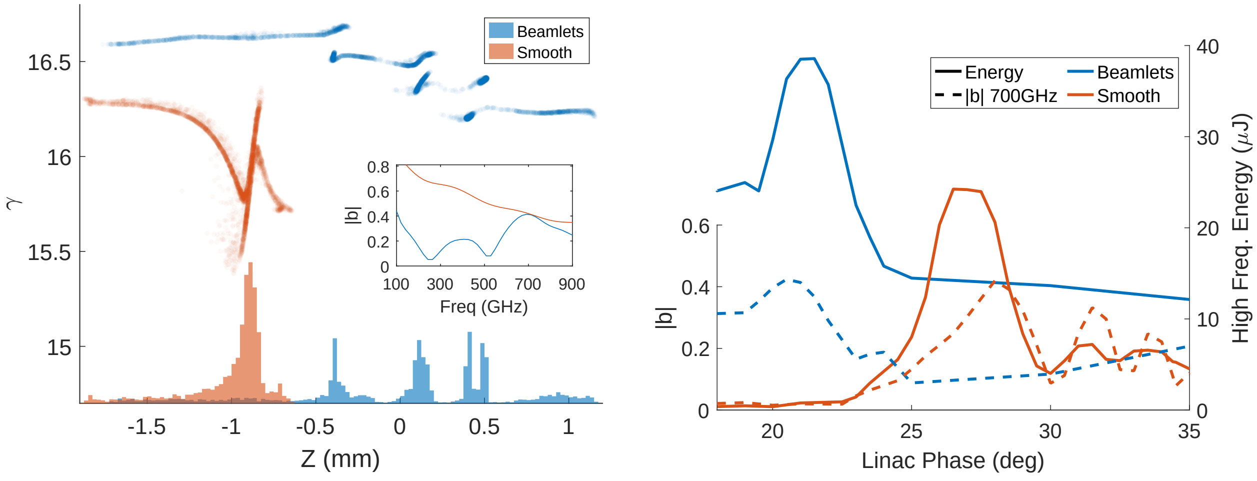

(a) (b)

Figure 4.21: Simulations of smooth and beamlet charge distributions. a) Longitudinal phase space at the undulator entrance with histogram projections and an inlay showing the spectral bunching factors. b) THz energy and bunching magnitude (computed at 700 GHz) versus the RF linac phase where 0° corresponds to the maximum energy setpoint.

4.4.4 Prebunching

In the absence of external radiation seeding, the beam must be manipulated to generate a large initial bunching b which can be defined as the amplitude of the normalized Fourier transform of the longitudinal current profile at a given frequency. At long wavelengths, seeding can be achieved by compression to sub-wavelength scale, but the challenges in reaching sub-ps bunch lengths with > 100 pC charges at moderately relativistic energies limits this scheme as frequencies approach 1 THz.

More importantly, detuning from group resonance introduces slippage that erodes the feedback between radiation and ultrashort beams. In order to compensate these shortcomings, we employed the prebunched, multicycle charge density generated from beamlets using α-BBO crystals. Even with similar bunching factors, the beamlets increase the intensity of the high frequency content with respect to the fully compressed, smooth distribution. Figure 4.21a shows a comparison of the longitudinal phase spaces for the two distributions at the undulator entrance with an arbitrary positional shift added for visual clarity. The effects of non-linearities in energy chirp and strong longitudinal space charge after compression can be seen in the folded z-shape of the smoothed distribution. The beamlets are generated using 8, 4 and 1 mm α-BBO crystals which have been found to maximize the bunching after the non-linear longitudinal space charge oscillations in the beamline [126]. Gun and linac phases are adjusted to tune the beamlet overlapping, resulting in a peaked current density with partially tunable period. It has been pointed out [133, 134] and experimentally demonstrated [135] that the emission of radiation can be significantly enhanced by using proper energy-phase correlation. In practice, the RF phases are fine-tuned as optimal bunching at the undulator entrance does not necessarily correspond to maximal emission due to the evolution of the longitudinal phase space along the undulator [134].

Figure 4.21b plots the simulated bunching and high frequency energy for each distribution at various compressing linac phases. Though both distributions have a maximal bunching factor above 40% at phase resonance, the beamlet distribution reduces uncorrelated energy spread and is more robust to slippage introduced off group resonance, leading to nearly double the high frequency content of the smooth distribution. The smooth distribution requires stronger compression and thus operates at a higher linac phase. When overcompressed, the nonlinear chirp results in two density peaks which causes oscillations in the bunching factor as their separation increases. Note that pulse energies are larger in ideal simulations than experiment due to optimal beam transport and alignment. Both the beamlets and smooth beam provide strong emission at the low frequency, generating 23 μJ and 31 μJ at 125 GHz, respectively.

Figure 4.22 shows normalized lineouts of EOS measurements proportional to field intensity where gun and linac phases were tuned to optimize the high frequency content. As expected, the beamlet distribution generates a waveform with a larger relative high frequency response. By integrating the lineouts over each frequency regime, it is estimated that the energy ratio for high frequency to low frequency is improved by a factor of 2.5 consistent with the simulation prediction.

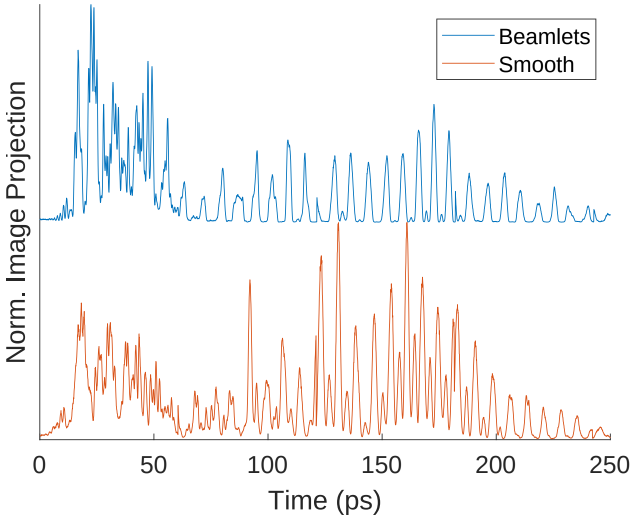

Figure 4.22: Normalized EOS measurements of temporal intensity for smooth and beamlet distributions at $\gamma = 16.3$.

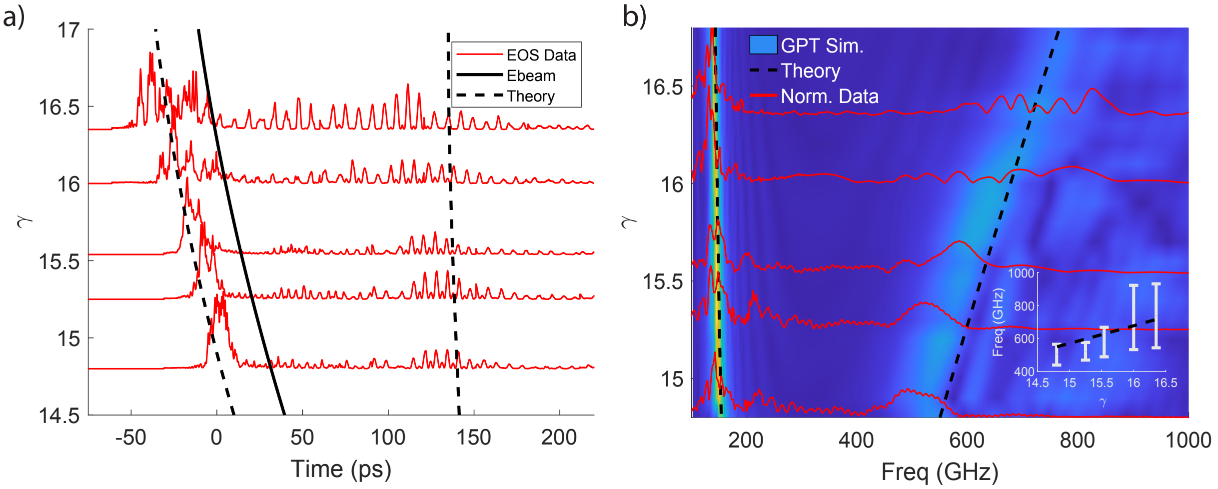

Figure 4.23: EOS temporal measurements and computed spectra as function of beam energy. (a) Ebeam arrival inferred from simulation. (b) Data traces are plotted over the start-to-end simulation results from GPT-FEL. The dotted lines show the phase resonances from the analytical theory. Inlay shows tunability of the central peak in the high frequency branch and the associated rms spectral bandwidth (white) over theory (black).

4.4.5 Frequency Tuning

While the zero-slippage condition is rigorously satisfied at a single frequency for a fixed waveguide, different frequencies can be targeted when the beam energy is detuned above resonance. Temporal EOS measurements are shown in Figure 4.23a as a function of beam energy where gun and linac phase are adjusted to optimize high frequency bunching for each measurement. The arrival times for the electron beam (solid) and phase-resonant frequencies (dashed) are simulated to account for the beam velocity/group velocities in the waveguide and for differences in beam propagation time to the undulator. Time zero is chosen as the high frequency arrival of $\gamma = 14.8$ for both measurement and simulation.

The measured waveform aligns well with the theoretical arrival of both resonant frequencies and the emission strength along the undulator can be indirectly inferred due to waveguide dispersion as radiation emitted near the entrance and exit corresponds to the waveform intensity near at the solid and dashed lines, respectively. The weak low frequency signal in the middle of the waveform can explained by a reduction in bunching factor and loss of charge transmission through the waveguide. At higher energies, charge is better transmitted through the system and both the low and high frequency generation is more uniform. While there is significant energy content in the low frequencies, the high frequencies experience less slippage and are more closely coupled with the longitudinal phase space dynamics.

Figure 4.23b shows the spectra calculated from the EOS measurements on top of GPT-FEL simulations and the analytic phase resonances for an effective waveguide diameter of 3.75 mm. As when operating the beamline, compression setpoints in simulation were chosen to optimize the bunching factor for the higher resonant frequency at the undulator entrance. The low frequencies line up well with simulation and theory with the bandwidth narrowing off resonance due to an increase in slippage. On the other hand, for the high frequency branch, there is a clear redshift at the lowest input beam energies both in the measurements and simulation which can be traced back to the large energy spread of the beam at the entrance of the undulator for these cases. For $\gamma > 16$, the central frequency in the pulse is in better agreement with the analytical theory, but a clear increase in bandwidth can be observed (again consistent with the simulation). This is attributed to the difficulty of attaining and maintaining strong bunching at these high frequencies leading to a broadening of the spectral form factor. The inset in Figure 4.21a more clearly shows tunability and bandwidth of the source as a function of beam energy.

Increasing the spectral range and improving frequency tunability makes the THz FEL a more flexible tool, and there are other implementation to consider. An interesting option is to recirculate a fraction of the terahertz radiation and use it as a high-intensity external seed for the interaction to improve the capture efficiency and maximize the final terahertz energy. The temporal separation of the electron bunches would have to be matched to the roundtrip of the terahertz cavity, typically on the order of $10-20$ ns for an undulator length of 1 m [136].

While a helical geometry features important advantages such as stronger FEL coupling and a circularly polarized output radiation, a planar undulator would allow the aspect ratio to be chosen in order to maximize charge transmission. Additionally, a planar geometry can be used with an adjustable-gap curved parallel-plate waveguide that allows the zero-slippage resonance condition to be tuned in order to obtain high efficiency over a larger frequency range. Eventually wakefield effects in the waveguide will limit the smallest dimensions (and therefore the highest frequency) achievable in the fundamental mode. In this case, zero-slippage resonance with higher order modes could trade a reduction in coupling for increased transmission and higher resonant frequency for a given waveguide.

APPENDIX A

Beamline Synchronization

The Pegasus beamline uses LabVIEW VIs on several computers to interface and collect measurements from various hardware. It is important that the data is synchronized and saved with the same primary key (aka rudyshot) as defined by the master VI on the main control computer.

An initial attempt to communicate the rudyshot from the master VI to multiple minion VIs used a static database table, but this slow approach led to race conditions whenever the repetition rate approached 2 Hz. With the installation of a new solid-state modulator that could operate up to 10 Hz, water cooling and data synchronization became limiting factors. A faster communication protocol using network streams has since been implemented, which can propagate rudyshot values across a network connection in < 30 ms with little overhead. A schematic of the Labview implementation is shown in Figure A.1.

First, we describe the main loop in a minion VI. Once data is acquired, the minion appends the current rudyshot and performs analysis before storing the record in the database. The time for acquisition can vary across VIs up to $\sim$100 ms depending on the data complexity (i.e. single value versus 16bit image). On the other hand, the main loop in the master VI starts by incrementing and publishing the new rudyshot to all available minions. After acquiring, analyzing, and storing in the database, the loop has to wait long enough to allow all minion data collection to finish before incrementing and publishing the next rudyshot. However, the wait cannot be too long such that minions read the next measurement before receiving the correct, updated rudyshot.

It is necessary that each VI can run independently, and that handshakes are appropriately handed when either VI is stopped or started. To be successful, both the master and minion

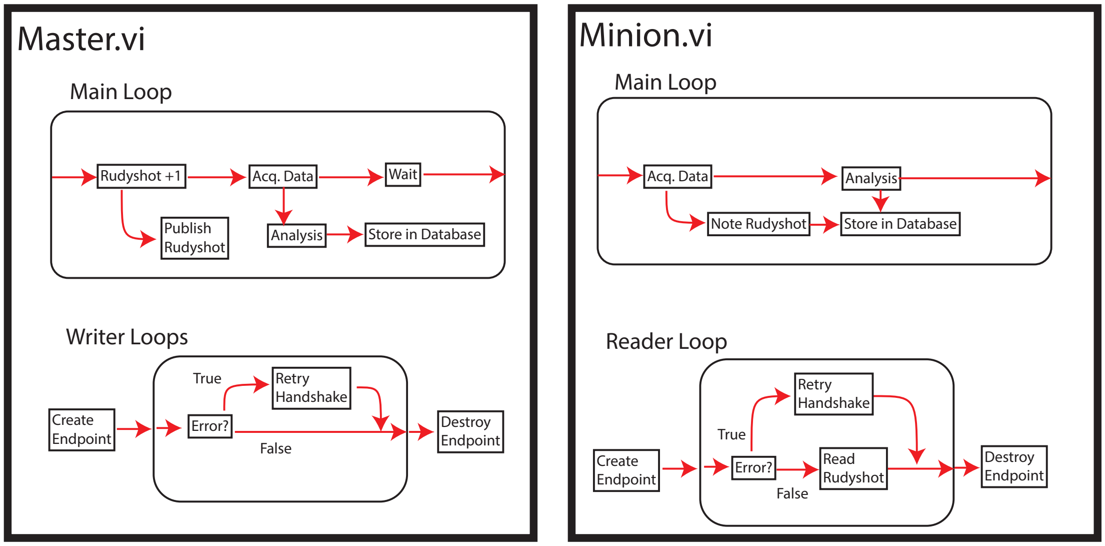

Figure A.1: Schematic of synchronization logic in Master and Minion Labview VIs.

have to attempt the handshake within the specified timeout, otherwise an error is returned. This process is controlled by the nearly identical writer and reader loops, creating a network endpoint when the VI starts and destroying the endpoint when the user ends the program. If there is an error, a handshake is attempted. If no error, the minion reads the last published rudyshot. Note that a separate writer loop exists for each minion in the master VI.

APPENDIX B

Dispersion

To quantify the effects of dispersion on a propagating waveform, we consider a gaussian pulse measured at $z = 0$ with central frequency ω_0, along with its Fourier transform

$$E(0,t) = e^{-t^2/2\sigma_t^2} e^{-i\omega_0 t} \quad \text{and} \quad E(0,\omega) = \frac{\sigma_t}{\sqrt{2\pi}} e^{-(\omega-\omega_0)^2/2\sigma_\omega^2} \tag{B.1}$$

where $\sigma_\omega \sigma_t = 1$ and we have used the identity $\int_{-\infty}^{\infty} e^{-ax^2+bx} dx = \sqrt{\pi/a}\ e^{b^2/4a}$. The phase advance of the different frequency components are determined by the dispersion relation $k(\omega)$ and the temporal waveform can be written as a integral over the Fourier components as

$$E(z,t) = \frac{\sigma_t}{\sqrt{2\pi}} \int_{-\infty}^{\infty} e^{-(\omega-\omega_0)^2/2\sigma_\omega^2} e^{ik(z)z-\omega t} d\omega \tag{B.2}$$

We apply a Taylor expansion about the central frequency to second order,

$$k(\omega) \approx k_0 + (\omega - \omega_0)/v_g + \beta_2(\omega - \omega_0)^2/2 \tag{B.3}$$

neglecting higher order terms and defining the group velocity $v_g = \partial\omega/\partial k\big|_{k=k_0}$ and group velocity dispersion $\beta_2 = \partial^2\omega/\partial k^2\big|_{k=k_0}$. Substituting Eq. (B.3) and regrouping terms yields

$$E(z,t) = \frac{\sigma_t}{\sqrt{2\pi}} e^{i(k_0 z-\omega_0 t)} \int_{-\infty}^{\infty} e^{-(\omega-\omega_0)^2(\sigma_t^2 - i\beta_2 z)/2}\ e^{i(\omega-\omega_0)(z/v_g - t)} d\omega \tag{B.4}$$

where the velocity of the phase fronts is given by ω_0/k_0. If we assume $\beta_2 = 0$, it is can be seen from the integrand that the field magnitude is constant for $z = v_g t$, such that the waveform envelope travels at the group velocity. On the other hand, it is clear that a finite β_2 symmetrically alters the bandwidth of the waveform. Higher order expansion terms would be needed to model asymmetric effects.

Taking the integral and simplifying, we find

$$E(z,t) = \frac{1}{\sqrt{1 - i\beta_2 z/\sigma_t^2}} e^{-(z/v_g - t)^2(1+i\beta_2 z/\sigma_t^2)/2\sigma^2} e^{ik_0 z - \omega_0 t}$$
$$\text{where} \quad \sigma = \sigma_t \sqrt{1 + \beta_2^2 z^2/\sigma_t^4} \quad \text{and} \quad |E(z,t)| = (1 + \beta_2^2 z^2/\sigma_t^4)^{-1/4} \tag{B.5}$$

where the effect of β_2 on the waveform width and amplitude is evident. Sometimes σ is used to represent the spread of the intensity instead of the field. Using the replacement $\sigma_E \to \sqrt{2}\sigma_I$, the change would be given as $\sigma = \sigma_t\sqrt{1 + \beta_2^2 z^2/4\sigma_t^4}$. For waveguide dispersion where $\omega^2/c^2 = k^2 + k_\perp^2$, it can be verified that $v_g = c^2 k_0/\omega_0$ and $\beta_2 = -k_\perp^2/c^2/k_0^3$.

REFERENCES

[1] Douglas J Paul. The progress towards terahertz quantum cascade lasers on silicon substrates. *Laser & Photonics Reviews*, 4(5):610–632, 2010.

[2] EF Nichols and JD Tear. Joining the infra-red and electric wave spectra. *Astrophysical Journal, vol. 61, p. 17*, 61:17, 1925.

[3] John H Booske, Richard J Dobbs, Colin D Joye, Carol L Kory, George R Neil, Gun-Sik Park, Jaehun Park, and Richard J Temkin. Vacuum electronic high power terahertz sources. *IEEE Transactions on Terahertz Science and Technology*, 1(1):54–75, 2011.

[4] Miriam Serena Vitiello, Giacomo Scalari, Benjamin Williams, and Paolo De Natale. Quantum cascade lasers: 20 years of challenges. *Optics express*, 23(4):5167–5182, 2015.

[5] SS Dhillon, MS Vitiello, EH Linfield, AG Davies, Matthias C Hoffmann, John Booske, Claudio Paoloni, M Gensch, Peter Weightman, GP Williams, et al. The 2017 terahertz science and technology roadmap. *Journal of Physics D: Applied Physics*, 50(4):043001, 2017.

[6] Peter H Siegel. Terahertz technology. *IEEE Transactions on microwave theory and techniques*, 50(3):910–928, 2002.

[7] Joscha Nehrkorn, Karsten Holldack, Robert Bittl, and Alexander Schnegg. Recent progress in synchrotron-based frequency-domain fourier-transform thz-epr. *Journal of Magnetic Resonance*, 280:10–19, 2017.

[8] Xiaojian Fu, Yujie Liu, Qi Chen, Yuan Fu, and Tie Jun Cui. Applications of terahertz spectroscopy in the detection and recognition of substances. *Frontiers in Physics*, 10:427, 2022.

[9] Kaveh Delfanazari, Richard A. Klemm, Hannah J. Joyce, David A. Ritchie, and Kazuo Kadowaki. Integrated, portable, tunable, and coherent terahertz sources and sensitive detectors based on layered superconductors. *Proceedings of the IEEE*, 108(5):721–734, 2020.

[10] Emilio A Nanni, Wenqian R Huang, Kyung-Han Hong, Koustuban Ravi, Arya Fallahi, Gustavo Moriena, RJ Dwayne Miller, and Franz X Kärtner. Terahertz-driven linear electron acceleration. *Nature communications*, 6(1):8486, 2015.

[11] Annalisa D'Arco, Marta Di Fabrizio, Valerio Dolci, Massimo Petrarca, and Stefano Lupi. Thz pulsed imaging in biomedical applications. *Condensed Matter*, 5(2):25, 2020.

[12] Alfred Leitenstorfer, Andrey S Moskalenko, Tobias Kampfrath, Junichiro Kono, Enrique Castro-Camus, Kun Peng, et al. The 2023 terahertz science and technology roadmap. *Journal of Physics D: Applied Physics*, 56(22):223001, apr 2023.

[13] LUISR Elias. Free-electron laser research at the university of california, santa barbara. *IEEE journal of quantum electronics*, 23(9):1470–1475, 1987.

[14] Gerald Ramian. The new ucsb free-electron lasers. *Nuclear Instruments and Methods in Physics Research Section A: Accelerators, Spectrometers, Detectors and Associated Equipment*, 318(1-3):225–229, 1992.

[15] D Oepts, AFG Van der Meer, and PW Van Amersfoort. The free-electron-laser user facility felix. *Infrared physics & technology*, 36(1):297–308, 1995.

[16] GP Gallerano, A Doria, E Giovenale, and A Renieri. Compact free electron lasers: From cerenkov to waveguide free electron lasers. *Infrared physics & technology*, 40(3):161–174, 1999.

[17] Young U Jeong, Byung Cheol Lee, Sun Kook Kim, Sung Oh Cho, Byung Heon Cha, Jongmin Lee, Grigori M Kazakevitch, Pavel D Vobly, Nicolai G Gavrilov, Vitaly V Kubarev, et al. First lasing of the kaeri compact far-infrared free-electron laser driven by a magnetron-based microtron. *Nuclear Instruments and Methods in Physics Research Section A: Accelerators, Spectrometers, Detectors and Associated Equipment*, 475(1-3):47–50, 2001.

[18] BA Knyazev, GN Kulipanov, and NA Vinokurov. Novosibirsk terahertz free electron laser: instrumentation development and experimental achievements. *Measurement Science and Technology*, 21(5):054017, 2010.

[19] Michael Gensch, Gianluca Geloni, Vivek Asgekar, Nikola Stojanovic, Jens Hauser, Holger Schlarb, Silke Vilcins, Bert Green, Nora Neumann, Anke-Susanne Müller, et al. Thz facility at elbe: a versatile test facility for electron bunch diagnostics on quasi-cw electron beams. *Proceedings of IPAC14, TUZA02*, 2014.

[20] Xiaojian Shu, Yuhuan Dou, Xingfan Yang, Ming Li, Hanbin Wang, and Xiangyang Lu. First lasing of caep thz fel facility. In *2017 42nd International Conference on Infrared, Millimeter, and Terahertz Waves (IRMMW-THz)*, pages 1–2. IEEE, 2017.

[21] He-Ting Li, Qi-Ka Jia, Shan-Cai Zhang, Lin Wang, and Yong-Liang Yang. Design of felichem, the first infrared free-electron laser user facility in china. *Chinese Physics C*, 41(1):018102, 2017.

[22] Ryszard S Romaniuk. Polfel-free electron laser in poland. *Photonics Letters of Poland*, 1(3):103–105, 2009.

[23] A Nause, A Friedman, A Weinberg, D Borodin, L Feigin, A Fukasawa, J Rosenzweig, R Roussel, and B Spataro. 6 mev novel hybrid (standing wave-traveling wave) photocathode electron gun for a thz superradiant fel. *Nuclear Instruments and Methods in Physics Research Section A: Accelerators, Spectrometers, Detectors and Associated Equipment*, page 165547, 2021.

[24] Prach Boonpornprasert, M Khojoyan, M Krasilnikov, F Stephan, B Marchetti, E Schneidmiller, M Yurkov, and S Rimjaem. Start-to-end simulations for ir/thz undulator radiation at pitz. In *Proc. FEL*, pages 153–158, 2014.

[25] M Krasilnikov, Z Aboulbanine, G Adhikari, N Aftab, A Asoyan, P Boonpornprasert, H Davtyan, G Georgiev, J Good, A Grebinyk, et al. Thz sase fel at pitz: lasing at a wavelength of 100 μm. In *Journal of Physics: Conference Series*, volume 2687, page 032016. IOP Publishing, 2024.

[26] A Perucchi, S Di Mitri, G Penco, E Allaria, and S Lupi. The terafermi terahertz source at the seeded fermi free-electron-laser facility. *Review of Scientific Instruments*, 84(2), 2013.

[27] P Musumeci, J Giner Navarro, JB Rosenzweig, L Cultrera, I Bazarov, J Maxson, S Karkare, and H Padmore. Advances in bright electron sources. *Nuclear Instruments and Methods in Physics Research Section A: Accelerators, Spectrometers, Detectors and Associated Equipment*, 907:209–220, 2018.

[28] Emma Curry, S Fabbri, J Maxson, P Musumeci, and A Gover. Meter-scale terahertz-driven acceleration of a relativistic beam. *Physical review letters*, 120(9):094801, 2018.

[29] A. Gover, E. Dyunin, Y. Lurie, Y. Pinhasi, and M. V. Krongauz. Superradiant and stimulated-superradiant emission in prebunched electron-beam radiators. ii. radiation enhancement schemes. *Phys. Rev. ST Accel. Beams*, 8:030702, Mar 2005.

[30] Nicholas Sudar, Pietro Musumeci, Joe Duris, Ivan Gadjev, M Polyanskiy, Igor Pogorelsky, Mikhail Fedurin, Christina Swinson, K Kusche, M Babzien, et al. High efficiency energy extraction from a relativistic electron beam in a strongly tapered undulator. *Physical review letters*, 117(17):174801, 2016.

[31] Song-Liang Chua, Christine A Caccamise, Dane J Phillips, John D Joannopoulos, Marin Soljačić, Henry O Everitt, and Jorge Bravo-Abad. Spatio-temporal theory of lasing action in optically-pumped rotationally excited molecular gases. *Optics Express*, 19(8):7513–7529, 2011.

[32] Mary S Tobin. A review of optically pumped nmmw lasers. *Proceedings of the IEEE*, 73(1):61–85, 1985.

[33] Rüdeger Köhler, Alessandro Tredicucci, Fabio Beltram, Harvey E Beere, Edmund H Linfield, A Giles Davies, David A Ritchie, Rita C Iotti, and Fausto Rossi. Terahertz semiconductor-heterostructure laser. *nature*, 417(6885):156–159, 2002.

[34] Iman Kundu, Paul Dean, Alexander Valavanis, Li Chen, Lianhe Li, John E Cunningham, Edmund H Linfield, and A Giles Davies. Discrete vernier tuning in terahertz quantum cascade lasers using coupled cavities. *Optics express*, 22(13):16595–16605, 2014.

[35] Koustuban Ravi, Wenqian Ronny Huang, Sergio Carbajo, Emilio A. Nanni, Damian N. Schimpf, Erich P. Ippen, and Franz. X. Kärtner. Theory of terahertz generation by optical rectification using tilted-pulse-fronts. *Opt. Express*, 23(4):5253–5276, Feb 2015.

[36] János Hebling, Gábor Almási, Ida Z. Kozma, and Jürgen Kuhl. Velocity matching by pulse front tilting for large-area thz-pulse generation. *Opt. Express*, 10(21):1161–1166, Oct 2002.

[37] Nitin Kumar, Udaybir Singh, Tejendr Pratap Singh, and AK Sinha. A review on the applications of high power, high frequency microwave source: Gyrotron. *Journal of fusion energy*, 30:257–276, 2011.

[38] Manfred Thumm. *State-of-the-Art of High Power Gyro-Devices and Free Electron Masers. Update 2017 (KIT Scientific Reports; 7750)*, volume 7750. KIT Scientific Publishing, 2018.

[39] Gian Piero Gallerano, S Biedron, et al. Overview of terahertz radiation sources. In *Proceedings of the 2004 FEL Conference*, volume 1, pages 216–221, 2004.

[40] Eberhard J Jaeschke, Shaukat Khan, Jochen R Schneider, and Jerome B Hastings. *Synchrotron light sources and free-electron lasers: accelerator physics, instrumentation and science applications*. 2016.

[41] Robert B Palmer. Interaction of relativistic particles and free electromagnetic waves in the presence of a static helical magnet. *Journal of Applied Physics*, 43(7):3014–3023, 1972.

[42] N. Kroll, P. Morton, and M. Rosenbluth. Free-electron lasers with variable parameter wigglers. *IEEE Journal of Quantum Electronics*, 17(8):1436–1468, 1981.

[43] N Sudar, P Musumeci, I Gadjev, Y Sakai, S Fabbri, M Polyanskiy, I Pogorelsky, M Fedurin, C Swinson, K Kusche, et al. Demonstration of cascaded modulator-chicane microbunching of a relativistic electron beam. *Physical review letters*, 120(11):114802, 2018.

[44] Y Jiao, J Wu, Y Cai, AW Chao, WM Fawley, J Frisch, Z Huang, H-D Nuhn, C Pellegrini, and S Reiche. Modeling and multidimensional optimization of a tapered free electron laser. *Physical Review Special Topics-Accelerators and Beams*, 15(5):050704, 2012.

[45] Alan Mak, Francesca Curbis, and Sverker Werin. Model-based optimization of tapered free-electron lasers. *Physical Review Special Topics-Accelerators and Beams*, 18(4):040702, 2015.

[46] Joseph Patrick Duris. *High efficiency electron-laser interactions in tapered helical undulators*. University of California, Los Angeles, 2015.

[47] Kwang-Je Kim, Zhirong Huang, and Ryan Lindberg. *Synchrotron radiation and free-electron lasers*. Cambridge university press, 2017.

[48] Ming Xie. Design optimization for an x-ray free electron laser driven by slac linac. In *Proceedings Particle Accelerator Conference*, volume 1, pages 183–185. IEEE, 1995.

[49] R. H. Dicke. Coherence in spontaneous radiation processes. *Phys. Rev.*, 93:99–110, Jan 1954.

[50] Avraham Gover, Reuven Ianconescu, Aharon Friedman, Claudio Emma, Nick Sudar, Pietro Musumeci, and Claudio Pellegrini. Superradiant and stimulated-superradiant emission of bunched electron beams. *Reviews of Modern Physics*, 91(3):035003, 2019.

[51] R Bonifacio, F Casagrande, M Ferrario, P Pierini, and N Piovella. Tapering and self tapering in a free electron laser. In *High Gain, High Power Free Electron Laser: Physics and Application to Tev Particle Acceleration*, pages 227–242. Elsevier, 1989.

[52] Luis R. Elias, William M. Fairbank, John M. J. Madey, H. Alan Schwettman, and Todd I. Smith. Observation of stimulated emission of radiation by relativistic electrons in a spatially periodic transverse magnetic field. *Physical Review Letters*, 36:717–720, Mar 1976.

[53] R Warren, B Newnam, J Winston, W Stein, L Young, and C Brau. Results of the los alamos free-electron laser experiment. *IEEE Journal of Quantum Electronics*, 19(3):391–401, 1983.

[54] TJ Orzechowski, BR Anderson, JC Clark, WM Fawley, AC Paul, D Prosnitz, ET Scharlemann, SM Yarema, DB Hopkins, AM Sessler, et al. High-efficiency extraction of microwave radiation from a tapered-wiggler free-electron laser. *Physical review letters*, 57(17):2172, 1986.

[55] J. T. Weir, T. J. Orzechowski, J. L. Miller, Y. P. Chong, F. Chambers, G. A. Deis, A. C. Paul, D. Prosnitz, E. T. Scharlemann, K. Halbach, and J. Edighoffer. Results Of The PALADIN Experiment. In Yves Petroff, editor, *Free Electron Lasers II*, volume 1133, pages 97 – 101. International Society for Optics and Photonics, SPIE, 1989.

[56] Claudio Emma, Kun Fang, Juhao Wu, and Claudio Pellegrini. High efficiency, multiterawatt x-ray free electron lasers. *Physical Review Accelerators and Beams*, 19(2):020705, 2016.

[57] C Emma, N Sudar, P Musumeci, A Urbanowicz, and C Pellegrini. High efficiency tapered free-electron lasers with a prebunched electron beam. *Physical Review Accelerators and Beams*, 20(11):110701, 2017.

[58] WD Kimura, M Babzien, I Ben-Zvi, LP Campbell, DB Cline, CE Dilley, JC Gallardo, SC Gottschalk, KP Kusche, RH Pantell, et al. Demonstration of high-trapping efficiency and narrow energy spread in a laser-driven accelerator. *Physical review letters*, 92(5):054801, 2004.

[59] P Musumeci, S Ya Tochitsky, S Boucher, CE Clayton, A Doyuran, RJ England, C Joshi, C Pellegrini, JE Ralph, JB Rosenzweig, et al. High energy gain of trapped

electrons in a tapered, diffraction-dominated inverse-free-electron laser. *Physical review letters*, 94(15):154801, 2005.

[60] Joseph Duris, P Musumeci, M Babzien, M Fedurin, K Kusche, RK Li, J Moody, I Pogorelsky, M Polyanskiy, JB Rosenzweig, et al. High-quality electron beams from a helical inverse free-electron laser accelerator. *Nature communications*, 5(1):4928, 2014.

[61] Joseph Duris, Alex Murokh, and Pietro Musumeci. Tapering enhanced stimulated superradiant amplification. *New Journal of Physics*, 17(6):063036, 2015.

[62] Pietro Musumeci, Ronald Agustsson, Loïc Amoudry, Daniel Broemmelsiek, David Bruhwiler, Paul Denham, Jonathan Edelen, Andrew Fisher, Christopher Hall, Tara Hodgetts, Alex Lumpkin, Alex Murokh, Sergei Nagaitsev, Youna Park, Jinhao Ruan, Marcos Ruelas, James Santucci, Giulio Stancari, Alexander Valishev, and Alexander Zholents. Fast-greens: A high efficiency free electron laser driven by superconducting rf accelerator. *JACoW*.

[63] J. Duris, P. Musumeci, N. Sudar, A. Murokh, and A. Gover. Tapering enhanced stimulated superradiant oscillator. *Phys. Rev. Accel. Beams*, 21:080705, Aug 2018.

[64] Andrea Fratalocchi and Giancarlo Ruocco. Single-molecule imaging with x-ray free-electron lasers: Dream or reality? *Physical Review Letters*, 106(10):105504, 2011.

[65] Erik R Hosler, Obert R Wood II, and William A Barletta. Free-electron laser emission architecture impact on extreme ultraviolet lithography. *Journal of Micro/Nanolithography, MEMS, and MOEMS*, 16(4):041009, 2017.

[66] Alex Murokh, Pietro Musumeci, Alexander Zholents, and Stephen Webb. Towards a compact high efficiency fel for industrial applications. In *Compact EUV & X-ray Light Sources*, pages EW4A–3. Optical Society of America, 2020.

[67] Evgeny L Saldin, Evgeny A Schneidmiller, and Mikhail V Yurkov. A simple method for the determination of the structure of ultrashort relativistic electron bunches. *Nuclear Instruments and Methods in Physics Research Section A: Accelerators, Spectrometers, Detectors and Associated Equipment*, 539(3):499–526, 2005.

[68] Andrew Zangwill. *Modern electrodynamics*. Cambridge University Press, 2013.

[69] E Curry, S Fabbri, P Musumeci, and A Gover. Thz-driven zero-slippage ifel scheme for phase space manipulation. *New Journal of Physics*, 18(11):113045, 2016.

[70] Andrey V Savilov. Stimulated wave scattering in the smith-purcell fel. *IEEE Transactions on Plasma Science*, 29(5):820–823, 2001.

[71] R Bartolini, A Doria, GP Gallerano, and A Renieri. Theoretical and experimental aspects of a waveguide fel. *Nuclear Instruments and Methods in Physics Research Section A: Accelerators, Spectrometers, Detectors and Associated Equipment*, 304(1-3):417–420, 1991.

[72] Zhirong Huang and Kwang-Je Kim. Review of x-ray free-electron laser theory. *Physical Review Special Topics-Accelerators and Beams*, 10(3):034801, 2007.

[73] C Pellegrini, A Marinelli, and S Reiche. The physics of x-ray free-electron lasers. *Reviews of Modern Physics*, 88(1):015006, 2016.

[74] SG Biedron, YC Chae, Roger J Dejus, B Faatz, HP Freund, SV Milton, H-D Nuhn, and S Reiche. Multi-dimensional free-electron laser simulation codes: a comparison study. *Nuclear Instruments and Methods in Physics Research Section A: Accelerators, Spectrometers, Detectors and Associated Equipment*, 445(1-3):110–115, 2000.

[75] S Reiche. Fel simulations: History, status and outlook. *Proceedings of FEL2010, Malmö, Sweden (JACoW, 2010), Vol. MOOCI1*, pages 165–172, 2010.

[76] Luca Giannessi. Simulation codes for high brightness electron beam free-electron laser experiments. *Physical Review Special Topics-Accelerators and Beams*, 6(11):114802, 2003.

[77] L Giannessi. Overview of perseo, a system for simulating fel dynamics in mathcad. In *Proceedings of the free-electron laser conference*, 2006.

[78] C Emma, N Sudar, P Musumeci, A Urbanowicz, and C Pellegrini. High efficiency tapered free-electron lasers with a prebunched electron beam. *Physical Review Accelerators and Beams*, 20(11):110701, 2017.

[79] William M Fawley. A user manual for ginger and its post-processor xplotgin. Technical report, Lawrence Berkeley National Lab.(LBNL), Berkeley, CA (United States), 2002.

[80] Sven Reiche. Genesis 1.3: a fully 3d time-dependent fel simulation code. *Nuclear Instruments and Methods in Physics Research Section A: Accelerators, Spectrometers, Detectors and Associated Equipment*, 429(1-3):243–248, 1999.

[81] EL Saldin, EA Schneidmiller, and MV Yurkov. Fast: a three-dimensional time-dependent fel simulation code. *Nuclear Instruments and Methods in Physics Research Section A: Accelerators, Spectrometers, Detectors and Associated Equipment*, 429(1-3):233–237, 1999.

[82] LT Campbell and BWJ McNeil. Puffin: A three dimensional, unaveraged free electron laser simulation code. *Physics of Plasmas*, 19(9):093119, 2012.

[83] HP Freund, PJM van der Slot, DLAG Grimminck, ID Setija, and P Falgari. Three-dimensional, time-dependent simulation of free-electron lasers with planar, helical, and elliptical undulators. *New Journal of Physics*, 19:023020, 2017.

[84] MJ De Loos and SB Van Der Geer. General particle tracer: A new 3d code for accelerator and beamline design. In *5th European Particle Accelerator Conference*, page 1241, 1996.

[85] Ivan V Bazarov and Charles K Sinclair. Multivariate optimization of a high brightness dc gun photoinjector. *Physical Review Special Topics-Accelerators and Beams*, 8(3):034202, 2005.

[86] Alexander Brynes. Understanding 1d to 3d coherent synchrotron radiation effects. In *39th Free Electron Laser Conf.(FEL'19), Hamburg, Germany, 26-30 August 2019*, pages 578–583. JACOW Publishing, Geneva, Switzerland, 2019.

[87] P Sprangle, A Ting, and CM Tang. Analysis of radiation focusing and steering in the free-electron laser by use of a source-dependent expansion technique. *Physical Review A*, 36(6):2773, 1987.

[88] Panagiotis Baxevanis, Ronald D Ruth, and Zhirong Huang. General method for analyzing three-dimensional effects in free-electron laser amplifiers. *Physical Review Special Topics-Accelerators and Beams*, 16(1):010705, 2013.

[89] Avraham Gover, Reuven Ianconescu, Aharon Friedman, Claudio Emma, Nick Sudar, Pietro Musumeci, and Claudio Pellegrini. Superradiant and stimulated-superradiant emission of bunched electron beams. *Reviews of Modern Physics*, 91(3):035003, 2019.

[90] Youna Park, Ronald Agustsson, Tara Campese, David Dang, Paul Denham, Ivan Gadjev, Christopher Hall, Alex Murokh, Pietro Musumeci, Nicholas Sudar, et al. Status update for the high gain high efficiency tessa-266 experiment. In *39th Free Electron Laser Conf.(FEL'19), Hamburg, Germany, 26-30 August 2019*, pages 730–733. JACOW Publishing, Geneva, Switzerland, 2019.

[91] HP Freund, L Giannessi, and WH Miner Jr. The effect of shot noise on the start up of the fundamental and harmonics in free-electron lasers. *Journal of Applied Physics*, 104(12):123114, 2008.

[92] BWJ McNeil, MW Poole, and GRM Robb. Unified model of electron beam shot noise and coherent spontaneous emission in the helical wiggler free electron laser. *Physical Review Special Topics-Accelerators and Beams*, 6(7):070701, 2003.

[93] William M Fawley. Algorithm for loading shot noise microbunching in multidimensional, free-electron laser simulation codes. *Physical Review Special Topics-Accelerators and Beams*, 5(7):070701, 2002.

[94] C Penman and BWJ McNeil. Simulation of input electron noise in the free-electron laser. *Optics communications*, 90(1-3):82–84, 1992.

[95] A Fisher, P Musumeci, and SB Van der Geer. Self-consistent numerical approach to track particles in free electron laser interaction with electromagnetic field modes. *Physical Review Accelerators and Beams*, 23(11):110702, 2020.

[96] Xi Yang, Najmeh Mirian, and Luca Giannessi. Postsaturation dynamics and superluminal propagation of a superradiant spike in a free-electron laser amplifier. *Physical Review Accelerators and Beams*, 23(1):010703, 2020.

[97] R Bonifacio, L De Salvo, P Pierini, N Piovella, and C Pellegrini. Spectrum, temporal structure, and fluctuations in a high-gain free-electron laser starting from noise. *Physical review letters*, 73(1):70, 1994.

[98] S Casalbuoni, M Hagelstein, B Kostka, R Rossmanith, M Weisser, E Steffens, A Bernhard, D Wollmann, and Tilo Baumbach. Generation of x-ray radiation in a storage ring by a superconductive cold-bore in-vacuum undulator. *Physical Review Special Topics-Accelerators and Beams*, 9(1):010702, 2006.

[99] Johannes Bahrdt and Efim Gluskin. Cryogenic permanent magnet and superconducting undulators. *Nuclear Instruments and Methods in Physics Research Section A: Accelerators, Spectrometers, Detectors and Associated Equipment*, 907:149–168, 2018.

[100] KE Robinson, DC Quimby, JM Slater, TL Churchill, A Pindroh, and A Valla. Hybrid undulator design considerations. *Nuclear Instruments and Methods in Physics Research Section A: Accelerators, Spectrometers, Detectors and Associated Equipment*, 250(1-2):100–109, 1986.

[101] Sven Reiche. Motion in the undulator. *CERN Yellow Reports: School Proceedings*, 1:347–347, 2018.

[102] F Ciocci, G Dattoli, L Giannessi, C Mari, and A Torre. Optical properties of helical undulators. *Nuclear Instruments and Methods in Physics Research Section B: Beam Interactions with Materials and Atoms*, 63(3):319–325, 1992.

[103] MJ De Loos and SB Van Der Geer. General particle tracer: A new 3d code for accelerator and beamline design. In *5th European Particle Accelerator Conference*, page 1241, 1996.

[104] Ryan N. Coffee, James P. Cryan, Joseph Duris, Wolfram Helml, Siqi Li, and Agostino Marinelli. Development of ultrafast capabilities for x-ray free-electron lasers at the linac coherent light source. *Philosophical Transactions of the Royal Society A: Mathematical, Physical and Engineering Sciences*, 377(2145):20180386, 2019.

[105] Pascal Elleaume, Oleg Chubar, and Joel Chavanne. Computing 3d magnetic fields from insertion devices. In *Proceedings of the 1997 Particle Accelerator Conference (Cat. No. 97CH36167)*, volume 3, pages 3509–3511. IEEE, 1997.

[106] Zachary Wolf. Introduction to lcls undulator tuning. Technical report, SLAC National Accelerator Lab., Menlo Park, CA (United States), 2018.

[107] RW Warren. Limitations on the use of the pulsed-wire field measuring technique. *Nuclear Instruments and Methods in Physics Research Section A: Accelerators, Spectrometers, Detectors and Associated Equipment*, 272(1-2):257–263, 1988.

[108] Alex D'Audney, Stephen Milton, Sandra Biedron, Thomas Johnson, et al. An ultrahigh resolution pulsed-wire magnet measurement system. 2016.

[109] O Shahal and R Rohatgi. Pulsed wire magnetic field measurements on a 4.3 m long wiggler. *Nuclear Instruments and Methods in Physics Research Section A: Accelerators, Spectrometers, Detectors and Associated Equipment*, 285(1-2):299–302, 1989.

[110] AA Varfolomeev, Yu P Bouzouloukov, SN Ivanchenkov, AS Khlebnikov, NS Osmanov, and SV Tolmachev. Wire method for magnetic field measurements in long undulators. *Nuclear Instruments and Methods in Physics Research Section A: Accelerators, Spectrometers, Detectors and Associated Equipment*, 359(1-2):93–96, 1995.

[111] NS Osmanov, SV Tolmachev, and AA Varfolomeev. Further development of the pulsed wire technique for magnetic field and focusing strength measurements in long undulators. *Nuclear Instruments and Methods in Physics Research Section A: Accelerators, Spectrometers, Detectors and Associated Equipment*, 407(1-3):443–447, 1998.

[112] D Arbelaez, T Wilks, A Madur, S Prestemon, S Marks, and R Schlueter. A dispersion and pulse width correction algorithm for the pulsed wire method. *Nuclear Instruments and Methods in Physics Research Section A: Accelerators, Spectrometers, Detectors and Associated Equipment*, 716:62–70, 2013.

[113] Matthew Kasa. Dsp methods for correcting dispersion and pulse width effects during pulsed wire measurements. *Measurement*, 122:224–231, 2018.

[114] Jared Maxson, David Cesar, Giacomo Calmasini, Alexander Ody, Pietro Musumeci, and David Alesini. Direct measurement of sub-10 fs relativistic electron beams with ultralow emittance. *Physical review letters*, 118(15):154802, 2017.

[115] D Cesar, J Maxson, P Musumeci, Y Sun, J Harrison, P Frigola, FH O'Shea, H To, D Alesini, and RK Li. Demonstration of single-shot picosecond time-resolved mev electron imaging using a compact permanent magnet quadrupole based lens. *Physical review letters*, 117(2):024801, 2016.

[116] K Kabra, S Li, F Cropp, Thomas J Lane, P Musumeci, and D Ratner. Mapping photocathode quantum efficiency with ghost imaging. *Physical Review Accelerators and Beams*, 23(2):022803, 2020.

[117] D Cesar, S Custodio, J Maxson, P Musumeci, X Shen, E Threlkeld, RJ England, A Hanuka, IV Makasyuk, EA Peralta, et al. High-field nonlinear optical response and phase control in a dielectric laser accelerator. *Communications Physics*, 1(1):46, 2018.

[118] EC Snively, J Xiong, P Musumeci, and A Gover. Broadband thz amplification and superradiant spontaneous emission in a guided fel. *Optics express*, 27(15):20221–20230, 2019.

[119] A Doria, M Faraone, and GP Gallerano. Theoretical and design aspects of a grooved waveguide for compact fel. *Optics communications*, 155(1-3):187–196, 1998.

[120] Yifan Liang, Zhuoyuan Liu, Qili Tian, Tong Li, Xiancai Lin, Lixin Yan, Yingchao Du, Renkai Li, Jiaru Shi, Cheng Cheng, et al. Widely tunable electron bunch trains

for the generation of high-power narrowband 1–10 thz radiation. *Nature Photonics*, 17(3):259–263, 2023.

[121] Zhen Zhang, Lixin Yan, Yingchao Du, Zheng Zhou, Xiaolu Su, Lianmin Zheng, Dong Wang, Qili Tian, Wei Wang, Jiaru Shi, et al. Tunable high-intensity electron bunch train production based on nonlinear longitudinal space charge oscillation. *Physical review letters*, 116(18):184801, 2016.

[122] S Antipov, M Babzien, C Jing, M Fedurin, W Gai, A Kanareykin, K Kusche, V Yakimenko, and A Zholents. Subpicosecond bunch train production for a tunable mj level thz source. *Physical review letters*, 111(13):134802, 2013.

[123] Francois Lemery, Philippe Piot, Gayane Amatuni, Prach Boonpornprasert, Y Chen, J Good, Bagrat Grigoryan, Matthias Gross, M Krasilinikov, Osip Lishilin, et al. Passive ballistic microbunching of nonultrarelativistic electron bunches using electromagnetic wakefields in dielectric-lined waveguides. *Physical review letters*, 122(4):044801, 2019.

[124] P Muggli, V Yakimenko, M Babzien, E Kallos, and KP Kusche. Generation of trains of electron microbunches with adjustable subpicosecond spacing. *Physical review letters*, 101(5):054801, 2008.

[125] Y-E Sun, P Piot, A Johnson, AH Lumpkin, TJ Maxwell, J Ruan, and R Thurman-Keup. Tunable subpicosecond electron-bunch-train generation using a transverse-to-longitudinal phase-space exchange technique. *Physical review letters*, 105(23):234801, 2010.

[126] P Musumeci, RK Li, and A Marinelli. Nonlinear longitudinal space charge oscillations in relativistic electron beams. *Physical review letters*, 106(18):184801, 2011.

[127] P Musumeci, RK Li, KG Roberts, and E Chiadroni. Controlling nonlinear longitudinal space charge oscillations for high peak current bunch train generation. *Physical Review Special Topics-Accelerators and Beams*, 16(10):100701, 2013.

[128] Shian Zhou, Dimitre Ouzounov, Heng Li, Ivan Bazarov, Bruce Dunham, Charles Sinclair, and Frank W Wise. Efficient temporal shaping of ultrashort pulses with birefringent crystals. *Applied optics*, 46(35):8488–8492, 2007.

[129] M Modena, A.R. Bainbridge, J.A. Clarke, N.A. Collomb, and B.J.A Shepherd. The zepto dipole: zero power tuneable optics for clic. *Proceedings of IPAC2017, THPIK105*, 2017.

[130] Takahiro Watanabe, Tsutomu Taniuchi, Shiro Takano, Tsuyoshi Aoki, and Kenji Fukami. Permanent magnet based dipole magnets for next generation light sources. *Physical Review Accelerators and Beams*, 20(7):072401, 2017.

[131] A Fisher, Y Park, M Lenz, A Ody, R Agustsson, T Hodgetts, A Murokh, and P Musumeci. Single-pass high-efficiency terahertz free-electron laser. *Nature Photonics*, 16(6):441–447, 2022.

[132] Maximilian Lenz, Andrew Fisher, A Ody, Y Park, and Pietro Musumeci. Electro-optic sampling based characterization of broad-band high efficiency thz-fel. *Optics Express*, 30(19):33804–33816, 2022.

[133] A Doria, GP Gallerano, E Giovenale, S Letardi, G Messina, and C Ronsivalle. Enhancement of coherent emission by energy-phase correlation in a bunched electron beam. *Physical review letters*, 80(13):2841, 1998.

[134] GP Gallerano, A Doria, E Giovenale, and A Renieri. Compact free electron lasers: From cerenkov to waveguide free electron lasers. *Infrared physics & technology*, 40(3):161–174, 1999.

[135] A. Doria, G. P. Gallerano, E. Giovenale, G. Messina, and I. Spassovsky. Enhanced coherent emission of terahertz radiation by energy-phase correlation in a bunched electron beam. *Phys. Rev. Lett.*, 93:264801, Dec 2004.

[136] Heishun Zen, Hideaki Ohgaki, and Ryoichi Hajima. High-extraction-efficiency operation of a midinfrared free electron laser enabled by dynamic cavity desynchronization. *Physical Review Accelerators and Beams*, 23(7):070701, 2020.